DEVICE-FREE DETECTION AND LOCALIZATION OF PEOPLE USING UWB NETWORKS

YAKUP KILIÇ

Device-Free Detection and Localization of People Using UWB Networks

by

Yakup Kılıç

Ph.D. Dissertation Committee:

Chairman & Secretary:

Prof.dr. P. M. G. Apers	University of Twente, the Netherlands

Promoter:

Prof.dr. W. G. Scanlon	University of Twente, the Netherlands and Queen's University Belfast, Northern Ireland, UK

Assistant Promoters:

Dr.ir. M. J. Bentum	University of Twente, the Netherlands
Dr.ir. A. Meijerink	University of Twente, the Netherlands

Internal Members:

Prof.dr.ir. F. B. J. Leferink	University of Twente, the Netherlands
Prof.dr.ir. R. N. J. Veldhuis	University of Twente, the Netherlands
Dr.ir. A. B. J. Kokkeler	University of Twente, the Netherlands

External Members:

Prof.dr.ir. P. G. M. Baltus	Eindhoven University of Technology, the Netherlands
Dr.ir. G. J. M. Janssen	Delft University of Technology, the Netherlands

CTIT

CTIT Ph.D. Thesis Series No. 15-350
Centre for Telematics and Information Technology,
P.O. Box 217, 7500 AE, Enschede, the Netherlands.

The research presented in this thesis was carried out at the Telecommunication Engineering group, Faculty of Electrical Engineering, Mathematics and Computer Science, University of Twente, P.O. Box 217, 7500 AE, Enschede, the Netherlands.

ISBN: 978-90-365-3851-0
ISSN: 1381-3617 (CTIT Ph.D. thesis Series No. 15-350)
DOI: 10.3990/1.9789036538510 (http://dx.doi.org/10.3990/1.9789036538510)

Printed by Gildeprint Drukkerijen
Typeset in LaTeX 2ε

Device-Free Detection and Localization of People Using UWB Networks

Dissertation

to obtain
the degree of doctor at the University of Twente,
on the authority of the Rector Magnificus
prof.dr. H. Brinksma
on account of the decision of the graduation committee,
to be publicly defended
on Thursday, 21 January 2016 at 16:45.

by

Yakup Kılıç

born on 28 May 1985
in Istanbul, Turkey

This thesis has been approved by:

Prof.dr. W. G. Scanlon (Promoter)
Dr.ir. M. J. Bentum (Assistant Promoter)
Dr.ir. A. Meijerink (Assistant Promoter)

Summary

Wireless localization and tracking have attracted a great deal of research interest from the research community, as location-awareness is fast becoming an essential feature in many application areas. For indoor scenarios, ultra-wideband (UWB) transmission is a promising technology, due to its high-resolution ranging and obstacle penetration capabilities. Most practical UWB localization systems rely on targets (e.g., objects, people) to carry an active UWB device, which is used to facilitate time-difference-of-arrival or time-of-arrival measurements. In some scenarios (e.g., intruder detection, elderly care, smart environments, emergency response) it is desirable to have the ability to track people and assets in a passive manner, without requiring them to be equipped with any radio-frequency (RF) device. This is commonly known as *device-free* localization and it is an emerging area in wireless localization research. Traditional device-free localization techniques were vision-based, relying on infrared motion detectors and video camera surveillance, but were limited to visible line of sight (LOS). Modern techniques overcome this problem through RF-based transmission, where received RF signals are affected by the presence of people or assets in a quantifiable way. Research in this area can be broadly differentiated based on the narrowband and wideband nature of the signals involved.

Because of the reflections due to a person, the multipath propagation differs when a person enters into an environment. This can be observed through the received signal strength (RSS) levels, which strongly decrease when the person is blocking the direct path. The varying multipath fading also causes variations in the RSS. Most narrowband techniques use this information through comparing the RSS levels when the person is in the environment or not, or model the changes in the signal strength for different positions of the person. In general, the high availability and low-cost implementation of narrowband radios are quite attractive for device-free localization. However, the susceptibility of the system to multipath fading makes it hard to develop accurate models for dense, cluttered environments or it requires to develop a training database which is vulnerable to any changes in the environment. These drawbacks can be overcome by considering larger RF bandwidths.

The high time resolution property of UWB radios can make it possible to resolve the human-body reflected path among all the other multipath reflections. This reflected path changes over time due to minuscule movements, even

though the person seemingly stands still. Because of this, the corresponding received signal samples also vary over time. This observation is presented for an experimental UWB system and forms the basis of the device-free person detection and localization technique in this thesis. The technique collects the energy in the variations of the signal and estimates the travelling distance for the human-body reflected path through its delay estimation. Each estimate draws an ellipse around the transmitter and the receiver for the position of the person. By combining multiple ellipses, a unique position estimate is given for many different positions of the person in an indoor environment. The technique detects the presence of the person in each case. The error related to the length of the human-body reflected path estimation is obtained on the order of 50 cm. The median and root-mean-square localization error is obtained as 0.75 m and 1 m, respectively, in an indoor office environment where a person stands on different grid positions in an area of 5×5 m.

The received signal samples show different variations depending on the random movement of each person. This gives us a way to detect a second person in the environment without extending the measurement setup. By quantifying the correlations between the samples of the received signal, we can understand if the samples are affected by the same person or not. The correlation value is higher if samples are affected by the same person and remains low if the samples are affected by different persons. A detection and device-free ranging method is given for the second person. By further quantifying the correlations between the samples of the received signal related to two different links, we can match the samples affected by the same person in different links. A localization method for multiple persons is developed, which combines multiple link correlations. The technique detects the second person in 70% of the measurements performed (i.e., in total seventeen different measurement scenarios). Furthermore, the median and root-mean-square localization errors of 0.4 m and 1.7 m are obtained, respectively.

Samenvatting

Draadloze lokalisatie en *tracking* (volgen) hebben veel belangstelling gewekt in de onderzoeksgemeenschap, aangezien kennis van de positie van een persoon of object hard op weg is een essentieel onderdeel te worden in veel toepassingsgebieden. Voor binnenhuis-scenario's is *ultra-wideband* (UWB) transmissie een veelbelovende techniek, dankzij de nauwkeurige afstandsmeting en de mogelijkheid om door belemmerende objecten heen te dringen. De meeste operationele UWB-lokalisatiesystemen zijn gebaseerd op de aanname dat de *targets* (doelen, bijvoorbeeld objecten of personen) een actief UWB-apparaat bij zich dragen dat gebruikt wordt om de metingen van tijdsverschil-van-aankomst of tijd-van-aankomst te faciliteren. In sommige scenario's (bijvoorbeeld indringerdetectie, ouderenzorg, intelligente omgevingen en rampenbestrijding) is het wenselijk de mensen en bezittingen, passief te kunnen volgen, oftewel zonder te vereisen dat ze uitgerust zijn met een radiofrequent (RF) apparaat. Dit staat bekend als *device-free* (apparaatloze) lokalisatie, een nieuw opkomend onderzoeksgebied in draadloze lokalisatie. Traditionele technieken voor device-free lokalisatie waren gebaseerd op zicht, vertrouwend op infrarood bewegingssensoren en videocameratoezicht, maar waren beperkt tot het gezichtsveld. Moderne technieken omzeilen dit probleem door gebruik te maken van RF-straling, waarbij de RF-signalen op een meetbare manier worden beïnvloed door de aanwezigheid van personen of objecten. Onderzoek in dit gebied kan grofweg worden onderverdeeld op basis van de smalbandige en breedbandige aard van de betrokken signalen.

Door de reflecties ten gevolge van een persoon verandert de *multipath*propagatie wanneer een persoon een omgeving binnen-komt. Dit kan worden waargenomen door een sterke afname van de ontvangen signaal-sterkte (received signal strength, RSS) als een persoon de directe baan blokkeert. De variaties in *multipath fading* veroorzaken ook variaties in de RSS. De meeste smalbandige technieken gebruiken dit soort informatie door RSS-niveaus te vergelijken wanneer een persoon aanwezig is of niet, of -modelleren de variaties in signaal-sterkte voor verschillende posities van de persoon. In het algemeen zijn de hoge beschikbaarheid en de lage implementatiekosten van smalbandige radio's -aantrekkelijk voor device-free lokalisatie. De gevoeligheid van het systeem voor multipath fading maakt het echter moeilijk nauwkeurige modellen te ontwikkelen voor drukke chaotische omgevingen, of het is noodzakelijk een

training database te ontwikkelen die weer kwetsbaar is voor veranderingen in de omgeving. Deze nadelen kunnen worden omzeild door het gebruik van grotere RF-bandbreedtes.

De hoge tijdsresolutie van UWB-radio's kan het mogelijk maken reflecties van het menselijk lichaam te detecteren tussen alle andere multipath-reflecties. Deze reflecties veranderen gedurende de tijd door minuscule bewegingen, ook al lijkt de persoon stil te staan. Hierdoor variren de overeenkomstige ontvangen signaal monsters ook in de tijd. Deze observatie wordt gepresenteerd voor een experimenteel UWB-systeem en dit vormt de basis van de device-free persoonsdetectie- en lokalisatietechniek in dit proefschrift. De techniek verzamelt de energie in de variaties van het signaal en schat de baanlengte van de reflectie van het menselijk lichaam door de vertraging te schatten. Elke schatting tekent een ellips rond de zender en de ontvanger door de positie van de persoon. Door het combineren van meerdere ellipsen wordt een unieke positieschatting gegeven voor vele verschillende posities van de persoon in een omgeving binnenshuis. De techniek detecteert de aanwezigheid van de persoon in iedere keer. Daarbij is vastgesteld dat de fout gerelateerd aan de schatting van de baanlengte van de reflectie van het menselijk lichaam in de ordegrootte van 50 cm ligt. De gevonden mediaan en de effectieve waarde van de lokalisatiefout zijn respectievelijk $0,75$ m en 1 m, in een kantooromgeving waar een persoon op verschillende roosterposities in een 5×5 m ruimte staat.

De ontvangen signaalmonsters laten verschillende variaties zien, afhankelijk van de willekeurige beweging van elk persoon. Dit geeft een manier om een tweede persoon in de omgeving te detecteren zonder de meetopstelling uit te breiden. Door de correlatie tussen de monsters van het ontvangen signaal te kwantificeren kunnen we vernemen of de monsters door dezelfde persoon worden beïnvloed of niet. De correlatiewaarde is hoger als de monsters beïnvloed worden door dezelfde persoon en blijven laag wanneer de monsters door verschillende personen worden benvloed. Een methode wordt gegeven voor detectie en device-free afstandsmeting voor de tweede persoon. Door het verder kwantificeren van de correlaties tussen de monsters van het ontvangen signaal, gerelateerd aan twee verschillende radioverbindingen, kunnen we de monsters koppelen die worden, beïnvloed door dezelfde persoon in verschillende radioverbindingen. Een lokalisatie-methode voor meerdere personen is ontwikkeld, welke correlaties tussen meerdere verbindingen combineert. De techniek detecteert de tweede persoon in 70% van de uitgevoerde metingen (d.w.z. in totaal zeventien verschillende meetscenario's). Verder zijn de mediaan en de effectieve waarde van de lokalisatiefout respectievelijk $0,4$ m en $1,7$ m.

Özet

Kablosuz konumlandırma ve takip, konum bilgisinin birçok uygulama alanında gerekli bir nicelik olmasından dolayı son zamanlarda pek çok arastırmacının ilgisini cekmiştir. Çok geniş bant (ultra-wideband, UWB) iletim teknolojisi, yüksek çözünürlüklü mesafe ölçümü ve engel girim yeteneklerinden dolayı, özellikle binaiçi senaryoları için kayda değer bir seçenektir. Uygulamada pek çok UWB konumlandırma sistemi, hedefin (ör., nesneler, insanlar) aktif bir UWB aygıtı taşımasını, ve bu aygıtın varış zamanı ve varış zamanları arasındaki fark ölçümleri yapmasını göz önünde bulundurur. Bazı uygulama senaryolarında (ör., hırsızlık algılama, yaşlı bakımı, akıllı ortamlar, tehlike anında yanıt verme), insanların ve değerli nesnelerin herhangi bir radyo-frekans (RF) cihazı taşımasına gerek kalmadan takibi gerekli görülebilir. Bu genel olarak aygıtsız (device-free) konumlandırma olarak bilinir ve kablosuz konumlandırma araştırmaları arasında son zamanlarda öne çıkan bir araştırma alanıdır. Geleneksel aygıtsız konumlandırma yöntemleri görüş tabanlıydı yani kızılötesi hareket algılama ve video kamera gözetleme üzerine dayanmaktaydı. Ancak bu sistemler insanla ya da nesneyle aradaki görüş çizgisinin açık, bir başka deyişle gözle görülebilir olmasına ihtiyaç duymaktaydı. Modern yöntemler ise bu gereksinimi RF-tabanlı iletimle, RF sinyallerinin insanların ya da nesnelerin varlığından nicelenebilir olarak etkilenmesi gerçeğinden yararlanarak aşarlar. Bu alandaki araştırma, genel olarak iletilen sinyallerin dar bant ya da geniş bant olmasına bağlı olarak ayrılabilir.

İnsanlardan kaynaklanan sinyal yansımalarından ötürü, çokyollu yayılma (multipath propagation) insanlar bir ortama girdiğinde farklılaşır. Bu etki alıcıda ölçülen alınan sinyal gücü (received signal strength, RSS) seviyelerinde gözlemlenebilir. Örneğin, bir insanın tam olarak iki cihaz arasında bulunduğu, yani alıcı ve verici arasındaki görüş çizgisini engellediği durumlarda, alınan sinyal gücü ciddi şekilde düşer. Bunun yanında değişen çokyollu sönümleme (multipath fading) de RSS seviyelerinde değişimlere sebep olur. Birçok dar bant çözümü, bu bilgiyi RSS seviyelerinin insanın ortamda olduğu ya da olmadığı durumlar için karşılaştırılması ya da sinyal gücündeki değişimlerin insanın farklı konumları için modellenmesi şeklinde kullanır. Genel olarak dar bant radyoların piyasada yüksek miktarda bulunması ve ucuza mal edilebilebiliyor olmasından dolayı, bu sistemler aygıtsız konumlandırma için çok cazip bir seçenek oluşturur. Ancak, bu sistemlerin çok yollu sönümlemeden kolayca etkileniyor

olması, özellikle yoğun ve darmadagın ortamlar için hassas modellerin geliştirilmesini zorlaştırır. Bu güçlük insanların ortamda olmadığı ve farklı konumlarda olduğu durumlar için, RSS seviyelerinden oluşan eğitim veritabanları yardımıyla cözülebilir. Ancak bu sefer de oluşturulan veritabanları ortamdaki en ufak bir değişiklikten (ör., mobilyanın yerinin değiştirilmesi) kolayca etkilenir ve yeniden oluşturulmaları gerekir. Bu güçlükler daha yüksek bant genişlikleri göz önünde bulundurularak ortadan kaldırılabilir.

UWB radyolarının yüksek zaman çözünürlüğü özelliği, insan vücudundan yansıyan sinyallerin diğer bütün yansımaların içinden ayrıştırılabilmesini mümkün kılar. Bu yansıyan sinyal, insan sabit bir şekilde duruyor gözükse bile, çok küçük hareketlere (ör., nefes alıp verme) bağlı olarak zamanla değişir. Bu etki, aynı zamanda, yansıyan sinyallere karşılık gelen alınan sinyal örneklerinin de zamanla degişmesine neden olur. Deneysel bir UWB sistemi için sunulan bu gözlem, bu tezde geliştirilen aygıtsız insan algılama ve konumlandırma yönteminin temelini oluşturur. Bu yöntem sinyaldeki değişimlerin enerjisini toplar ve insandan yansıyan sinyallerin ne kadar seyahat ettiğini gecikme kestirimi yardımıyla kestirir. Her bir kestirim, insanın konumu için alıcı ve verici etrafında bir elips çizer. Birden fazla elipsin birleştirilmesiyle, tek bir konum kestirimi mümkün olmaktadır ve bu tezde binaiçinde insanın bulunduğu pek çok farklı pozisyon için konum kestirimleri gösterilmiştir. Geliştirilen yöntem herbir durumda insanın var olup olmadığını bulabilmektedir. Bunun yanında, insandan yansıyan sinyallerin katettiği yol kestirimi için bulunan hata 50 cm seviyesindedir. Medyan ve ortalama karesel konumlandırma hataları, insanin grid üzerinde farklı konumlarda bulundugu 5×5 m'lik bir alanda binaiçi ofis ortamı için sırasıyla $0,75$ m ve 1 m olarak bulunmuştur.

Alınan sinyal örnekleri, herbir insanın raslantısal hareketleri için farklı degişimler gösterir. Bunu kullanarak ölçüm düzeninde herhangi bir değişikliğe gitmeden ortamdaki ikinci bir insanın varlığını algılayabiliriz. Alıcı sinyal örnekleri arasındaki ilintinin miktarının ölçülmesiyle, örneklerin aynı ya da farklı insanlar tarafından etkilendiği ya da etkilenmediği söylenebilir. Bulunan ilinti değeri eğer örnekler aynı insan tarafından etkilenmisse yüksek, farklı insanlar tarafından etkilenmişse düşük çıkar. Bu tezde ikinci bir insan için bir algılama ve aygıtsız mesafe ölçümü yöntemi geliştirilmiştir. Alıcı sinyal örnekleri arasındaki ilinti miktarının iki farklı iletim hattı için ölçülmesiyle, bu iletim hatlarında aynı kişi tarafından etkilenen örnekleri birbirleriyle eşleştirilebilinir. Buna bağlı olarak bu tezde aynı zamanda birden fazla insanin konumlandırılması için bir yöntem geliştirilmiştir. Bu yöntem birden fazla iletim hattı için alınan sinyal örnekleri arasındaki ilintiyi ölçer ve ikinci bir insanı toplamda onyedi farklı ölçüm içerisinden, ölçümlerin %70i için algılamıştır. Bunun yanında medyan ve ortalama karesel konumlandırma hataları sırasıyla $0,4$ m ve $1,7$ m olarak elde edilmiştir.

To my grandfather Mustafa Kılıç

Contents

Chapter 1

Introduction

1.1 Indoor Wireless Localization

Location awareness is fast becoming an essential feature in many indoor application areas since indoor wireless localization and tracking have attracted a great deal of interest from the research community [1–4]. These application areas vary from rescue operations (e.g., locating fire fighters or victims in emergency situations) to asset tracking (e.g., locating the equipment in a warehouse or in hospitals), direction finding (e.g., guiding customers through a shopping mall, or in museums), patient/elderly or environment monitoring, and entertainment (e.g., 3D motion detection for gaming or the movie industry).

Most localization systems are either developed based on the existing wireless infrastructure, considering the localization as an additional service, or wireless systems developed for a specific positioning[1] application. Global Positioning System (GPS) is a world-wide available satellite-based positioning technology, but it is limited to outdoor environments because of its lack of capability to penetrate through obstacles (e.g., walls). In fact, indoor signal propagation environments are often very complex because of the presence of obstacles and, of course, any human occupants. Wireless signals either have to go through these obstacles, resulting in an attenuation of the signals (also known as shadowing), and/or are reflected from these obstacles, causing a multipath fading effect. Because of these propagation effects, building an accurate indoor localization system is often a challenging task.

To overcome the limitations of GPS in indoor environments, the Assisted-GPS (A-GPS) technology was developed by SnapTrack (now part of Qualcomm). In addition to the GPS satellites, A-GPS also employs the GSM network to determine the location and provides localization accuracies of 5–50 m [5]. Mobile cellular networks have also been utilized for location estimation, originally achieved by simply establishing the cell identifier. However, the ac-

[1] In this thesis, the terms localization and positioning are used interchangeably for finding the position of a wireless node or an object/person in a reference coordinate system.

curacy, being the absolute error between the estimated and the true positions, of such systems is generally very low, in the range of 50–200 m, depending on the density of the base stations or the cell size [4]. [6] had a median accuracy of 5 m, by employing six strongest GSM cells and readings of up to 29 additional GSM channels, whose signals are too weak for normal communication service.

Wireless local area networks (WLANs), another commonly available technology, were also utilized for localization purposes, in addition to their high data rate indoor communication capability. IEEE 802.11 is currently the dominant WLAN standard family with a typical range of 50–100 m and suitable for indoor localization applications. The earliest works [7, 8] were based on establishing a relationship between the received signal strength (RSS) and the distance by relying on the fact that the wireless signals attenuate by distance (i.e., the attenuation increases with increasing distance due to geometrical spreading). However, it is often hard to find a reliable model that explains such a relation, because of the challenging characteristics of the indoor propagation environment. Specifically, in [7], the localization error is calculated based on the standard deviation of the position estimates and found out to be 1.4–2.8 m and 2.1–5.6 m in a 30×30 m simulation environment with five and three anchors, respectively. The localization accuracies based on the mean absolute localization error of these systems are usually in between 3 and 30 m [9]. [10] proposed an approach, based on the empirical measurements of access point signal strength in different locations. The authors first recorded the radio signal strength information with the actual positions of the user to construct and validate models for signal propagation. This was referred to as the offline phase. During this phase the system is trained using the signal strength and actual positions of the user to infer the location in real time when only the signal strength information is available. The latter step, during which the location estimation is performed, is commonly referred as the online or real-time phase. During the online phase, the authors adopted an empirical method, which they called the nearest neighbors in the signal space, to find the user position based on the measurements in the offline phase. With this approach, [10] achieves around 3-m median location errors in a 43.5×22.5-m measurement environment. The authors also proposed an approach based on the radio propagation modelling and obtained 4.3-m median location error for the same setup.

The former approach in [10] was further advanced by fingerprinting techniques, which have an offline measurement stage to create a radio map of the environment, and an online phase in which the device (to be located) compares the actual received signal strength information with the existing radio map to determine its position. There are different methods employed during the online phase, such as the clustering approach [11], the machine-learning approach [12], the Bayesian network approach [13] and stepwise refinement algorithms [14]. In [11] and [12], the achieved median location errors were as low as 1.2 m and 1.45 m for the measurements performed in 68×26-m and 16×40-m environments. According to the measurements performed in a 68×30-m environment, in [13] the localization system could detect the large conference rooms with

a probability between 0.8 and 1, but largely failed to detect adjacent offices with dimensions of 2.4×4.2 m. In this case, the detection probability was in between 0.4 and 0.6. The proposed refinement algorithms in [14] improved the localization performance of [10] and [12] by up to 40% and 23%, in three different simulation environments of 686, 1050 and 1104 m^2, respectively. Even though the reported localization errors with WLAN fingerprinting techniques are lower, in general the system is vulnerable to changes in the propagation environment (e.g., movement of the furniture), because these changes also affect the multipath characteristics of the environment. A new radio map needs to be created each time to adapt the system to these changes. Furthermore, indoor environments are usually populated and people affect these systems quite severely because of their effect on radio propagation between the devices. For instance, a radio map created without any person in the environment might not be a good reference when there are people.

Radio-frequency identification (RFID) is another alternative for indoor localization, which consists of small tags, easily worn by the people or attached to the objects to be tracked. There are passive and active RFID tags for indoor positioning. Although they are very inexpensive and operate without a battery, passive RFID systems have a very small coverage, about 2–3 m [9,15]. SpotON [16] is an earlier example of an active RFID-based indoor localization system, which employs RSS information to locate assets in a three-dimensional (3D) space. LANDMARC [17] is another active-RFID-based system, which, in addition to the RFID readers, also employs extra fixed reference tags to improve the accuracy of the system. The system does not increase the cost much by using more tags instead of readers (i.e., tags are usually cheaper than the readers). In [17], experimental results were shown for measurements performed in a 5×10 m environment for two different configurations with four RF readers, sixteen reference tags and eight target tags to be located. According to these results, the LANDMARC system had a median error of around 1 m and maximum errors which were lower than 2 m.

Other indoor positioning technologies include Bluetooth, which has a short coverage (typically 10–15 m) and offers around room-level accuracy [9, 15], and hybrid methods which employ all the available resources to be used for an accurate positioning system. For instance, in [18], a multi-modal localization approach is developed using the information from WLAN radio, cellular infrastructure, and the acceloremeter and magnetometer that are commonly available in current smart phones. The system proposed in their work achieves an accuracy up to 1.5 m.

1.2 UWB Positioning

Ultra-wideband (UWB) is claimed to be a very promising technology for indoor positioning because of its high time resolution capabilities [19–23]. UWB systems generally have a bandwidth on the order of a few gigahertz, which potentially provides sub-nanosecond scale resolution in time. When combined

with time-based range estimation methods such as time of arrival (TOA), two-way TOA or time difference of arrival (TDOA), this property may lead UWB to achieve ranging accuracies in the order of few centimeters. Furthermore, the huge bandwidth feature also provides good penetration through obstacles, since UWB contains low-frequency components, which can penetrate through obstacles. This is an advantage over the limitations of GPS for indoor usage. However, the output power density of the UWB signals are limited to let the UWB transmission occur without causing a significant interference to other wireless technologies. This in turn limits the range of the system despite the low-frequency advantage over GPS.

Moreover, UWB systems are commonly implemented as an impulse radio (IR) which transmits very short pulses with a duration in the nanoseconds scale. IR-UWB schemes do not require an upconversion step, which normally requires a mixer and a local oscillator. This is another advantage of UWB over other techniques for low-cost and low-power positioning applications.

In the rest of this section, more details of UWB positioning will be given, by first describing the regulations on UWB, and then, the details of the time-based positioning techniques with UWB will be explained.

1.2.1 Regulations on UWB

In this part, the output power limitations imposed by the Federal Communications Commission (FCC) in the United States (US) and the Electronic Communications Committee (ECC) in Europe will be described.

FCC Regulations

While early names for UWB technology include baseband, carrier-free, and non-sinusoidal, the name of UWB was first coined by the US department of defence in the late 1980s [3]. In general, UWB signals are distinguished from the traditional narrow-bandwidth signals by their ultra-wide bandwidth nature. According to the FCC, a signal is defined as a UWB signal, if it has a fractional bandwidth that is larger than 20%, or an absolute bandwidth of at least 500 MHz. The absolute bandwidth is defined by the difference between upper and the lower frequencies, which are measured at -10 dB below the peak emission point (i.e., -10-dB bandwidth). The fractional bandwidth is defined as the ratio of the bandwidth to the center frequency, which can be found from the summing the highest and the lowest frequency and then dividing by two.

Because of its very wide bandwidth nature, UWB may partly occupy the frequency bands of other wireless technologies potentially causing high levels of interference and jam their transmission. Therefore, UWB emission power is subject to to strict regulation. As the interest grew in UWB (especially for high-speed data communications), the FCC in the US started a specification definition system in the late 90s and issued their first report on the power regulations in 2002 [24]. The FCC spectral mask specifies the limits of the allowed transmitted power density for a useful spectrum of 7.5 GHz for most

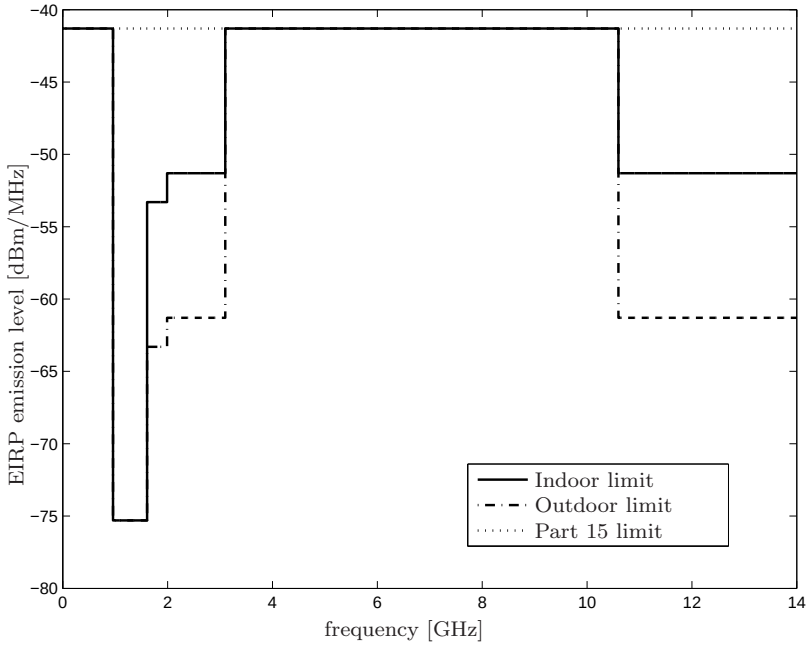

Figure 1.1: FCC emission limits for indoor and outdoor UWB ranging and communication systems [24].

UWB systems. The limitations are specified in terms of the equivalent isotropically radiated power (EIRP), which is defined as the product of the power supplied to an antenna and its gain in a given direction relative to an isotropic antenna. Fig. 1.1 shows the maximum allowed EIRP emission levels defined for indoor and outdoor UWB communication and ranging systems. The figure also shows the Part 15 limit, which describes the maximum emissions allowed for unintentional radiators such as television and computer monitors. According to the FCC spectral mask, the maximum emission cannot go beyond the Part 15 limit, which is defined to be -41.3 dBm in any 1-MHz signal bandwidth, making UWB signalling as a noise-like transmission for other systems. The difference between indoor and outdoor emission limits lies in the frequency band between 1.61 and 3.1 GHz, and beyond 10.6 GHz. According to the regulations, the transmission in outdoor environments should be attenuated by an additional 10 dB for these frequency intervals. Furthermore, as the spectral mask in Fig. 1.1 shows the limitations on average power emissions, peak power emissions are not allowed to be larger than 0 dBm EIRP within any 50 MHz signal bandwidth.

Regulations in Europe

In Europe, the technical studies for UWB regulations were undertaken by the ECC of the European Conference of Postal and Telecommunications Administrations (CEPT). In 2005, the first draft decision on *the harmonized conditions for devices using UWB technology in bands below 10.6 GHz* was forwarded to the ECC by Task Group 3 within CEPT [25]. The recommendations of ECC were considered by the Radio Spectrum Committee (RSC) of the European Commission (EC), which published the final decision on *allowing the use of the radio spectrum for equipment using UWB technology in a harmonized manner in the Community* at the beginning of 2007. The spectrum mask imposed by the EC, which is valid after the end of 2010, is as shown in Fig. 1.2. According to these regulations, UWB is allowed to operate between 6 and 8.5 GHz with a maximum emission level of -41.3 dBm/MHz, and with a maximum peak power limit of 0 dBm, defined in any 50-MHz signal bandwidth. The operation in the lower frequency range between 3.4 and 4.8 GHz is also allowed with higher EIRP limits if appropriate interference mitigation techniques are employed. Namely, a maximum EIRP density of -41.3 dBm/MHz is allowed in the 3.4–4.8 GHz band, provided that a low duty cycle restriction is applied with the following requirements [25]:

- $T_{\text{on}}(\text{maximum}) = 5$ ms,
- $T_{\text{off}}(\text{mean}) \geq 38$ ms (averaged over 1 second),
- $\Sigma T_{\text{on}} < 5\%$ per second and 0.5% per hour.

where T_{on} is the duration of a burst, and T_{off} is the time interval between consecutive bursts, when the UWB emission is kept idle. T_{on} is considered irrespective of the number of pulses in the burst and ΣT_{on} shows the total time when the transmitter is on.

The EC decision on UWB is currently under revision [26]. For instance, there are also ongoing efforts to consider other mitigation techniques. In the most recent report of ETSI [26], it is mentioned that within the 3.1–4.8-GHz and 8.5–9-GHz bands, the devices implementing Low Duty Cycle and Detect and Avoid mitigation techniques are permitted to operate with a maximum spectral density of -41.3 dBm/MHz and a maximum peak power of 0 dBm defined in any 50 MHz signal bandwidth. According to the definition of Detect and Avoid mitigation, the system should sense the channel to detect the possible presence of other systems within its operating bandwidth before transmitting any signal. The system should avoid transmission if another system is detected and starts again only after the detected system has disappeared.

1.2.2 Localization Methods

In a wireless localization system, the problem of interest is to find the position of a target node in a system which also involves anchor/beacon node(s) with

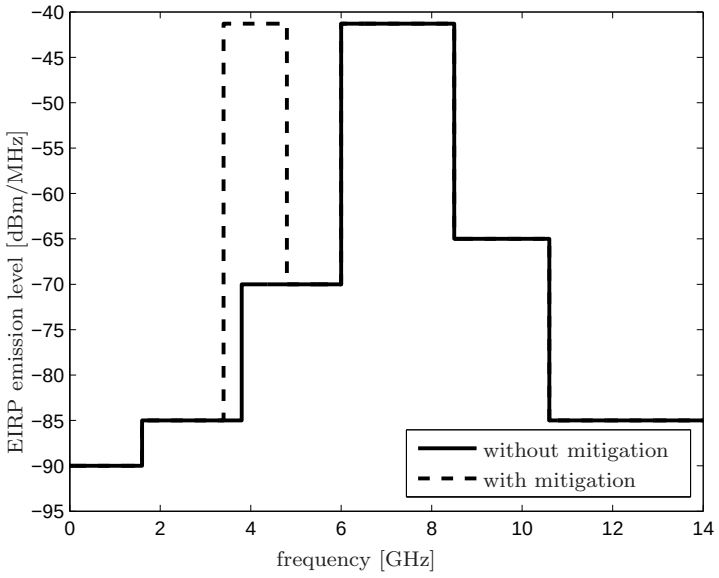

Figure 1.2: ECC emission limits without and with appropriate interference mitigation techniques [26].

known position(s). Range-based wireless positioning systems consist of two steps. In the first step, the distance and/or angle information is extracted from the received wireless signals, transmitted between an anchor node and the target node. In the second step, the distance or angle information from different anchor-target pairs is combined to find the final position of the target. Depending on the application, both steps can be performed in the target node, or the ranging step can be performed in the anchor nodes and the position-related information is forwarded to a central unit (e.g., a host computer) for the positioning step.

So far, RSS-based, angle-based and time-based methods have been considered for the ranging step in UWB localization literature. While we will give brief information about the first two, more details will be given for time-based ranging techniques, since they are more promising than RSS-based techniques in terms of localization accuracy, and less complex compared to angle-based techniques.

RSS-based Techniques

RSS-based techniques exploit the distance dependency of the RSS to estimate the range, as earlier mentioned in Section 1.1. They are mainly attractive because of the availability of the RSS information in almost all wireless receivers.

In general, the received signal power decays with the increase in the distance. Given a reference signal power $P_{\mathrm{r},0}$ at a reference distance $d_{\mathrm{r},0}$, the received signal power at distance d is usually approximated as [3]

$$P_{\mathrm{r}} = P_{\mathrm{r},0} - 10\eta \log_{10}\Big(\frac{d}{d_{\mathrm{r},0}}\Big), \tag{1.1}$$

where P_{r} and $P_{\mathrm{r},0}$ are expressed in dBm or dBW, and η is the path-loss exponent, which is (usually) environment-dependent. For instance, the path loss exponents obtained in line-of-sight (LOS) environments are usually smaller than the ones obtained in non-line-of-sight (NLOS) environments. The relation in (1.1) does not include multipath fading (also known as small-scale fading) and shadowing effects [27]. Small-scale fading causes local variations (i.e., for small changes in distance such as on the order of half wavelength) of the received signal power around the local mean, while the shadowing effect causes larger scale variations around the local mean. The effect due to the small-scale fading diminishes in UWB systems because of the good multipath resolution capability [3]. However, P_{r} strongly depends on the number of multipath sources as the received signal power will be higher for the same distance in multipath-rich environments. This requires good calibration of the parameters η and $P_{\mathrm{r},0}$ for different environments, and a priori knowledge (or an accurate estimate) of the environment. Furthermore, there is still the effect of shadowing. For instance, indoor environments are densely populated and the movements of people cause temporal variations in the signal strength, when they block the signal transmission [28–30]. This may decrease the accuracy of the signal-strength-based techniques.

Angle-of-Arrival (AOA)

AOA measurement provides the direction information of an incoming signal, travelling from the transmitter to the receiver. Commonly, antenna arrays are employed at the receiver to estimate the AOA of a signal. AOA information is obtained by measuring the differences in arrival times of an incoming signal at different antenna elements [3]. When only AOA information is used, two reference nodes are enough to locate the target node in a two-dimensional space, assuming the two reference nodes and the target node do not lie in a straight line, and the reference nodes share the same orientation reference [31]. In this case, localization is performed as shown in Fig. 1.3, by combining two straight lines that can be drawn from two reference nodes to the target node with the given AOA information [23]. This is also known as triangulation. If the distance information is also available, a target node can be localized by combining the distance and AOA information and using only one reference node. AOA did not attract much research effort in comparison to time-based ranging approaches, as it requires an antenna array for estimation of the AOA. In general, time-based approaches can already provide centimeter-level accuracy without an antenna array requirement and therefore utilize the advantages of UWB for positioning, without requiring the additional complexity [3].

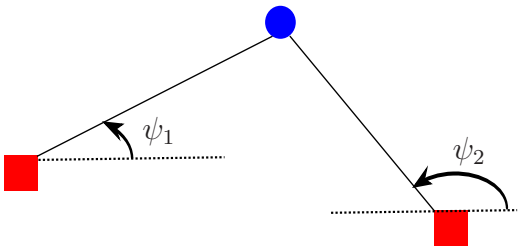

Figure 1.3: Triangulation: anchor nodes are shown as red squares, the target node is shown as a blue circle, and ψ_1 and ψ_2 denote the measured angles.

Time-based Techniques

As briefly mentioned in the beginning of this section, the time-based ranging techniques have attracted more interest for UWB positioning, since they provide accuracies on the order of a few centimeters. If the transmitter and receiver have a common clock, the arrival time of the signal can be found by TOA estimation methods at the receiver. Knowing the reference time (i.e., the time instant that the signal is transmitted), the propagation delay can simply be calculated by subtracting the reference time from the arrival time. Therefore, the distance between the transmitter and the receiver can be found from $d = c \cdot \tau$, where c is the speed of light (i.e., 3×10^8 m/s) and τ stands for the propagation delay. In practice, it is quite hard to synchronize the clocks in the transmitter and the receiver, and even small errors such as on the order of nanoseconds result in large errors in distance estimation. For that reason, two other time-based ranging methods are commonly considered as alternatives to TOA ranging.

The first one is the two-way TOA, which finds the round-trip travel time of the signal. As depicted in Fig. 1.4, considering that the signal left Node A at t_1 and arrived at Node B at t_2, and left Node B at t_3 and arrived at Node

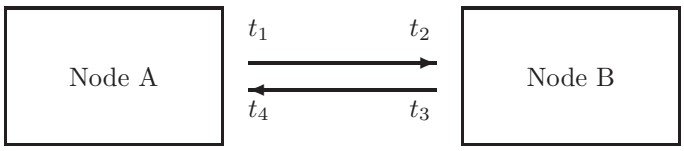

Figure 1.4: Two-way TOA.

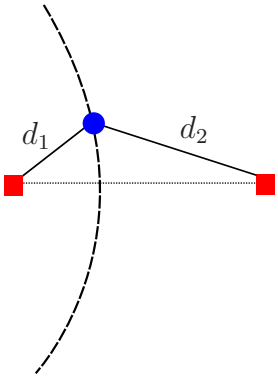

Figure 1.5: The difference between the target to anchor node distances ($d_2 - d_1$) draws a hyperbola, passing through the position of the target node.

A at t_4, the round-trip travel time can be found calculated from

$$\tau_{\text{rt}} = \frac{(t_4 - t_1) - (t_3 - t_2)}{2}. \tag{1.2}$$

Both t_4 and t_1 are recorded at the same device. Therefore, the synchronization is not an issue anymore. There is only an additional requirement to know $t_3 - t_2$, which is the processing delay at Node B. The processing delay can be considered as a constant value that is available in the localization system.

The other commonly employed alternative is TDOA, which requires synchronization only among the anchor nodes. In TDOA, the difference in arrival time of two signals from the target node to two anchor nodes is calculated. Then, the target node can be located on a hyperbola, which is the set of points at a constant range difference from two foci. In this case, the foci are given as anchor positions as shown in Fig. 1.5. Although both two-way TOA and TDOA require TOA estimation, they do not require synchronization between the target and the anchor nodes.

In TOA or RSS-based techniques, with only one anchor node the target is located on a circle, whose center is determined by the position of the anchor node, and has a radius determined by the distance estimates. Therefore, with two more anchor nodes (hence two more distance estimates and two more circles), the target can be unambiguously localized, as shown in Fig. 1.6. While Fig. 1.6 considers the error-free distance estimates, in reality, the distance estimates are subject to estimation errors, leading the circles not intersecting at a single point. A simple method to find the position of the target is searching the location which minimizes the total squared ranging error. This is also called the least-squares (LS) method, which is an effective method when there is no knowledge about the range errors. The LS estimate $\hat{\mathbf{x}} = [\hat{x} \quad \hat{y}]^T$ can be

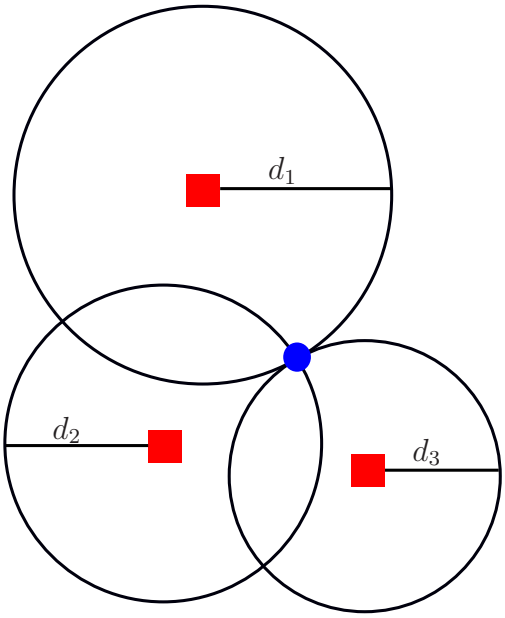

Figure 1.6: Positioning in TOA and RSS-based techniques. The red squares denote the anchor positions, while the blue circle represents the target position on the intersection of the circles.

found as

$$\hat{\mathbf{x}} = \arg\min_{\mathbf{x}} \sum_{i=1}^{N_\mathrm{a}} (\hat{d}_i - ||\mathbf{x} - \mathbf{X}_i||)^2, \tag{1.3}$$

where $\mathbf{X}_i = \begin{bmatrix} x_i & y_i \end{bmatrix}^T$ is the position of the ith anchor node where $[.]^T$ stands for the transpose operation, $||.||$ denotes the Euclidean norm operation, $||\mathbf{x} - \mathbf{X}_i||$ represents the distance between the vectors $\mathbf{x}$ and $\mathbf{X}_i$, $\hat{d}_i$ is the range estimate from the ith anchor node to the target node, and N_a is the number of anchor nodes.

In realistic environments, the range estimation could be a challenging task because of the multipath and NLOS propagation conditions (i.e., due to these two propagation conditions, the estimated TOA might deviate largely from the true TOA instant). The TOA estimation methods in practical environments will be further reviewed in Chapter 2.

1.3 Device-Free Localization

In some application scenarios, such as intrusion detection and tracking, protecting outdoor assets (e.g., pipelines, agricultural fields), elderly care, emergency

cases (e.g., when a building is on fire) and/or smart environment systems, it may not be possible for the target to carry any device, or we may want to know the positions of targets that are not actively cooperating with the localization system. This research area has recently gained interest under different names, such as device-free localization, passive localization, deviceless localization, tag-free localization, sensorless sensing, radio-frequency (RF) sensor networks, radar sensor networks, and noncooperative localization. All of these names, among which we will continue with device-free localization, refer to the same class of systems, in which targets are not required to carry any device.

Among the classical device-free localization techniques, video camera surveillance is the most common approach, especially for performance-driven applications, such as security systems. One of the main advantages of camera systems is that they give a lot of information about the object (next to the position), such as the shape, size, and color [32]. For instance, face recognition [33] is an active research area for person identification, which can be combined with human tracking in video camera surveillance systems. As one of the earliest works, the EasyLiving project [34] aimed to trigger events based on the location of a person (e.g., switching on a device near to the user), and to understand the behavior of a person in order to assist him or her or invoke a particular user's preferences, such as lighting in a certain room. Although these systems give more precise information about the target compared to other techniques, they fail when there is no visible light in the environment, limiting the use in some practical scenarios. For instance, it is not possible to detect the presence of people behind an object or a wall, in foggy environments, or when there is smoke in the environment.

Pyroelectric infrared detectors form another widely used technology to detect the movement of people in home security systems or smart office environments [35]. These sensors work on the principle that pyroelectric materials induce a charge as a response to a change in temperature, and detectors convert incident thermal radiation into an electric signal. These sensors are usually low in range, such as around 6 m. Moreover, detection behind an obstruction is not possible with these sensors, similar to video surveillance systems. They are also unable to detect stationary people [36].

An alternative method is provided by pressure-sensitive tiles, whereby tracking is performed by measuring the pressure of the human foot. For instance, as an early work, [37] uses piezoelectric wires under a carpet which are capable of sensing the foot pressure. Instead of placing the pressure sensors, capacitive sensors are introduced as a more practical alternative in [38], as the pressure sensors require a somewhat flexible floor and some installation space below the floor level to hide the sensors. Pressure-sensitive tiles are not practical in some application scenarios (e.g., emergency cases), as there is a large installation requirement.

Most modern techniques for device-free localization are based on RF transmission, where received RF signals are affected by the presence of people or objects in a quantifiable way [39]. Changes in the wireless channel properties

provide information about the position of objects in the environment. The main advantage of using RF signals is that they can penetrate through smoke and nonmetal walls.

The research in this area can be broadly differentiated based on the bandwidth of the signals that are involved in the localization process. We will briefly review the earlier works done in narrowband and UWB domains in Section 1.3.1 and Section 1.3.2, respectively.

1.3.1 Narrowband Techniques

In this section, device-free localization techniques that are based on measuring the effect of targets on narrowband channels will be discussed. Most narrowband receivers cannot provide information about each individual multipath component (MPC), but they combine the contributions from all the MPCs and provide the received signal magnitude and phase. On the other hand, they are produced in large quantities, and their low complexity and low-cost nature allow to build large-scale networks where we can combine the effects of a target person on each link to infer the position.

Most narrowband device-free localization techniques rely on the received signal strength indicators (RSSI), which are largely available in narrowband receiver implementations. RSSI is a quantized value of received power, which is the square of the complex received signal magnitude, obtained by summing up all the contributions of multipath reflections in the channel. Given static transmitter and receiver positions, the received signal strength changes because of the shadowing and multipath fading effects when the person enters the environment. Device-free localization techniques in the narrowband domain exploit these two phenomena, as briefly explained below.

Shadowing happens when a person or an object diffracts or even blocks the LOS path between the transmitter and the receiver. This results in an attenuation of the received signal compared to the case when there is no person or object in the environment for the same transmitter and receiver distance. This further results in a sudden drop in RSSI level, which can be exploited to detect the presence of the person when the link is blocked [40] or to infer the position using the shadowing of multiple links [41, 42].

In a typical wireless transmission, multipath fading occurs because of the constructive and destructive sum of signal contributions from each multipath source in the environment. This may result in variations in the received signal power levels due to changes in the multipath profile of the channel, which occur, for instance, when moving the transmitter or receiver on a very short distance scale such as on the order of one wavelength. The multipath profile of the channel also changes when there is a physical change in the environment (for fixed transmitter and receiver positions), such as the entrance of a new person to the environment. In this case, as the person moves in the environment, the received signal power fluctuates due to the changes in the MPCs. In general, the reflection coefficient of the human tissues is quite high at ultra-high and

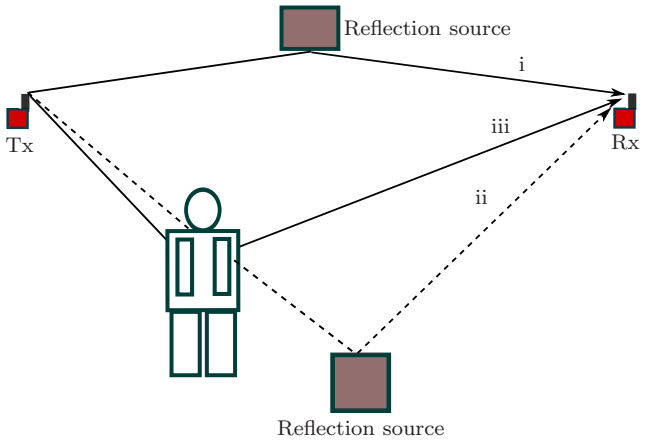

Figure 1.7: The effect of a person on MPCs: the existing MPCs, before the entrance of the person, which are i) unaffected and ii) affected by the presence of the person, and iii) a new MPC, that is created by the person.

microwave frequency bands, irrespective of incidence angle or specific frequency. This combined with the complex morphology of the human body leads to a complex "scattering" effect or even the creation of a strong MPC on specific conditions. As illustrated in Fig. 1.7, the effect of a person on the MPCs can be classified into three categories [39]:

i) The person does not have any effect on some MPCs.

ii) The person changes the amplitude and/or the phase of other MPCs.

iii) New MPCs are created by the presence of the person.

Previously, many methods were introduced to exploit multipath fading to infer the position of the person. Among the earliest works in narrowband device-free localization, in [43], a database of offline training measurements was used to compare the RSSI values, to locate the person during the online phase. The localization was performed with WLAN devices, operating at 2.4 GHz. The technique is similar to fingerprinting-based approaches, that are also used in active (device-to-device) localization systems. In each experiment the WLAN devices recorded for approximately 1800 seconds, and during this recording, a person walks and pauses for roughly 60 seconds at a series of four positions. This process is repeated for 10 different events. [43] states that the accuracy of the system is found to be between 0.15 m and 0.2 m for measurements obtained by four links in an environment that is divided into ten regions the subject walks through. In [44], the environment was partitioned into 32 cells of 0.75 m by 0.75 m, and, for each cell, offline training measurements were taken when the

person was present. The experiments were performed with radios operating in unlicensed bands around 433 MHz and 909.1 MHz, and discriminant analysis techniques were applied to detect the presence of the person in these cells. The obtained cell estimation accuracy, which is defined as the ratio of the number of successful cell estimations and the total number of estimations in [44], is found to be around 97%. The disadvantage of offline training based approaches is that the training phase requires a lot of effort, depending on the environment size. The required number of measurements even increases exponentially with the number of people. Furthermore, the environment is subject to the changes. Therefore, the radio map obtained during the offline phase will be different for different transmitter and receiver positions, and for different positions of, for instance, furniture.

The required number of measurements can be decreased when only comparing the received signal strength levels between the links when the person is absent and present in the environment [45, 46]. In this case, training measurements were not performed for every possible position of the person (i.e., unlike the approaches in [43,44]), but only when the person is absent. Based on this principle, a motion detector is proposed for moving people using WLAN infrastructures in [45], and tracking multiple people is considered in [46, 47]. However, in some cases, it might not be possible to perform training measurements when there is no person (e.g., detecting people in emergency cases, such as fire). Furthermore, it is again vulnerable to changes in the environment. Therefore, the database, containing the measurements of links in the absence of the person, needs to be updated frequently, reducing the applicability of the system.

To remove the requirement for training, one can consider developing models for the change of RSS information with respect to the change of position of the person. In [39], reflection and scattering models were discussed for the variations on the RSS levels (i.e., the change in signal strength when a person is in the environment). In general, the actual dominant propagation mechanism in a particular environment is determined by the wavelength and the relative size of the objects (i.e., the roughness of the surface that the electromagnetic wave is interacting with). As an extension of [39], in [30], approximate expressions were derived for the relation between the person's position and the expected value of the total affected power. This work also showed that there is a linear relationship between the RSS variance (i.e., the variance of the RSS levels when the person moves in the environment), and the expected value of the total affected power. This further leads to the conclusion that there is a relation between RSS variance and the person's position. The performance of the RSS variance based localization was shown in [48] by an experimental setting with 34 Zigbee nodes, deployed outside of a home, and the reported average accuracy was around 0.5 m. In [49], a log-normal model was considered for RSS mean and variance fluctuations, and a Bayesian tracking method was considered for the experimental measurements setting in an environment with 14 nodes in a 5×4 m area. The resulting errors were up to 2.4 m with an

average error of 0.5 m.

Finally, apart from RSS-based works, in [50], a polarization-based detection technique is proposed. This method utilizes the change in polarization of the electromagnetic waves in a dual-polarized architecture compared to a reference state, when the person is present in the environment. No quantitative results are available for localization accuracy.

As pointed out in this section, RSS-based device-free localization techniques were commonly considered in the narrowband domain. Among these techniques, in general, two approaches were followed. The first approach is based on developing a training database, which is usually environment-specific and requires a lot of effort. The second approach is based on statistical models, which explain the relationship between the RSS and the position of the person. In fact, if the variation of the RSS can be explained through statistical models showing the behavior of the received signal power for different positions of the person, then the final position of the person can be found by combining signal strength variations in multiple links. However, it is quite hard to obtain a generic model, that is available for all environments and for multiple people.

1.3.2 UWB Techniques

Because of transmitting very short pulses, UWB systems offer time resolutions on the order of nanoseconds, which can also be employed for device-free localization purposes. The fine time resolution property offers the possibility of distinguishing multipath signal components due to the environment (e.g., walls, furniture) from those due to the target to be detected and located. Once the reflection due to the target is detected, the arrival time of this reflection can be found from the received signal. This gives a big advantage over narrowband techniques, which mostly rely on RSS information that is hard to model. Therefore, most narrowband methods, discussed in Section 1.3.1, use many narrowband radios to expand the information about the channel. On the other hand, highly accurate device-free localization systems can be built in a UWB network as the time resolution allows fine device-free ranging resolution. The required number of UWB radios, in this case, is determined by geometrical considerations (i.e., to obtain an unique location estimate). Below, we briefly mention a few of the earlier works in the UWB domain.

UWB was demonstrated as an effective technique for human-being detection through respiratory movement in [51, 52]. Both showed experimental demonstrations of the variations in the signal due to the reflections of the signal from the chest. Demonstrations were performed by transmitting very narrow pulses generated by a pulse generator. In [51], a UWB radar in the range of 0.9–12.6 GHz (i.e., the pulse characteristic was described in terms of the frequency range) was developed and the distance between the radar antenna and the person was set to 2.6 m. The distance was set up to 5 m in [52], which also considered the case where there is a wall between the antenna and the person for a distance of 0.86 m. The radar built in [52] transmitted pulses of 300 ps

width and the sampling of the received signal was performed by an oscilloscope with a sampling interval of 2 ps. Using very narrow pulses, in both works the authors pointed out that it is possible to detect the movements of the human chest due to the breathing which causes a very small displacement. A clear demonstration of the respiratory frequency was given in [52], while in [51] it was also shown that the estimated range to a person varies within 0.6 cm due to the breathing.

Recently, experimental demonstrations were also given for the detection of the person under the debris from the respiratory movement [53–55]. Specifically, in [53], a respiratory movement detection algorithm was developed considering also the other moving reflection sources (i.e., nonstationary clutters) in the environment. In this work, the authors included the knowledge of the average respiratory frequency to filter out the other signal components which are not related to variations due to the respiration, and applied the Singular Value Decomposition (SVD) technique to remove the effects of the other moving reflection sources. They also proposed to visually inspect the output by the radar operator after the SVD operation to avoid false alarms and missed detections. The experiments were performed in a dump site, where the rubble was artificially created by placing an approximately 1.2-m pile of standard-sized bricks and a test person, lying inside a concrete pipe of 80-cm inner diameter and 10 cm of wall thickness. It was shown that the proposed algorithm gives improvement in the detection compared to cases when the effects of the other moving reflection sources were not removed from the signal. The experimental demonstration was also given for the respiratory detection with a MIMO UWB system. In this system, there was one transmitter antenna element, while eight antenna elements were used for reception. The authors used a clustering approach to detect three persons, standing 4 m away from the array for the first person and 5 m away for the second and the third persons.

For the estimation of respiration and heart rates, an analytical framework and a frequency-domain technique were developed for a single person in [56]. The authors had an accurate estimate of the respiration rate of the subject when there is no obstruction and a 5 cm thick wooden panel between the antennas and the person, respectively. They performed four and three experiments when there is no obstruction and an obstruction between antennas and the person, respectively. In these experiments, the total distance between the person and the transmitter and the receiver antennas was around 6 m. They also showed heart rate estimation for four experimental scenarios when there is no obstruction. The average heart rate estimation error was 0.06 Hz. Based on the analytical framework developed in [56], Cramér–Rao lower bounds for the heart and respiration rate estimation were calculated in [57]. Experimental results were also given for multiple targets in [58]. In these experiments, the total distance between the transmitter and the receiver was up to 2 m, and the clustering and MUSIC algorithms were applied to distinguish the respiration and heart beat frequencies of different targets. These two techniques gave similar performance results. The estimation error for the respiration rates was around

0.05 Hz for the two-person case, and the estimation error for the heart rate estimation was 0.06 Hz and 0.05 Hz for two-and three-persons cases, respectively. Furthermore, a time-variant channel response model was introduced for breathing detection and human target ranging in [59], and the harmonics and the intermodulation between respiration and heart signals were analyzed in [60]. Whereas these works dealt with the detection of static people from breathing information, human-body detection and tracking were studied experimentally for moving people in an open area in [61, 62]. Furthermore, in [63], multiple moving people were considered in an indoor experimental setting.

While the above-mentioned works focused on the effect of a stationary or moving person on a single UWB link, passive object detection and tracking were also studied in UWB networks. An initial study on tracking was performed in [64], which derived Cramér-Rao lower bounds based on a model, assuming that the signals are simply delayed, phase-shifted and attenuated by the objects they encounter. Imaging of environments and objects based on a single UWB transmission link was considered in [65, 66], and extended to multiple receivers in [67–69]. Specifically, [67] and [68] investigated the impact of the system geometry on detectability of the objects and imaging of the environment, respectively. [69] developed optimum detection metrics, and in [70] a new TOA algorithm for passive localization was proposed. In [71], imaging of the environment was considered based on NLOS propagation, which delays the direct-path signal between the fixed anchor nodes and the mobile node whose track is known.

[72] proposed a Hidden Markov Model (HMM) approach for bistatic range estimation from UWB impulse responses. The method considers the change between the signal energy measured during the period when the environment is static (i.e., no person is present) and the actual period when the presence of the person is detected and actual location estimations are performed. The CIRs are partitioned into delay windows each with 1-ns length and the changes in these delay windows (relative to the case when the environment is static) are modeled by HMM. The experimental results were shown for bistatic range and location estimates with off-the-shelf UWB equipment for a person who was standing still in two different environments. In these experiments, 31 positions were chosen for one environment and 73 positions were chosen for the other environment. The results were shown for a thresholding-based approach, which sets a threshold to these changes to find the bistatic range, and the HMM-based method. For the bistatic range estimation, root-mean-square (rms) errors of around 1.5 m and 0.9 m were obtained for the thresholding and HMM-based approaches, respectively. For localization, only the HMM-based method was reported with rms errors of 1.5 m and 0.75 m for the two different environments.

Most of the works, done so far, give demonstrations for the effect of a person on UWB channels, but there is still a need of signal processing methods for detection, device-free ranging and localization. For instance, there are not many performance reports for ranging and/or localization accuracy with UWB systems. Apart from the work presented in this thesis and [72], which was pub-

lished while this thesis was written, to our knowledge there is no other work showing the experimental performance of ranging and device-free localization using UWB transmission systems. With the recent interest in device-free localization systems and recent advances in the narrowband domain, there is also a need for more studies on localization techniques in the UWB domain. There is not a lot of work done on device-free detection and localization of people using UWB networks. Only a few works considered passive detection of objects and imaging using UWB networks, but these works are mostly based on the theoretical models of any object's influence on the UWB transmission channel. However, these models are lacking the experimental validation for the effect of people. Furthermore, multiple people detection and localization is another challenging area which attracted only a few studies previously. These studies only considered detection, respiration [53, 58] and heart rate [58] estimation. However, none of them was also extended to localization, which introduces additional challenges.

1.4 Research Objectives

In this thesis, the main research questions are:

- How do UWB propagation channels differ because of the presence of a person in the environment?
- How can the changes in received UWB signals be utilized to detect and locate people without them requiring to carry any radio device in indoor environments and using UWB networks?

Therefore, the main objective is to empirically investigate the effect of people on UWB propagation channels, and to develop signal processing methods for indoor device-free people detection, ranging and localization using UWB networks. The UWB network is assumed to be consisting of nodes with known locations and capability to transmit and receive UWB signals. We will first consider a single person and later extend the work for multiple people. The research is confined to the case when the person is stationary in a LOS indoor environment. Therefore, the tracking of moving people and their influence on UWB signals, and detection and localization behind walls are left out of our scope. Furthermore, we assume that there is no other nonstationary or moving object in the environment.

In summary, the following tasks are performed in this thesis:

- studying the UWB signalling techniques, propagation channel descriptions, and the effects of UWB propagation on device-to-device range estimation techniques;
- investigating the impact of a person on UWB propagation channels and in particular the effect of the person on device-to-device UWB ranging in realistic indoor environments;

- analyzing the impact of multiple people on UWB signalling, and developing techniques for device-free detection and localization of single and multiple persons using UWB networks.

1.5 Contributions of the Thesis

The contributions of this research can be summarized as follows.

1. The impact of the human body on the measured UWB propagation channel, and in particular on the energy of the direct-path signal component and the time-of-arrival range estimates is shown.

2. A signal model, that is supported with experimental observations and includes the effect of a stationary person on indoor UWB channels, is adopted from the time-variant tapped delay line model for device-free ranging and localization purposes.

3. A novel signal processing method is developed for device-free detection, and its performance is quantified via theoretical calculations and experimental results.

4. Three practical estimation criteria are proposed for the delay of the human-body reflection, and their performance is shown in experimental settings for both ranging and localization.

5. A new method is developed for multiple people detection and localization and its performance is shown in experimental settings for two persons.

1.6 Organization of the Thesis

The rest of the thesis is organized as follows. Chapter 2 introduces the analytical descriptions of the transmitted UWB signal and the UWB propagation channel, and discusses the propagation effects on TOA ranging. The chapter continues with an experimental analysis of the human-body effect on UWB propagation from a TOA ranging perspective. Chapter 3 starts with showing experimental observations on the influence of a stationary person, which is investigated not only in the delay domain (i.e., on the order of few nanoseconds), but also on the time domain (i.e., on the order of sub-seconds). Based on these observations and the knowledge about generic UWB propagation channel descriptions, a signal model is developed for device-free person detection and ranging purposes. This model is followed by a decision statistic, and the theoretical performance analysis of this statistic. This chapter ends with theoretical and experimental results for the detection performance and points out the practical problems. Chapter 4 provides an experimental analysis of the device-free ranging and localization performance. In Chapter 5, the effect of multiple people on UWB propagation is investigated in a way to find out whether the

correlations between the variations due to the presence of different people can be exploited to distinguish different people and locate them using an UWB network. The chapter describes the effect of practical problems on the correlations and proposes a normalization method to deal with these issues. First, results are provided for detecting a second person in the environment and the estimation of the corresponding bistatic ranges. Then, a method is developed for combining different correlation matrices for multiple people localization. Finally, Chapter 6 points out the concluding remarks and recommendations.

Chapter 2

UWB Time-Based Ranging and Human-Body Shadowing

2.1 Introduction

In this chapter, more details on UWB time-based ranging are given and the impact of human-body presence on these techniques is investigated. Considering the TOA technique in UWB ranging systems, the main interest is on the arrival time and the amplitude of the direct-path signal component. Threshold-based first peak detection techniques are common to employ, as the strongest path in UWB channels is not always a good indicator for TOA estimation. Therefore, the impact of the human-body presence is investigated by analyzing the arrival time and the amplitude of the first-path signal for different positions of the human body.

This chapter is organized as follows. First, an analytical description of the transmitted IR-UWB signal is given and then the common representation for UWB propagation channels is explained. Later, the common propagation effects on UWB time-based ranging are introduced, and common methods for TOA estimation are explained. That is followed by the analysis of the human-body shadowing effect on TOA estimation in UWB ranging[1].

2.2 Analytical Description of the Transmitted Signal

In IR-UWB systems, the transmitted ranging symbol is generally defined according to the signal model, which will be explained in this section. This signal model is not exactly the same as the one defined in the IEEE 802.15.4a

[1]The contribution of this chapter was published in [73].

standard, which specifies the IR-UWB signalling format. It provides a general description and is helpful to develop a framework for UWB ranging systems [3].

IR-UWB transmission systems are based on transmitting a stream of very narrow pulses, with a duration on the order of a nanosecond. The data is usually conveyed by the position and the polarity of these pulses. The transmitted IR-UWB symbol is defined as follows.

$$s(t) = \sqrt{E_{\mathrm{p}}} \sum_{j=0}^{N_{\mathrm{f}}-1} b_j p(t - jT_{\mathrm{f}} - c_j T_{\mathrm{c}}), \tag{2.1}$$

where E_{p} is a parameter to define the transmitted pulse energy at the output of the transmitter antenna, $p(t)$ denotes the UWB pulse shape of duration T_{p} and unit energy, N_{f} is the number of pulses in $s(t)$, $b_j \in \{\pm 1\}$ denotes the polarity code, T_{f} is the duration of the frame, $c_j \in \{0, 1, \ldots, N_{\mathrm{h}} - 1\}$ is the time-hopping code, and T_{c} and N_{h} are the chip duration and the number of chip intervals per frame, respectively. The pulse duration T_{p} is assumed to be $T_{\mathrm{p}} \leq T_{\mathrm{c}}$. Therefore each pulse resides within a chip interval. Within each frame, only one pulse is transmitted. Hence the number of pulses is, in total, equal to N_{f} for each symbol. The total duration of the symbol is $T_{\mathrm{s}} = N_{\mathrm{f}} T_{\mathrm{f}}$. Therefore, as the number of frames (or pulses) increases, the duration of the symbol gets larger. Similarly, the symbol energy E_{s} is also proportional to the number of frames in the symbol and it is given as $E_{\mathrm{s}} = E_{\mathrm{p}} N_{\mathrm{f}}$. Therefore, for a higher value of N_{f}, E_{s} also gets higher, at the expense of a longer symbol duration T_{s}. Furthermore, the duration of the symbol is smaller than T_{rep}, which is the repetition period of each symbol.

To get a better understanding of the mathematical representation, we show an example IR-UWB transmitted symbol for four frames, each of which contains four chips, in Fig. 2.1. In each frame, the chip positions are chosen as $\{1, 0, 2, 3\}$. Furthermore, corresponding to each chip, the polarity code b_j is chosen as $\{+1, -1, -1, +1\}$. For this example, the pulse shape is chosen as the second derivative of the Gaussian pulse (also known as Gaussian doublet).

In general, the Gaussian pulse is given by

$$g(t) = A \cdot \exp(-2\pi t^2/\zeta^2) \tag{2.2}$$

where A is a positive parameter and denotes the amplitude of the Gaussian pulse, and ζ is the width parameter, which defines the pulse duration. After differentiating it with respect to t, the second derivative is obtained as

$$p(t) = A(4\pi/\zeta^2)(1 - 4\pi t^2/\zeta^2)\exp(-2\pi t^2/\zeta^2), \tag{2.3}$$

where a minus sign was added in order to give a positive peak value $p(0)$.

The energy of $p(t)$ can be calculated from

$$\begin{aligned} E &= \int_{-\infty}^{\infty} p^2(t) dt \\ &= A^2 6\pi^2/\zeta^3. \end{aligned} \tag{2.4}$$

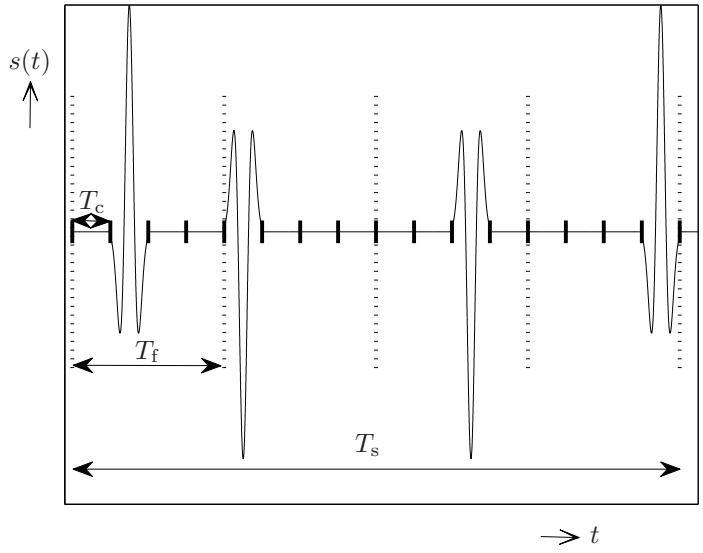

Figure 2.1: An example IR-UWB transmitted symbol with duration T_s which is divided into four frames, each with duration T_f. The frames are further divided into four chips, numbered from 0 to 3 and each having duration T_c.

Therefore, for a unit energy pulse, $A = (\zeta/\pi)\sqrt{\zeta/6}$. In general, the value of ζ also determines the bandwidth of the transmitted signal. Hence its value should be considered, together with E_p, in order to comply with the FCC rules.

The stream of transmitted pulses is usually subject to reflections, caused by walls and other objects in the environment. In some conditions, it might be the case that the delay of the reflection is larger than the interval between two consecutive pulses. In these cases, the consecutive pulses interfere with each other. This phenomena is called *inter-frame interference* (IFI). In order to avoid IFI, the duration between two consecutive pulses must be larger than the maximum delay due to the reflection sources. According to the IEEE 802.15.4a standard, there is a guard interval after every frame duration T_f. During this interval, no pulse transmission occurs. The duration of the guard interval is set in a way to prevent IFI. In the standard, the guard interval is set to T_f for $T_f \geq \tau_{max}$, where τ_{max} defines the maximum delay due to the reflections. Therefore there is an empty frame interval in between every two successive frames.

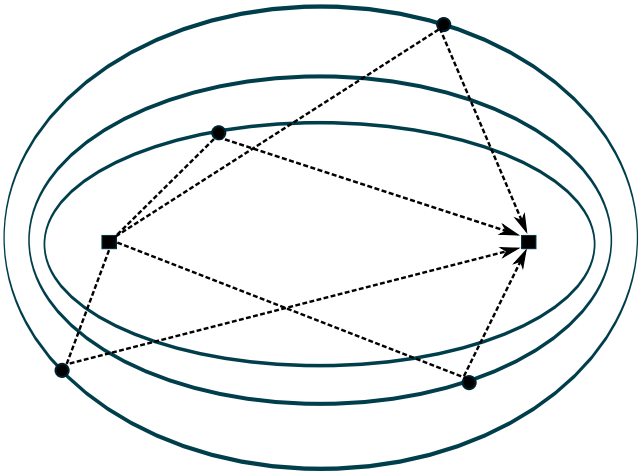

Figure 2.2: Ellipses connecting the physical positions of the reflection sources (denoted as points) that introduce MPCs with the same arrival delay. The squares denote the transmitter and the receiver positions.

2.3 UWB Propagation Channel Representation

2.3.1 General Description

The impulse response of a typical wideband wireless propagation channel can be represented by summing the contributions of the individual MPCs. According to this representation, the baseband equivalent of the impulse response is given as [27]

$$h(\tau) = \sum_{i=1}^{N} \alpha_i \delta(\tau - \tau_i), \tag{2.5}$$

where N is the number of physical MPCs, each of which has the complex channel amplitude α_i and delay τ_i. $\delta(.)$ represents the Dirac delta function. τ_1 is the arrival delay of the direct path, which corresponds to the shortest traveling distance between the transmitter and receiver. Each MPC travels a distance $d_i = c \cdot \tau_i$, where c is the speed of light. Considering all the reflection sources as points in the space (i.e., each reflection source causes a single reflection), in total we have $N-1$ reflection sources. These reflection sources, with given total distances to the transmitter and receiver d_i for $i = 2, \ldots, N$, can be located on ellipses around the transmitter and receiver as shown in Fig. 2.2. Each ellipse has focal points and major axis length, defined by the transmitter and receiver positions, and the total distance d_i for $i = 2, \ldots, N$, respectively. The reflection sources which are on the same ellipse introduce MPCs that arrive

at the same time as they travel the same distance. The representation in (2.5) is an approximation of the reality as it does not include the frequency dependency of the interactions of the transmitted signal with the reflection sources [74] (e.g., the reflection coefficient of an object may vary for different frequencies). Therefore, in reality, the impulse response of a single MPC is no longer a dirac function, but rather a distorted pulse. The shape of this distorted pulse depends on the interactions that the MPC experiences on the way from the transmitter to receiver[2].

2.3.2 Tapped Delay Line Model

The description in (2.5) is rather general as it describes the influence of the physical multipath sources to the signal on its way from the transmitter to receiver. However, any real system has a finite bandwidth B and therefore we are commonly interested in the behavior of the channel for a certain band that the system is operating in. The tapped delay line model is commonly adopted for wideband channels to describe the behavior of the channel in a certain band. According to the tapped delay line representation, the baseband equivalent of the impulse response is written as

$$\begin{aligned} h_{\mathrm{TDL}}(\tau) &= \sum_{i=1}^{N'} c_i \delta(\tau - i \cdot \Delta\tau) \\ &= \sum_{i=1}^{N'} \sum_{k} \widetilde{\alpha}_{i,k} \delta(\tau - i \cdot \Delta\tau), \end{aligned} \tag{2.6}$$

where N' is the number of taps, c_i is the complex channel coefficient for each tap and $\Delta\tau$ is the delay between the successive taps. In the tapped delay line model, each channel tap approximately corresponds to a group of closely spaced MPCs, which are nonresolvable because of the band limitation of the channel. In this case, each complex channel amplitude c_i represents the sum of many nonresolvable MPCs as shown in the second line of (2.6), where the $\widetilde{\alpha}_{i,k}$s denote the complex amplitude of each physical MPC. This can also be seen as reflections from the physical objects staying within the same channel bin, if these reflections arrive at the receiver between the delays τ and $\tau + \Delta\tau$. In a different perspective, a group of MPCs contributes to the same channel bin, if the corresponding reflecting objects are located between two

[2]Specifically, in [75], to show the distortions in the channel, the impulse response is further written as $h(\tau) = \sum_{i=1}^{N} \alpha_i \chi_i(\tau) \otimes \delta(\tau - \tau_i)$ where $\chi_i(\tau)$ denotes the distorted pulse for the ith MPC and $\otimes$ is the convolution operation. It is also noted in [75] that each MPC departing from the transmitter and arriving at the receiver is affected by the complex antenna patterns, which introduce amplitude scaling and phase shifts. $\chi_i(\tau)$ represents the convolution of the complex antenna patterns with the distortion in the channel, if the complex antenna pattern is also frequency-dependent. The most literature in UWB does not include the distortions in the channel model. One reason might be that it is hard to characterize the distortions due to the interaction of the signal with all objects.

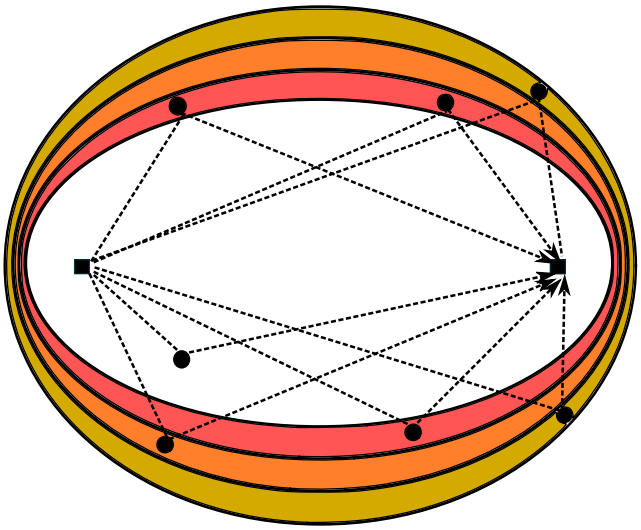

Figure 2.3: Ellipses corresponding to the delay values $\Delta\tau$, $2\Delta\tau$, $3\Delta\tau$, $4\Delta\tau$.

successive ellipses which are drawn around the transmitter and receiver with a major axis length $d_i = i \cdot \Delta\tau$. An example case is shown in Fig. 2.3, which shows the ellipses for the delays $\Delta\tau$ to $4\Delta\tau$ in excess of the direct path (i.e., the zeroth delay instant corresponds to the arrival delay of the direct path). Apparently, summation of the $\widetilde{\alpha}_{i,k}$s result in constructive or destructive fading for the channel tap amplitudes c_i. Based on the description in (2.6), the main difference of the UWB propagation channel appears with its huge bandwidth. Given the bandwidth B, the delay between the successive channel taps $\Delta\tau$ (i.e., the time resolution of the channel) is commonly chosen as $\Delta\tau = 1/B$ [27]. For UWB channels, $\Delta\tau$ gets very small (on the order of subnanoseconds for bandwidths of a few GHz), because of the large B. Therefore, the space between the ellipses becomes smaller and more MPCs are resolvable, resulting in less effect of the multipath fading.

Spill-over Effect

Grouping of MPCs into a single bin is an approximation [76]. The reason is that the physical MPCs do not always arrive with excess delay in multiples of 1/B (e.g., exactly at the sampling instants), and so spill over to adjacent channel taps. This phenomenon will briefly be explained below.

Let us denote $H_{\mathrm{R}}(f)$ as the frequency domain representation of any real channel. In general, we are interested in the response of the channel in a certain frequency band depending on the operating characteristics of our system. Therefore, we multiply the frequency response $H_{\mathrm{R}}(f)$ with a rectangular function that is shifted with the central frequency f_{c} and scaled with the bandwidth

B as

$$H_{\mathrm{w}}(f) \quad = \quad H_{\mathrm{R}}(f)\mathrm{rect}\left(\frac{|f|-f_{\mathrm{c}}}{B}\right). \tag{2.7}$$

$H_{\mathrm{w}}(f)$ can be written in terms of the equivalent baseband representation $H_{\mathrm{b}}(f)$ as

$$H_{\mathrm{w}}(f) \quad = \quad H_{\mathrm{b}}(f-f_{\mathrm{c}}) + H_{\mathrm{b}}^{*}(-f-f_{\mathrm{c}}). \tag{2.8}$$

where $(.)^{*}$ denotes the complex conjugate operation. According to the tapped delay line model, the continuous channel impulse response (CIR) $h_{\mathrm{b}}(t)$, that is obtained with the inverse Fourier transform of $H_{\mathrm{b}}(f)$, is sampled with a sampling rate $B = 1/\Delta\tau$ which is determined by the Nyquist theorem [27]. $h_{\mathrm{b}}(t)$ can also be found from the relation

$$h_{\mathrm{b}}(\tau) \quad = \quad h(\tau) \otimes B\mathrm{sinc}(\pi B\tau), \tag{2.9}$$

where $h(\tau)$ is the baseband equivalent of the CIR, defined in (2.5). The definition of the sinc function, used in (2.10), is given as $\mathrm{sinc}(x) = \sin(x)/x$. Hence, the impulse response according to the tapped delay line model is

$$\begin{aligned} h_{\mathrm{TDL}}(\tau) \quad &= \quad \Big(h(\tau) \otimes B\mathrm{sinc}(\pi B\tau)\Big) \sum_{k=-\infty}^{\infty} \delta(\tau - k/B) \\ &= \quad B \cdot \sum_{i=1}^{N} \alpha_i \mathrm{sinc}\Big(\pi B(\tau-\tau_i)\Big) \sum_{k=-\infty}^{\infty} \delta(\tau - k/B) \end{aligned} \tag{2.10}$$

If the MPCs do not arrive with a spacing in multiples of $1/B$, then the sinc(.) function will not be sampled at its zero crossings. Therefore, those MPCs, which are not arriving in multiples of $1/B$ will have spill-over to adjacent bins. A graphical representation of this phenomenon is shown in Fig. 2.4. In Fig. 2.4(a), the MPC arrives exactly at the sampling instant, and the sinc function (which is convolved with this MPC) is sampled at its zero crossings. Therefore, this particular MPC does not influence the adjacent tapped delay line bins, but only the bin which corresponds to the actual arrival delay of this physical MPC. On the other hand, Fig. 2.4(b) shows the case in which the MPC does not arrive at the sampling instants. In this case, this MPC has contributions to the adjacent tapped delay line bins and it is not sampled exactly at it is arrival instant. This effect is usually considered in the frequency domain measurements as we will briefly explain below.

The frequency domain channel measurement technique is a common method to characterize a wireless channel. As frequency domain measurements provide the channel frequency response, the impulse response of that particular channel can easily be obtained after inverse Fourier transformation. Measurements in the frequency domain are most easily performed using vector network analyzers (VNAs) which measure the transfer function by exciting the channel with

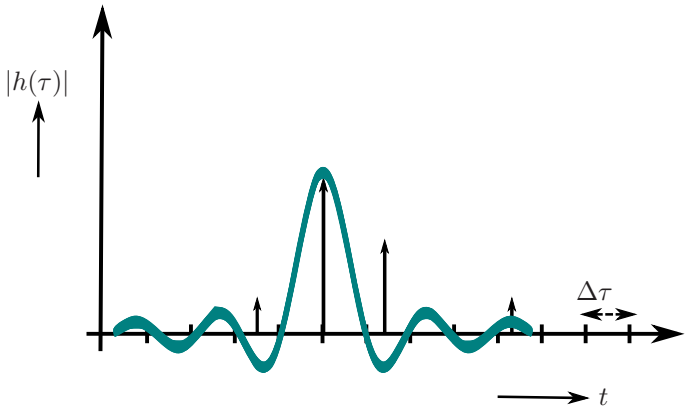

(a) No contribution to adjacent tapped delay line bins.

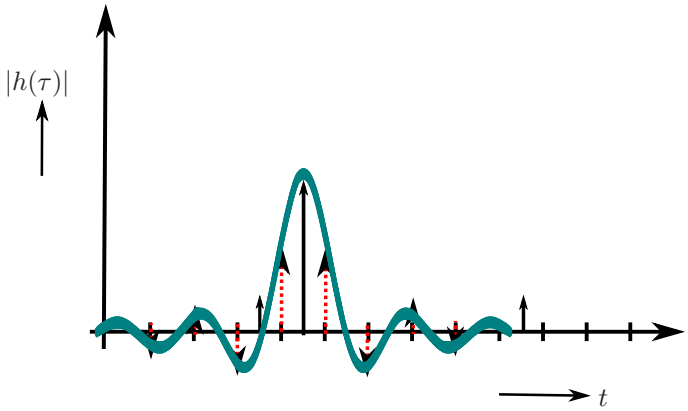

(b) Spill-over to adjacent tapped delay line bins. Dashed red deltas represent the sampling instants of the sinc function.

Figure 2.4: Illustration of how a real physical MPC affects the tapped delay line bins. The deltas represent $|h(\tau)|$ and the green lines show the sinc function of the convolution operation given in (2.10).

sinusoidal waveforms. Typically, a VNA divides a certain bandwidth B into a number of frequencies N_{step} with a certain spacing f_{step}, transmits sinusoidal waveforms for each of these frequencies, and records the transfer function.

Ignoring the VNA noise and other impacts (e.g, antennas, connectors, cables), ideally the equivalent baseband representation of the channel transfer function sampled by the VNA can be written as

$$H_{\text{VNA}}(f) \quad = \quad H(f)\text{rect}\Big(\frac{f}{B}\Big) \sum_{k=-\infty}^{\infty} \delta(f - k f_{\text{step}}) \tag{2.11}$$

If we compute the impulse response from the channel response we get

$$h_{\mathrm{VNA}}(\tau) \quad = \quad B \cdot \Big(h(\tau) \otimes \mathrm{sinc}(\pi B \tau)\Big) \otimes \sum_{k=-\infty}^{\infty} \delta(\tau - \frac{k}{f_{\mathrm{step}}}). \qquad (2.12)$$

This shows that the CIR $h(\tau)$ is repeated with repetition delay $1/f_{\mathrm{step}}$ after convolution with the sinc function. Therefore, f_{step} is determined by the maximum excess delay of the channel $\tau_{\max}$. One should choose $f_{\mathrm{step}} \leq 1/\tau_{\max}$ to avoid aliasing. Typically, the VNA performs continuous measurements and after each sweep (e.g., collecting responses for N_{step} frequencies), a new sweep is performed. The total sweep number N_{sweep} is defined by the user. In practical settings, we get N_{sweep} CIRs in total. Collecting more measurements for a single measurement point leads to additional processing gain by averaging the measurements, provided that the channel can be assumed static during the measurement.

As introduced earlier, the adjacent bins will be affected because of the spill-over effect. Typically, the main lobe to first side lobe difference is around a magnitude of 13.5 dB. Therefore, in practical measurements windowing functions are used to reduce the levels of the side lobes. In this case, the complex VNA output is multiplied with a windowing function, before inverse discrete Fourier transformation. While the windowing functions provide additional side lobe suppressions (e.g., for Hamming window the side-lobe suppression is around 42 dB), applying a windowing function increases the main lobe width compared to the case where rectangular windowing is used.

Temporal variations

The impulse response in (2.6) is defined for the cases when the transmitter, the receiver, and the objects (i.e., multipath sources) are not moving in the environment. Because of their movement, the impulse response will in general be time-dependent, and can be written in tapped delay line notation as [27]

$$h_{\mathrm{TDL}}(t, \tau) \quad = \quad \sum_{i=1}^{N'} c_i(t) \delta(\tau - i \cdot \Delta\tau). \qquad (2.13)$$

Here, τ denotes the delay index which spans time intervals over which the channel can be considered as static. For UWB channels, τ corresponds to the delay values up to few microseconds. Meanwhile, t shows the slow variations in the channel and is in the order of seconds. Since the delay between successive channel taps $\Delta\tau$ is fixed, the temporal variations will only change the amplitudes of the channel taps over time (i.e., $c_i(t)$) in (2.13). On the other hand, for the general channel description given in (2.5), both the complex channel amplitude α_i and the delay τ_i for each MPC are considered to be time-dependent for time-varying channels [75].

In Chapter 3, a time-varying UWB channel model will be considered for describing the received signal in the presence of a person for static transmitter and receiver positions.

2.4 UWB Time-Based Ranging

In all time-based ranging methods, such as in TOA, TDOA, or two-way TOA, the ranging problem is closely related to the estimation of the arrival time of the direct-path signal, which travels the shortest path between the transmitter and the receiver. As the direct-path signal component (if it exists) is the first component to arrive at the receiver, its delay value is given as τ_1 in (2.5). Then, the ranging problem becomes the estimation of τ_1 from the CIR or the received signal. If τ_1 is estimated perfectly, then the error in the TOA estimation will be limited only by the pulse duration T_{p}, assuming perfect synchronization. However, there are certain propagation effects which make the arrival time estimation of the direct-path signal component a nontrivial task, especially for indoor localization applications [3,22,23]. These effects will be briefly discussed below.

2.4.1 Multipath Propagation

Dense multipath propagation results in many received copies of the transmitted signal, among which the determination of the direct-path signal might be a difficult task. In general, one may expect that the amplitude of the direct-path signal component, which travels the shortest-path between the transmitter and the receiver, is larger than the later-arriving MPCs, as they are reflected off objects before arriving at the receiver. We illustrate this propagation effect in Fig. 2.5(a), where the MPC related to the direct path arrives at a delay τ_1, and has an amplitude that is larger than the amplitude of an MPC which arrives later at a delay τ_2. For such a case, τ_1 can be estimated by, for instance, searching for the index of the maximum amplitude among all the other channel coefficients.

2.4.2 Obstructed-Direct-Path Condition

In this case, illustrated in Fig. 2.5(b), the direct path is obstructed by an object, such as a wall, and the signal needs to travel through this object. Although the direct-path component can still be detected by the receiver, it is attenuated and might no longer be the strongest channel component. Furthermore, the signal travels slower than in the air while propagating through this object because the speed of the electromagnetic waves traveling in a homogenous material is reduced by a factor related to the relative electrical permittivity of the material [22]. This causes excess delays in the arrival time of the signal, as it needs to propagate through the material. In these cases, the TOA estimation is subject to a positive bias. The measurements in [77,78] revealed that the bias in these cases is proportional to the wall thickness. Furthermore, the direct-path signal component might have lower amplitude than the later arriving MPCs, because there might be still a reflection source within the region around the direct path, which is not resolvable. Because of this reflection source, multipath fading happens for the first resolvable channel component and its amplitude might become

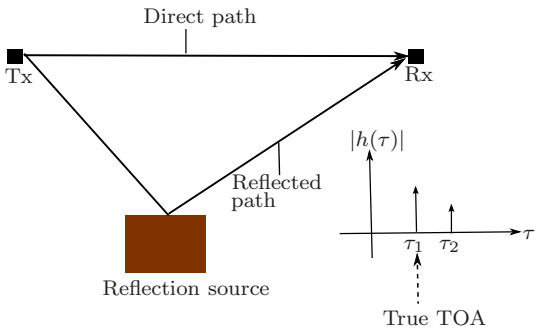

(a) Multipath propagation condition.

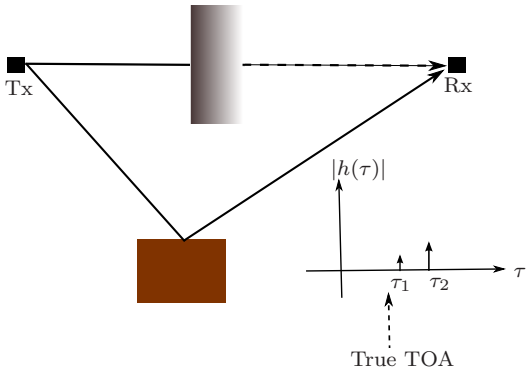

(b) Obstructed-direct-path condition.

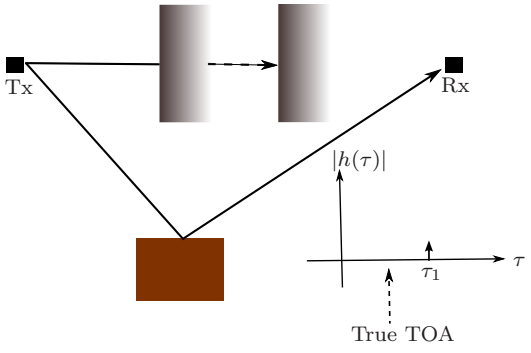

(c) Blocked-direct-path condition.

Figure 2.5: Possible propagation effects:(a) is drawn to illustrate multipath propagation, while (b) and (c) are drawn for obstructed-direct-path and blocked-direct-path conditions, respectively. The insets are examples of resulting CIRs.

smaller than the later-arriving channel components. Because of these effects, the first resolvable signal path might not be the strongest channel component, and, a TOA estimation, based on the detection of the strongest path, may result in large errors. For that reason, a threshold-based first peak detection algorithm is commonly employed to deal with the situations that the first arrived path is not the strongest channel component [79, 80]. In this scheme, the first threshold-crossing instant is determined as the TOA instant. The choice of the threshold commonly depends on the receiver operating characteristics, such as the noise and the interference levels, which can be determined when the actual signal is not present.

2.4.3 Blocked-Direct-Path Condition

In this case, the obstruction for the direct-path signal component is very strong. Therefore, it is not possible to detect the direct-path signal component anymore. This can be the case, for instance, if there is more than one wall, as illustrated in Fig. 2.5(c), or the obstruction is made up from thick metallic materials. In such cases, TOA estimation is based on one of the later-arriving multipath signal components which travels longer than the real distance. The positive bias related to this case is usually much larger than the obstructed-direct-path condition [81], as the direct path is no longer detectable.

Obstructed-direct-path and blocked direct-path conditions are commonly grouped under NLOS conditions, as the direct sight between the transmitter and the receiver is blocked. In [82–86], NLOS identification and mitigation methods have been developed to compensate for the positive bias, by extracting certain channel statistics from the received waveforms and/or CIRs. The main idea in these works is that the statistics of features such as the Kurtosis, the mean excess delay, the root-mean-square delay spread, the energy of the received signal, the maximum amplitude level, and the energy in the first peak of the signal, differ in a significant manner so that these features can be used to identify a LOS or an NLOS environment. After identifying the channel as NLOS, two methods were commonly employed to reduce the effect of NLOS conditions on the final localization performance. In the first one, the features were also used to estimate the NLOS bias by establishing a relationship between the value of the bias and the statistics of the features based on the measurement data. Therefore, the estimated NLOS bias can be mitigated from the range estimates before the final localization step. As an alternative, the weighted least squares method [87] is employed, such that rather than assigning equal weights to all range estimates, relatively lower weights are assigned to the range estimates of NLOS cases. These weights can be determined based on the statistics of the feature values.

2.5 Human-body Shadowing Effect on UWB Propagation

As previously pointed out in Section 2.4, the deployment of UWB ranging systems in indoor environments faces challenges such as the presence of walls or other obstructions, which bias the range estimation, resulting in a localization performance degradation. Among other obstructions, to the best of our knowledge, none of the previous research efforts has incorporated the effect of the presence of the human body on UWB propagation channels from the TOA ranging aspect, although indoor environments might be densely populated with people.

The human-body shadowing effect on indoor UWB propagation channels was previously investigated on communication aspects in [88], [28]. In [88] the measurements for UWB channels were conducted and analyzed for typical wireless personal area network applications in an office environment. In [28], a model was developed and validated for the human-body shadowing effect, based on the IEEE 802.15.3a channel model, for performance study of upper communication layers. In [89], the main propagation mechanisms through the human head were investigated, based on the results of anechoic chamber measurements. The analysis revealed that diffraction is the dominant effect, while transmission through the head is negligible. It was also concluded that reflection and absorption effects are existing but only have a subsidiary role. In [90], the presence of the human body was modeled by a conducting cylinder model and the model was validated by static and dynamic measurements, carried out at a frequency of 10.5 GHz while they did not specify the measurement bandwidth. These works were performed from communication aspects and they did not consider the effect of the human body for TOA ranging.

Considering the TOA ranging, the main interest is on the arrival time and the amplitude of the direct-path signal component, from which we find the distance between the transmitter and the receiver. In Section 2.4.1, we also noted that threshold-based first peak detection techniques are common to employ, as the strongest path in UWB channels is not always a good indicator for TOA estimation. Therefore, the main objective of this part is to analyze the effect of the human body on the arrival time and the amplitude of the first-path signal. For that reason, we conducted measurements in an anechoic chamber and a laboratory environment. Measurements are performed in the frequency domain using a VNA, in the frequency range 3–5.5 GHz. The TOA range estimation is performed by the threshold-based first peak detection technique.

In the rest of this section, the measurement setup will be introduced and it will be followed by the analysis of the measurement results.

2.5.1 Measurement Setup

Channel measurements were performed in the frequency range of 3–5.5 GHz, using a four-port Rohde & Schwarz ZVB-8 VNA and using two identical Time

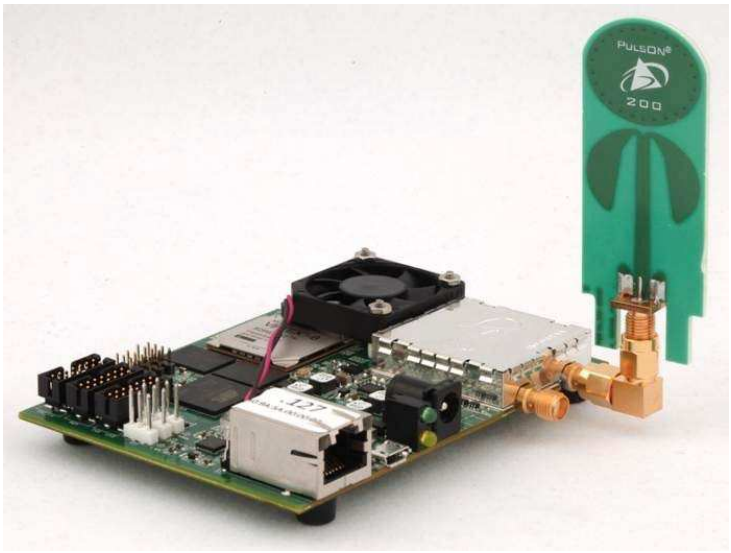

Figure 2.6: Time Domain Broadspec UWB antenna attached to a P400 RCM ranging and communication module.

Domain Broadspec UWB antennas as shown in Fig. 2.6, having 3-dBi nominal antenna gain and omnidirectional patterns [91]. The distance between the SMA connector and the phase centre of the antenna is 6 cm and it is subtracted from the TOA-based distance estimates to calibrate antenna effects on the propagation delay. To eliminate the effects of the cables and connectors (i.e., to connect the cables to the antennas), we used the VNA calibration kit. At the end of this calibration, the transfer function becomes unity when the cables are connected directly. The VNA was programmed using LabVIEW, and remotely controlled to transmit continuous wave at 601 discrete points thereby sweeping across the chosen frequency range. The complex channel transfer at each uniformly spaced frequency was recorded by measuring the S_{21} parameter. This setup gives a 0.4-ns delay resolution (as the bandwidth is 2.5 GHz) corresponding to a distance resolution of 12 cm. Since we have 601 equally spaced tones over the bandwidth of 2.5 GHz, we get the CIR up to 240 ns. This was discussed earlier in Section 2.3.2. The resolution bandwidth was set to 100 kHz and the sweep time for the measurements was 54 ms. The noise floor power in the time domain can be calculated as [92] $P_{\text{noise}} = \phi_0 \beta_{\text{rb}} / N_{\text{points}}$, where ϕ_0 denotes the typical power spectral density of the VNA and β_{rb} denotes the resolution bandwidth. For the VNA used in these measurements, ϕ_0 is given as $\phi_0 < -115$ dBm/Hz [93] between 4 GHz and 8 GHz. The scaling with $1/N_{\text{points}}$ is due to the inverse fast Fourier transform (IFFT) scaling factor according to the Matlab implementation of the IFFT. In our case, P_{noise} is

calculated lower than -92.8 dBm given the parameters $\phi_0 < -115$ dBm/Hz, $N_{\text{points}} = 601$ and $\beta_{\text{rb}} = 100$ kHz. In our experiments, the noise power was found to be -93.6 dBm by calculating the time average of the power delay profile in the delay interval where there is no signal. In other words, the mean of the earlier samples of power delay profiles before the signal arrival instant was computed. Also, this noise power was obtained for the power delay profiles, for which only rectangular windowing was applied. In general, the calculated and measured noise power values are in good agreement. Finally, for all the measurement cases, the feed points of the antennas were set to 1.3 m from the ground level, corresponding to the chest height of the test subject, who was an adult male with a height of 1.80 m and weight of 80 kg.

2.5.2 Measurement Environments and Procedures

The channel measurements were conducted in two different environments: the Advanced Network Laboratory and the anechoic chamber in the ECIT institute, Queen's University Belfast, U.K. The main difference between these two environments is that the laboratory environment consists of dense multipath sources such as tables and computers. On the other hand, the anechoic chamber, because of its design properties to absorb wireless signals, does not introduce any significant multipath reflection. For both environments, the human body was positioned between the transmitter and the receiver in two different orientations and for different distances to the antennas during the measurements. The measurements were repeated for different antenna separation distances which will be explained in more detail below.

Laboratory Measurements

This typical laboratory environment (70 m^2) consisted of metal-studded dry walls, a metal-tiled floor covered with polypropylene-fibre, rubber-backed carpet tiles, and a metal ceiling with mineral fibre tiles and recessed louvered luminaries, suspended 2.7 m above the floor level. The laboratory contained a number of computers, monitors, chairs, and desks constructed from medium-density fibreboard. Four double-glazed windows with metallic frames were located at one end of the room, with a 1.35 m-high metal-studded dry wall partition dividing the center.

In this environment, we conducted the channel measurements when there was no obstruction other than the test subject. The antenna separation was set to 7 m and 4 m, and the test subject was positioned along three different horizontal lines T2, T4 and T6; and T1 to T3, respectively, as shown in Fig. 2.7. For each horizontal line, there were nine different positions where the test subject stood in parallel and perpendicular orientations. Hence, $2 \times 3 \times 9 \times 2 = 108$ measurement scenarios were defined in total. For each scenario, 200 different channel frequency responses were stored. Furthermore, measurements were also made without the test subject for each antenna separation. A picture of an example measurement scenario is shown in Fig. 2.8.

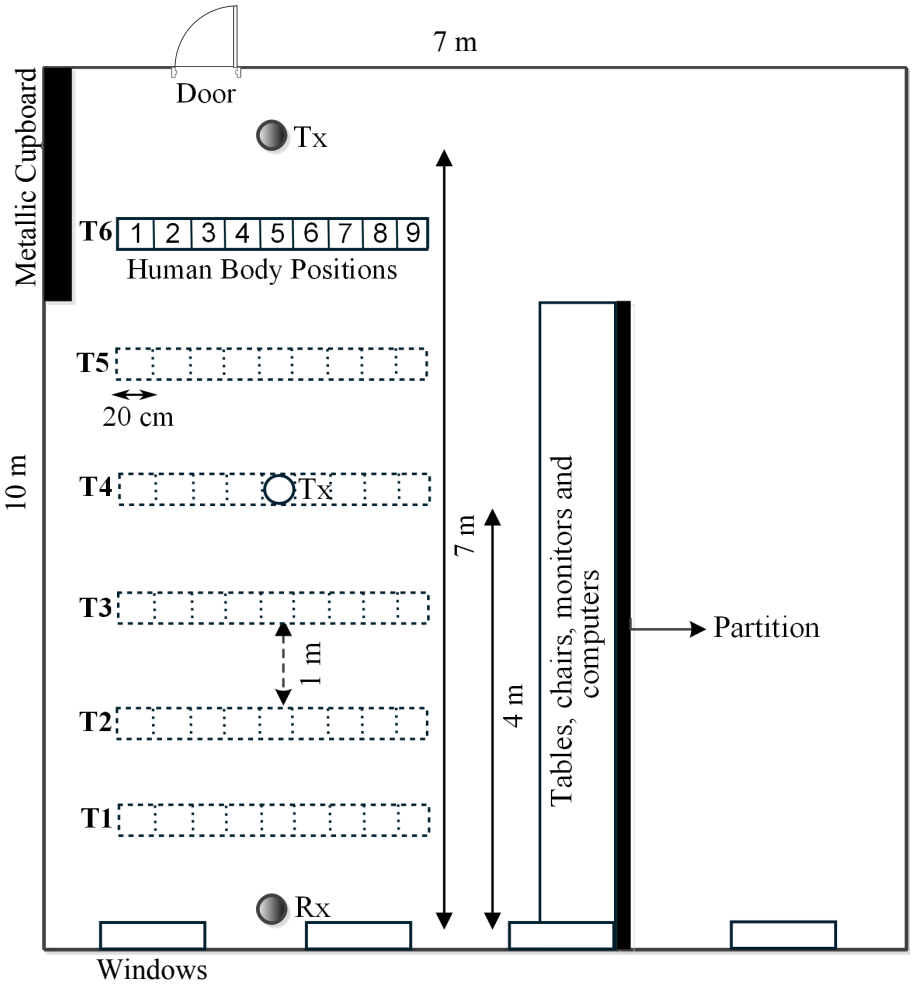

Figure 2.7: Outline view of the human-body positions (squares) and transmitter (Tx) and receiver (Rx) antenna positions for the laboratory measurements.

Anechoic Chamber Measurements

The use of the anechoic chamber enabled the effective isolation of the direct-path signal component, which is of interest in UWB time-based ranging and localization systems. The anechoic chamber has a size of $10 \times 5 \times 5$ m, and contains an L-shaped walking-path, as shown in Fig. 2.9. The path between the transmitter and the receiver was divided into seven positions with 1 m intervals. The subject was positioned on these points, in two different orientations: perpendicular (facing the antennas) and parallel to the direct path.

Figure 2.8: An example measurement scenario during the laboratory measurements: the subject is positioned on the fourth vertical (T4) and ninth horizontal position (H9) in a perpendicular orientation, with an antenna separation of 7 m.

Postprocessing

During the offline phase, the frequency domain data was first processed by a Hamming window to suppress undesired side-lobes in the time domain. The

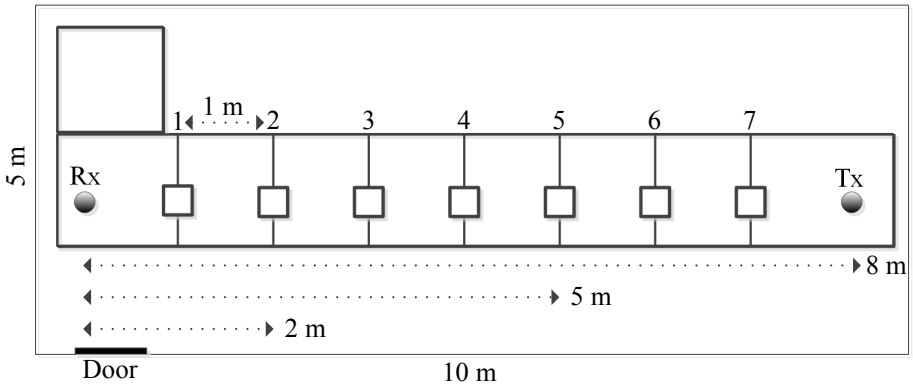

Figure 2.9: Outline view of the human-body standing points (squares), and transmitter (Tx) and receiver (Rx) antenna positions for the anechoic chamber measurements.

Hamming window provides a side-lobe suppression of 42 dB from the strongest signal component. Then, CIRs were obtained from the windowed frequency responses by IFFT. After that, the power delay profile was calculated by taking the squared magnitude of each complex CIR and range estimates were obtained by employing the leading edge detection algorithm. In this algorithm, the TOA of the signal is estimated as the delay instant of the first sample which crosses the predetermined threshold, P_{T}. Note that the power delay profile was obtained by measuring the forward path gain (magnitude of the S_{21} parameter) between two ports of the VNA (i.e., it includes the effect of the antennas). Hence, P_{T} is the threshold expressed in terms of the forward path gain. The unit of the threshold is dB because the forward path gain does not have any unit. Therefore, the power delay profiles that were obtained from the forward path gain measurements, have a dB unit after converting to the logarithmic scale. The range error for the ith measurement is defined as

$$\epsilon_i = d - c \cdot \tilde{\tau}_i, \tag{2.14}$$

where d is the actual distance, c is the speed of light and $\tilde{\tau}_i$ is the estimated TOA of the ith signal. We analyze the ranging performance in terms of the rms range error which is given by

$$\epsilon_{\mathrm{rms}} = \sqrt{\frac{1}{N}\sum_{i=1}^{N}\epsilon_i^2}, \tag{2.15}$$

where N is defined as the total number of sweeps for each scenario (200 in our case).

2.5.3 Analysis of the Results

In Fig. 2.10(a) and Fig. 2.10(b), the rms range error is plotted at different horizontal human body positions in the laboratory environment, for transmitter-receiver separations of 4 m and 7 m, respectively. As described in the previous section and shown in Fig. 2.7, there are three different measurement sets (i.e., T1, T2 and T3 for 4 m, and T2, T4 and T6 for 7 m) for each horizontal human body position. Therefore, the rms range error was calculated by combining a total of 600 CIRs for each horizontal position. Three different P_{T} values were chosen to analyze the effect of the human-body position on the range error for different choices of the threshold. In order to be able to calculate the range, the P_{T} value should be lower than the path gain of the dominant signal component, which was measured to be in the range of -57 dB to -68 dB and -61 dB to -69 dB, for 4 m and 7 m antenna separations, respectively. The lowest path gain values for the strongest signal component are obtained when the subject is standing at the fifth position for both cases, because the subject attenuates the direct path-signal component the most at this position. In our experimental analysis, we found that the maximum signal power is around -70 dB at the fifth position. Thus, we chose -70 dB as the highest detection threshold.

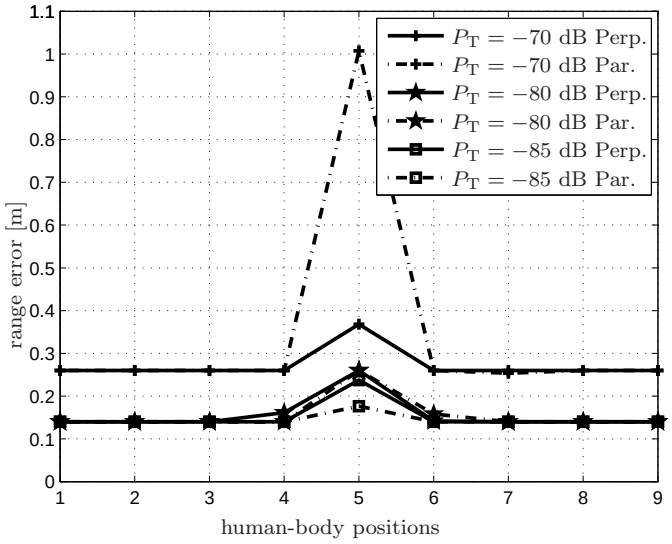

(a) Antenna separation of 4 m.

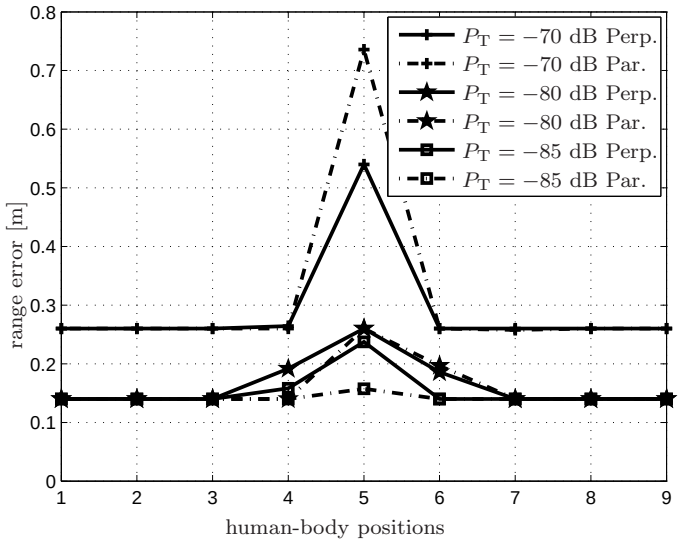

(b) Antenna separation of 7 m.

Figure 2.10: Rms range error for different human-body positions and threshold values. (The human-body positions on the horizontal axis are defined as shown in Fig. 2.7.)

The results are shown both for the perpendicular and the parallel standing cases. In both figures, the human-body effect on the ranging is clearly observed when the human body is standing between the antennas (i.e at the fifth position) and the detection threshold is set to -70 dB. Our analysis showed that the strongest signal component is no longer the direct-path component at this position. The later samples have higher power than the samples where the direct-path signal component is expected. The direct-path sample can be determined from the measurements when there was no subject standing on any of the measurement points. The power difference between the sample with the maximum power and the sample, where the direct-path signal component is expected, is around 7 dB for both orientations when the person stands at T6. At T2, the difference is 5 dB and 1 dB for perpendicular and parallel orientations, respectively. Finally, when the person stands at T4, there is almost no difference for the parallel case, and the difference is 4 dB for the perpendicular orientation. For other positions a range error of 26 cm is obtained. When P_{T} is decreased to -80 dB and -85 dB, the range error decreases for all the cases. For the first to third and seventh to ninth positions, the measured range error is 14 cm, since the leading edge detection algorithm detects another sample just crossing the threshold before the strongest path. In fact, this observation is consistent with the power delay profiles in the absence of the subject in the environment as shown in Fig. 2.11. In this case, as the figure depicts, there are two strong samples just before the strongest sample. The nearest sample to the strongest sample has just 2 dB lower power than the strongest sample, while the other one (i.e., the sample which is around the power of -85 dB) has a power difference of around 27 dB. Both of these samples are due to the effect of the windowing. Therefore, in the empty case, we need to set the detection threshold below -85 dB to detect the first sample and obtain the ranging error value of 14 cm. This value is obtained after removing the bias because of the distance between the SMA connector and the phase centre of the antenna. The resolution of the system is 12 cm, and the ranging error is normally expected to be smaller than this value, when there is no obstruction between antennas and if the TOA is properly detected. However, in our measurements, it is observed that there is always one sample of systematic error (i.e., our system detects the TOA one sample later than the actual instant) even though the threshold is set as low as possible. This can be due to unseen effects of the antennas on the delay of the transmission.

In order to analyze the ranging performance dependence on the detection threshold in a more detailed way, with the subject standing in the fifth position, the rms range error is plotted as a function of the detection threshold in Fig. 2.12 for 4 m antenna separation. The results are shown for different vertical positions, as described in Fig. 2.7. The behavior of the range error differs in three distinct regions labeled as I, II and III in both figures. We briefly discuss the causes of the results in these regions below.

- In Region I, the noise samples are falsely detected as the first peak. Therefore, the range error increases as the threshold is getting below approxi-

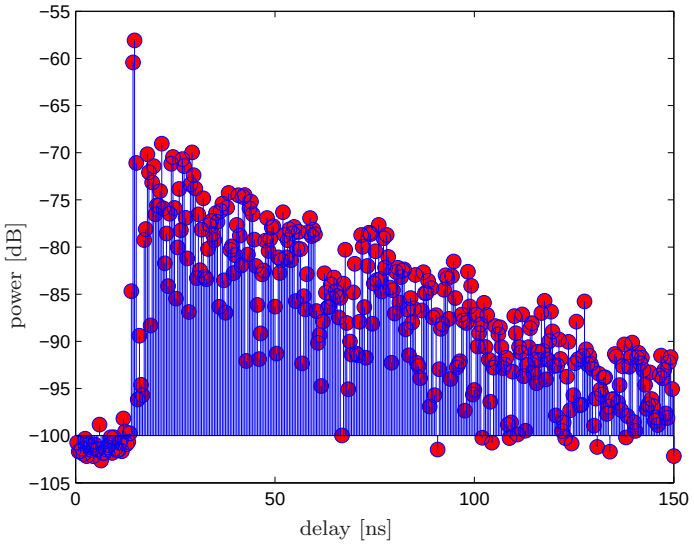

Figure 2.11: Measured power delay profile for the case in the absence of the subject. Power delay profile is averaged over 500 measurements.

mately −90 dB.

- In Region II, the lowest range error values are obtained, because the path gains of the diffracted paths around the body are above the detection threshold.
- In Region III, because the direct path is mostly attenuated and the TOA estimation algorithm detects the strongest signal component, which arrives later than the diffracted paths around the body. The range error is higher for the positions where the subject is standing close to the antennas, because in these cases the attenuation due to the diffraction is higher and the detection threshold should be set lower. For example, if the detection threshold is set to −69 dB for the parallel orientation at T3 (see Fig. 2.12), the first sample that crosses the threshold comes around 25 samples later than the sample corresponding to true TOA. As the detection threshold is set lower than −73 dB, the error gets lower because the early samples cross the threshold.

It is also observed that the effect of the body orientation is less when the detection threshold is set to lower values. The range error difference between orientations is more significant for the antenna separation of 4 m and the detection threshold of −70 dB, as shown in Fig. 2.10a. This is mainly because of the different attenuation levels of the diffracted paths when the subject is

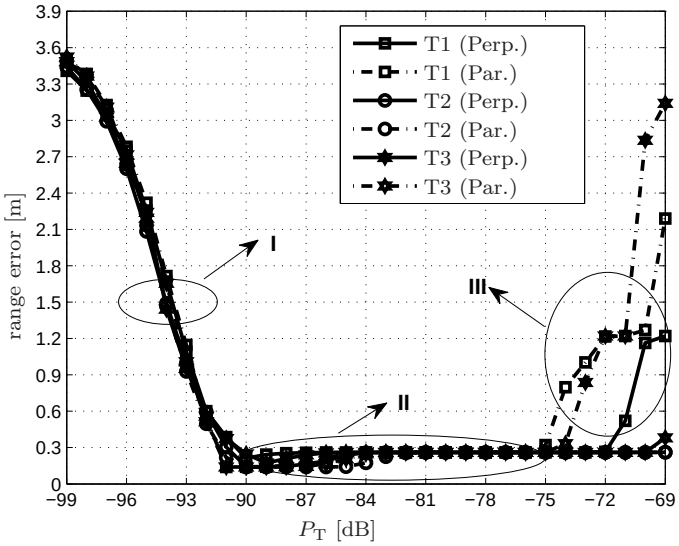

Figure 2.12: Rms range error as a function of different values of the first peak detection threshold with the subject standing in the fifth position along T1, T2 and T3 (see Fig. 2.7) with 4 m antenna separation.

close to the receiver or the transmitter. According to the measurement results, along T1 and T3, the attenuation for the parallel orientation is 4 dB and 5 dB higher than for the perpendicular case, respectively.

In order to see the effect of the human-body position on the first peak power level, the attenuation by the human body as a function of the position is plotted in Fig. 2.13(a) for 8 m antenna separation in the anechoic chamber. The mean value is computed by averaging all 200 measurements in linear scale. The final results are shown in dB scale. This result shows that the human body attenuates the direct path by around 12 dB and 9 dB, when it is close to the receiver and transmitter antennas, respectively. When the body is further away from the antennas, the attenuation slightly decreases for both the perpendicular and parallel orientations. As the human body is positioned close to the center between the antennas, there is less attenuation for parallel standing. This may result from the fact that the width of the body is larger than the depth of the body.

The standard deviations of the first-peak path gain values over 200 different sweeps are calculated in linear scale and shown in dB scale in Fig. 2.13(b). The

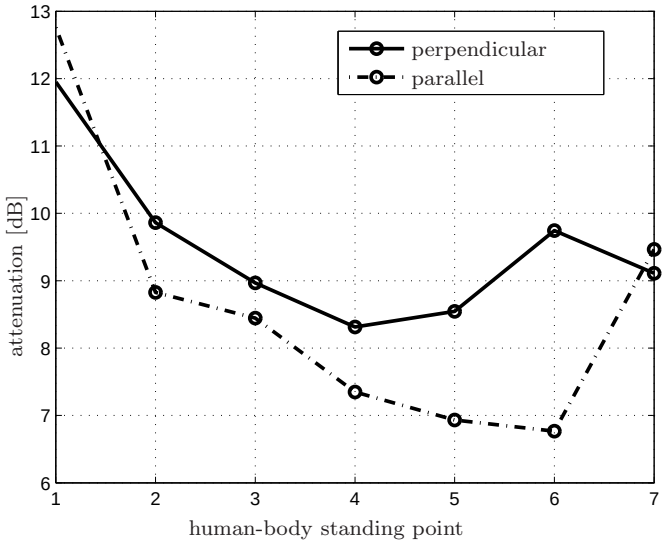

(a) Mean.

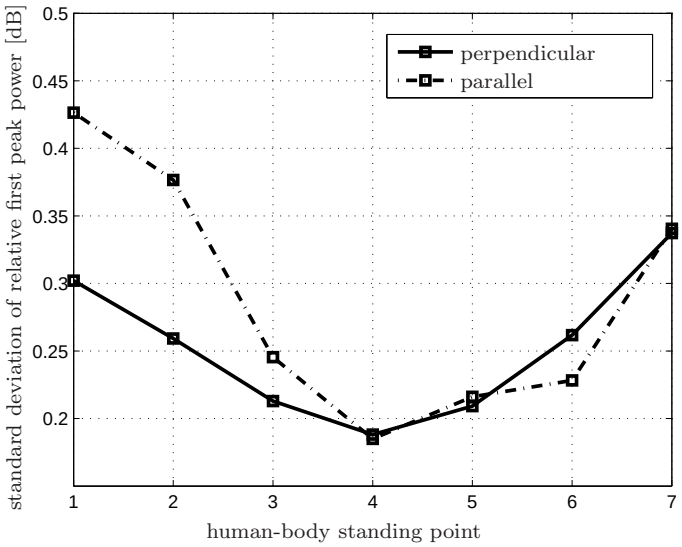

(b) Standard deviation.

Figure 2.13: Attenuation as a function of the human-body position for 8 m antenna separation in the anechoic chamber. (The human-body positions on the horizontal axis are defined as shown in Fig. 2.9.)

standard deviation is estimated as

$$P_{\mathrm{f,std}} = \sqrt{\frac{1}{199}\sum_{i=1}^{200}\left(P_{\mathrm{f,lin}}(i) - \overline{P_{\mathrm{f,lin}}}\right)^2}, \tag{2.16}$$

where $P_{\mathrm{f,lin}}(i)$ denotes the first-peak path gain and $\overline{P_{\mathrm{f,lin}}}$ denotes the mean of the 200 first-peak path gain values. Both $P_{\mathrm{f,lin}}(i)$ and $\overline{P_{\mathrm{f,lin}}}$ are defined in linear scale. The results show that the standard deviation also decreases when the human body is standing away from the antennas, similar to the mean values. This is due to the fact that the signal is affected less by body movements such as resulting from respiration. Fig. 2.13(a) and Fig. 2.13(b) clearly indicate that the human body has a severe effect on the first peak path gain value of the signal.

2.6 Conclusion

Although UWB theoretically achieves centimeter-level ranging accuracy, complex indoor propagation effects decrease the time-based ranging performance in these systems. We briefly introduced these effects and common works done in this domain so far, and investigated the effect of a human body when it is standing between the transmitter and the receiver. We performed measurement campaigns in an anechoic chamber and a laboratory environment for different positions and orientations of the body in between the antennas. We applied the leading edge detection algorithm for TOA estimation. The results revealed that no significant range error occurs due to the presence of the human body if the first peak represents the diffracted paths around the body, which can be detected with the proper choice of the detection threshold. The results also show that the power of the direct path is strongly attenuated by the presence of the human body. Due to the power limitations of the UWB system, the attenuation by the body may result in loss of the direct-path signal component under low signal-to-noise ratio cases.

Furthermore, our experiments revealed that the human body affects the UWB channel even though the person is standing still such as due to the respiration. This key observation will be used in the upcoming chapters for device-free detection and localization purposes.

Chapter 3

Device-Free Person Detection

3.1 Introduction

The detection of people with UWB transmission requires an understanding of how the person affects the received UWB waveforms, or the effect of the person on the UWB propagation channel. In fact, the presence of the person induces slow temporal variations in the amplitudes of received UWB waveforms, even for fixed transmitter and receiver positions, and when the person is stationary. With "stationary", it is meant that the person intentionally stands still, while small movements occur due to the breathing and body imbalance. Our goal is to investigate the appropriate signal processing methods that can capture the small changes in body posture and detect the presence of the person, and, accordingly, estimate the position without the requirement of a template received signal that is obtained at the receiver during the offline training phase while the person is absent in the environment.

This chapter[1] shows both numerical and experimental results to quantify the performance of the detection technique. The results will be shown for common detection performance indicators: probability of false alarm and probability of missed detection. These two performance metrics are dependent on the operating SNR conditions, the position of the person with respect to the transmitter and the receiver positions and the number of measurement repetitions. This dependence will be shown for analytical results. Analytical results will also show the dependence of the detection threshold, which can be chosen from the analytical false alarm probability. Experimental results will also be shown for these detection metrics to validate the model upon which the analytical results are developed. These results will also provide quantitative evaluation of the performance in practical settings.

While the device-free ranging and position estimation is postponed to the next chapter, this chapter deals with the development of a signal processing technique for the detection of a stationary person.

[1] The contents of this chapter and Chapter 4 were published in [94, 95].

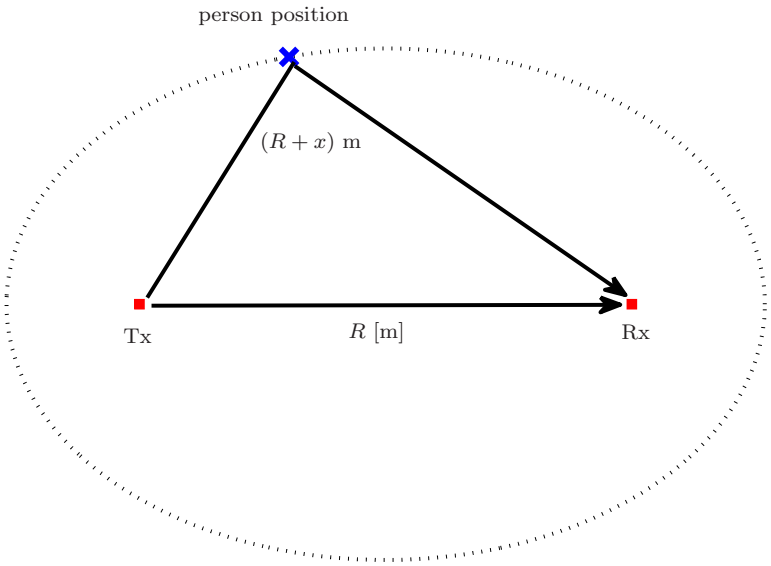

Figure 3.1: An example measurement scenario. The position of the person is shown as a blue cross, and the transmitter (Tx) and the receiver (Rx) are shown as red squares.

This chapter is organized as follows. First, experimental observations will be given for waveforms, received in an indoor environment and over a single UWB link, in the absence and the presence of the person. Therefore, an understanding for the influence of the person on UWB propagation will be attained, before proceeding with a received UWB signal model, that is based on our experimental observations. A decision statistic will then be defined to determine the presence of the person, followed by theoretical calculations of achievable false alarm and missed detection probabilities by this detection technique. To verify the analytical approximations that are used throughout the calculations, simulation results will also be given. Finally, experimental results will be presented to quantify the performance of the system in realistic environments.

3.2 Experimental Observations

In this section, experimental observations will be given to indicate the effect of the presence of a person on UWB signals. Here, our goal is to provide example measurement results, that are obtained from a set of indoor LOS

measurements, to motivate the signal model, introduced in the next section. The measurements were performed with two identical, commercially available and FCC-compliant UWB radios (Time Domain P400 radios). The radios are capable of performing communications and ranging using UWB signaling within the frequency range of 3–5.5 GHz. They are equipped with identical antennas that are omni-directional within the operating frequency range. While these radios are primarily designed for two-way TOA ranging, they are capable of capturing a waveform. At the receiving radio, the waveforms are sampled with a sampling period of 61 ps over a window of approximately 10 ns.

Let us consider the following scenario shown in Fig. 3.1: a transmitter and a receiver, separated by a distance of R meters in an indoor LOS environment, and a person standing on a position near the transmitter and the receiver. Considering the position of the person as a point at the center of the body, the person can be located on an ellipse whose foci are the transmitter and the receiver positions, and major axis length is $(R + x)$ meters[2]. In this case, the distance traveled by the reflected signal is $(R + x)$ meters. In other words, it is equivalent to a delay of x/c with respect to the arrival instant of the direct-path signal, where c denotes the speed of light. We transmit N_{rep} ranging symbols from the transmitter to the receiver, and align these corresponding N_{rep} received waveforms by postprocessing in the delay domain, starting from the arrival time of each ranging symbol.

View in the delay domain

Fig. 3.2 shows the mean of $N_{\text{rep}} = 100$ received UWB waveforms, collected with off-the-shelf UWB radios over 20 seconds, when a person is present (red dashed line) or absent (blue solid line). The mean is calculated as the time average of the received waveforms over 20 seconds (i.e., average over the 100 waveforms). In this case, the distance R between the transmitter and the receiver is 5 m, and the major axis length $(R + x)$, corresponding to the position of the person, is 7.7 meters. Hence, we expect the effect of the person on UWB signals around $x/c = 9$ ns after the arrival time of the signal. According to the result in Fig. 3.2, we observe that the person affects the signal to some small extent around 9 ns. However, the difference between the means of the signals is small. Therefore, without a clean template signal (i.e., in the same environment, in the absence of the person), it is hard to determine the signal changes due to the presence of a person.

[2]In this work, the position of the person is considered as a point at the center of the body. In practice, the signal will be reflected from different parts of the body depending on, for instance, the body size and the orientation of the body relative to transmitter and the receiver antennas. Therefore, if the definition of the bistatic range (i.e., the total transmitter to person and person to receiver distance) is based on the center of the body, then its estimate will always be biased.

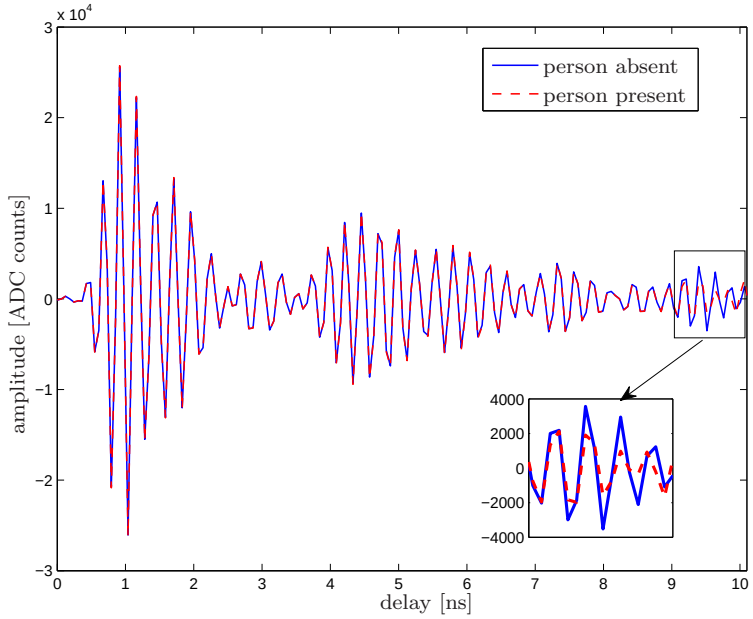

Figure 3.2: Mean of 100 UWB measurements, taken continuously within 20 seconds in an indoor LOS environment, in the presence and absence of a person.

View in the time domain

Fig. 3.3 offers a different perspective, and shows the variation of the signal over the N_{rep} repetitions at a fixed delay of 9.7 ns (i.e, the zeroth delay instant corresponds to the arrival time of the signal), in the presence and the absence of the person. It is clear that, without a person, the signal shows only little variation around $-3,500$ analog-to-digital converter (ADC) counts, as it is mainly affected by the noise. In contrast, when the person is present, the signal shows more significant variations, albeit slowly over time, even in a fixed position.

Similar observations are also obtained, in [51,56,58]. In [56,58] this effect is explained through a propagation model, capturing minor temporal variations, induced by, amongst others, the breathing of the person. In particular, in [56, 58] a sinusoidal model is used to analyze the effect of the breathing movement, and in [57], estimation of parameters related to this periodic movement is considered.

In our work, our goal is to use these variations to detect the presence of the person, and to locate in a passive manner. To this end, we will not go into complex propagation models related to the effect of the human body on UWB

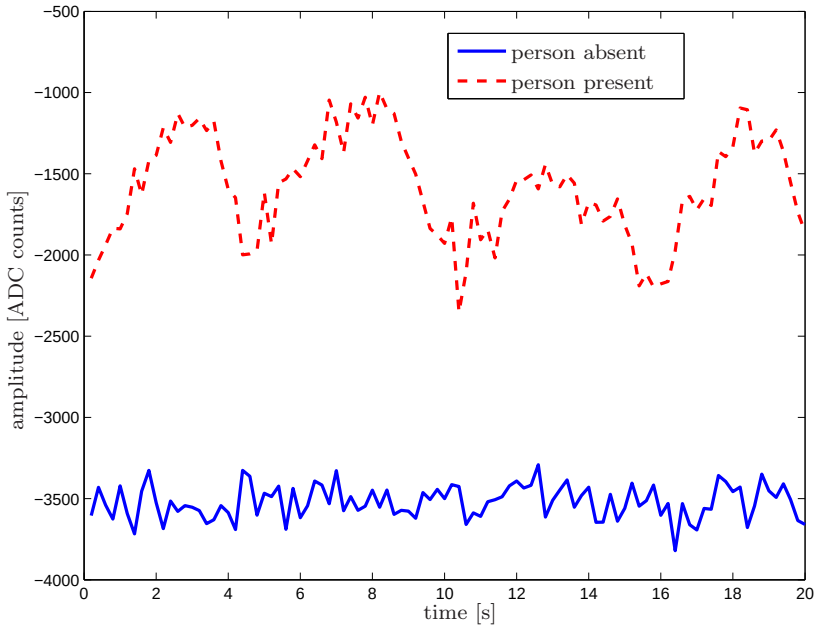

Figure 3.3: Variation of the received waveform over time at delay instant 9.7 ns, in the presence and absence of a person.

signaling, but rather view the signal in Fig. 3.3, in the presence of the person, as a generic low-frequency signal plus background noise.

3.3 Signal Model

Based on our observations in the previous section, we pose the following signal model. The transmitted UWB ranging symbol defined as in Chapter 2, Section 2.2, consists of N_f pulses with a total duration of $T_\mathrm{s} = N_\mathrm{f} T_\mathrm{f}$, where T_f is the frame duration. T_s is smaller than the period T_rep, denoting the repetition period of the ranging symbol, and E_s is the transmitted symbol energy which is defined as $E_\mathrm{s} = N_\mathrm{f} E_\mathrm{p}$.

For each ranging symbol, the receiver coherently combines N_f pulses during each of the N_rep repetitions, leading to the following received signal

$$\begin{aligned} r_\mathrm{rep}(t) =& \sqrt{E_\mathrm{s}} \sum_{k=1}^{N_\mathrm{rep}} \sum_{l=1}^{L} \alpha_l p(t - \tau_l - kT_\mathrm{rep}) \\ &+ \sqrt{E_\mathrm{s}} \sum_{k=1}^{N_\mathrm{rep}} \alpha_\mathrm{p}(t) p(t - \tau_\mathrm{p} - kT_\mathrm{rep}) + n(t). \end{aligned} \tag{3.1}$$

The received signal is obtained after convolving the transmitted signal with the CIR that is modeled as

$$h_{\mathrm{ch}}(t,\tau) = \underbrace{\sum_{l=1}^{L} \alpha_l \delta(\tau - \tau_l)}_{\text{static}} + \underbrace{\alpha_{\mathrm{p}}(t)\delta(\tau - \tau_{\mathrm{p}})}_{\text{time-varying}}, \tag{3.2}$$

i.e., the CIR is written in terms of the static and time-varying parts. The static part comprises L signal paths, which are due to the static reflections in the environment and do not vary due to the movement of the person. Here, α_l and τ_l are the channel coefficient and the delay of the lth discrete path, respectively. Assuming the delays are ordered, τ_1 corresponds to the LOS path. In (3.2), real-valued channel coefficients are considered because the received signal model is based on real samples, as that is what our measurement hardware provides. The second term in (3.1) corresponds to the reflection due to the person, with $\alpha_{\mathrm{p}}(t)$ varying slowly over time due to the effects of the human body. τ_{p} is the corresponding delay for the path, reflecting from the person. For the time-varying channel part, a simplified channel description is written by assuming that only the channel coefficient α_{p} depends on time but not the corresponding delay τ_{p}.

In (3.1), the noise $n(t)$ is assumed to be zero-mean white Gaussian noise with power spectral density $N_0/2$. Direct sampling of $r_{\mathrm{rep}}(t)$ at a sufficiently high rate W over a window with duration T_{delay}, and aligning the N_{rep} copies, we obtain a two-dimensional received signal model for $k = 0, 1, \ldots, N_{\mathrm{rep}} - 1$ and $m = 0, 1, \ldots, M - 1$ as

$$\begin{aligned} \widetilde{r}(k,m) = r(kT_{\mathrm{rep}} + m/W) = & \sqrt{E_{\mathrm{s}}} \sum_{l=1}^{L} \alpha_l p(m/W - \tau_l) \\ & + \sqrt{E_{\mathrm{s}}}\widetilde{\alpha}_{\mathrm{p}}(k) p(m/W - \tau_{\mathrm{p}}) \\ & + \widetilde{n}(k,m), \end{aligned} \tag{3.3}$$

with $\widetilde{\alpha}_{\mathrm{p}}(k) = \alpha_{\mathrm{p}}(kT_{\mathrm{rep}} + m/W)$ and $\widetilde{n}(k,m) = n(kT_{\mathrm{rep}} + m/W)$, where

$$\mathbb{E}\left\{\widetilde{n}(k,m)\widetilde{n}(k',m')\right\} = \frac{N_0 W}{2}\delta_{kk'}\delta_{mm'}. \tag{3.4}$$

$\mathbb{E}\{.\}$ denotes the statistical expectation and δ_{ij} is the discrete (or Kronecker) delta function, which is defined as

$$\delta_{ij} = \begin{cases} 1, & i = j, \\ 0, & i \neq j. \end{cases} \tag{3.5}$$

The second line in (3.3) corresponds to the person, which introduces a single resolvable channel coefficient that varies slowly over time (i.e., only as a function of k). In view of this model, it is assumed that the variation of $\alpha_{\mathrm{p}}(t)$ over one channel snapshot is negligible, because the person is considered to be

stationary during each of the N_{rep} repetitions and hence the dependence on m in $\widetilde{\alpha}_{\text{p}}(k)$ is omitted (i.e., only the variation from snapshot to snapshot is considered). For simplicity, the secondary reflections due to the person are also neglected in the above model. Further discussion about this point is postponed to the section on experimental results.

We can further break up the channel coefficient corresponding to the person in a static part (i.e, independent of k) and a slowly-varying part as

$$\widetilde{\alpha}_{\text{p}}(k) = \widetilde{\alpha}_{\text{p,s}} + \sqrt{G(\tau_{\text{p}})}w(k) \tag{3.6}$$

where $\widetilde{\alpha}_{\text{p,s}}$ denotes the constant part of the channel coefficient, depending on the propagation effects of the human body. The second part in (3.6) shows the varying part of the channel coefficient, where we introduce the terms $G(\tau_{\text{p}})$ and $w(k)$ to separate the effect of the propagation loss from the shape of the variations for the time-varying part of the channel coefficient. For this purpose, $w(k)$ is introduced to represent the unknown fluctuations and is assumed to be of low frequency, zero mean and unit mean power in the time dimension (i.e., $\sum_k w^2(k) = N_{\text{rep}}$). Furthermore, $G(\tau_{\text{p}})$ is defined to show the relation between the propagation loss and τ_{p}. Due to the propagation loss, the received power related to the human-body reflected path decreases as the length or the delay of the path (i.e., the distance traveled by the human-body reflected path) increases. We note here that the variations will be higher, for instance, for a strongly moving person. Therefore, in general, the values of $G(\tau_{\text{p}})$ may also depend on the movement of the person. However, we consider a static person, whose variation effect on the channel coefficient is due to minor movements, such as breathing activity, and assume that there is no variation in the relation between $G(\tau_{\text{p}})$ and τ_{p} because of the differences in movement of the person. Based on our experimental analysis, we model $G(\tau_{\text{p}})$ as

$$G(\tau_{\text{p}}) = G(\tau_{\text{ref}}) \left(\frac{\tau_{\text{p}}}{\tau_{\text{ref}}} \right)^{-\eta} \tag{3.7}$$

for a reference value $G(\tau_{\text{ref}})$ at a reference delay τ_{ref} and an exponent η[3]. The relation in (3.7) is defined based on the results of our experimental data, that will be introduced in Section 3.7.1. It does not include the small-scale fading (e.g., the influence of the multipath transmission, that is caused by the stationary objects, to the human-body induced variations) and large-scale fading (e.g., shadowing by walls) effects. It rather gives an indication of how the energy of human-body induced variations change with the propagation delay, excluding these fading effects. To this end, we also note that $G(\tau_{\text{p}})$ does not have such a strict relationship with τ_{p} as given in (3.7) and may show random

[3]The relation in (3.7) can also be viewed similar to the typical path-gain models which describe the distance dependence of the received signal power. Given a reference received signal power $P_{\text{r},0}$ at a reference distance $d_{\text{r},0}$ and path-gain exponent η, the received signal power at distance d is usually expressed in dB as $P_{\text{r}} = P_{\text{r},0} - 10\eta\log_{10}(d/d_{\text{r},0})$, as also shown in (1.1).

fluctuations for each value of τ_p around the main curve (e.g., a linear line if we consider (3.7) in the dB domain.). We did not consider these fluctuations as we observe them to be relatively small for a stationary person. Furthermore, we also note that $w(k)$ is assumed to be independent from the noise $n(k, m)$.

Note that, as also mentioned in Section 2.2, the signal-to-noise ratio SNR $= E_s/N_0$ depends on the number of pulses as E_s scales proportional to the number of pulses. Because of the power limitation in UWB systems, combining less pulses may lead to low SNR at reception. On the other hand, transmitting more pulses in the ranging symbol results in larger symbol duration T_s, and accordingly, larger T_{rep}. Therefore, the sampling rate of the received signals in the time domain (i.e., $1/T_{rep}$) will be lower. Hence, given the power limitations in UWB systems, there is a trade-off between the received SNR and the system update rate.

In our setting, L, α_l and τ_l ($l = 1, 2, \ldots, L$) are not known to the detection and device-free localization system, but assumed to be constant as a function of time, during $1 \leq k \leq N_{rep}$. Moreover, τ_1 is the delay of the direct path and can be estimated using TOA estimation techniques discussed earlier in Chapter 2.

3.4 The Detection Method

Given the model in Section 3.3, we can describe the behavior of the signal in the presence and the absence of the person. If we consider a single received delay bin m/W over time, we have two cases, where the time-varying signal and noise are present, and only the noise is present, respectively. The former case happens when the person is present, while the latter is possible in the absence of the person. Based on this, we can formulate two hypotheses (i.e., the person is present and the person is absent) and develop a decision statistic based on the signal properties for each case.

This section is devoted to the development of a detection method to decide whether the person is present or absent, based on the signal model in (3.3). We will proceed as follows: we first consider a fixed delay sample m and determine a meaningful decision statistic. Then, these statistics will be combined over multiple delay bins, since the person affects multiple delay bins over the pulse duration. A theoretical performance analysis of the final decision statistic will be deferred to Section 3.5.

3.4.1 Statistic for a Single Delay Bin

The first line in (3.3) contains the signal part that is fixed over time. It does not contain any relevant information for our purpose, as it is due to the static background reflections. The effect of these static reflections can be removed from the signal, by computing the mean of the signal over a number of time samples N_{rep} and subtracting the mean from the signal. Note that estimating the fixed signal part from the mean of the signal is subject to an estimation error, but for large N_{rep} and low noise power spectral density $N_0/2$, this error

can be ignored [96]. In our case, we assume that N_{rep} is sufficiently large to be able to neglect the estimation error with respect to the variations that we are trying to detect.

Subtraction of the mean from the signal leads to the following signal model

$$r_m(k) = \begin{cases} n_m(k), & \text{no person affects delay } m, \\ x_m(k) + n_m(k), & \text{a person affects delay } m, \end{cases} \tag{3.8}$$

where we have moved the delay index m to a subscript to emphasize the dependence on the time index k. Here, $x_m(k)$ is a low-frequency signal induced by the presence of the person and $n_m(k)$ is assumed to be time-discrete white Gaussian noise with variance $N_0W/2$. As the fixed part of the signal was removed by subtracting the mean of the signal, $x_m(k)$ is written as the second term in the right-hand side of (3.6) multiplied by the transmitted pulse and $\sqrt{E_{\text{s}}}$ (as in the second term of (3.3)), resulting in

$$x_m(k) = \sqrt{E_{\text{s}}G(\tau_{\text{p}})}w(k)p(m/W - \tau_{\text{p}}). \tag{3.9}$$

In order to filter out high-frequency noise components from the low-frequency variations induced by the person, we decompose the received signal as

$$r_m(k) = r_{m,\text{L}}(k) + r_{m,\text{H}}(k) \tag{3.10}$$

where $r_{m,\text{L}}(k)$ and $r_{m,\text{H}}(k)$ are the low- and the high-frequency components, with normalized bandwidths (i.e., bandwidths that are normalized to $1/T_{\text{rep}}$) of β and $0.5-\beta$, respectively, where $\beta \ll 0.5$. In practice, β depends upon how fast the movements of the person occur within the time window of duration $T_{\text{rep}}N_{\text{rep}}$. For instance, β/T_{rep} should be around 0.1 to 0.4 Hz for normal breathing rates.

Stacking the time samples yields the vectors $\mathbf{r}_m$, $\mathbf{x}_m$, and $\mathbf{r}_{m,\text{L}}$, where $\mathbf{r}_m = [r_m(0)\ r_m(1)\ \ldots\ r_m(N_{\text{rep}}-1)]^T$, $\mathbf{x}_m = [x_m(0)\ x_m(1)\ \ldots\ x_m(N_{\text{rep}}-1)]^T$ and $\mathbf{r}_{m,\text{L}} = [r_{m,\text{L}}(0)\ r_{m,\text{L}}(1)\ \ldots\ r_{m,\text{L}}(N_{\text{rep}}-1)]^T$. Here, $\mathbf{x}_m$ is an unknown signal vector and we only know that it has low-frequency components of our interest in the presence of the person. A meaningful decision statistic can be developed based on the energy of $\mathbf{r}_m$, as the energy will be higher when the person is present compared to the case where the person is absent. Although $\mathbf{x}_m$ is unknown, it is known that $\mathbf{x}_m$ only affects the low-frequency part of the received signal. This leads to a decision statistic which is based on the collection of the energy of the low-frequency received signal component as

$$y(m) = \|\mathbf{r}_{m,\text{L}}\|^2. \tag{3.11}$$

The above decision statistic is also optimum in the sense that, for a signal with an unknown phase in additive white Gaussian noise, the energy detector is the optimum detection method. In the absence of the person, the expected value of the metric defined in (3.11) becomes $\mathbb{E}\{y(m)\} = N_0\beta W N_{\text{rep}}$. We normalize

$y(m)$ with $N_0 \beta W N_{\text{rep}}$ and obtain

$$y(m) = \frac{\|\mathbf{r}_{m,\text{L}}\|^2}{N_0 \beta W N_{\text{rep}}} \tag{3.12}$$

as the decision statistic for the fixed delay bin (i.e., in the absence of the person, $\mathbb{E}\{y(m)\} = 1$). This decision statistic $y(m)$ is intuitively appealing as it collects the energy of the low-frequency variation, resulting from the movement of the person.

In practice, the noise spectral density N_0 must be estimated as well. The practical issues related to the estimation of N_0 will be discussed in Section 3.7.3.

3.4.2 Statistic for a Delay Window

In Section 3.4.1, the decision static was developed for a single delay bin m. As we can see from the second line of the signal model in (3.3), the channel coefficient related to the person is multiplied by the transmitted pulse. Therefore, not only a single bin m but also a number of received signal bins over the duration of the pulse length T_{p} will show slow fluctuations over time due to the presence of the person. We can aggregate the information over multiple delay bins by averaging the delay-specific statistic over a rectangular window around a trial delay τ, which is, together with $T_{\text{p}}/2$, assumed to be an integer multiple of $1/W$, as

$$D(\tau) = \frac{1}{T_{\text{p}} W} \sum_{m=(\tau - T_{\text{p}}/2)W}^{(\tau + T_{\text{p}}/2)W} y(m). \tag{3.13}$$

Note that we chose a rectangular window although different bins are affected differently, depending on where the pulse $p(t)$ is sampled and at which bins the presence of the person affects the signal. As we do not know the exact delay because of the person, the factor $p(m/W - \tau_{\text{p}})$ can be considered as unknown. In other words, we do not know if a certain bin has a high variation due to the presence of the person and therefore a high value of $y(m)$. Besides, we also do not know which portion of the pulse this delay sample corresponds to. Therefore, we can combine the statistic over $T_{\text{p}} W$ delay bins, with equal weights (i.e., the weights are considered to be $1/(T_{\text{p}} W)$ above). The final statistic is calculated by a moving average. The presence of a person can thus be determined by comparing $D(\tau)$ to a threshold. Hence, the person is detected as

$$\begin{cases} D(\tau) \leq \gamma, & \text{no person present,} \\ D(\tau) > \gamma, & \text{person present,} \end{cases} \tag{3.14}$$

where γ is a threshold. The selection of γ is related to the performance trade-off, and will be treated in Section 3.5.

3.5 Performance Analysis

Typically, the performance of binary detectors are analyzed in terms of the false alarm and the missed detection probabilities [97]. For our case, a false alarm occurs when the detector chooses the hypothesis that the person is present while the person is absent. Conversely, a missed detection occurs in the case when the person is present while the detector chooses the hypothesis that the person is absent. An analysis of the missed detection and false alarm probabilities gives us an opportunity to analyze on which parameters the performance of the detector depends. Therefore, we can tune these parameters to minimize the errors related to the false alarm and the missed detection according to our needs. For instance, we can sacrifice on the false alarm probability to get a better missed detection probability, or vice versa. Furthermore, we can define the detection threshold γ based on a criterion defined by the false alarm and missed detection probabilities.

In this section, we determine the false alarm and missed detection probabilities of the detector proposed in (3.14), for an estimate τ^* of the delay of the human-body reflected path. The value of τ^* also determines the bistatic range, that is the total distance from the transmitter to the person and from the person to the receiver. The estimation techniques for the bistatic range are deferred to Chapter 4, where we will discuss the device-free ranging and localization.

3.5.1 Probability of False Alarm

In the absence of the person, substitution of (3.12) into (3.13), accounting for the fact that $r_{m,\mathrm{L}}(k) = n_{m,\mathrm{L}}(k)$ is low-frequency noise, yields

$$D(\tau^*) = \frac{1}{T_\mathrm{p} N_0 \beta W^2 N_\mathrm{rep}} \sum_{m=(\tau^*-T_\mathrm{p}/2)W}^{(\tau^*+T_\mathrm{p}/2)W} \|\mathbf{n}_{m,\mathrm{L}}\|^2 . \tag{3.15}$$

$\{n_{m,\mathrm{L}}(k)\}$ are Gaussian noise samples obtained after filtering the noise samples with a low-pass filter with unity gain over the normalized frequency band $[-\beta, \beta]$. Because of the filtering, the variance of $n_{m,\mathrm{L}}(k)$ becomes $N_0 W \beta$. For sufficient number of time samples N_rep and delay samples $T_\mathrm{p} W$, we can invoke the central limit theorem (CLT)[4], and approximate $D(\tau^*) \sim \mathcal{N}(\mu_\mathrm{f}, \sigma_\mathrm{f}^2)$, where we already know that

$$\mu_\mathrm{f} = 1. \tag{3.16}$$

[4]Because of the filtering, roughly every consecutive $1/\beta$ samples of $n_{m,\mathrm{L}}(k)$ are correlated (also dependent) for each delay bin m. Based on (3.4), we already know that delay samples over $T_\mathrm{p} W$ bins are uncorrelated (also independent). For the CLT to hold, there should be sufficient independent samples. For this reason, the number of samples N_rep, that is needed to obtain a good approximation, is much larger than $1/\beta$. This is discussed in detail in Section 3.6.1, where we compare analytical and simulation results.

σ_{f}^2 is calculated, using the assumption $\beta N_{\mathrm{rep}} \gg 1$, in Appendix A.1, and found to be

$$\sigma_{\mathrm{f}}^2 = \frac{1}{T_{\mathrm{p}}\beta W N_{\mathrm{rep}}}. \tag{3.17}$$

Finally, we can obtain the probability of false alarm P_{FA} as

$$\begin{aligned} P_{\mathrm{FA}} &= \Pr\left\{D(\tau^*) > \gamma \,|\, \text{no person present}\right\} \\ &= Q\left(\frac{\gamma - \mu_{\mathrm{f}}}{\sigma_{\mathrm{f}}}\right) \\ &= Q\left((\gamma - 1)\sqrt{T_{\mathrm{p}}\beta W N_{\mathrm{rep}}}\right), \end{aligned} \tag{3.18}$$

where $Q(.)$ denotes the Q-function, given by

$$Q(z) = \int_z^\infty \frac{1}{\sqrt{2\pi}} \exp\left(-\frac{1}{2}x^2\right) \mathrm{d}x. \tag{3.19}$$

We can determine the required value of γ for a given P_{FA} by finding the argument of the Q-function. Symbolically, denoting $Q^{-1}(.)$ as the inverse Q-function [97], we obtain an equation for γ as

$$\gamma = 1 + \frac{Q^{-1}(P_{\mathrm{FA}})}{\sqrt{T_{\mathrm{p}}\beta W N_{\mathrm{rep}}}}. \tag{3.20}$$

$Q^{-1}(.)$ can be determined by means of a look-up table or a numerical solver.

3.5.2 Probability of Missed Detection

In the presence of the person, substitution of (3.12) into (3.13), accounting for the fact that $r_{m,\mathrm{L}}(k) = x_m(k) + n_{m,\mathrm{L}}(k)$, yields

$$D(\tau^*) = \frac{1}{T_{\mathrm{p}} N_0 \beta W^2 N_{\mathrm{rep}}} \sum_{m=(\tau^* - T_{\mathrm{p}}/2)W}^{(\tau^* + T_{\mathrm{p}}/2)W} \left\|\mathbf{x}_m + \mathbf{n}_{m,\mathrm{L}}\right\|^2. \tag{3.21}$$

Substitution of (3.9) into (3.21) and expanding the square yields

$$\begin{aligned} D(\tau^*) =& \frac{1}{T_{\mathrm{p}} N_0 \beta W^2 N_{\mathrm{rep}}} \sum_{m=(\tau^* - T_{\mathrm{p}}/2)W}^{(\tau^* + T_{\mathrm{p}}/2)W} \left(\left\|\mathbf{x}_m\right\|^2 + \left\|\mathbf{n}_{m,\mathrm{L}}\right\|^2 + 2\mathbf{x}_m^T \mathbf{n}_{m,\mathrm{L}}\right) \\ =& \frac{1}{T_{\mathrm{p}} N_0 \beta W^2 N_{\mathrm{rep}}} \sum_{m=(\tau^* - T_{\mathrm{p}}/2)W}^{(\tau^* + T_{\mathrm{p}}/2)W} \Big(G(\tau_{\mathrm{p}}) E_{\mathrm{s}} p^2(m/W - \tau_{\mathrm{p}}) \left\|\mathbf{w}\right\|^2 \\ & + \left\|\mathbf{n}_{m,\mathrm{L}}\right\|^2 + 2\mathbf{x}_m^T \mathbf{n}_{m,\mathrm{L}}\Big). \end{aligned} \tag{3.22}$$

Invoking again the CLT for sufficiently large N_{rep}, $D(\tau^*) \sim \mathcal{N}(\mu_{\text{d}}, \sigma_{\text{d}}^2)$, where μ_{d} and σ_{d}^2 are calculated in Appendix A.2 and found as

$$\mu_{\text{d}} = 1 + \frac{G(\tau_{\text{p}})E_{\text{s}}}{T_{\text{p}}N_0\beta W}, \tag{3.23}$$

and

$$\sigma_{\text{d}}^2 = \frac{1}{T_{\text{p}}\beta W N_{\text{rep}}}\left(1 + \frac{2G(\tau_{\text{p}})E_{\text{s}}}{T_{\text{p}}N_0\beta W}\right). \tag{3.24}$$

Finally, the probability of missed detection P_{MD} is obtained as

$$\begin{aligned} P_{\text{MD}} &= \Pr\{D(\tau^*) \leq \gamma \,|\, \text{person present}\} \\ &= 1 - Q\left(\frac{\gamma - \mu_{\text{d}}}{\sigma_{\text{d}}}\right) = Q\left(\frac{\mu_{\text{d}} - \gamma}{\sigma_{\text{d}}}\right). \end{aligned} \tag{3.25}$$

Note that we can obtain a relation between the false alarm and missed detection probabilities through substitution of (3.20) in (3.25).

3.6 Numerical Evaluation and Discussion

In this section, we quantify the performance of the detection technique, developed in Section 3.4. We will first compare the analytical results with simulation results for different numbers of ranging symbols N_{rep}. Then, we will show analytical results for the missed detection probability in different SNR conditions and bistatic ranges.

3.6.1 Simulation Setup

We performed simulations in order to validate the approximations in the theoretical calculations for the false alarm and the missed detection probabilities. Unless otherwise stated, the seventh derivative of a Gaussian pulse is considered as the transmitted signal with a duration $T_{\text{p}} = 1.42$ ns. The pulse shape and the pulse duration T_{p} are chosen with the consideration that they are close to the pulse shape and the duration of the experimental equipment whose properties will be discussed in Section 3.7.1. Because of this reason, it is chosen different from the pulse shape shown in Fig. 2.1, where the main goal was to illustrate an example IR-UWB transmitted symbol. The seventh derivative can be obtained from the Gaussian monocycle, discussed in Section 2.2. The shape of the transmitted pulse is hence chosen as [98]

$$p(t) = \frac{256\pi^4 t \exp(-2\pi t^2/\zeta^2)}{\zeta^{14}}(105\zeta^6 - 420\pi t^2\zeta^4 + 336\pi^2 t^4\zeta^2 - 64\pi^3 t^6), \tag{3.26}$$

where t denotes time, and $\zeta = 7,14 \times 10^{-10}$ is chosen to obtain the pulse width $T_{\text{p}} \approx 2\zeta$ of the experimental equipment. During the simulations, the pulse,

described in (3.26), is also normalized to its energy. Therefore, the transmitted pulse has unit energy. The receiver sampling time is set to 61 ps, resulting in 23 delay samples over the transmitted pulse duration.

We collect a varying number of repetitions N_{rep} with a period $T_{\text{rep}} = 0.2$ s. The variation due to the person is assumed to have a sinusoidal shape [56, 57] with a normalized frequency of 0.04 cycles/sample (i.e., an absolute frequency of 0.2 Hz). For our purpose of the simulation, the shape of the variation does not have an influence, as we are interested in the energy in the variations. The normalized bandwidth of the filter, applied over time, is set to $\beta = 0.05$ (i.e., an absolute bandwidth of 0.25 Hz). Hence, it is fully possible to capture the temporal variations induced by the person. We applied an ideal (rectangular) low-pass filter, which is implemented in the frequency domain by multiplying the Fourier Transform of the signal with the rectangular transfer function.

Based on our measurement data, we set the model parameters in (3.7) as $G(\tau_{\text{ref}}) = 3.6 \times 10^{-3}$, $\tau_{\text{ref}} = 17.8$ ns and $\eta = 5.5$. The following procedure is pursued to find these parameters. We first define a reference received signal as the first $T_{\text{p}}W$ samples of the received waveform after the leading edge at a given transmitter and the receiver distance. For the same distance, we calculate the total energy of the human-body-induced variations (again over the length of $T_{\text{p}}W$) after removing the mean from the signal. Finally, we divide this by the energy of the reference signal. Here, for the practical estimation of E_{s} at the receiver, we consider that the signal is scaled by $1/\alpha_1$ (that is the channel coefficient of the direct-path signal component) to also include the effects of the attenuation due to the propagation. In this way, the α_{p}s are normalized so that $\alpha_1 = 1$ and E_s is obtained as the received energy in the LOS component. While extracting these parameter values, we only consider the cases when the person is not blocking the LOS (i.e., we exclude the shadowing effect induced by the person). This procedure is described in more detail and the result is plotted in Appendix B. Finally, the bistatic range is denoted as $d_{\text{p}} = c \cdot \tau_{\text{p}}$, and the received signal-to-noise ratio (SNR) is defined as $\text{SNR} = E_{\text{s}}/N_0$.

3.6.2 Results and Discussion

We first validate the false alarm and missed detection probabilities derived in (3.18) and (3.25), respectively. The validation was based on simulating the system described above and determining the false alarm and missed detection probabilities through Monte Carlo simulation. Fig. 3.4 shows the false alarm probability as a function of the threshold γ for the input and intermediate parameter values, tabulated in Table 3.1. Note that this performance does not depend on the SNR, as the relationship obtained between the false alarm probability and the threshold in (3.18) does not depend on the SNR. We observe a good agreement between the simulations and the predicted performance, especially for larger values of N_{rep}, as the Gaussian approximation is more accurate when more observations are collected.

Fig. 3.5 shows the missed detection probability as a function of the thresh-

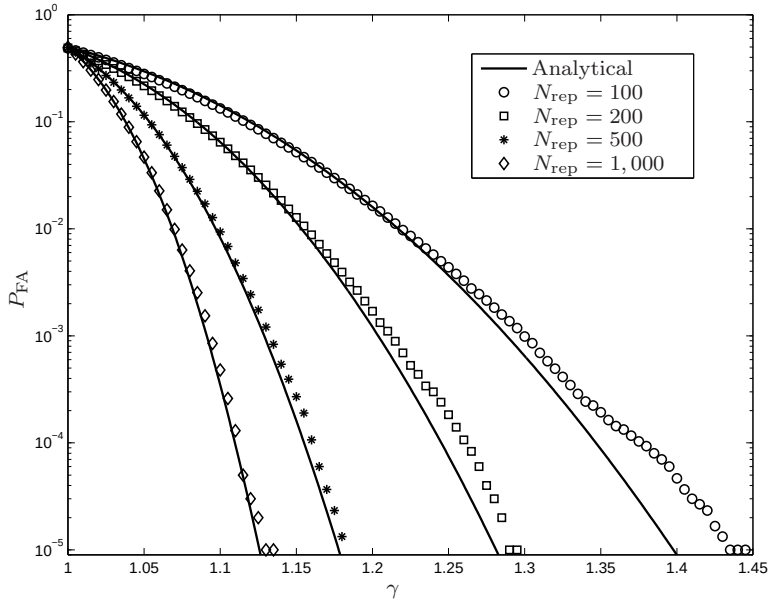

Figure 3.4: Simulated and analytical false alarm probability versus threshold for different number of samples over time.

old γ, for two different SNR values, and for different values of N_{rep}. The input and intermediate parameter values for the relationship in this figure are provided in Table 3.2. We again observe a good agreement for large N_{rep}, for both low and high SNR. When N_{rep} is low, the predicted performance is worse than the simulated performance. This is due to the fact that the Gaussian approximation does not completely fit to the distribution of (3.21). The mismatch occurs in the left-side tail, where the Gaussian approximation overestimates the true probability density. To show this clearly, empirical and numerical results

Table 3.1: Input and intermediate parameter values for false alarm probability versus threshold, shown in Fig. 3.4.

Input parameters
$T_{\text{p}}W = 23$ ($T_{\text{p}} = 1.4$ ns, $W = 61$ ps), $\beta = 0.05$, $N_{\text{rep}} = 100,\ 200,\ 500,\ 1,000$
Intermediate parameters
(3.16) $\mu_{\text{f}} = 1$
(3.17) $\sigma_{\text{f}}^2 = \frac{1}{0.05 \cdot 23 \cdot N_{\text{rep}}} = \frac{0.87}{N_{\text{rep}}}$
(3.18) $P_{\text{FA}} = Q\left(\frac{\gamma - \mu_{\text{f}}}{\sigma_{\text{f}}}\right) = Q\left(1.07(\gamma - 1)\sqrt{N_{\text{rep}}}\right)$

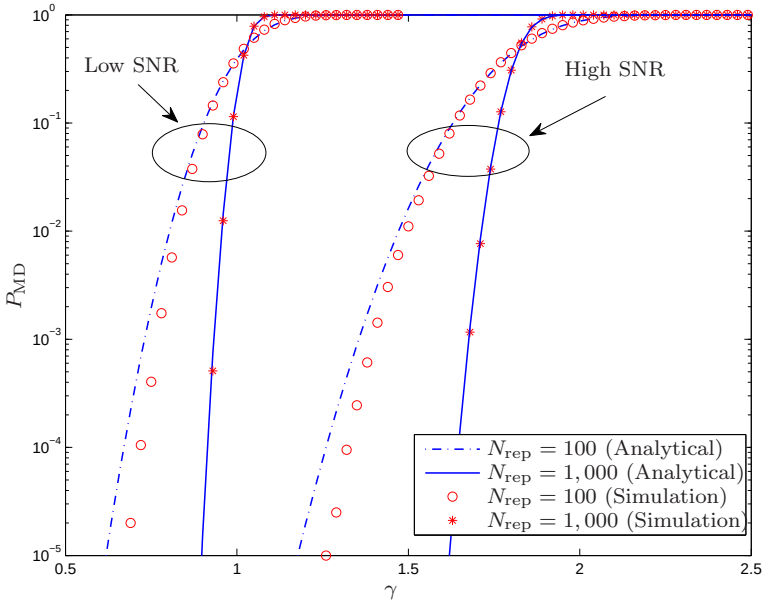

Figure 3.5: Simulated and analytical missed detection probability versus threshold for different number of samples over time at low (12 dB) and high (27 dB) SNR and $d_{\mathrm{p}} = 6$ m.

Table 3.2: Input and intermediate parameter values for missed detection probability versus threshold, shown in Fig. 3.5.

Input parameters
$T_{\mathrm{p}}W = 23$ ($T_{\mathrm{p}} = 1.4$ ns, $W = 61$ ps), $\beta = 0.05$, $N_{\mathrm{rep}} = 100,\ 1,000$ $d_{\mathrm{p}} = 6$ m, $\tau_{\mathrm{p}} = 20$ ns, SNR(E_{s}/N_0)=12, 27 dB
Intermediate parameters
(3.7) $G(\tau_{\mathrm{p}}) = 1.9 \cdot 10^{-3}$,
(3.23) $\mu_{\mathrm{d}} = 1 + \frac{1.9 \cdot 10^{-3} E_{\mathrm{s}}}{23 \cdot 0.05 \cdot N_0} = \begin{cases} 1.03, & \mathrm{SNR} = 12 \text{ dB}, \\ 1.83, & \mathrm{SNR} = 27 \text{ dB} \end{cases}$
(3.24) $\sigma_{\mathrm{d}}^2 = \frac{1}{0.05 \cdot 23 \cdot N_{\mathrm{rep}}} \left(1 + \frac{2 \cdot 1.9 \cdot 10^{-3} E_{\mathrm{s}}}{23 \cdot 0.05 \cdot N_0}\right) = \begin{cases} \frac{0.91}{N_{\mathrm{rep}}}, & \mathrm{SNR} = 12 \text{ dB}, \\ \frac{2.3}{N_{\mathrm{rep}}}, & \mathrm{SNR} = 27 \text{ dB} \end{cases}$
(3.25) $P_{\mathrm{MD}} = Q\left(\frac{\mu_{\mathrm{d}} - \gamma}{\sigma_{\mathrm{d}}}\right) = \begin{cases} Q\left(\frac{(1.03-\gamma)\sqrt{N_{\mathrm{rep}}}}{0.95}\right), & \mathrm{SNR} = 12 \text{ dB}, \\ Q\left(\frac{(1.83-\gamma)\sqrt{N_{\mathrm{rep}}}}{1.52}\right), & \mathrm{SNR} = 27 \text{ dB} \end{cases}$

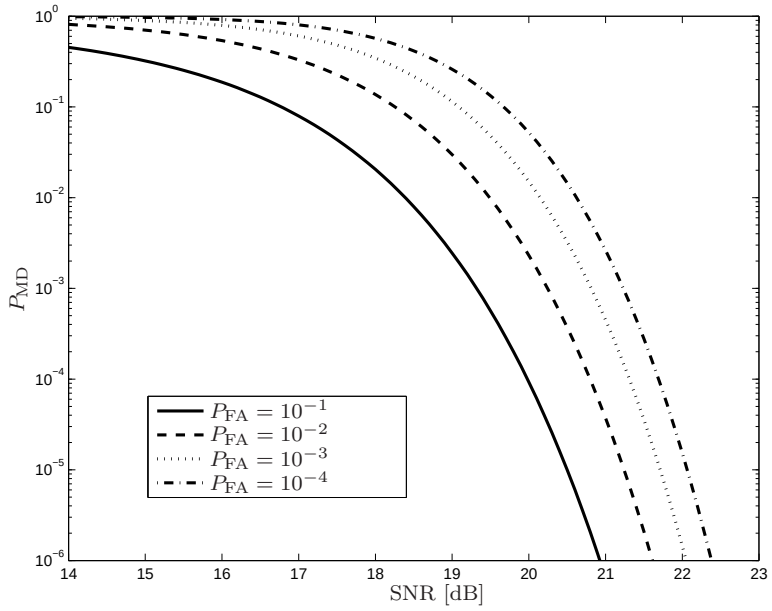

Figure 3.6: Analytical missed detection probability versus SNR (E_{s}/N_0) for different false alarm probabilities ($d_{\mathrm{p}} = 6$ m, $N_{\mathrm{rep}} = 1,000$).

are given in Appendix C for the distribution of the decision statistic $D(\tau)$ when $N_{\mathrm{rep}} = 100$ and $N_{\mathrm{rep}} = 1,000$. In general, N_{rep} is dependent on both the total observation duration and the measurement update rate ($1/T_{\mathrm{rep}}$). Therefore, the performance can be described well with analytical results for high update rates over shorter time windows (sufficiently long to capture slow variations) or slower update rates (again sufficiently fast to capture slow variations) over longer time windows. In the following part, we will only show the analytical results assuming that the update rate is sufficiently high to collect $N_{\mathrm{rep}} = 1,000$ samples over the time window.

Fig. 3.6 and Fig. 3.7 show the dependence of the missed detection probability on the SNR and the bistatic range, respectively, for varying values of the false alarm probability P_{FA}. Here, the relation between the false alarm and the missed detection probabilities is established through the choice of γ. Hence, the threshold value corresponding to each false alarm probability is chosen according to the analytical results shown in Fig. 3.4 for $N_{\mathrm{rep}} = 1,000$, and these threshold values are used to get the analytical results for the missed detection probability. Fig. 3.6 illustrates that, for a given bistatic range d_{p} and P_{FA}, we need about 1 dB of SNR improvement for every order of magnitude reduction in P_{MD} (e.g., around 3 dB to get from $P_{\mathrm{MD}} = 10^{-1}$ to $P_{\mathrm{MD}} = 10^{-4}$).

Furthermore, the performance of the system also depends on the position of

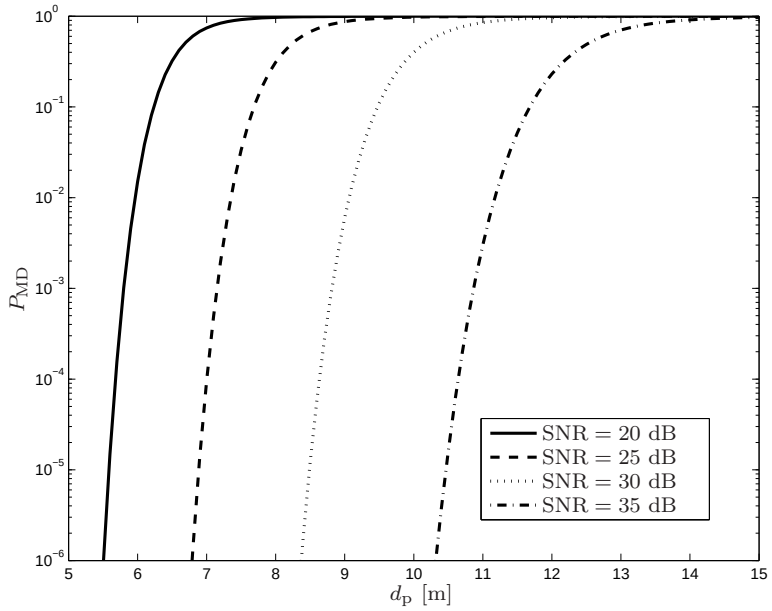

Figure 3.7: Analytical missed detection probability versus bistatic range for different SNR values ($P_{\mathrm{FA}} = 10^{-3}$, $N_{\mathrm{rep}} = 1,000$).

the person with respect to the transmitter and the receiver, as we observed and described in (3.7): the slow variation of the signal is attenuated by the increase in the reflected-path length. Fig. 3.7 predicts that, considering $P_{\mathrm{MD}} = 10^{-3}$, it is possible to detect the person up to 11 m bistatic range at high SNR (e.g., 35 dB). Note that the bistatic range is always larger than the distance traveled by the direct-path signal ($d_{\mathrm{p}} > d_1$). Therefore, one should note that, although the results show that the measurable bistatic range increases at higher SNRs, the SNR decreases with the distance between the transmitter and the receiver due to the path loss. Thus, in practice the bistatic range is limited by the transmitter and the receiver distance. Moreover, the model for $G(\tau_{\mathrm{p}})$ is based on a very limited set of measurements and therefore valid for only a very specific case. It may also depend on other parameters such as transmitter-receiver distance, the person's size, the breathing activity of the person, or the body orientation.

Fig.3.8 shows the relationship between the probability of detection and probability of false alarm for different SNR values. Such a summary for detection performance is commonly known as receiver operating characteristic [97]. For very large threshold values (i.e., $\gamma \to \infty$), both detection and false alarm probabilities become zero. When the threshold is zero (i.e., $\gamma = 0$), the probability of detection goes to one as the detector decides upon the presence of the

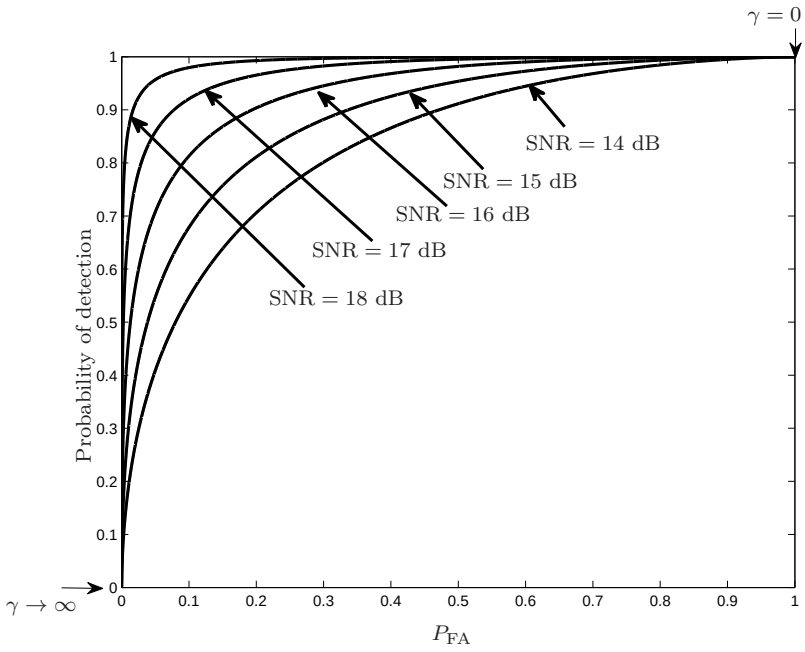

Figure 3.8: Analytical probability of detection versus probability of false alarm for different SNR values ($d_{\mathrm{p}} = 6$ m, $N_{\mathrm{rep}} = 1,000$).

person for every measurement cases which include scenarios when the person is actually present. However, in this case the false alarm probability also becomes one as the detector falsely decides upon the presence of the person for every measurement case, even though the person is not present in those scenarios. The ideal case would be when the probability of false alarm is zero and the probability of detection is one. This can be attained by larger SNR values as the curves are getting close to the upper left corner. Specifically, the ideal case is obtained when the SNR is around 23 dB.

3.7 Overview of the Experimental Activities

We performed experiments to check the validity of the model and give quantitative results of the detection performance in practical settings. We will show experimental results of the decision statistic and the missed detection and false alarm rates. We will also provide indicative results for the empirical choices of the fractional bandwidth β and the measurement duration T_{rep}.

3.7.1 Experiment Setup

We performed experiments in a fitness room at the Chalmers University of Technology Horsalsvagen building with identical Time Domain P400 radios. The transmitted pulse was measured with a high-sampling-rate oscilloscope, which has a sampling rate of 40 gigasamples/second, and plotted in Fig. 3.9. In the Time Domain devices, the transmitted pulse duration was found to be approximately 1.4 ns, resulting in approximately $T_{\mathrm{p}}W = 23$ samples in the delay dimension. Furthermore, the time between the consecutive pulses in a ranging symbol is 95 ns. This value should be larger than the maximum excess delay of the channel. Otherwise the successive pulses will interfere with each other. The pulse duration and the time between the consecutive pulses are set in the hardware and cannot be changed by the user. One of the limitations of our hardware setup is that the received waveforms are sampled over a window of approximately 10 ns. This limits the maximum captured excess multipath length to be less than approximately 3 m. In other words, given the distance between the transmitting and the receiving anchors as R, with the current radios the person can only be detected within an ellipse whose focal points are the anchor positions and whose major axis length is $R + 3$ m. This, in fact, limits the detection region for the person in our experiments. With the current hardware release, beyond the 10 ns window, captured waveforms are no longer stable. For instance, when 200 waveforms are collected, some of these waveforms are longer than 10 ns, but most of the time they are around 10 ns. Therefore, it is possible to obtain 10 ns of maximum delay window for the

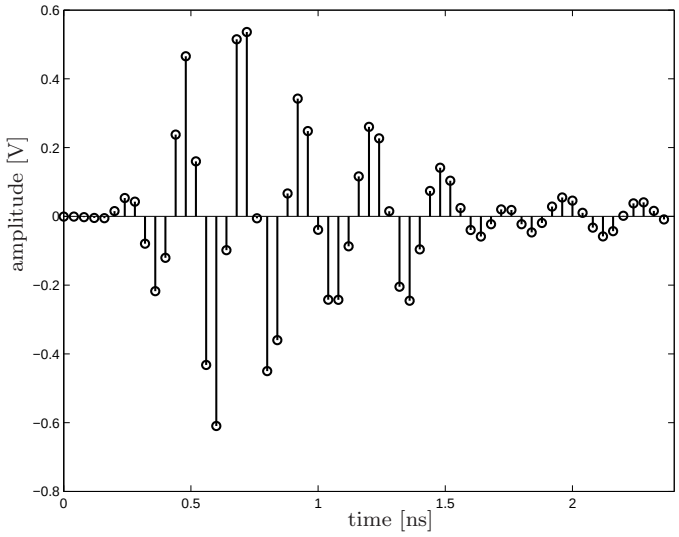

Figure 3.9: The transmitted pulse.

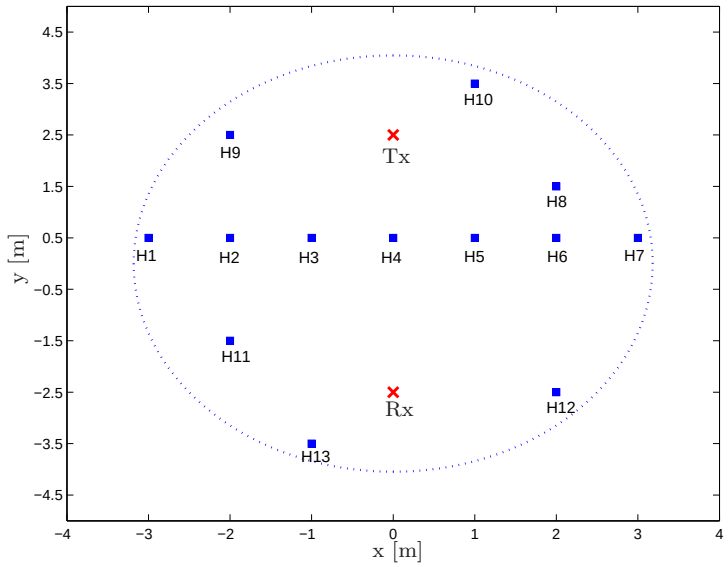

Figure 3.10: Overview of measurement scenarios: the transmitter (Tx), the receiver (Rx) (red cross) and 13 possible subject positions (blue rectangular), and device-free detection range (dotted ellipse) limited by the current radios.

consecutive waveforms.

Two sets of measurements were performed in the fitness room with fixed transmitter (Tx) and receiver (Rx) positions, and different measurement rates. In the first measurement set, there is no additional reflection source (except the person and the ground) within the detection region of the radios, whereas in the second measurement set, there are also other reflection sources such as walls and/or metallic fitness equipment, as will be described below.

Measurement Set 1: In this set, the person was standing in 13 different positions, as shown in Fig. 3.10. For each position, the person stood in two orthogonal orientations, so that the body is either perpendicular or parallel to the LOS between the radios. During the experiments, the radios were mounted on tripods at a height of 1.23 m above the ground and were connected by Ethernet cables. Measurements were taken using the graphical user interface, provided by the Time Domain Corp., at a rate of 5 measurements per second. Therefore, in these experiments T_{rep} is equal to 0.2 seconds. The waveforms were collected over 20 seconds, allowing us to obtain 100 snapshots over time for each scenario. A typical measurement scenario is shown in Fig. 3.11. (As the picture shows, within the detection region there is no reflection source except the ground. The walls are far away from the detection region of the radios.)

Figure 3.11: UWB setup for device-free detection and ranging measurements. The person is standing at H1 (see Fig. 3.10) with a perpendicular body orientation.

Measurement Set 2: In order to collect more measurement data, including scenarios with more multipath reflection sources, we performed more experiments in the same area. In the second set, the fitness room was divided into three parts, as shown in Fig. 3.12. Five radios, serving as anchors, were placed in these regions. The person was standing in 18, 20, and 18 different positions, respectively, separated by 50 cm, and for each position, we established transmission between AN1 and AN2, AN3 and AN4, and AN5 and AN4, respectively, in Region 1, Region 2, and Region 3. Mapping the environment to a coordinate system, we calculated the exact positions of the anchors and the person, with the aid of a laser distance measurement tool. Although the measurement plan is presented in a two-dimensional space in Fig. 3.12, the anchors were positioned at different heights of 0.54 m (AN1), 2.66 m (AN2), 0.73 m (AN3), 0.64 m (AN4) and 0.97 m (AN5), in order to consider realistic implementations. Moreover, the antenna-to-antenna distances between the anchors were approximately 5.68 m, 6.66 m and 7.85 m, for the pairs AN1-AN2, AN3-AN4, and AN5-AN4, respectively. In this case, the waveforms were col-

lected by connecting the radios through a Matlab interface, and with a rate of 50 measurements/second. This allowed us to obtain 100 snapshots over 2 seconds for each position of the person. Whereas there were not many reflection sources in Region 2 of the fitness room (as can be partly seen in Fig. 3.11), especially in Region 1 and Region 3, there was fitness equipment, having metallic structures. Furthermore, some of these measurements were taken when the person was close to the wall. Thus, there were several measurements to test our methods in multipath environments.

During both of the above measurement activities, care was taken to keep the environment static by making sure that there was no other person within the bistatic range limited by the radios (i.e, the operator, who was carrying out the experiments, was also outside this range).

In this case, the receiver was set to coherently combine 128 pulses to improve the SNR at reception. The number of combined pulses also determines the measurement rate and ranges from 16 to 1024 (only powers of 2) for the given setup. For instance, by choosing 1024 instead of 16, an SNR improvement of 18 dB can be obtained. However, with the current hardware 154 measurements/second is possible if 16 pulses are combined, whereas only 8 measurements/second is obtained if 1024 pulses are combined [99]. Considering the SNR and the measurement rate tradeoff, we chose the above-mentioned value (128 is also set as the default value for this hardware). During the offline postprocessing, fine alignment around the leading edge point was performed by cross-correlating all the waveforms with a reference waveform, chosen among them, and shifting waveforms according to the index of the maximum cross-correlation value. This was performed in an automated fashion for all the measurements. This operation was performed to make sure that all the waveforms were aligned over the time window. The starting instant of the waveform (i.e., the zero delay instant) is defined based on the leading edge detection point, obtained by the radio. As most of the device-to-device ranging measurement errors were very small (around 2 cm on average), we did not consider the effect of possibly choosing the wrong starting sample of the waveform.

3.7.2 Background Noise and Timing Jitter

The radios are subject to a number of hardware impairments. Among them, the timing jitter is a known issue within impulse radio UWB systems [100–103], which causes deviation of the transmitted pulses from reception at integer multiples of the sampling time. Because of the timing jitter, at each transmission instant transmitted pulses deviate from the nominal transmission instant as shown in Fig. 3.13.

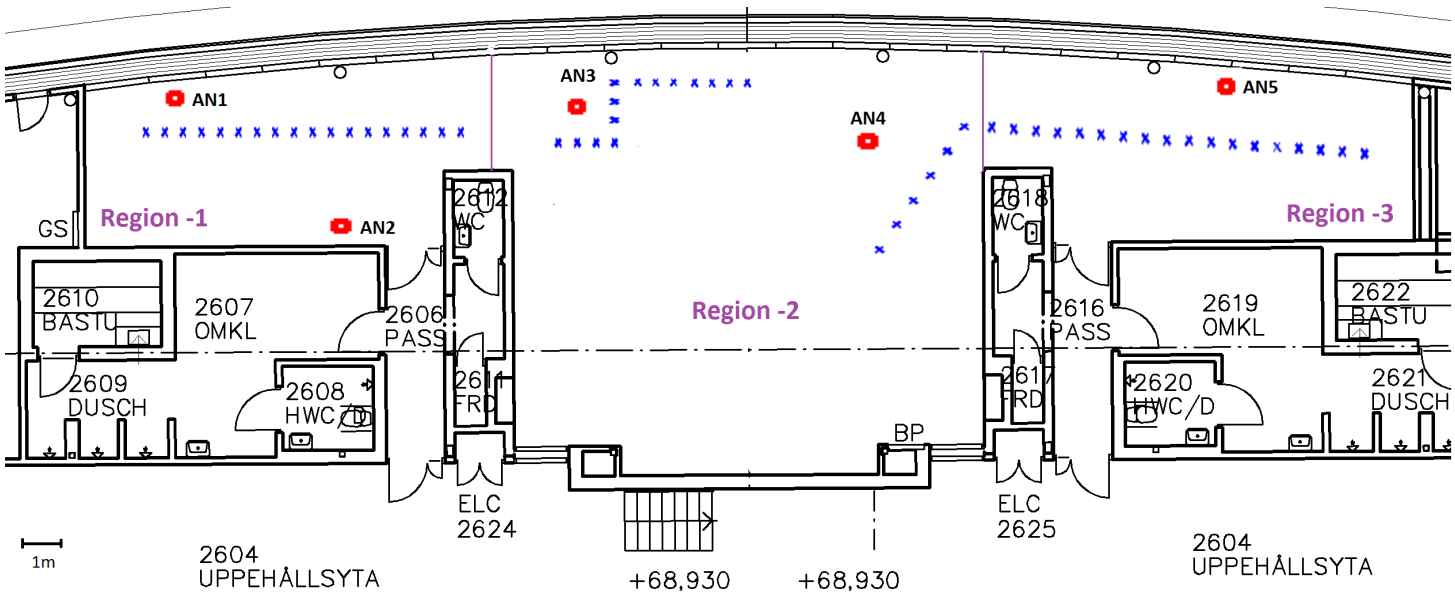

Figure 3.12: Overview of the measurement floor plan: the floor was divided into three regions, and for each region, the person was standing on several positions (shown as blue crosses), while the anchors (shown as red squares labeled AN1 to AN5) were taking ranging measurements in such a way that, for each position of the person, the measurements were taken in between AN1 and AN2 (Region 1), AN3 and AN4 (Region 2), and AN4 and AN5 (Region 3).

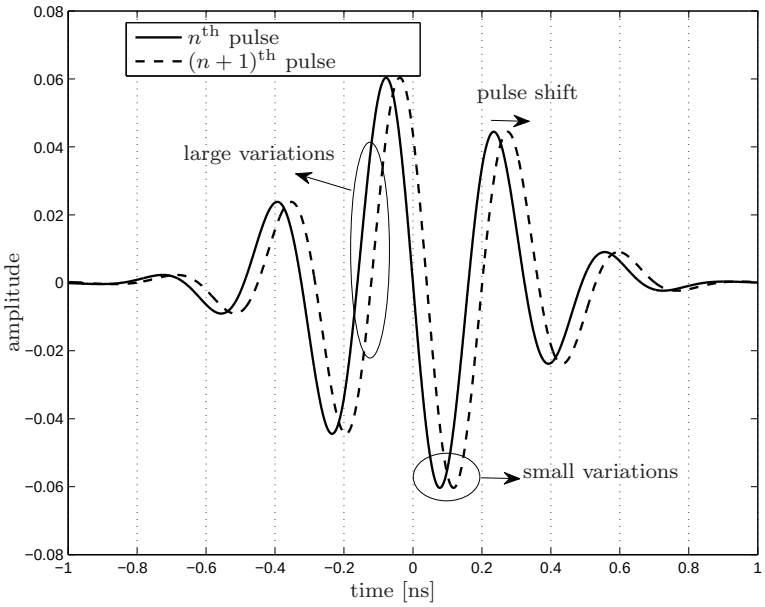

Figure 3.13: Transmitted pulse shifts because of the timing jitter (for a seventh derivative Gaussian pulse).

At a certain delay sample, the signal amplitude varies over time according to the slope of the received waveform (i.e., the derivative of the received waveform with respect to time). This variation will be greater if the sample is on a steep part of the pulse (as illustrated in Fig. 3.13). This variation will also be greater for higher amplitudes, since the change in the amplitude will be greater, leading to a higher impact of the timing jitter for these samples. This results in different amounts of background signal variations over time for delays with high signal values, compared to delays with low signal values. Another issue with the current hardware, which has a similar effect, is related to the choice of the lock spot. For each ranging symbol, the receiver locks onto a spot in the received signal and start sampling the signal relative to this point. However, in the current hardware release, the receiver may lock onto different lock spots which results in sampling at different instants of the received waveform. This also causes background variations regardless of the presence of the person. As this problem is mainly an implementation issue and less known in UWB literature than the timing jitter, we give more details related to this issue in Appendix D.

Fig. 3.14 shows, for the measurement data presented earlier in Fig. 3.2, the standard deviation of the received bin amplitudes over 100 measurement snapshots. As shown in the figure, the standard deviation of the delay bins,

corresponding to the direct-path signal component and early-arriving reflections, are higher than of the delay bins, influenced by the person. This can be clearly understood when we compare the amplitudes in Fig. 3.2 for these bins. Because the background variations are not the same over the delay bins, we first consider the resulting variation over time as additive white noise (i.e., possible correlations between successive errors are neglected), and estimate N_0 on a delay by delay basis. For a given delay, m, we estimate the noise power $N_{0,m}$ as

$$\hat{N}_{0,m} = \frac{1}{W(0.5-\beta)N_{\text{rep}}} \sum_{k=1}^{N_{\text{rep}}} r_{m,\text{H}}^2(k). \tag{3.27}$$

where $r_{m,\text{H}}(k) = r_m(k) - r_{m,\text{L}}(k)$, is the part of the signal that contains only noise, and variations induced by jitter and the choice of lock spot, irrespective of the presence of a person (i.e., β is chosen in such a way that the influence of the person only lies within $r_{m,\text{L}}$). The estimate was then substituted in (3.12) to allow detection and ranging in the presence of hardware imperfections.

Note that, if N_0 were not estimated for each delay bin, the decision statistic $D(\tau)$ would get high values for delay bins with high amplitude (i.e., bins containing strong static multipath components) even though these bins are not subject to the effect of the person, simply because the low-frequency energy would also become high. Then, it would become hard to identify the effect of the person on the delay bins.

3.7.3 Experimental Results and Discussion

Decision Statistic

Before providing detailed results on the detection rates, we first consider the decision statistic. Fig. 3.15 shows an example of the measured decision statistic $D(\tau)$ as a function of delay, where the subject was standing on four different positions in *Measurement Set 1* shown in Fig. 3.12. While calculating $D(\tau)$, we applied a low-pass filter with a fractional bandwidth of $\beta = 0.05$, similar to the simulation settings. The figures also depict the detection threshold, chosen as $\gamma = 1.4$, for which the false alarm probability is predicted to be around 10^{-5} (see also (3.20) and Fig. 3.4 for $N_{\text{rep}} = 100$ and $\beta = 0.05$).

Fig. 3.15(a) shows the example case, where the position of the person corresponds to the delay instant around 6.3 ns (shown as a red square), whereas for the cases shown in Fig. 3.15(b) and Fig. 3.15(c), the positions of the person correspond to the delay instants around 3.4 ns and 2.7 ns, respectively. These delay instants correspond to differences between the human-body reflected path distance and node distance of approximately 1.9 m, 1 m and 0.8 m, respectively. This difference was 0 m when the person was standing exactly in between the transmitter and the receiver antennas, for the case shown in Fig. 3.15(d).

As seen in Fig. 3.15(a), the decision statistic has one clear distinct peak within 10 ns of delay window, while it has more than a single peak above

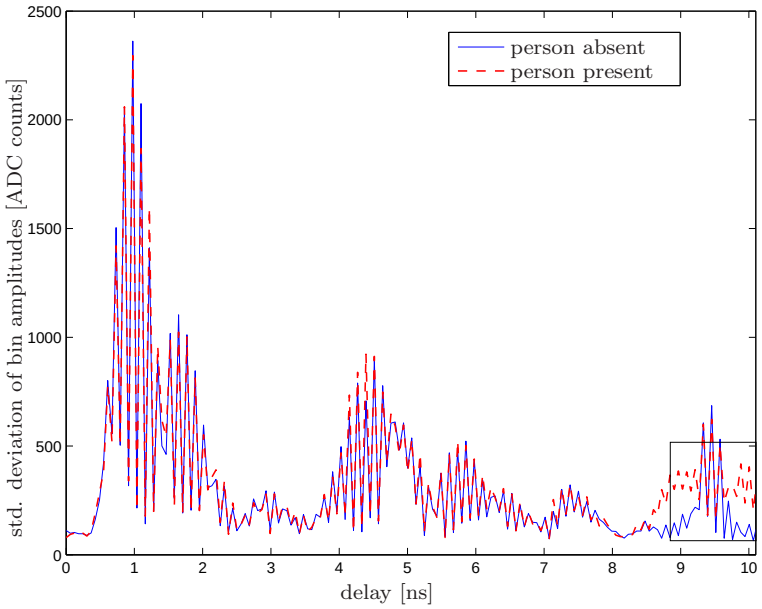

Figure 3.14: The measured standard deviation of the delay bins for 100 measurement snapshots, in the presence and the absence of the person. The same measurement data is used as in Fig. 3.2

the detection threshold in Fig. 3.15(b),(c). This is because, in addition to the direct reflection, the human body also introduces later-arriving reflections (i.e., indirect reflections). These occur when the person stands close to strong reflectors such as metallic objects and walls. In these cases, the signals that reflect off the person also interact with those reflection sources before arriving to the receiver. Similar results are also obtained in Fig. 3.15(d), where the person is standing in between the antennas, blocking the LOS. One explanation of this observation can be that in this case the signal diffracts around the body and these diffracted paths also interact with the other objects before arriving at the receiver. We also note that, for the position of the person, we obtain that $D(\tau) < \gamma$. However, the decision statistic is higher than the threshold for the later bins and we can still detect the person. We also note that the leading edge algorithm of the equipment gave on average 2 cm of ranging error in this position as well. In general, these last three figures show that we can observe slow variations due to the movement of the person in the later arriving signal components as well.

The signal model in (3.1) does not include the above-mentioned effect. It

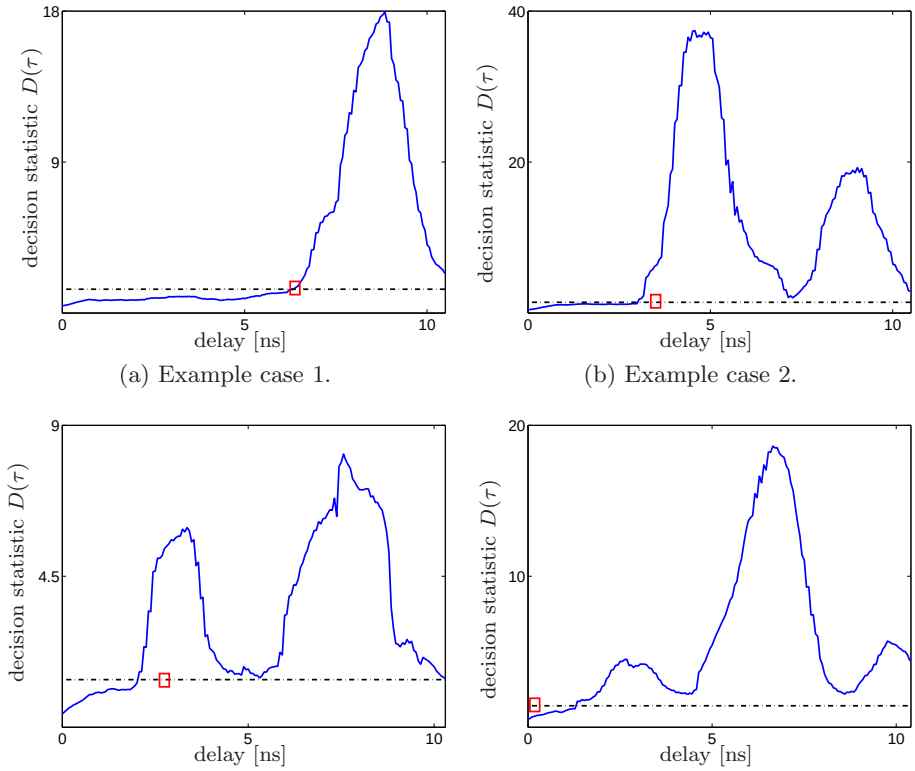

(a) Example case 1.

(b) Example case 2.

(c) Example case 3.

(d) Example case 4.

Figure 3.15: Examples of measured decision statistics $D(\tau)$ as a function of delay after the leading edge signal arrival time. The delay instants corresponding to the real positions of the person are shown as red squares and the detection threshold is shown as a horizontal black dashed line.

can be included by rewriting it as

$$\begin{aligned} r_{\mathrm{rep}}(t) =& \sqrt{E_{\mathrm{s}}} \sum_{k=1}^{N_{\mathrm{rep}}} \sum_{l=1}^{L} \alpha_l p(t - \tau_l - kT_{\mathrm{rep}}) \\ &+ \sqrt{E_{\mathrm{s}}} \sum_{k=1}^{N_{\mathrm{rep}}} \sum_{l=1}^{M} \alpha_{\mathrm{p},l}(t) p(t - \tau_{\mathrm{p},l} - kT_{\mathrm{rep}}) + n(t), \end{aligned} \tag{3.28}$$

where, in this case, the second line again corresponds to the person, and there are now M channel coefficients ($\alpha_{\mathrm{p},l}(t)$) varying slowly over time due to the effects of the human body. Among them, $\alpha_{\mathrm{p},1}(t)$ represents the signal path that is directly reflected off the person (i.e., direct reflection), whereas the

remaining ones are related to signal paths that are reflected off the person and other reflection sources in the environment (i.e, indirect reflections). The delay associated with the direct reflected path ($\tau_{\mathrm{p},1}$) is always smaller than the delays associated with the indirect reflected paths ($\tau_{\mathrm{p},l}$ for $l = 2, \ldots, M$), since the direct reflected path always travels a shorter distance. We also note that this effect does not affect our detection problem, as we are only interested in the existence of $\alpha_{\mathrm{p},1}$, i.e., whether the decision statistic is above the detection threshold. However, for the device-free ranging, which will be discussed in the following chapter, we will be interested in estimation of $\tau_{\mathrm{p},1}$ as well.

Furthermore, as we again look at Fig. 3.15(c) and Fig. 3.15(d), the decision statistic gets higher values for delay instants corresponding to later-arriving signal components. This is the result of the timing jitter (and the issue with the choice of the lock point), which causes the background signal variations to depend on the delay. In particular, the decision statistic gets high values for the delay values where the signal has a slowly varying component (also due to the indirect reflections) with low amplitude (i.e., the amplitude of the total signal before removing the mean), since for the lower amplitudes, the effect of the timing jitter (and the issue with the choice of the lock point) will also be less, resulting in an estimated value for N_0 that is low, through (3.27).

Detection Results and Discussion

Analysis of our measurement results shows that the proposed method was able to detect the presence of the person in all 26 cases (13 parallel and 13 perpendicular cases), depicted in *Measurement Set 1*. For the same measurement set, we had a single measurement in which the person was not in the detection range, limited by the radios. In this case, the algorithm did not detect any person. These results were obtained when the fractional bandwidth of the low-pass filter was set to $B = 0.05$ and the detection threshold to $\gamma = 1.4$, as was done in the previous part of this section, where we discussed the decision statistics.

We further analyze the dependence of the false alarm and the missed detection rates on the normalized bandwidth β and the number of measurement snapshots N_{rep}. Such an analysis will give an indication of the values that need to be considered for β and N_{rep} in practical implementations of the system. We used *Measurement Set 2*, where the subject stood on 56 unique positions, as indicated in Fig. 3.12. Of those 56 positions, ten were out of the bistatic range, limited by the radios. We again chose the detection thresholds that are predicted to give a false alarm probability of approximately 10^{-5}, based on the analytical results. We first note that the system does not give any false alarm in most of these ten positions, except the cases with the measurement duration of 2 seconds and fractional bandwidths $\beta = 0.1$ and $\beta = 0.25$ (or absolute bandwidths of 5 Hz and 12.5 Hz), in which for one and three positions, respectively, the detection algorithm falsely reported the presence of the person. For the remaining 46 positions, Table 3.3 shows the measured missed detection rates, for

different values of the fractional bandwidth of the filter ($\beta \in \{0.05, 0.1, 0.25\}$) and the observation duration in the time dimension $N_{\text{rep}} \cdot T_{\text{rep}}$, corresponding to durations of 2, 1.6, 1.2, 0.8 and 0.4 seconds).

The results reveal that the missed detection rate increases for higher values of the fractional bandwidth. This can be clearly observed when we compare the fractional bandwidths 0.05 and 0.1, with 0.25. As can be expected with our understanding of the signal model, it is due to the fact that we collect more noise energy when we increase the bandwidth of the filter, resulting in a scaling to lower values for the decision statistic. The fractional bandwidth of 0.05 is better than 0.1 in general except for the cases when we set the measurement duration to 2 seconds and 0.4 seconds. In both of these cases, we get one more missed detection for the fractional bandwidth of 0.05 as the variations due to the person occur beyond the filter bandwidth, which results in a higher decision statistic for the bandwidth of 0.1.

Furthermore, the missed detection rate increases as the measurement duration decreases. This again can be expected with the understanding of the signal model, as the slow variations due to the movement of the person result in enough energy at the output of the low-pass filter, for instance, for 2 seconds of measurement time in most cases. In contrast, short durations (e.g., 0.4 seconds) are not sufficient to detect the body-induced slow variations. These results may also be linked to the physical properties of the person, where the body can be considered to be approximately motionless at the sub-second scale (i.e., no noticeable effect of the respiration on the movement of the chest cavity). The measurement duration that is needed to detect the presence of the person also determines the update rate of the system. The update rate shows how many outputs the system gives for the detection of the person per unit time (e.g., a minute). For lower values of the measurement duration, the system can give a fast response to variations due to the human body, but as it is shown, the missed detection rate also increases. Therefore, there is a trade-off between the update rate of the system and the extent of detecting the presence of the person.

Moreover, our experimental results also reveal that the theoretical findings deviate from practice as we get false alarms for scenarios in the absence of the person. For these cases, due to the hardware limitations such as related to the timing jitter and the choice of lock spots, the background variations show a few spectral spikes (even after the perfect alignment) which disturb the consideration that the background variations are white. These spikes may lie in the low-frequency region and cause the decision statistic to be larger than the detection threshold.

Comparable results were also reported in [45] to detect the motions using WLAN RSSI readings. The missed detection and false alarm probabilities were around 0.2 and 0.07 for the initial method presented in [45], respectively. This method was improved by also incorporating noise handling (i.e., for robustness against the changes in the noisy readings of RSSI values) and profile update (i.e., for robustness against the changes in the environment.). In this case, the

Table 3.3: Experimental results for detection. The detection thresholds were chosen to give false alarm probability of 10^{-5} based on the analytical results.

Fractional bandwidth	Measurement duration [sec]	Missed det. rate
0.05	2	0.04
	1.6	0.07
	1.2	0.13
	0.8	0.27
	0.4	0.69
0.1	2	0.02
	1.6	0.18
	1.2	0.29
	0.8	0.38
	0.4	0.67
0.25	2	0.09
	1.6	0.69
	1.2	0.82
	0.8	0.89
	0.4	1

missed detection and false alarm probabilities were 0.05 and 0.04, respectively. This result is quite similar to the missed detection rate we obtained for measurement duration of 2 seconds and fractional bandwidth of 0.05. However, in [45], the person was walking in the environment while with UWB system even through smaller movements, the similar detection performance can be achieved. In [59], the detection method was developed for a UWB radar with a working principle relying on the backscattering from the target. In that work, the detection was possible in all of 19 measurement scenarios, where the person was in LOS. For the false alarm probability the results showed strong dependence on the detection threshold. With an appropriate choice of threshold, it was shown that the false alarm probability can be as low as 0.05. However, this threshold was chosen in an empirical way and therefore it was dependent on the hardware and the environment. The threshold is required to be tuned for each environment.

3.8 Conclusion

In this chapter, a novel algorithm was developed to detect the presence of a stationary person in indoor environments. Our method does not require any knowledge about the environment, but relies solely on exploiting the temporal

variations in the received signal induced by the presence of the person. We observed that the signal evolves slowly over time, even when the person is standing still. This observation was presented by aligning multiple copies of the received signal in the delay window, and considering the delay instants affected by the person. Based on this, a signal model was introduced and a detection method was developed. Our experiments pointed out practical problems. One of them is that the transmitted pulses are subject to random delay shifts at each transmission instant. This is called timing jitter, which introduces different amplitude variations over time for each delay instant. In order to deal with this problem, we modeled these variations as white noise and estimated the noise power spectral density from the high-frequency components of the signal for each delay instant, which are hardly affected by the presence of the person. Our experiments also revealed that there are secondary reflections, that occur due to the interaction of the signal with the environment after (or before) reflecting from the person. The method gives only few detection errors, when considering longer time windows and properly choosing the fractional bandwidth of the low-pass filter.

The next chapter will deal with practical bistatic range estimation methods, based on the decision statistic developed in this chapter.

Chapter 4

Device-Free Ranging and Localization

4.1 Introduction

In the previous chapter, a method for the detection of a stationary person was proposed and for this purpose a decision statistic was developed. In this chapter[1], the criteria to extract the delay of the human-body reflected path from the decision statistic will be introduced. The delay of the reflection leads to the bistatic range (i.e., when multiplied by the speed of light), that is the sum of the distances from the person to the transmitter and receiver positions. As the single-link measurement locates the person on an ellipse with an ambiguity, as explained in Section 3.2 and illustrated in Fig. 3.1, at least three link measurements are needed to find the position of the person.

The results of the device-free ranging will be based on the experimental activities of the previous chapter. For device-free localization, a new set of indoor measurements will be introduced. The results will be shown for the bistatic range and location estimates for different bistatic range estimation criteria and positions of the person in an indoor environment.

The rest of the chapter is organized as follows. First, the localization system will be described, and this will be followed by introducing the practical bistatic range estimation criteria. Then a discussion on the experimental results for device-free ranging and localization will be given, before giving the concluding remarks.

4.2 Localization System

A system with N_{a} UWB radios (called beacon or anchor nodes) is considered, with a priori known positions $\mathbf{x}_i = \begin{bmatrix} x_i & y_i \end{bmatrix}^T$, and a passive, human target

[1]The contents of this chapter were published in [94, 95].

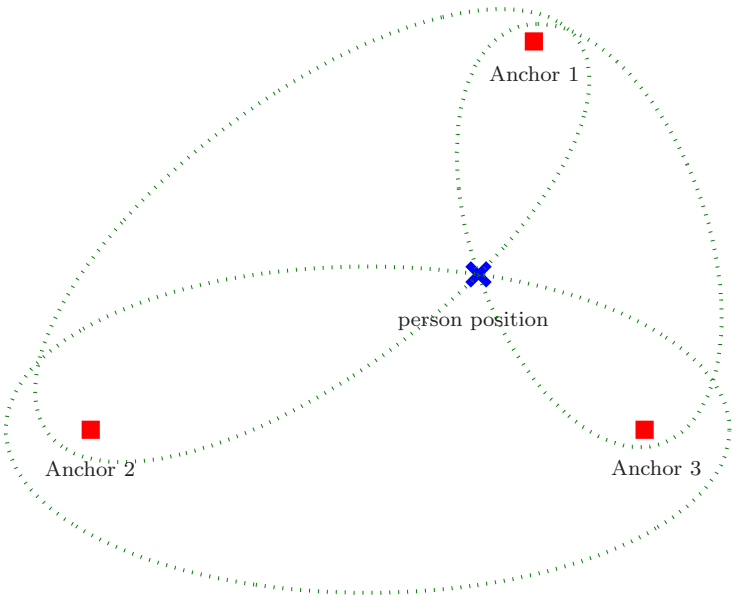

Figure 4.1: An example device-free localization scenario. The position of the person is shown as a blue cross, and the anchor positions are shown as red squares.

with an unknown position $\mathbf{x} = \begin{bmatrix} x & y \end{bmatrix}^T$. Both the elements of $\mathbf{x}_i$ and $\mathbf{x}$ are defined in $\mathbb{R}^2$ (i.e., specify the coordinates of a point as real numbers in a two-dimensional space) and hence the localization system is limited to a two-dimensional space. It is assumed that the anchors exchange signals which reflect off the target. Based on each measurement between anchors, the person can be located on ellipses around the transmitter and the receiver positions as shown in Fig. 4.1. The position of the person can be found from the combinations of the ellipses as shown in this figure, which shows an error-free case for bistatic range estimation. In general, the true distance traveled by the reflected path from Anchor i to Anchor j can be found from

$$d_{i,j} = ||\mathbf{x} - \mathbf{x}_i|| + ||\mathbf{x} - \mathbf{x}_j||. \tag{4.1}$$

As an estimate of the time of flight is obtained for the reflected signal, the corresponding distance estimate becomes

$$\hat{d}_{i,j} = d_{i,j} + e_{i,j}, \tag{4.2}$$

where $e_{i,j}$ is the measurement error. This enables the system to approximately locate the target on an ellipse whose foci are $\mathbf{x}_i$ and $\mathbf{x}_j$, and with the length

of the major axis equal to $\hat{d}_{i,j}$. Given a collection of such measurements, the least-squares estimate of $\mathbf{x}$ is

$$\hat{\mathbf{x}} = \arg\min_{\mathbf{x}} \sum_{(i,j)} \left(\hat{d}_{i,j} - ||\mathbf{x} - \mathbf{x}_i|| - ||\mathbf{x} - \mathbf{x}_j|| \right)^2, \tag{4.3}$$

where the summation goes over all pairs of transmitters i and receivers j that have a measurement. As the positions of the anchor nodes are known, $\hat{d}_{i,j}$ needs to be determined to find the position of the person. The equation in (4.3) is used to find the point for the position of the person with minimum total squared bistatic range difference and in this sense similar to the least-squares position estimation given in (1.3) for device-based localization. Common techniques to solve the least squares problem include search methods [104].

In the next section, the goal is to determine $\hat{d}_{i,j}$ based on human-body induced signal variations, and without a template waveform.

4.3 Ranging Criteria

The bistatic range estimates $\{\hat{d}_{i,j}\}$ can be found by estimating the delay of the human-body reflection of each link and multiplying by the speed of light. The decision statistic $D(\tau)$ also conveys information about the delay of the human-body-induced reflections, in addition to the presence of the person. As discussed in Section 3.7.3, the human body may introduce multiple reflections in some cases. Considering also this result, our interest is in the estimation of $\tau_{\mathrm{p},1}$, denoting the delay of the direct reflection from the person. Other reflections related to the person always come later than the direct reflection ($\tau_{\mathrm{p},l} > \tau_{\mathrm{p},1},\ l = 2, ..., M$). Identifying one of these reflections as the direct reflection would hence result in a positive bias in bistatic range estimation.

Here, three practical estimation criteria are introduced to find $\tau_{\mathrm{p},1}$. The criteria, introduced below, are similar to the ones used to estimate the time of flight between devices, as these problems are similar. While the estimation of the time of flight between devices is done based on extracting the earliest arrived signal component (i.e., the direct-path signal component) from the CIR or the received signal, the below-mentioned criteria are applied on the decision statistic that was developed for our purpose, i.e., finding the first-arriving time-varying component.

Line Search

This criterion is based on the selection of the largest sample in $D(\tau)$ over the defined total delay window with duration T_{delay}, and specifically given by

$$\hat{\tau}_{\mathrm{p},1} = \arg \max_{\tau \in [0, T_{\mathrm{delay}}]} D(\tau). \tag{4.4}$$

Threshold Crossing

As discussed in Section 3.7.3, the maximum value of $D(\tau)$ may not always correspond to $\tau_{\mathrm{p},1}$ but may come from a later arriving indirect reflected path with delay $\tau_{\mathrm{p},l}$ with $l = 2, \ldots, M$. To provide robustness against these failures, another criterion is introduced. This criterion estimates $\tau_{\mathrm{p},1}$ based on the first threshold crossing:

$$\hat{\tau}_{\mathrm{p},1} = \min \left\{ \tau | D(\tau) > \tilde{\gamma} \right\}. \tag{4.5}$$

$\tilde{\gamma}$ is also a threshold and can be different from the detection threshold γ that was introduced in Section 3.4.2, depending on the desired detection and ranging performance criteria. In our analysis, it is considered that $\gamma = \tilde{\gamma}$.

Maximum Rise Search

Although the previous approach provides additional robustness, its performance depends on the threshold value, which may be hard to determine in some practical cases such as due to the effect of the timing jitter. The threshold value is determined based on the false alarm probability, calculated in Section 3.5, from the signal model which does not account for these practical effects. Because of these practical effects, the decision statistic may falsely cross the threshold, even though the person does not affect the delay samples for which the decision statistic is above the threshold.

As shown previously in Fig. 3.15, the decision statistic usually shows a sudden rise due to the presence of the person. Therefore, we can also exploit the shape of $D(\tau)$ in which the maximum increase is searched and thereby the requirement for the threshold determination is removed. Specifically, the maximum rise search criterion is given by

$$\hat{\tau}_{\mathrm{p},1} = \arg \max_{\tau \in [0, T_{\mathrm{delay}}]} \Big(D(\tau + T_{\mathrm{win}}/2) - D(\tau - T_{\mathrm{win}}/2) \Big), \tag{4.6}$$

where T_{win} is the duration of the interval over which the increase of the statistic is calculated. In our analysis, T_{win} will be set to $T_{\mathrm{win}} = T_{\mathrm{p}}$, considering the effect of the person over the pulse duration.

4.4 Experimental Results and Discussion

In this section, experimental results are presented for device-free ranging and localization. For ranging, the results for *Measurement Set 1* and *Measurement Set 2* are shown, which were described in the previous chapter. Moreover, new experiments were performed to quantify the performance of the device-free localization.

4.4.1 Device-Free Ranging

Throughout our analysis, the fractional bandwidth β of the low-pass filter was chosen as 0.05, since it gave the best detection performance. Experimental

results for the device-free ranging are tabulated in Table 4.1, showing, for each of the measurement positions shown in Fig. 3.10, the true bistatic range and the bistatic range error (calculated as the difference between the estimated and the true bistatic ranges) for the three ranging criteria introduced in Section 4.3, both for parallel and perpendicular body orientations.

When the Line Search approach is employed, the bistatic range error is found to be always positive (for both orientations) and less than 62 cm for all the cases, except the case where the person blocks the LOS (case H4). However, if the Maximum Rise Search approach is employed, the ranging error can be slightly decreased for some cases, while making it negative for some other cases (again except the case H4). Considering the other positions than H4, the average absolute ranging errors for the Line Search and Maximum Rise Search methods are found to be 35 cm and 13 cm, respectively. For both of these methods, the orientation of the person does not introduce a significant difference in range estimates for most cases, and absolute differences are found to be less than 20 cm and 33 cm for the Line Search and Maximum Rise Search methods, respectively, for all positions except H4.

For the case H4, as discussed earlier in Section 3.7.3, temporal variations are not only observed in a single delay window, but in multiple delay windows of the received waveform. Furthermore, the maximum value of the decision statistic occurs at a much later delay instant, corresponding to a later-arriving human-body-reflected path (similar to the case plotted in Fig. 3.15(d). This results in large positive errors for the Line and Maximum Rise Search criteria. On the other hand, the Threshold Crossing method improves the bistatic range estimation performance, since the threshold is already crossed by the early delay instants (corresponding to the earliest reflection by the person). In particular, the threshold is crossed by the first sample for both the parallel and perpendicular measurements at H4. Hence only 2 cm of measurement error was obtained by the Threshold Crossing method.

On the other hand, the bistatic range errors for the Threshold Crossing criterion are very high in some other cases (i.e., H1, H2, H7, H8, H9, H10 and H13) because of the early crossings of the threshold. This is mainly due to the fact that the decision statistic shows larger deviations above the threshold, which is determined based on the theoretical calculations. However, these theoretical calculations do not take into account practical problems such as timing jitter and the effect of the lock spot choice. Because of these issues, it might be the case that the variations of the bins are not completely white even when the bins are not affected by the person. Then, estimating the noise power as in (3.27) or choosing the threshold based on the theoretical performance analysis which is derived from the received signal model in (3.3) will not be a good approach, because this signal model assumes white noise. Increasing the threshold may lead to better results, although, in general, the determination of the optimum value might be a difficult task, because these effects need to be considered in the received signal model. Moreover, then the calculations also need to include the statistical distributions of these practical effects, and

Table 4.1: Experimental results for device-free ranging: true bistatic range and error in measured bistatic range for the different positions shown in Fig. 3.10, for three different ranging criteria and for parallel and perpendicular body orientations.

Position	**True range [m]**	**Range error [m]**					
		Line Search		Thres. Crossing		Max. Rise Search	
		Par.	Perp.	Par.	Perp.	Par.	Perp.
H1	7.85	0.2	0.19	−0.41	**−2.83**	0.01	0.01
H2	6.43	0.49	0.32	**−1.42**	−0.48	0.1	0.08
H3	5.4	**0.61**	0.5	−0.2	−0.31	0.19	0.15
H4	5	0.6	**2.2**	0.02	0.02	0.42	1.19
H5	5.4	**0.61**	0.59	0.02	−0.29	0.37	0.21
H6	6.43	0.41	0.34	−0.35	**−0.45**	0.03	0.07
H7	7.85	0.21	0.17	**−2.74**	−0.65	0.01	−0.25
H8	6.7	0.27	0.27	−0.88	**−1.61**	−0.12	−0.17
H9	7.39	0.36	0.18	**−2.26**	−0.67	−0.02	−0.04
H10	7.5	0.07	0.07	−0.81	**−2.48**	−0.36	−0.26
H11	6.7	**0.54**	0.34	−0.26	−0.43	0.12	0.08
H12	7.39	0.25	0.4	**−0.63**	−0.45	−0.17	0.09
H13	7.5	0.36	0.56	−2.46	**−2.48**	0.01	0.34

parameters of the distributions such as the mean and the standard deviation. These might be hard to obtain as these effects are also device-specific. The rms device-free ranging errors, computed as

$$e_{\mathrm{rms,r}} = \sqrt{\frac{1}{N_{\mathrm{pos}}} \sum_{i=1}^{N_{\mathrm{pos}}} ||\widehat{d}_i - d_i||^2}, \tag{4.7}$$

where $\widehat{d}_i$ and d_i are the estimated and true bistatic ranges for each of the N_{pos} positions, are found to be 0.53, 1.23 and 0.27 for the Line Search, Threshold Crossing and Maximum Rise Search criteria, respectively.

The device-free ranging errors for the above-mentioned criteria are also analyzed for *Measurement Set 2*, and shown in Fig. 4.2. To visualize the device-free ranging performance, the three regions from Fig. 3.12 are considered separately. The results are shown for, in total, 44 positions where the presence of the person is detected. Considering only the measurements where the person was

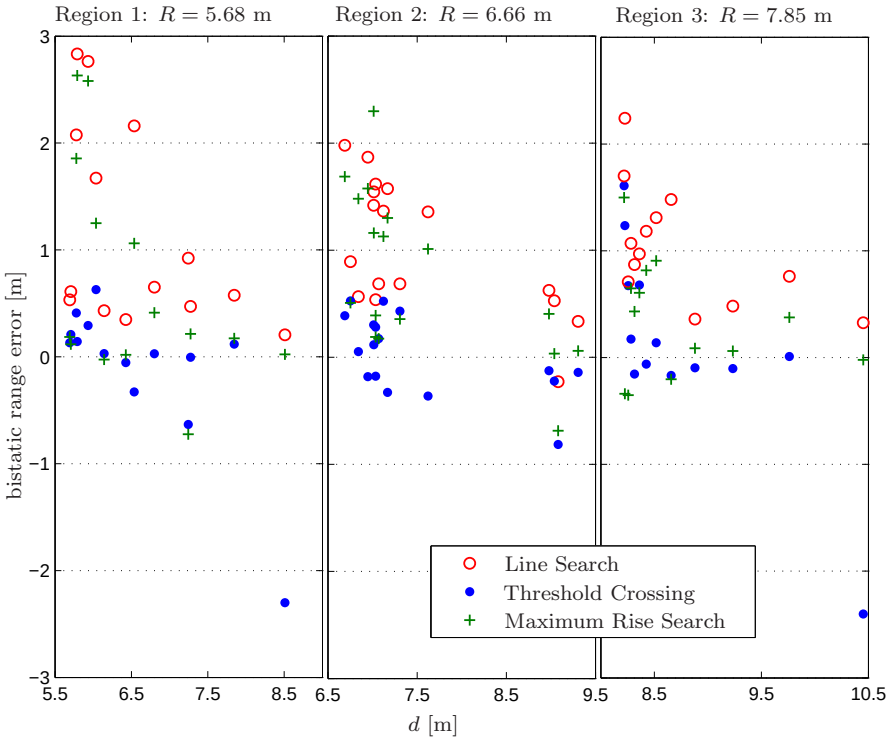

Figure 4.2: Bistatic range error versus true bistatic range (d) for the Threshold Crossing (blue dot), Line Search (red circle) and Maximum Rise Search (green cross) criteria with anchor distances of 5.68 m (leftmost), 6.66 m (center) and 7.85 m (rightmost), $\beta = 0.05$ and a measurement duration of 2 seconds (see Fig. 3.12 for the postions of the person).

standing within the device-free detection range limited by the radios, the detection method could not detect presence of the person in two measurement cases ($\beta = 0.05$, $N_{\text{rep}} = 100$ within 2 seconds, $\gamma = 1.4$). Hence, there are 14 positions for Region 1, 17 positions for Region 2, and 13 positions for Region 3.

A similar observation is obtained again. The Threshold Crossing method outperforms the Line Search and Maximum Rise Search methods for most of the cases, when the person is close to the LOS. This is especially clear in Region 2, where more measurements are made (compared to the other regions) for the person in close proximity to the LOS. In this scenario, the rms ranging errors are obtained as 1.18 m, 0.35 m and 0.9 m for the Line Search, Threshold Crossing and Maximum Rise Search methods, respectively. In Region 1 and Region 3, the Threshold Crossing method gives two large negative outliers

(around −2.4 m), because of the early crossing of the threshold. For these two cases, the Line Search and Maximum Rise Search methods give much better estimates. In these scenarios, the rms ranging errors are 0.68 m, 1.4 m and 1.1 m, and 0.91 m, 1.16 m and 0.72 m, for the Threshold Crossing, Line Search and Maximum Rise Search methods, in Region 1 and Region 3, respectively. Specifically, in Region 3, Maximum Rise Search is better, because the Threshold Crossing method gives almost the same order of error (e.g., for two cases both give close errors above 1 m), when the person is close to the LOS between the devices. For these cases, the decision statistic also gets lower values (for both cases lower than 2), compared to the other cases. This results from the reason that the slow variations due to the motion of the stationary person was not very strong in these cases within 2 seconds of measurement duration. In general, the movement of the person is random and it may move more in some cases than in other cases.

4.4.2 Device-Free Localization

Here, indicative results of the localization capabilities of the proposed system are presented in an experimental setting. For this purpose, additional measurements were done as our previous measurements consist of a single link for each measurement scenario. However, at least three bistatic range measurements are needed to compute the final location without an ambiguity. This requires at least three link measurements which involve the effect of the person on the received signal for each position of the person. Experiments were performed in a room, located at the top floor of the Carré building at the University of Twente. The room was partly furnished with tables and chairs, and also had thick metallic pipes for ventilation and water supply. Four anchor nodes were deployed, connected to a computer via network cables and an Ethernet switch, and arranged in a square. The anchor nodes were placed on the corners of the square, separated by 5 m. A person stood on 24 different positions in a grid within a 3 meter by 5 meter area. Again, the person was standing with the center of the body in the marked positions. For each position, six anchor-to-anchor measurements were taken, corresponding to the six possible combinations of two of the four anchor nodes. However, for some positions the person was in the detection range of only four or five links, due to the 10 ns of delay window limitation of the current radios. For each anchor pair, measurements were performed over 20 seconds with a rate of 50 measurements per second (i.e., 1,000 snapshots). Hence, it was possible to locate the person, as there were more than three bistatic range measurements per position. Finally, the receiver coherently combined 128 pulses for each ranging measurement.

The position of the person was estimated according to (4.3) by first dividing the area into points, separated by 7 cm along the X and Y dimensions. Then, a search operation was performed to find the position that corresponds to the least-squares estimate given in (4.3). The rms localization error is computed

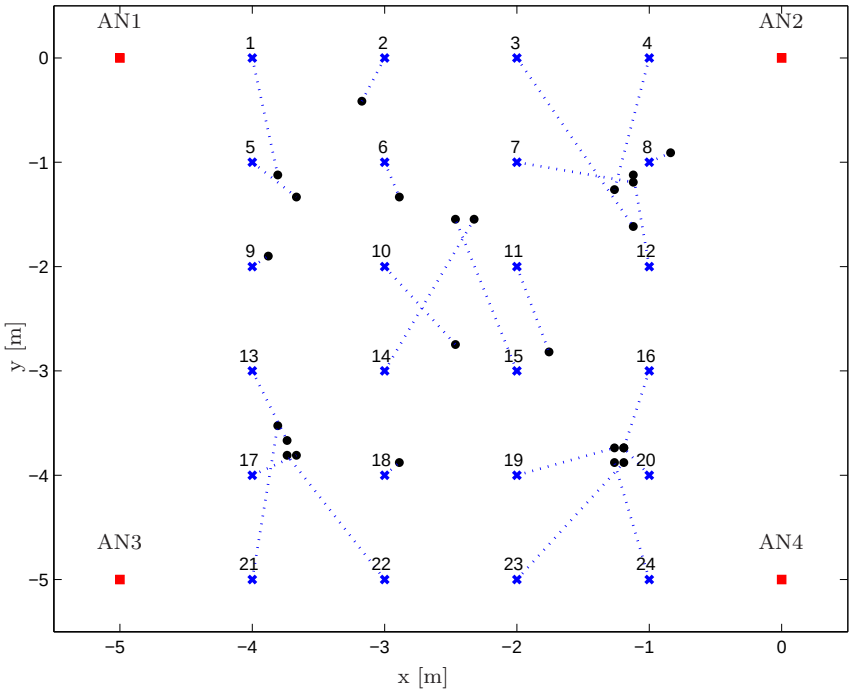

Figure 4.3: Experimental results for localization, obtained when the person stands on 24 different positions in an indoor environment with four anchor nodes (marked as red squares). The Threshold Crossing criterion is applied to obtain the bistatic range estimates. The true positions are shown as blue crosses, and the estimates as black dots.

as

$$e_{\mathrm{rms,loc}} = \sqrt{\frac{1}{N_{\mathrm{pos}}} \sum_{i=1}^{N_{\mathrm{pos}}} ||\widehat{\mathbf{x}}_{\mathrm{p},i} - \mathbf{x}_{\mathrm{p},i}||^2}, \tag{4.8}$$

where N_{pos} denotes the number of standing positions of the person (24 in this case), and $\widehat{\mathbf{x}}_{\mathrm{p},i}$ and $\mathbf{x}_{\mathrm{p},i}$ are the estimated and true positions of the person, respectively.

In Fig. 4.3, the results for localization are shown, for the cases where bistatic range estimation is performed according to the Threshold Crossing criterion. The threshold is chosen as $\tilde{\gamma} = 1.1$, which corresponds to a P_{FA} of 10^{-4} for $N_{\mathrm{rep}} = 1,000$, based on the analytical results in Fig. 3.4. Error values ranging from 0.12 m (measurement point 18) to 1.8 m (measurement point 3) and an overall rms localization error of 0.93 m are obtained.

To have a more detailed view of the position estimates, in Fig. 4.4(a) and

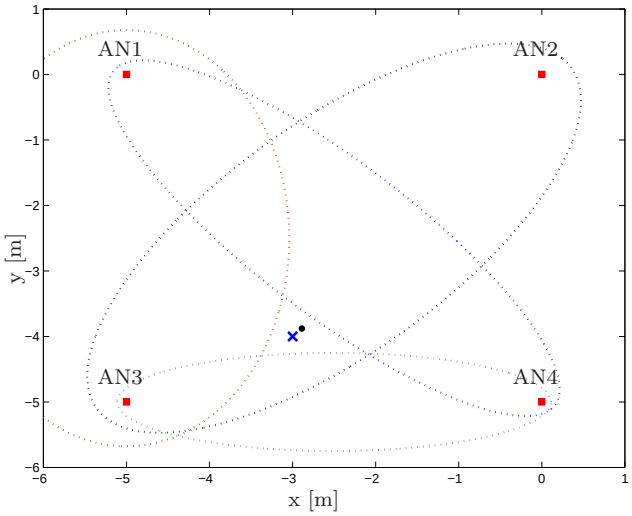

(a) Localization result for measurement point 18 in Fig. 4.3.

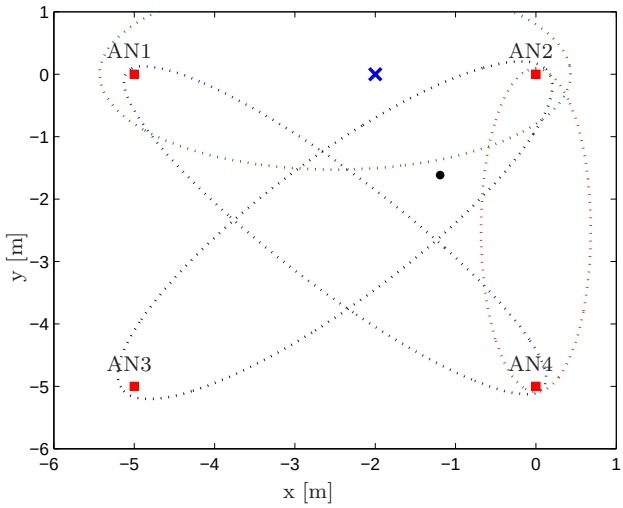

(b) Localization result for measurement point 3 in Fig. 4.3.

Figure 4.4: Localization results with Threshold Crossing range estimates. Ellipses corresponding to the range estimates between AN1 and AN2, AN1 and AN3, AN1 and AN4, AN2 and AN3, AN2 and AN4, and AN3 and AN4 are shown in green, brown, blue, black, red and gray dotted lines, respectively. The blue cross and black dot show the real and estimated position of the person, respectively.

Fig. 4.4(b), the ellipses corresponding to the range estimate of each link are plotted for the cases when the person was standing in measurement point 18 and measurement point 3, respectively. For measurement point 18 (shown in Fig. 4.4(a)), there are three good bistatic range estimates, between AN1 and AN3 (−0.35 m error), AN1 and AN4 (−0.25 m error), AN3 and AN4 (−0.17 m error), and a relatively high bistatic range error between AN2 and AN3 (0.53 m error). However, for measurement point 3 (shown in Fig. 4.4(b)), large outliers between AN2 and AN4 (−2.2 m error), AN1 and AN4 (−1.13 m error), and relatively better estimates between AN1 and AN2 (0.86 m error), and AN2 and AN3 (−0.46 m error) are obtained. These large outliers are due to the very early crossings of the threshold, and because of the large outliers, the least square position estimate (black dot) also gets a large error.

As previously mentioned, the threshold is chosen based on the analytical results in Fig. 3.4. However, these analytical derivations do not include the practical issues of the hardware, e.g., timing jitter. Therefore, choosing the threshold in this manner would not be the optimum solution. In Fig. 4.5(a), the relationship between the rms localization error and the threshold is shown for 24 measurement scenarios. The rms localization error is calculated considering only unambiguous location estimates. An ambiguity occurs when the number of bistatic range estimates is lower than three. For each measurement point, there are at least four measurements in which the person can be detected given the bistatic range limitation of the radios. In measurement points 10, 11, 14 and 15, all six measurements can be used for localization, whereas for the rest, only four measurements can be used. According to this result, an rms localization error of 0.7 m is obtained when the threshold is set to 1.8. This is the minimum localization error that can be obtained by choosing one of these threshold values. As the threshold value is increased further, higher localization errors are observed. Such a result suggests to increase the threshold up to 1.8 to improve the localization performance. On the other hand, it might be the case that the decision statistic is no longer above the chosen threshold for some of the measurements (i.e., the maximum value of the decision statistic is lower than the chosen threshold.). In Fig. 4.5(b), the number of ambiguous location estimates is shown for these threshold values. According to this result, no ambiguity occurs until the threshold of 1.5, but it increases after this threshold value. For instance, the location ambiguity occurs in two measurements when the threshold is set to 1.8 m, which gives the lowest rms localization error.

To further show the effect of the threshold choice on the bistatic range estimates, the results in Fig. 4.6 are shown. Specifically, the relationship between the threshold choice and the rms bistatic range error is shown in Fig. 4.6(a). The results were obtained for the 24 measurement scenarios in Fig. 4.3 and in total 104 possible bistatic range estimates, which were obtained by collecting 20 measurement scenarios with four bistatic range estimates and four measurement scenarios with six bistatic range estimates. In general, Fig. 4.6(a) shows that the rms bistatic range error decreases as the threshold is increased except between 1.9 and 2.1, and between 2.3 and 2.5, where there are slight increases

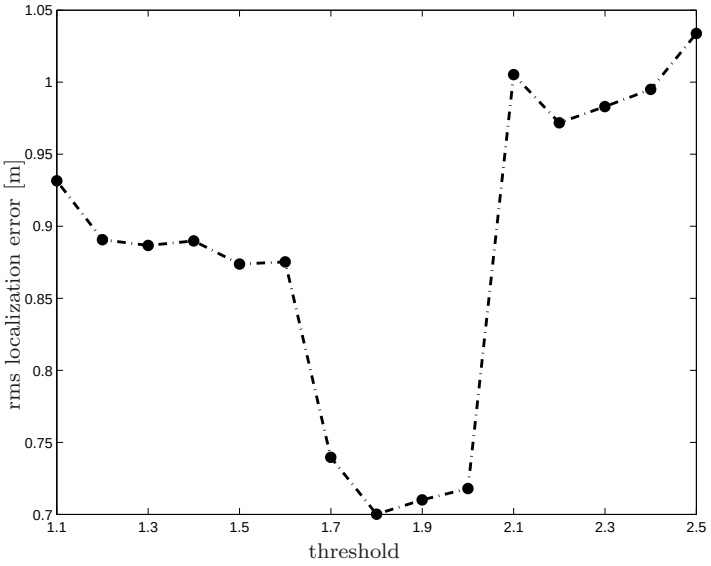

(a) RMS localization error versus threshold value.

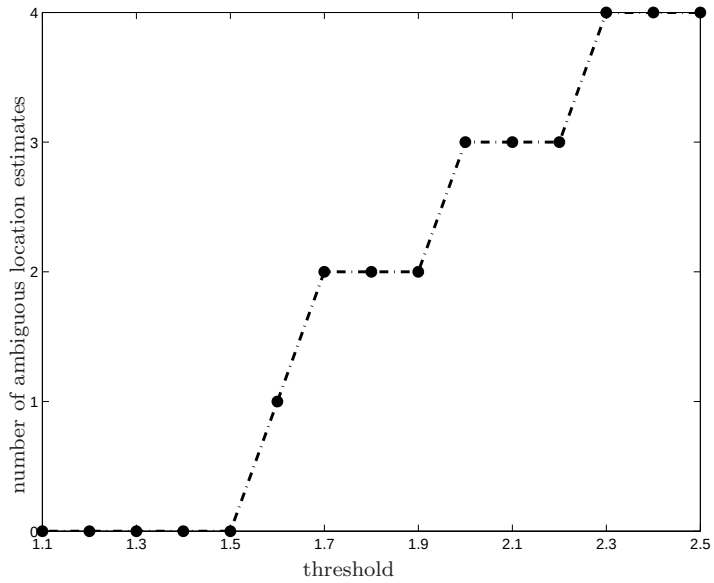

(b) Number of ambiguous location estimates versus threshold value.

Figure 4.5: Rms localization error and number of ambiguous location estimates versus threshold value chosen for the Threshold Crossing criterion over 24 localization measurements.

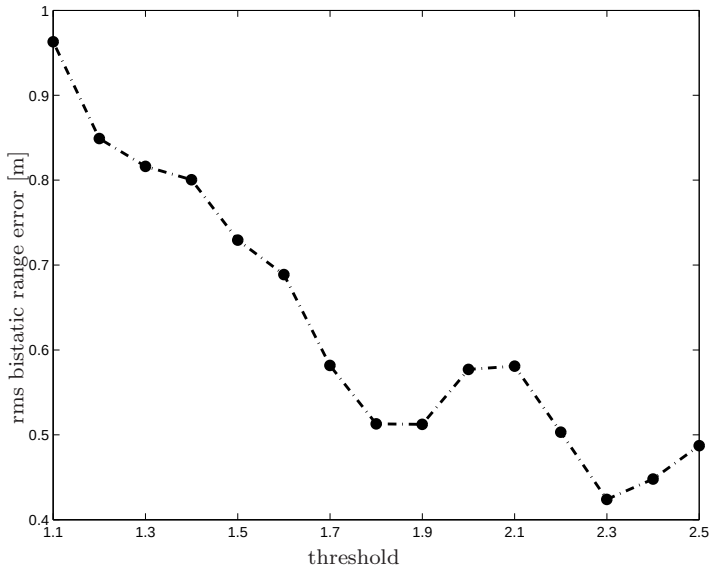

(a) RMS bistatic range error versus threshold.

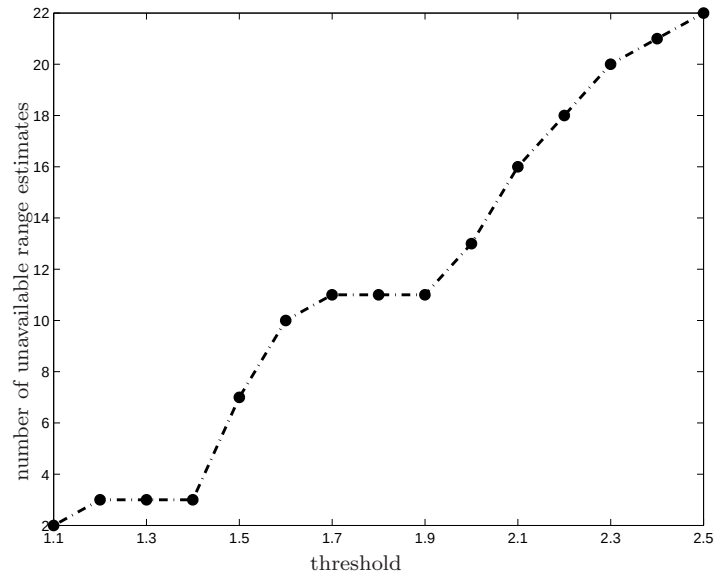

(b) Number of unavailable range estimates versus threshold.

Figure 4.6: Rms bistatic range error and number of unavailable bistatic range estimates versus threshold value chosen for the Threshold Crossing criterion over a total of 104 bistatic range estimates.

in the error values. Fig. 4.6(b) shows the number of unavailable range estimates for the threshold increase from 1.1 to 2.5. This result reveals that the number of unavailable range estimates is rather low until 1.4 (i.e., three out of 104 measurements) and then increases up to 22, which corresponds to around 21% of the measurements, for a threshold value of 2.5. This result can also be interpreted as that the maximum value of decision statistic is lower than 2.5 for 21% of the measurements.

When compared to the rms localization error result in Fig. 4.5(a), the rms range error result shows a different trend. The rms localization error increases slightly after the threshold value of 1.8, has a sudden jump (an error increase of around 0.28 m) between 2.0 and 2.1 and reaches 1 m, and stays around this value. This trend is not observed in the range error results in Fig. 4.6(a), because, as the threshold is increased, the number of range estimates used for the localization estimate decreases from four to three in most of the measurement scenarios. This leads to a higher localization error in some scenarios. An example of this case is shown in Fig. 4.7(a), where there are three available range estimates. Two of these three range estimates have very low bistatic range errors: the error is 0.04 m between AN1 and AN4 and it is -0.09 m between AN2 and AN4. For the other measurement, between AN2 and AN3, the error is higher: 0.44 m. The final location error is 3.2 m. Even though there is not really an outlier in the bistatic range estimates, the final localization error is high because of the geometry of the scenario and the low number of available bistatic range estimates. The location estimate for the same scenario with the threshold value of 1.1 is shown in Fig. 4.7(b). In this case, there are four available range estimates. Three of these range estimates have low bistatic range errors: the error is -0.07, -0.07 and 0.18 for the measurements between AN1 and AN2, AN1 and AN4, and AN2 and AN3, respectively. However, there is an outlier observed for the measurement between AN2 and AN4: the error is -1.47. Even though this outlier is larger compared to the case in Fig. 4.7(a), the final location error is lower (i.e., it is 0.9 compared to 3.2) because there are more bistatic range estimates available.

Localization results are also shown for the Line Search and Maximum Rise Search ranging criteria, in Fig. 4.8 and Fig. 4.9, respectively. The localization error varies from 5 cm (measurement point 11) to 2.5 m (measurement point 8) for the Line Search, and 5 cm (measurement point 11) to 2.4 m (measurement point 1) for the Maximum Rise Search criterion. Furthermore, when employing the Line Search and Maximum Rise Search methods, the rms localization error increases up to 1.6 m and 1.33 m, respectively. In general, similar to the observations in Section 4.4.1, the Line Search and Maximum Rise methods give large errors in ranging when the person is close to the LOS between the transmitter and the receiver. These large errors in range estimates result in large outliers in location estimates when these range estimates are incorporated. It is also observed that some of the estimates are outside the region enclosed by the anchors. In general, it depends on the geometry and the error in bistatic range estimations. For instance, at measurement point 1 in Fig. 4.8,

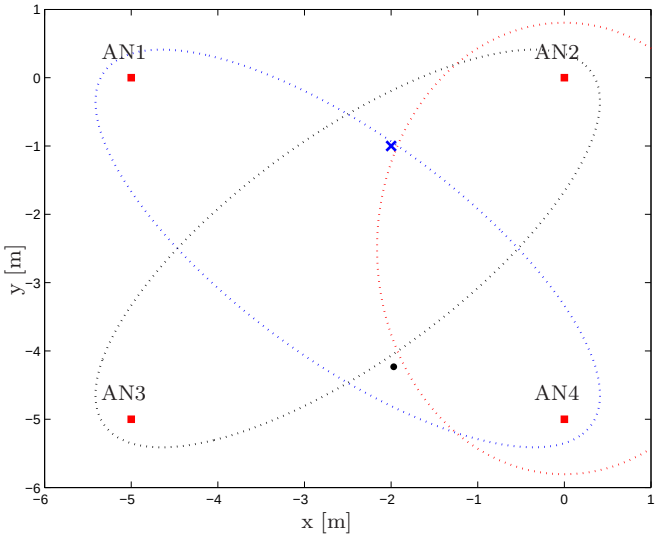

(a) The threshold is set to 2.1

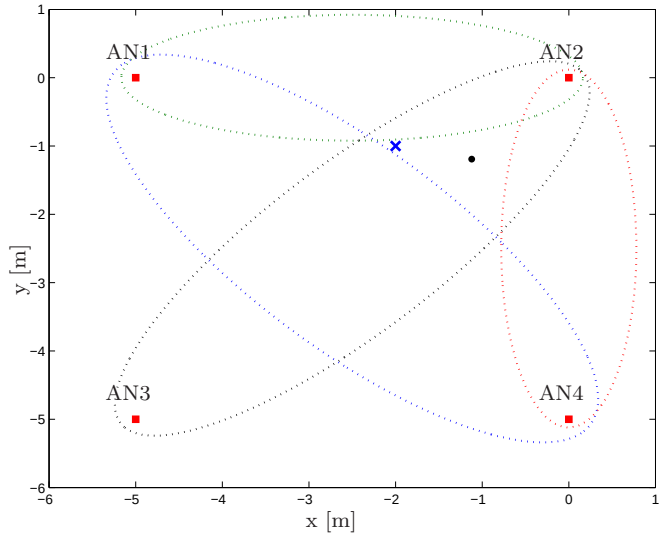

(b) The threshold is set to 1.1.

Figure 4.7: Localization result for measurement point 7 in Fig. 4.3. Ellipses corresponding to the range estimates between AN1 and AN2, AN1 and AN4, AN2 and AN3, and AN2 and AN4 are shown as green, blue, black and red dotted lines, respectively. The blue cross and black dot show the real and estimated position of the person, respectively.

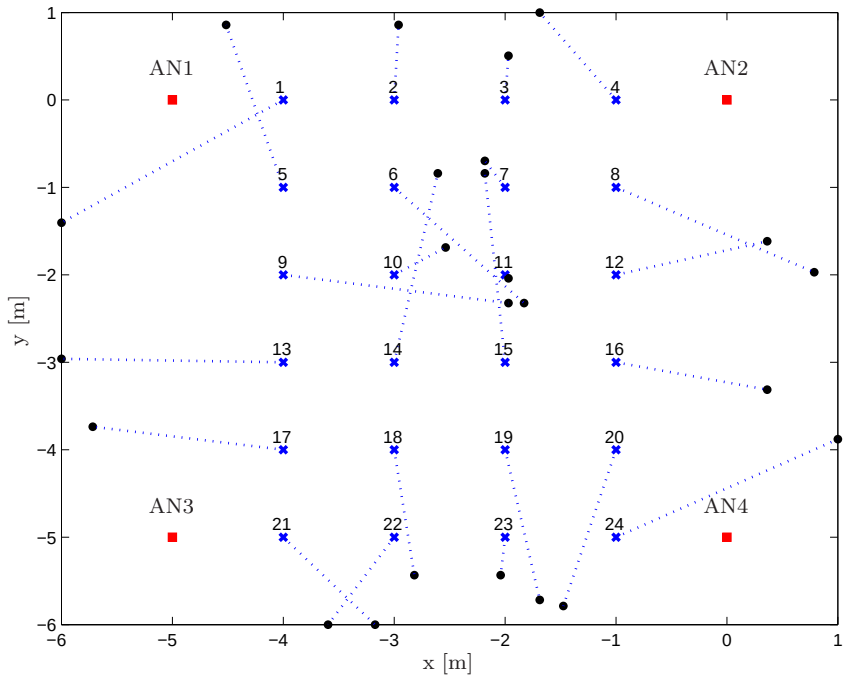

Figure 4.8: Experimental results for localization, obtained when the person stands on 24 different positions in an indoor environment with four anchor nodes (marked as red squares). The Line Search criterion is applied to obtain the bistatic range estimates.

there are very large outliers in bistatic range estimation between AN1 and AN2, and AN1 and AN4, i.e., the bistatic range errors are 2.6 m and 2.34 m, respectively. The bistatic range errors are 1.23 m and 0.39 m between AN1 and AN3, and AN2 and AN3. As there are three relatively large errors, also depending on the geometry of the anchors, the final position estimate is chosen outside the region enclosed by the anchors. If there had been no large error in least one of the bistatic range estimates in between AN1 and AN2, and AN1 and AN4, the final position estimate could have been in the region enclosed by the anchors. For instance, at measurement point 9, the only bistatic range estimate which is an outlier, is the one between AN1 and AN3. In this measurement, the bistatic range error is 2.35 m. For the other three measurements (i.e., between AN1 and AN2, AN1 and AN4, and AN2 and AN3) the bistatic range estimates are below 0.5 cm. Because of the large outlier between AN1 and AN3, the final position estimate also has a large error. However, because of the low bistatic range errors between the other anchor pairs the final position estimate is within the region enclosed by the anchors.

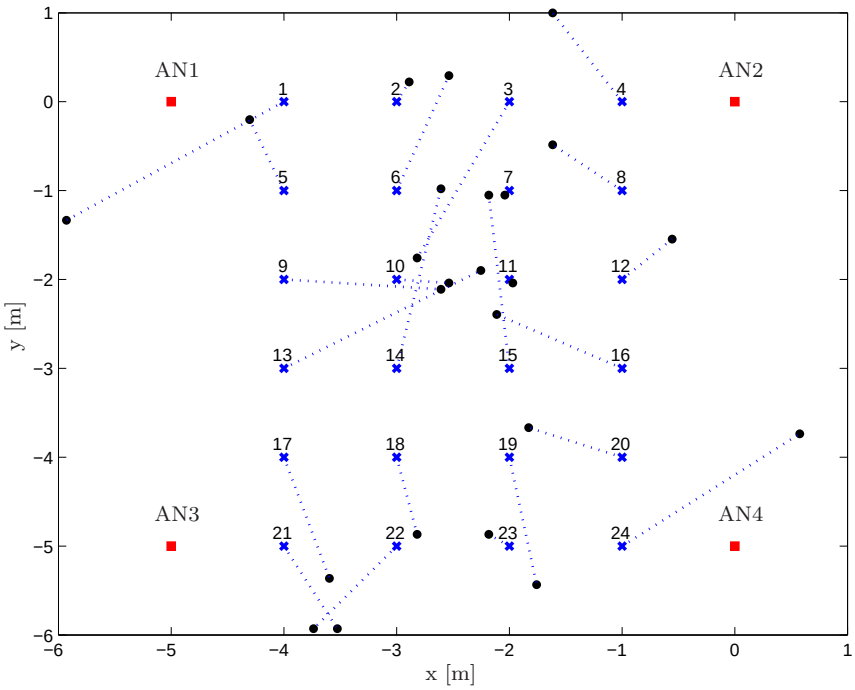

Figure 4.9: Experimental results for localization, obtained when the person stands on 24 different positions in an indoor environment with four anchor nodes (marked as red squares). The Maximum Rise Search criterion is applied to obtain the bistatic range estimates.

Comparing these results to the results presented in the previous studies, in [43] the localization accuracy of around 0.2 m was obtained. This work includes training measurements in the environment when the person was not present. The methods presented in [48] and [49] were based on the variations in the RSS and in these works the localization accuracies of 0.5 m with 34 and fourteen nodes were obtained, respectively. This localization accuracy is better than the method presented for UWB system in this thesis. However, in our work, only four UWB nodes were employed for localization. In comparison to the results in UWB domain, in [72], the performances of a first threshold crossing and a HMM-based approaches were shown and the rms bistatic range errors were obtained around 1.6 m and 0.9 m, respectively. The rms localization errors were 1.5 m and 0.75 m with the bistatic range estimations using HMM-based approach in two different environments. In general, both the first threshold crossing and HMM-based approaches were a bit different as the authors built the techniques on the changes of the CIR between the presence and the absence

of the person. The HMM-based approach has a better localization performance compared to the our results and gives a good aspect when detecting the person and perform the localization since it also involves the changes in the later delay samples which are due to the indirect reflections.

4.5 Conclusion

In this chapter, an experimental analysis of the device-free ranging and localization was provided. The measurements were performed in an indoor environment with many reflection sources. Three practical bistatic range estimation criteria were introduced, based on the decision statistic introduced in the previous chapter.

The experimental results for ranging showed that the Threshold Crossing method outperforms the other two when the person is close to the LOS between the transmitter and the receiver. However, as the person gets further away from the direct vicinity, the Threshold Crossing method may be subject to early crossings of the threshold, and for these cases the Maximum Rise and Line Search methods gave better estimates. On the other hand, these two criteria are affected by indirect reflections, causing the maximum value and/or the maximum rise of the decision statistic to correspond to delay values that are larger than the one corresponding the position of the person.

Large outliers in the range estimates also degrade the final localization performance. Overall, our results indicate that the Threshold Crossing Method gives better localization estimates. These results may be improved with an investigation of the optimum selection of the threshold. The optimum value should be calculated by also considering the number of available bistatic range estimates, because, if the chosen threshold is higher than the decision statistic, no bistatic range estimate is obtained. This results in a localization ambiguity if the number of range estimates becomes lower than three. In order to investigate the optimum threshold, the effects that have an influence on the maximum value of the decision statistic should be taken into consideration, e.g., practical issues such as timing jitter and the strength of the person's movement.

Chapter 5

Device-free Detection and Localization of Multiple People

5.1 Introduction

In this chapter, the main objective is the detection of more than one person, obtaining the bistatic range estimates for each person and locating them using an UWB network. Chapter 3 showed that later-arriving delay samples may also show variations because of the indirect reflections. In order to discriminate these indirect reflections and variations due to additional persons, correlations between the delay bins within the same link will be analyzed. Furthermore, the correlations between the delay bins in different links will be considered to determine which delay bins belong to reflections upon the same person and, hence, to enable the localization of multiple people. The effect of hardware impairments, discussed in Chapter 3, also have an influence on the correlations, especially when the correlations within the same link are considered. Considering these hardware effects, a discussion on the normalization choice will also be provided in this chapter.

This chapter will show many normalized correlation graphs. The first set of results will be shown for the cases when there is no person in the environment. These results will help to understand how the hardware impairments influence the correlation between the delay samples and determine the choice of the normalization to reduce undesired effects on the final correlation metric. Then the correlation results will be shown for the single person and multiple persons cases to visually show that the detection is possible with the chosen correlation metric. When considering the detection and bistatic range estimation, the threshold is one of the key parameters to be optimized. In this chapter, the cumulative distribution of the threshold will be shown based on the measure-

ment results. The correlation graphs will also be shown to explain how the correlation between the delay samples of the same link and different links are affected in different settings. This will help to develop understanding for when and why the method fails. Finally, the results for the detection, bistatic range estimation and localization will be shown to quantify the performance of the developed technique.

This chapter is organized as follows. First, the motivation behind our approach will be explained together with the methodology. Then, the description of the test environment and scenarios will be given. This will be followed by a discussion on the choice of the correlation metric. Here, the influence of the hardware impairments on the choice of the correlation metric will be discussed. Then, the correlation results for a single link and between multiple links will be analyzed. After that, a localization algorithm, which is based on combining the correlation matrices, will be developed. Finally, the localization results will be discussed, before the concluding remarks are provided.

5.2 Motivation and Methodology

In this section, it is first explained why more information beyond the decision statistic is needed to detect multiple people affecting the same measurement link. Then, the description of the methodology will be presented for the detection of more than one person with a single link and locating them using multiple links.

Let us consider an example scenario where two persons are standing on certain positions with corresponding ellipses as shown in Fig. 5.1(a). In this experimental setting, the positions of the anchors are $(0, 0)$ m and $(-5, -5)$ m, and the distance between anchors is 7.07 m. The positions of the persons are $(-3.5, 0.5)$ m and $(-3, -5)$ m for the first and second person, respectively[1]. Given the positions of anchors and persons, the bistatic range for the first person is 9.24 m, while it is 7.83 m for the second person. The experimental equipment, which has already been introduced in Section 3.7.1, is used in this experiment as well. The measurement is performed in an open indoor environment, whose details will be given in Section 5.3.

The decision statistic, which was developed in Section 3.4, clearly shows two distinct peaks due to the slight movements of each person. However, it is not enough to determine the presence of two people, since it might also show more than one peak because of the indirect reflections as shown in Figs. 3.15(b), (c) and (d). Therefore, more information than the decision statistic is needed to distinguish those bins, influenced by different people.

Motivated from the assumption that the random movements of two different persons will be different, their influence on the received waveforms will also be different. Therefore, the received signal bins, which are influenced by different

[1]Similar to Chapter 3 and Chapter 4, the position of each person is considered as the point that is corresponding to the center of the body.

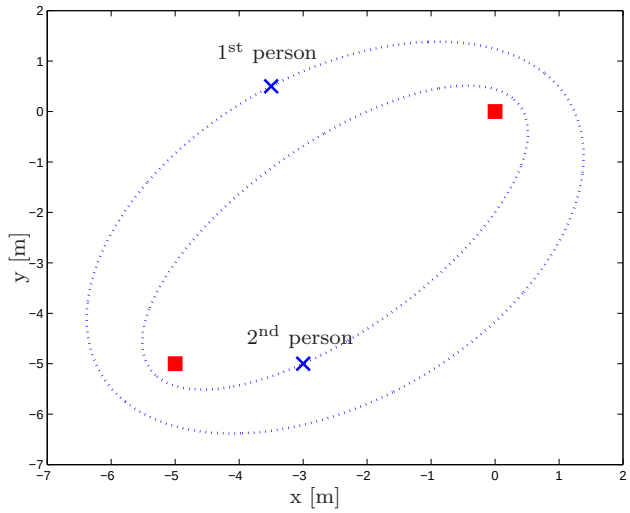

(a) The measurement scenario. The positions of the persons and anchors are shown as blue crosses and red squares, respectively. Ellipses corresponding to the position of each person are shown as dashed blue lines.

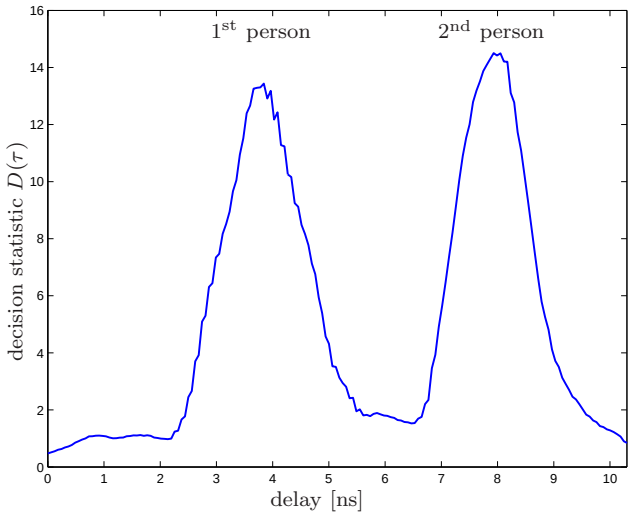

(b) The corresponding decision statistic.

Figure 5.1: An example measurement scenario considering multiple person detection and localization, and the corresponding measured decision statistic.

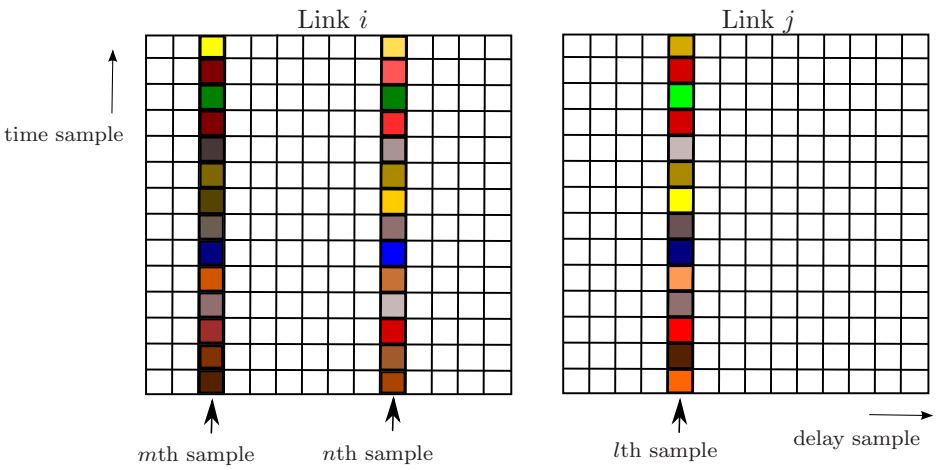

Figure 5.2: Received delay samples over delay and time for two links. Correlation analysis can be performed between the mth and nth samples of Link i, and/or the mth or nth samples of Link i and lth samples of Link j. Different colors indicate different amplitudes.

persons, will have low correlations. On the other hand, if two different delay bins are influenced by the same person, they will show similar variations with a relatively high correlation value.

In this chapter, it will be investigated whether the correlations between the variations due to the random movements of two stationary persons can be used to detect and locate these two people. First the correlation analysis between the received delay samples of the same link (e.g., in Fig. 5.2 between the mth and nth delay samples of Link i) will be made to perform the detection and estimate the bistatic ranges. While the correlation analysis of a single link can be enough to perform detection and estimate bistatic ranges for each person, at least three bistatic range estimates are needed to find the position of each person. This requires matching the bistatic range estimates of each link for each person with the other links (i.e., to find which bistatic range estimate corresponds to the first person for Link i and Link j). Therefore, the correlations between the delay samples of different links will also be considered to determine the delay samples that are affected by the same person for each link (e.g., in Fig. 5.2 between the mth delay sample of Link i and the lth delay sample of Link j.).

5.3 Measurement Environment and Scenarios

Measurements were performed in Sportzaal 2, which is located in the Sports Centre at the University of Twente. The size of the room is 22×18 m with a height of 7 m. The measurement setup was established around the center of

Figure 5.3: UWB setup for multiple people detection and localization measurements.

the room, to prevent additional reflections due to the walls within the device-free detection range, limited by the radios. Considering also the height of the room, there were no reflections from the ceiling of the room within the observation window. Again the ceiling is high enough and it was not possible to detect these reflections because of the device-free detection range of our radios. Therefore, the only reflection source was the floor. In general, there will always be reflections unless absorbers are placed at these locations. An example measurement scenario for a single link (i.e., with two anchor nodes) is shown in Fig. 5.3.

Two different sets of measurements were performed. In the first measurement set, only single-link measurements were considered for the detection and bistatic range estimation. For these measurements the positions of the anchors AN1 and AN2 were $(0, 0)$ m and $(0, -5)$ m, respectively. An overview of the measurement positions for the two persons is plotted in Fig. 5.4, to give a general idea of the scenarios which are considered. Furthermore, the positions of each person are tabulated in Table 5.1, so that the exact positions for each scenario can be seen. While choosing the positions of each person, it was taken into consideration that the bistatic ranges should be sufficiently different. Therefore, the positions of each person were arranged in such a way that there are around 70 samples difference between the delay samples corresponding to the first and second persons's position.

In the second measurement set, the localization was also considered and the measurements were performed with four anchor nodes. The positions of the anchors AN1 to AN4 were $(0, 0)$ m, $(0, -5)$ m, $(-5, 0)$ m and $(-5, -5)$ m, respectively. Six links were established among these anchors in total. The

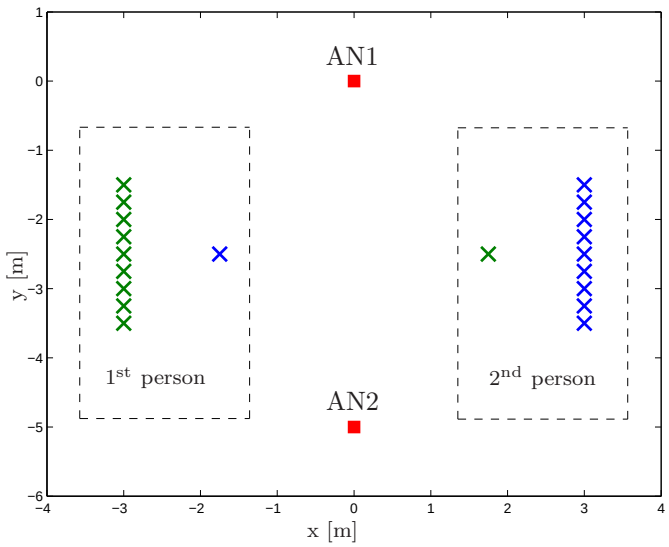

Figure 5.4: Overview of the positions of the two persons for the single-link detection and ranging measurements. The blue and green crosses represent the positions of the two persons for the measurement points 1–9 and 10–18 given in Table 5.1, respectively.

link indices and the corresponding anchor pairs, from which the measurement were taken, are tabulated in Table 5.2. In total, 17 different combinations of positions for the persons were chosen. These positions were chosen in such a way that in at least three of the six link measurements both persons were present within the detection region, limited by the radios. Furthermore, in at least three measurements, where both persons were in the detectable region, the two persons were not blocking the LOS between the antennas (i.e., no body shadowing) and the bistatic ranges corresponding to each person's position were sufficiently different. An overview of the measurement positions for the two persons is plotted in Fig. 5.5, to give a general idea of the scenarios which are considered. The positions of the two persons are also tabulated in Table 5.3.

For these measurements, the measurement configuration was slightly different, to be able to sample the movements of the persons in different links. Unfortunately, our measurement setup did not enable us to take measurement snapshots in different links simultaneously (i.e., broadcasting UWB signals from an anchor node and receiving them by all the other nodes at the same time). Therefore, each measurement snapshot was taken one link after the other link, in the order $\{\text{Link } 1, \text{Link } 2, \text{Link } 3, \text{Link } 4, \text{Link } 5, \text{Link } 6, \text{Link } 1, \ldots\}$. In this way, the movements of the people were sampled consecutively in every link. 200 snapshots were collected for each link, and hence 1200 measurements were

Table 5.1: Positions of the two persons for the single-link detection and ranging measurements

	Measurement positions [m]	
Measurement point	**Person 1**	**Person 2**
1	$(-1.75, -2.5)$	$(3, -3.5)$
2	$(-1.75, -2.5)$	$(3, -3.25)$
3	$(-1.75, -2.5)$	$(3, -3)$
4	$(-1.75, -2.5)$	$(3, -2.75)$
5	$(-1.75, -2.5)$	$(3, -2.5)$
6	$(-1.75, -2.5)$	$(3, -2.25)$
7	$(-1.75, -2.5)$	$(3, -2)$
8	$(-1.75, -2.5)$	$(3, -1.75)$
9	$(-1.75, -2.5)$	$(3, -1.5)$
10	$(-3, -3.5)$	$(1.75, -2.5)$
11	$(-3, -3.25)$	$(1.75, -2.5)$
12	$(-3, -3)$	$(1.75, -2.5)$
13	$(-3, -2.75)$	$(1.75, -2.5)$
14	$(-3, -2.5)$	$(1.75, -2.5)$
15	$(-3, -2.25)$	$(1.75, -2.5)$
16	$(-3, -2)$	$(1.75, -2.5)$
17	$(-3, -1.75)$	$(1.75, -2.5)$
18	$(-3, -1.5)$	$(1.75, -2.5)$

Table 5.2: Link indices and corresponding anchor pairs.

Link index	Anchor pair
1	AN1–AN2
2	AN1–AN3
3	AN1–AN4
4	AN2–AN3
5	AN2–AN4
6	AN3–AN4

obtained for all six links over 56 seconds. This corresponds to a measurement rate of roughly 21.4 measurement snapshots per second and a duration between two consecutive snapshots of 46.7 ms. Therefore the duration between the snapshots of the first and sixth link is 233 ms for one measurement round[2].

[2]It should be noted that the localization measurements of Section 4.4.2 were slightly different. In these measurements, $1,000$ snapshots were collected for one link and then another $1,000$ snapshots were taken for the next link. This way is more efficient as a communication link does not have to be established for each of the $1,000$ snapshots but it has to be established only once at the beginning of the first snapshot. In these measurements, $1,000$ snapshots of all links were taken within 20 seconds and with a rate of 50 measurement/second. Here, the

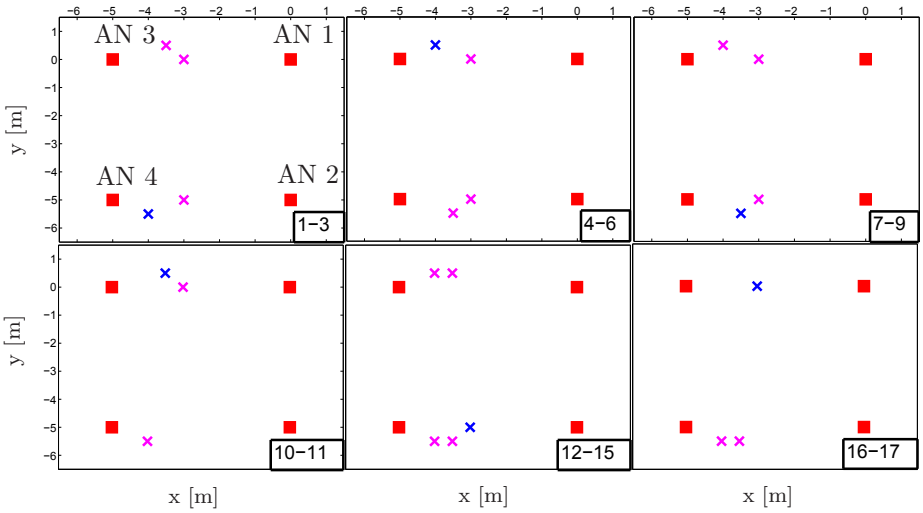

Figure 5.5: Overview of the positions of the two persons for the localization measurements. The blue and magenta crosses represent the positions of the first and second persons in each scenario for the measurement points from 1 to 17, given also in Table 5.3, respectively.

This is a limitation of our measurement setup. However, it will be assumed that the persons do not show significant movement within a duration of up to 233 ms. Similar to the previous experiments, the delay window length was around 10 ns. Throughout the analysis, the normalized bandwidth of the low-pass filter was chosen as $\beta = 0.05$, and the same postprocessing was performed to obtain the waveforms.

5.4 Normalization of Correlation Between Delay Samples

In this section, the way of normalizing the correlation between the delay samples will be discussed in detail. Then, an experimental analysis of the threshold for the correlation analysis method will be provided.

5.4.1 Rationale Behind the Choice of Normalization Method

Similar to Section 3.4.1, the sample mean of each delay bin over N_{rep} repetitions is removed from the signal, as the means of the delay bins do not convey

same procedure could not be repeated because otherwise the correlation analysis would be meaningless.

Table 5.3: Positions of two persons for the localization measurements

	Measurement positions [m]	
Measurement point	**Person-1**	**Person-2**
1	$(-4, -5.5)$	$(-3.5, 0.5)$
2	$(-4, -5.5)$	$(-3, -5)$
3	$(-4, -5.5)$	$(-3, 0)$
4	$(-4, 0.5)$	$(-3.5, -5.5)$
5	$(-4, 0.5)$	$(-3, -5)$
6	$(-4, 0.5)$	$(-3, 0)$
7	$(-3.5, -5.5)$	$(-4, 0.5)$
8	$(-3.5, -5.5)$	$(-3, -5)$
9	$(-3.5, -5.5)$	$(-3, 0)$
10	$(-3.5, 0.5)$	$(-4, -5.5)$
11	$(-3.5, 0.5)$	$(-3, 0)$
12	$(-3, -5)$	$(-4, -5.5)$
13	$(-3, -5)$	$(-4, 0.5)$
14	$(-3, -5)$	$(-3.5, -5.5)$
15	$(-3, -5)$	$(-3.5, 0.5)$
16	$(-3, 0)$	$(-4, -5.5)$
17	$(-3, 0)$	$(-3.5, -5.5)$

information for the sample correlation analysis. The low-frequency correlations are considered as our signals of interest are slowly varying. The sample covariance value between the mth delay bin of Link i and nth delay bin of Link j can be calculated from the measured waveforms by

$$C_{m,n,i,j} = \mathbf{r}_{m,i,\mathrm{L}}^T \mathbf{r}_{n,j,\mathrm{L}}, \tag{5.1}$$

where $\mathbf{r}_{m,i,\mathrm{L}} = [r_{m,i,\mathrm{L}}(0)\ r_{m,i,\mathrm{L}}(1)\ \ldots\ r_{m,i,\mathrm{L}}(N_{\mathrm{rep}}-1)]^T$ is defined in a similar way as in Section 3.4.1 with a slight modification to also include the link indices i and j.

It is already known from Section 3.7.2 that, in our setup, the energies of the variations for each delay bin are different, regardless of the presence of the person. Therefore, the sample covariance value in (5.1) needs to be normalized. The common way of normalizing the correlation between two data vectors is to divide by the Euclidean norm of each data vector as

$$\rho_{m,n,i,j} = \frac{\mathbf{r}_{m,i,\mathrm{L}}^T \mathbf{r}_{n,j,\mathrm{L}}}{\|\mathbf{r}_{m,i,\mathrm{L}}\| \, \|\mathbf{r}_{m,j,\mathrm{L}}\|}. \tag{5.2}$$

Since the data vectors are the low-frequency part of the delay bins, in this case the normalization can be performed by dividing (5.1) by the square root of the low-frequency energies of the signal (i.e., the energy of the low-frequency part of the delay bin m of the ith link is $E_{m,i,\mathrm{L}} = \mathbf{r}_{m,i,\mathrm{L}}^T \mathbf{r}_{m,i,\mathrm{L}} = \|\mathbf{r}_{m,i,\mathrm{L}}\|^2$).

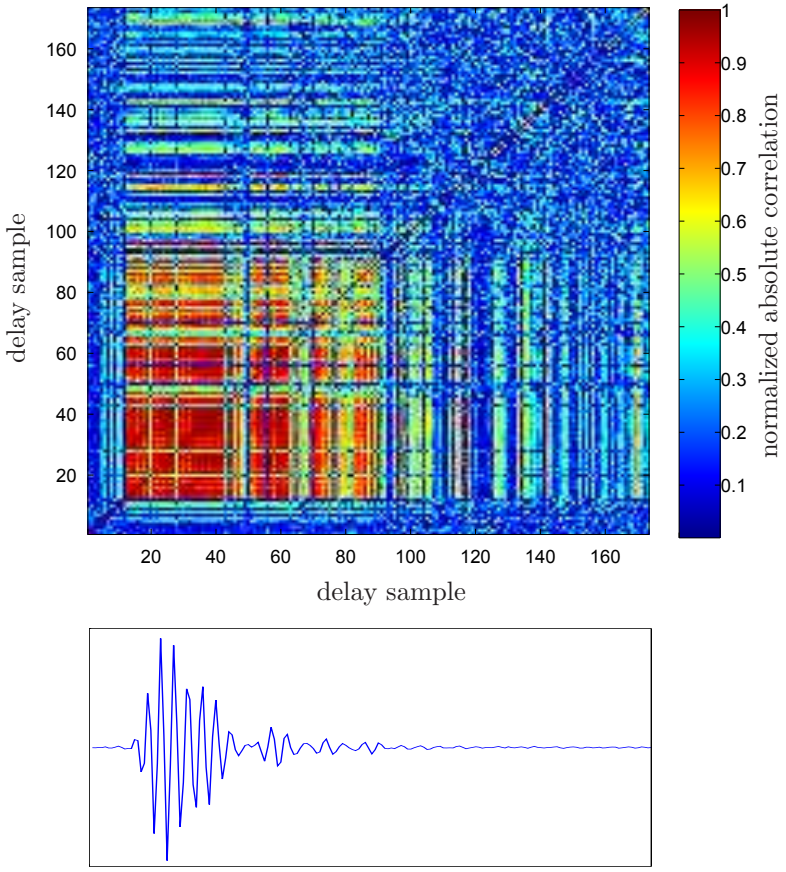

Figure 5.6: Normalized absolute correlation values between the delay samples of a single link with an example received waveform (in the bottom) in the absence of a person. The normalization is performed as in (5.2).

The amplitudes of the received waveform samples take positive and negative values. Hence, the correlation coefficient $\rho_{m,n,i,j}$ lies between -1 and 1, and no correlation occurs when its value is 0. Two highly correlated delay samples with amplitudes of opposite sign have a correlation coefficient which is close to -1. Our interest is on how strongly two received delay samples are correlated, regardless of their amplitude values being positive or negative. Therefore, the absolute value of the correlation coefficient is considered in the analysis. In this case, the correlation coefficient lies between 0 and 1.

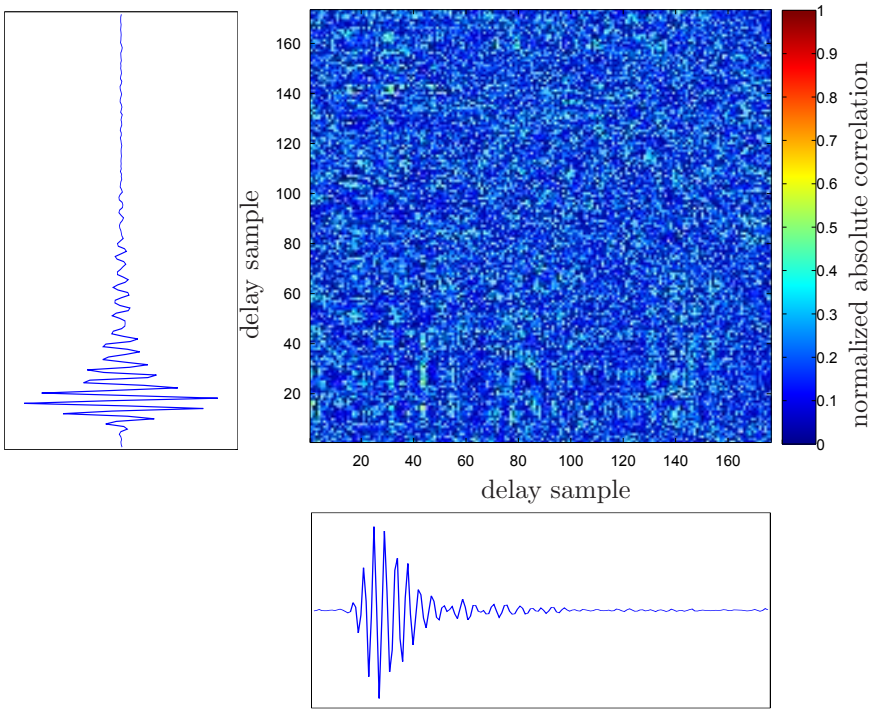

Figure 5.7: Normalized absolute correlation values between delay samples of two different links with example received waveforms (in the bottom and on the left) corresponding to each link in the absence of a person. The normalization is performed as in (5.2).

In the absence of the person, if the received delay samples were only affected by the additive white Gaussian noise, as defined in (3.4), then $\rho_{m,n,i,j} = 1$ would be obtained for $m = n$ and $i = j$ (i.e., the same delay bin in the same link), and low ρ values would be obtained for other combinations of the delay bins.

A measurement result of the absolute correlation coefficients between the delay samples of a single link for the case, where there is no person in the environment, is shown in Fig. 5.6. The values on the diagonal are indeed 1, and the figure is symmetric around the diagonal. Some combinations of delay bins of the same link show high correlation values even when there is no person in the environment. This is because of the timing jitter and the effect of the lock spot choice on background variations. In the same figure, an example received waveform is also plotted to explain for which delay samples the correlation values are high. The correlation values between the delay samples with high

amplitudes are very high, so that the absolute correlation values are close to 1. This is because the delay samples with high amplitudes usually correspond to the direct-path signal and strong reflections, and the timing jitter and background variations due to the lockspot choice have an influence mainly on these delay samples. The correlation coefficients among delay samples with very low amplitudes (e.g., in Fig. 5.6 after 120 delay samples) are comparably low because these samples are mostly affected by the noise, which can be considered to be uncorrelated between different delay samples.

On the other hand, the correlation values among the delay samples of two different links will be lower, because the timing jitter and the variations due to the lock spot choice can be considered as uncorrelated for different links. This is shown with an example measurement result in Fig. 5.7. This figure shows the normalized absolute correlation values between the delay samples of two links in the absence of the person. In the same figure, the example received waveforms are also plotted for each link on the left and in the bottom. As the figure shows, the correlations are much lower than in Fig. 5.7, and they do not depend on whether the delay bins correspond to a direct-path signal or strong reflections.

So far, the results have revealed that normalizing the sample covariance by the low-frequency energies of each pair of delay samples could be a way to use the correlation information between different links, while it may not be a way for correlations within the same link. Therefore, another way of normalizing the sample covariance is considered. In this way, the sample covariance is divided by the square root of each bin's total energy (i.e., not only its low-frequency part). With this way of calculation, the correlation values can be found from

$$\rho_{m,n,i,j} = \frac{\mathbf{r}_{m,i,\mathrm{L}}^T \mathbf{r}_{n,j,\mathrm{L}}}{\|\mathbf{r}_{m,i}\| \, \|\mathbf{r}_{m,j}\|}. \tag{5.3}$$

where $\mathbf{r}_{m,i} = [r_{m,i}(0) \; r_{m,i}(1) \; \ldots \; r_{m,i}(N_{\mathrm{rep}}-1)]^T$ is the received signal over N_{rep} repetitions for the mth delay bin and ith link. In the absence of the person, let us assume that the effect of the timing jitter and variations due to the lock spot choice are white[3]. For these delay samples affected by the hardware impairments, $\rho_{m,n,i,i}$ will be around 0.1 for two highly correlated delay samples m and n when $\beta = 0.05$ is set, because of the ratio $\beta/0.5$ (i.e., β is divided by 0.5, because 0.5 will be obtained when the full band is considered). On the other hand, delay bins that are affected by a person, are not white because of the low-frequency variations due to the movement of people. Therefore, for two bins of the same link that are affected by the movement of the same person (e.g., the delay samples m and n are affected by the person), the value of $\rho_{m,n,i,i}$

[3]The delay samples become white if the effects of the timing jitter and variations due to the lock spot choice are uncorrelated at different transmission instants. For the timing jitter, pulse shifts are assumed to be uncorrelated in [100–102]. For the other effect, there is no result available as it is a hardware implementation issue, that was observed from our experimental equipment. In this part, our technique is formed based on the assumption that the delay bins are white.

will be considerably higher than 0.1, because these delay samples are not white anymore. This results from relatively high energies in the low-frequency signal parts of these bins.

Fig. 5.8 shows absolute correlation values normalized according to (5.3) for the same measurement cases shown in Fig. 5.6 and Fig. 5.7. When Fig. 5.6 is compared to Fig. 5.8(a), the diagonal values are no longer 1 because for the diagonal the low-frequency energy of each delay sample is divided by the total energy this time. Furthermore, the normalized absolute correlation values are mostly around 0.1 to 0.15 for the combinations of the delay samples corresponding to the direct-path signal or strong reflections. This is also aligned well with the expectations because these delay samples are highly correlated (i.e., for the combinations of these delay samples, correlation values were close to 1 in Fig. 5.6). On the other hand, for these highly correlated delay samples, the correlation values are usually higher than 0.1 and go up to around 0.2. This is because the delay samples (affected by hardware impairments such as timing jitter) are not completely white and also there is more energy in the low-frequency part of the signal because of these hardware effects. Fig. 5.8(b) shows that the normalized absolute correlation values between the delay samples of two different links are very low, mostly below 0.05. This result is similar to Fig. 5.7 and can be explained in the same way. Only the scale is different because of the different normalization.

Fig. 5.9 shows the normalized absolute correlation values when there is one person in the environment. Compared to Fig. 5.8(a), correlation values between the delay samples, affected by the person, are mostly higher than 0.2 and go up to 0.6. This is because there is more energy in the low-frequency region of these delay samples (because of the person's effect) compared to the delay samples only affected by hardware issues such as timing jitter. There is also an area of high correlations, because the person does not affect only a single delay sample but a number of delay samples. As introduced in Section 3.7.1, the pulse duration of around 1.4 ns corresponds to 23 samples for a sampling period of 61 ps. Therefore, there will be correlations to some extent for at least these 23 delay samples. Usually, there are regions of high correlation values that are much larger than 23 samples. This is because of the delay dispersion due to the person, as the human body does not behave as a point reflector and the signal reflects from different parts of the body.

Fig. 5.10 shows the normalized absolute correlation values between two different links when there is one person in the environment. The correlation values between the delay samples, which are affected by the person, are higher compared to Fig. 5.7: more than 0.2 and up to 0.6. With this way of calculating correlations, Fig. 5.9 and Fig. 5.10 show that the effect of the timing jitter and the lock spot choice do not show significant correlations compared to the bins affected by people.

Fig. 5.11 and Fig 5.12 show the normalized absolute correlation values when two persons are present in the environment. The correlation values are calculated according to (5.3), between the delay samples of the same link (in

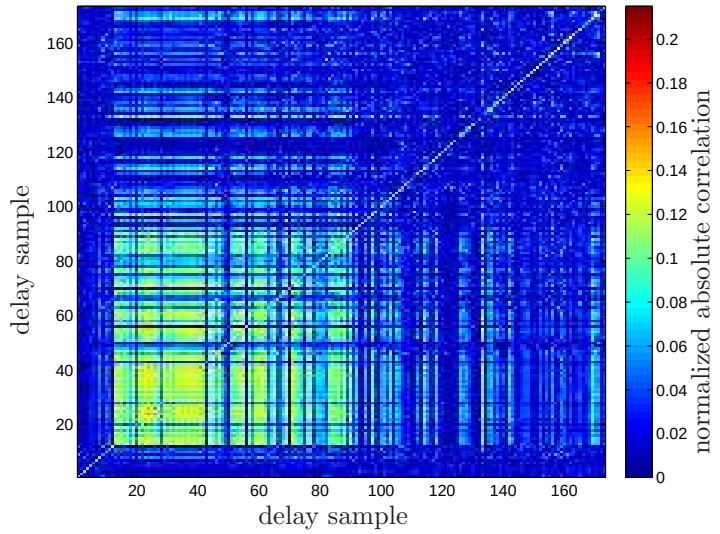

(a) Normalized absolute correlation values between the delay samples of a single link.

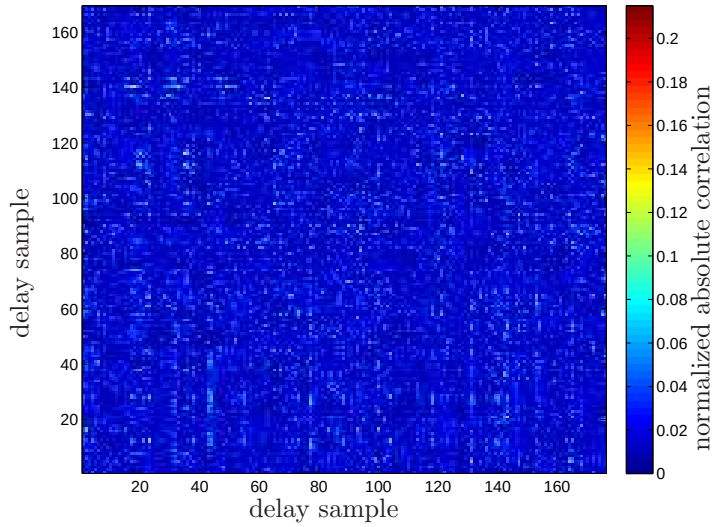

(b) Normalized absolute correlation values between the delay samples of two different links.

Figure 5.8: Normalized absolute correlation values when there is no person in the environment (for the same measurement scenarios as in Fig. 5.6 and Fig. 5.7) where the correlation values are calculated according to (5.3).

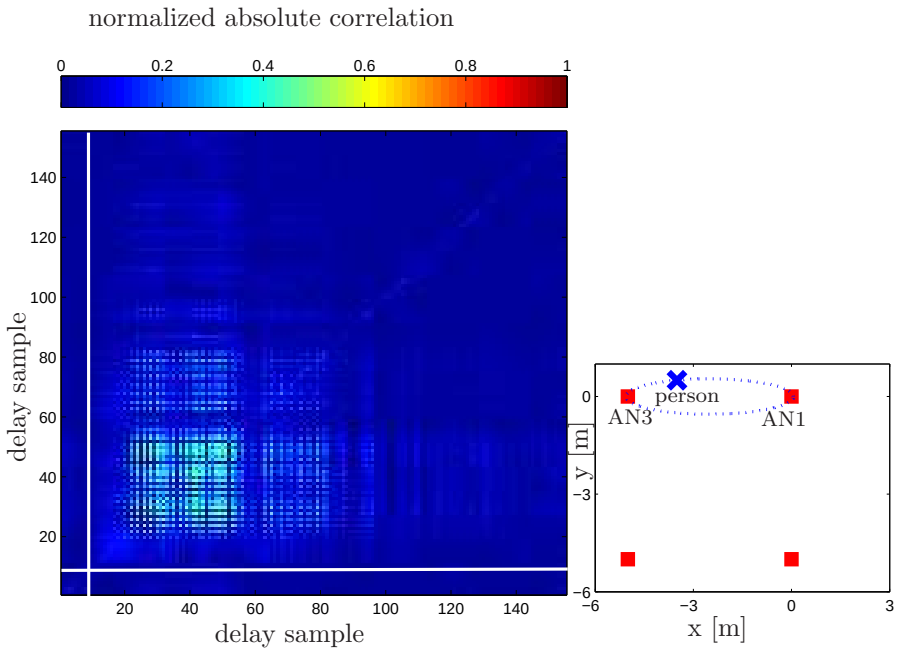

Figure 5.9: Normalized absolute correlation values between the delay samples of a single link when there is one person in the environment, where the correlation values are calculated according to (5.3). The solid white line shows the delay sample which corresponds to the true position of the person, shown in the figure on the right.

Fig. 5.11) and two different links (in Fig. 5.12). Fig. 5.11 shows high correlations for combinations of samples around the delay values that correspond to the positions of the persons. The correlation values between the delay samples corresponding to the position of the second person are higher compared to the delay samples corresponding to the position of the first person. This is because the random movements of different people may show different variations depending on for instance the breathing activity and the size of the persons. In this case, the random movement of the second person causes higher variations in the signal.

For the correlation between the delay samples of two different links, Fig. 5.12 reveals that the bins affected by the second person for both links, show high correlation values, whereas the delay samples influenced by the first person for Link AN2–AN3 and second person for Link AN3–AN4, show very low correlations. The correlation between the delay bins affected by the first person for both links, are lower compared to those affected by the second person. Furthermore, the delay bins, which are affected by the first person for Link AN3–AN4

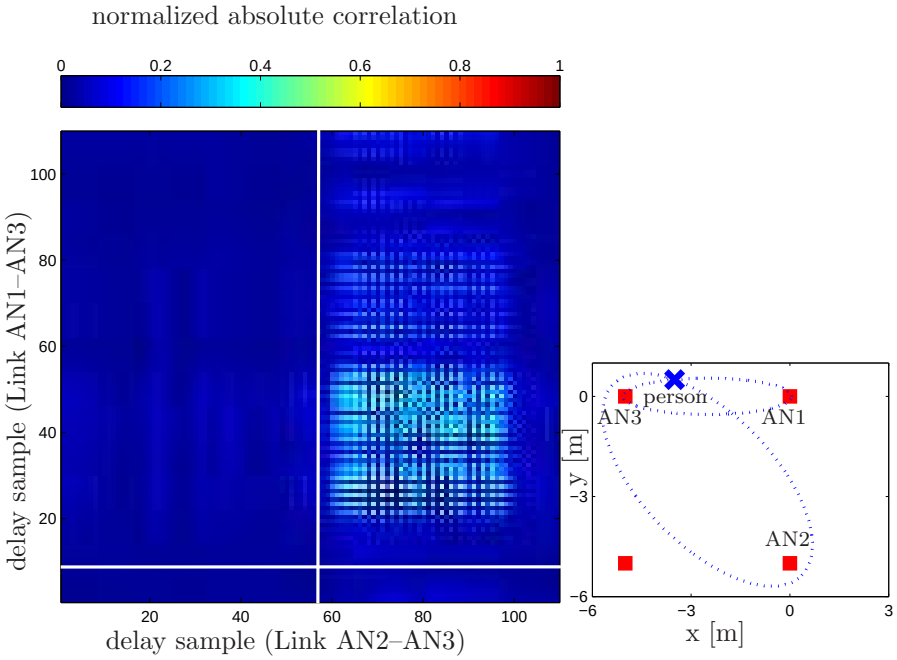

Figure 5.10: Normalized absolute correlation values between the delay samples of two different links when there is one person in the environment, where the correlation values are calculated according to (5.3). The solid white line shows the delay sample which corresponds to the true position of the person, shown in the figure on the right.

and the second person for Link AN2–AN3, show high correlations for some of those delay bins. In general, both of these results show that it is possible to distinguish multiple people with this correlation definition, but the threshold needs to be determined to decide if the bins are affected by the same person or not. More detailed analysis of the correlation between multiple links will be provided in Section 5.6.

Our observations show that, for the highly correlated bins, the values of the correlations are not all the same, and some bins might even show very low correlations with others (e.g., in Fig. 5.10 delay bins 21, 23, 25 and 36 show very low correlations with the neighboring bins). Therefore, the correlations over the number of delay samples are averaged as

$$R_{m,n,i,j} = \frac{1}{(T_\mathrm{p}W)^2} \sum_{m=m_0-T_{\mathrm{p}/2}W}^{m_0+T_{\mathrm{p}/2}W} \sum_{n=n_0-T_{\mathrm{p}/2}W}^{n_0+T_{\mathrm{p}/2}W} \rho_{m,n,i,j} \tag{5.4}$$

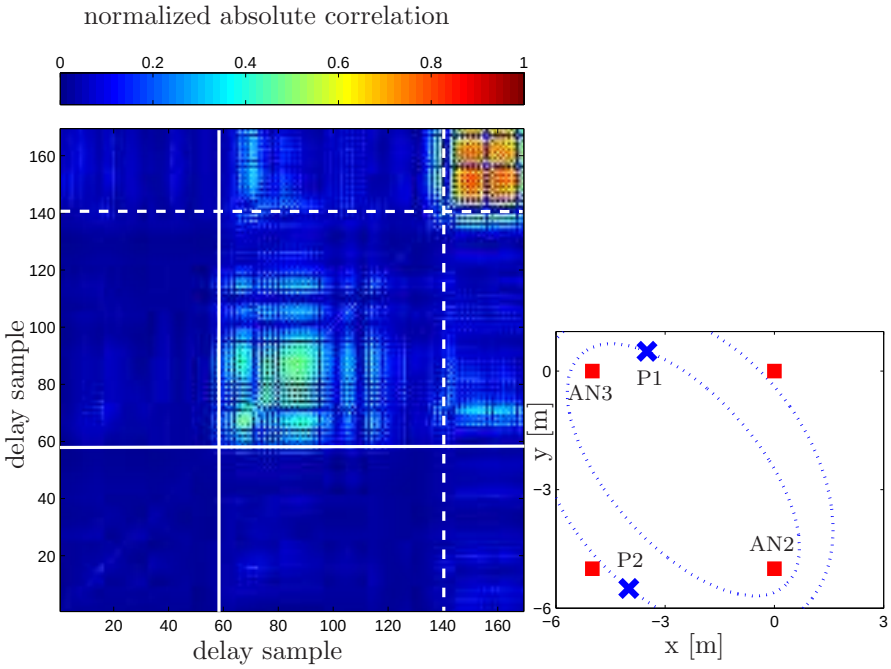

Figure 5.11: Normalized absolute correlation values between the delay samples of the same link. The solid and dashed white lines show the delay samples which correspond to the true position of the first and second persons, shown in the figure on the right as P1 and P2, respectively.

where both m_0 and n_0 are trial sample numbers, and $T_\mathrm{p}/2$ is assumed to be an integer multiple of $1/W$ (i.e., for our experimental setup, $T_\mathrm{p}W$ corresponds to 23 delay samples.). Similar to (3.13), the averaging over the pulse duration is considered, because the influence of the person will cause variations for delay bins over (at least) the pulse duration, and those delay bins will show high correlations. As discussed previously, the number of samples affected by the person might be larger than 23 and more samples can be averaged. However, the exact number of the delay samples affected by the person is not known in advance, and it may depend on factors such as the person's position relative to the transmitter and the receiver positions and the size of the person. In general, there is a tradeoff between the resolution and getting more information. Increasing the number of samples will lower the resolution while it may give more information in some cases.

In the following section, a suitable threshold for $R_{m,n,i,j}$ will be determined.

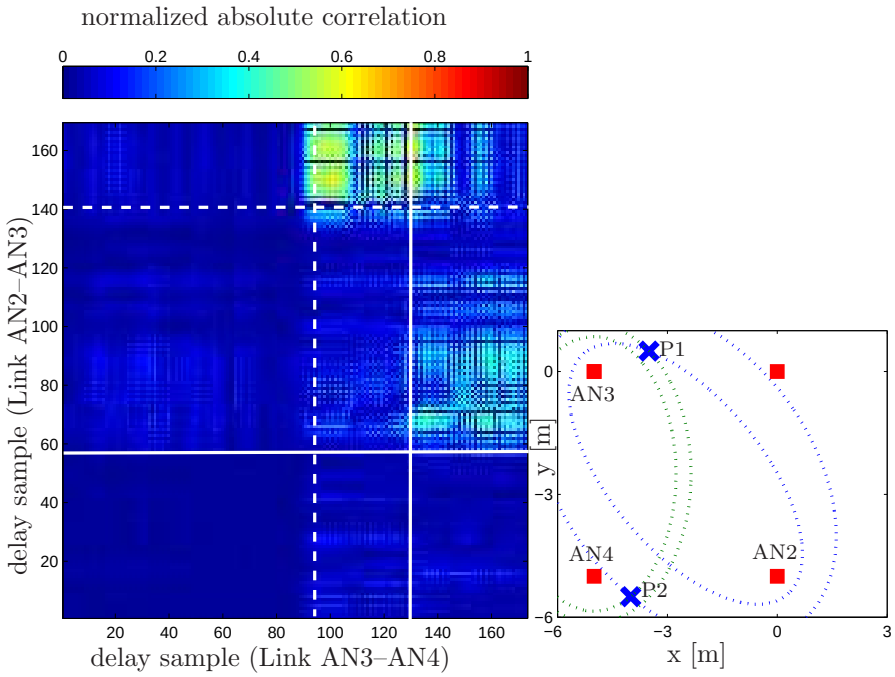

Figure 5.12: Normalized absolute correlation values between the delay samples of two different links. The solid and dashed white lines show the delay samples which correspond to the true position of the first and second persons, shown in the figure on the right as P1 and P2, respectively.

5.4.2 Threshold Analysis

There are two factors which influence the values of the correlation matrices. One of them consists of the timing jitter and the variations due to the lock spot choice. Both of these hardware issues will have an effect on the correlation values between the delay samples of the single-link measurements. The other factor is the random movement of the persons which will introduce some degree of correlation. In this section, the threshold selection will be discussed for the single-link and multiple-link correlations separately.

Correlations Between the Delay Samples of a Single Link

One way to determine the threshold for the single-link measurements is to choose the threshold higher than the maximum correlation value, calculated according to (5.4) and for the measurements when the person is not present in the environment. In this way, it can be found out up to what correlation

value is obtained due to the effect of the timing jitter and the lock spot choice. In Fig. 5.13, the empirical cumulative distribution function (CDF) is shown for the maximum correlation value (red solid line), obtained for each of the 72 single-link measurements where the person is not present. 40 of these measurements were collected in the environment described in Section 4.4.2, and the other 32 measurements were taken in the sport hall, described in Section 5.3. The 40 measurements were obtained from the single-person localization measurements, which consist of 24 different positions with six link measurements for each position. The person was standing outside the detectable region at ten different positions for the measurements between AN1 and AN2, AN1 and AN3, AN2 and AN4, and AN3 and AN4 (can be also seen from Fig. 4.2). Therefore, in total there are four AN combinations and ten measurements per AN combination. Besides that these measurements include 1000 snapshots per measurement. The 32 measurements consist of fourteen different AN combinations. Six of these AN combinations are as shown in Fig. 5.5. For the other eight combinations, the anchors were placed in the same environment and at each setting the distances between the anchors were 5 m. For these eight AN combinations, there were two measurement per AN combination. For the other six AN combinations, there were eleven measurements between AN1 and AN2, and five measurements for the other AN combinations. Furthermore, these measurements include 200 snapshots. Fig. 5.13 shows that almost all of the correlation values in these 72 measurements are below 0.12 (except one scenario in which the correlation value is 0.14).

Correlations Between the Delay Samples of Different Links

In Fig. 5.13, the empirical CDF for the maximum correlation value, obtained between the delay samples of different links and in the absence of the person, is also shown (black line). This result is shown for $1,217$ different link correlations. 457 of these combinations are obtained from part of the 32 measurements, mentioned in the previous section, and 760 of the combinations are obtained from the part of the 40 measurements which were obtained from the single-link localization measurements. The result shows that the maximum correlation values are mostly around 0.02 (where there is a sharp increase in CDF), and overall they rarely exceed 0.05. The values are mostly smaller than for the single-link case, since the effects of the timing jitter and the choice of the lock spot are uncorrelated for different measurements.

By computing the correlations between different links, it is also possible to find out up to what extent the random movements of two persons may have correlations. For this purpose, the maximum correlation values were calculated between the delay samples of different links when one person is present in the environment. The link measurements, described in Section 4.4.2, were used for this purpose. For these measurements, the movement of the person influences only one link measurement in a given time interval. Even though the measurements were performed with the same person, the links are affected

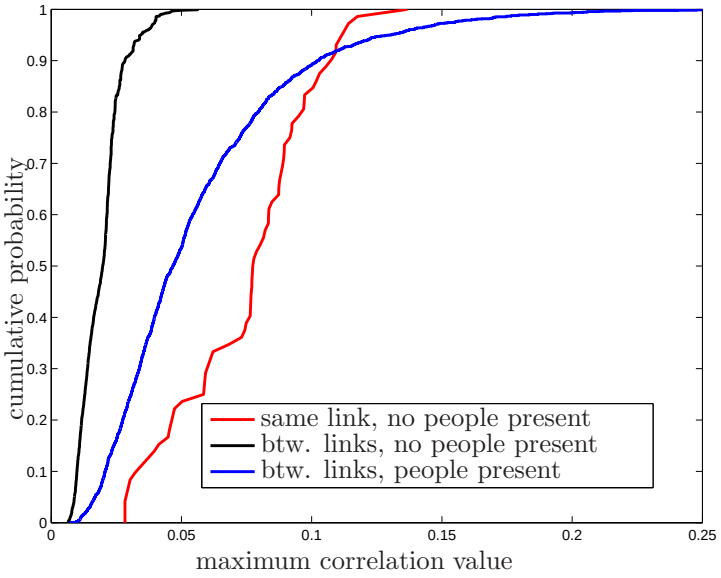

Figure 5.13: Empirical cumulative distribution function for the maximum correlation value obtained for the same link (red solid line) and between different links (black solid line) when there is no person in the environment, and between different links (blue solid line) when only a single person is present for each link measurement.

by the movement of the person in different time intervals. Hence, these results can be used to simulate the situation in which two persons affect two different links simultaneously. In this way, it is possible to exclude the other effects (e.g., timing jitter) and get a more specific understanding of correlations between the random movements, because the maximum correlation values will be obtained for the delay samples affected by the person and other effects are uncorrelated in different links. The empirical CDF is shown in Fig. 5.13 for $1,800$ measurements (blue line). These $1,800$ measurements are obtained from the single-person localization measurements, described in Section 4.4.2. Among these $1,800$ measurements, 144 of them are obtained from correlation between the links when the person was standing at the same position (e.g., one of the 24 positions). The other $1,656$ measurements are obtained from the correlations between links when the person was standing at different positions. This figure shows that the maximum correlation values are higher in the presence of a person compared to the case when no person is present (blue and black lines, respectively). The figure also shows that in around 85% of the cases, the correlation values are smaller than 0.1, and almost all values are lower than 0.25. When this result is compared to the cases when there is no person in the environment (red and black lines), it is observed that the correlations between

samples affected by the movement of different people are not really negligible and should be accounted for in the threshold choice.

5.5 Correlation Analysis for Single-Link Measurements

In this section, example results will be given first. After that a detection and ranging method based on single-link correlation analysis will be proposed. Then, the detection and ranging results will be presented.

5.5.1 Experimental Observations

Two example correlation matrices are plotted for a single link in Fig. 5.14 and Fig. 5.15. Fig. 5.14 shows that high correlation values are obtained around combinations of delay samples corresponding to the positions of the persons. Between the delay samples corresponding to different people, the correlation values are very low. This is because the random movement of these two persons do not show a significant correlation. The correlation values are below 0.1, which is also obtained in Fig. 5.13 for 80% of the measurement cases obtained between different links, and each affected by one person. Therefore, each person can be clearly distinguished in this case by appropriately setting the threshold. However, Fig. 5.15 shows another case, where the correlation values between the delay samples, corresponding to different persons, are also high. Specifically, the correlations between the delay samples 60 to 80 and 150 to 165 are around 0.2. This value is higher than the maximum value for the same link in the absence of the person, according to Fig. 5.13. This means that the hardware issues such as timing jitter are not a problem, because the maximum correlation value, obtained in these cases was 0.14. However the delay samples affected by the random movements of two different persons may also show very high correlations. This result shows that a threshold, defined based on the measurements where there is no person, is not always enough to distinguish between the presence of one or more persons. However, if the threshold is increased to a sufficient level, it might be possible to detect the second person. For instance, for the measurement result in Fig. 5.15, this means choosing the threshold higher than 0.2. However, the threshold should be lower than the maximum correlation values between the delay samples affected by each person (e.g., the correlations between the delay samples 60 to 100, and 150 to 165.). Otherwise, these correlations would also be below the threshold. In the next section, the effect of the threshold increase on the detection will be investigated for different threshold values, which are determined considering the result for the same link and no people present case in Fig. 5.13 (i.e., the threshold values will be chosen in the range starting from 0.12).

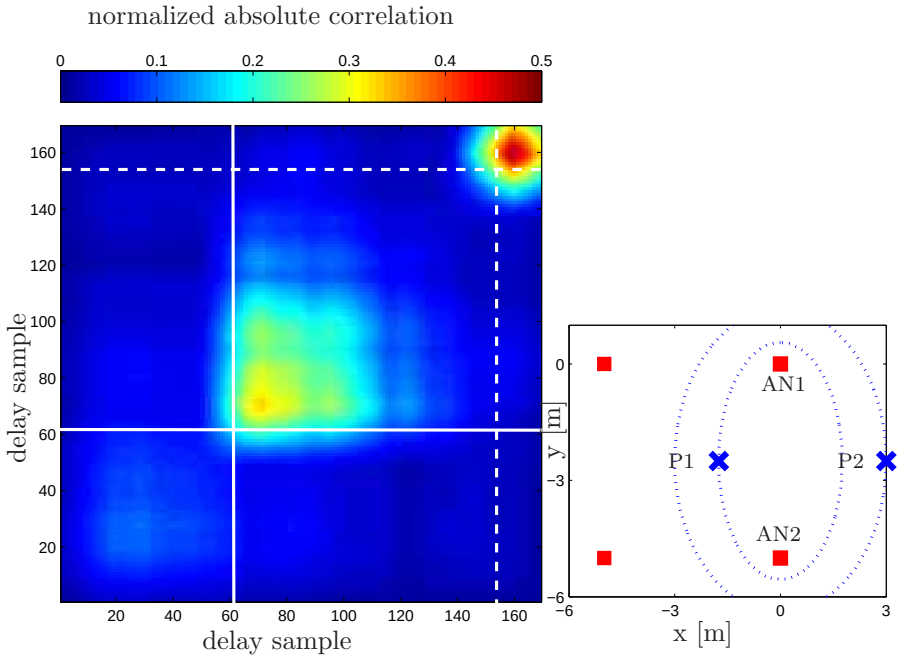

Figure 5.14: The correlation matrix, calculated according to (5.4) for a single link. The solid and dashed white lines show the delay samples which correspond to the true position of the first and second persons, shown in the figure on the right as P1 and P2, respectively.

5.5.2 Detection and Ranging Method

In this section, an automated way to detect the presence of the second person and estimate the bistatic ranges from a single-link correlation matrix will be discussed. In Fig. 5.16, we show the visualization of a correlation matrix in which the combinations of the delay samples whose correlations are above the correlation threshold are shown in red. Furthermore, the delay samples which are affected by a person is shown in yellow, i.e., the delay samples 1,2, 9 and 14 are not affected by any person. This example map, which can also be obtained as a measurement result, shows two islands with each consisting of group of delay samples affected by one person. In this example, the delay samples 3 to 8, and 10 to 13 are affected by two persons. Therefore, the normalized correlation values between the delay samples affected by the same person is above the threshold. Furthermore, the normalized correlation values between the delay samples in these two islands are below the threshold so that their colors are shown in yellow. The latter observation is necessary to conclude

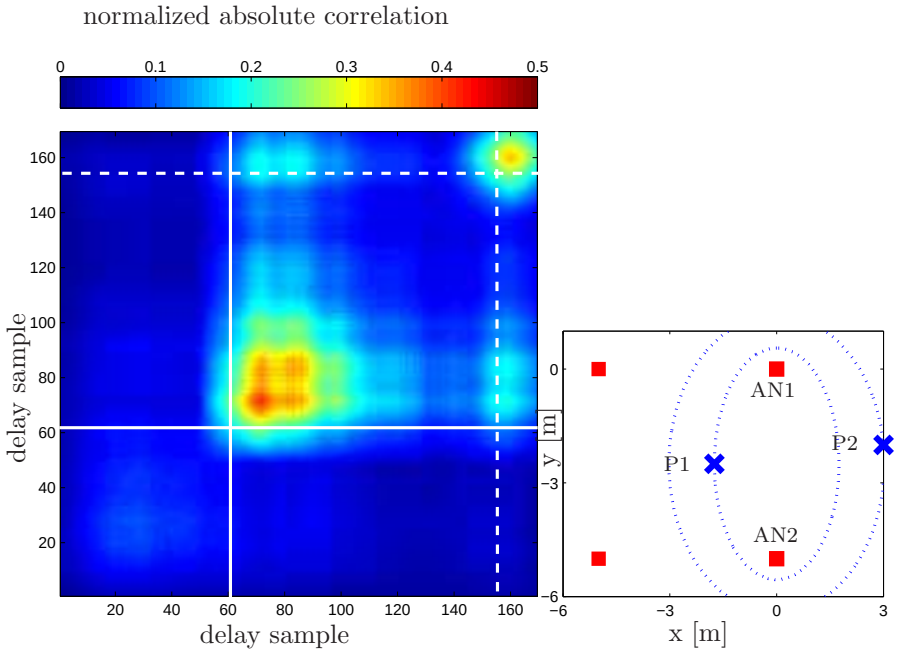

Figure 5.15: The correlation matrix, calculated according to (5.4) for a single link. The solid and dashed white lines show the delay samples which correspond to the true position of the first and second persons, shown in the figure on the right as P1 and P2, respectively.

that the group of delay samples between 10 and 13 are affected by a different person than the ones between 3 and 8. Given such a measurement result, the objective is to determine the number of islands (i.e., the number of people) and the delay samples (i.e., the bistatic range can be estimated.) in each island.

The detection and bistatic range estimation method comprises of three steps.

Step 1: Single person detection

In the first step the delay samples, which are affected by the persons can be determined. This step is performed by finding the delay samples that exceed the detection threshold for the single person, using the method developed in Chapter 3. According to the example in Fig. 5.16, after this step the delay samples 3, 4, 5, 6, 7, 8, 10, 11, 12 and 13 are known to be affected by one or more persons.

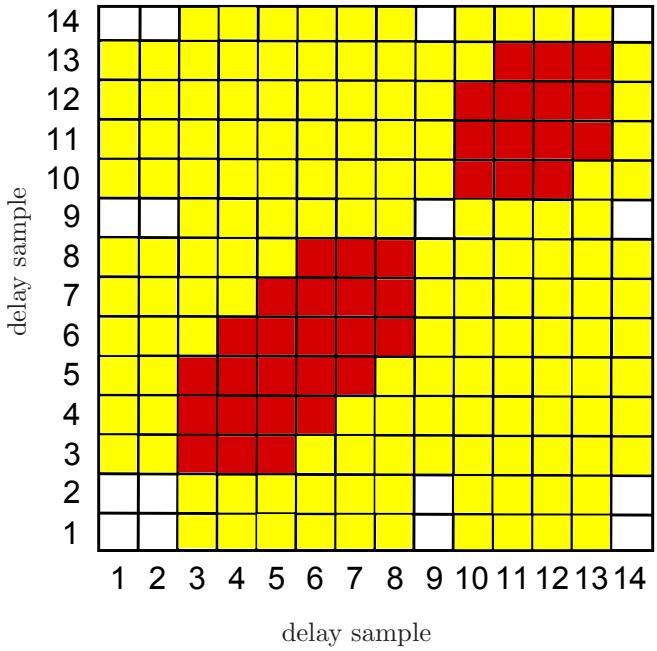

Figure 5.16: A visualization of the correlation matrix for a single link. The red color indicates that the correlation between these delay samples is above the threshold. The yellow color indicates the delay samples which are above the threshold for the person detection.

Step 2: Finding the delay bins whose pairwise correlation values are above the threshold

In the second step, the normalized correlation values between these delay bins are calculated according to (5.4), and compared with the correlation threshold. For each delay bin, we obtain a set whose elements consist of the indices of the delay bins with which the correlation value is over the threshold. According to the example in Fig. 5.16, each of these delay bins form the following sets after this step: $S_3 = \{3, 4, 5\}$, $S_4 = \{3, 4, 5, 6\}$, $S_5 = \{3, 4, 5, 6, 7\}$, $S_6 = \{3, 4, 5, 6, 7, 8\}$, $S_7 = \{5, 6, 7, 8\}$, $S_8 = \{6, 7, 8\}$, $S_{10} = \{10, 11, 12\}$, $S_{11} = \{10, 11, 12, 13\}$, $S_{12} = \{10, 11, 12, 13\}$, and $S_{13} = \{10, 11, 12, 13\}$.

Step 3: Finding the sets of delay samples which are affected by persons

In the final step, the intersections of these sets with each other are checked to find a minimum group of subsets whose intersection sets with at least one set in the same group is not an empty set (i.e., contains at least one element). In this way, we can determine the different islands such that the delay samples in each island do not have the normalized correlation value higher than the correlation

threshold with the delay samples of the other islands. The number of groups will determine the number of people, and the delay bins, corresponding to each set in the same group, will determine the bins affected by the same person. Following the example in Fig. 5.16, the sets which have at least one element in their intersection with S_3 can be found as follows. $S_3 \bigcap S_4 = \{3,4,5\}$, $S_3 \bigcap S_5 = \{3,4,5\}$, $S_3 \bigcap S_6 = \{3,4,5\}$, $S_3 \bigcap S_7 = \{5\}$. In a similar way, S_4 has intersections with S_3, S_5, S_6, S_7, S_8, and S_5 with S_3, S_4, S_6, S_7, S_9, and S_6 with S_3, S_4, S_5, S_7, S_8, and S_7 with S_3, S_4, S_5, S_6, S_8, and S_8 with S_4, S_5, S_6, S_7. Therefore, an island with the delay bins $G_1 = \{3,4,5,6,7,8\}$ can be formed. In this way, the combinations of the bins whose correlations are below the threshold, can be also in the same island. For instance, the delay bin 3 has no correlation with 8 and they do not have bins, with which they have correlations above the threshold, in common. The method is chosen in this way because the islands do not have a known shape. For instance, in Fig. 5.14 and Fig. 5.15, the normalized correlation values between the bins 60 to 100 and 140 to 165 show different shapes when for instance the threshold is set to 0.14. Therefore, correlation matrices such as depicted in Fig. 5.16 are commonly obtained in practical cases. Similar to G_1, another island can be obtained as $G_2 = \{10,11,12,13\}$. The bistatic range for each person can be found by considering the arrival delay of the first delay bin of each island, in a similar way to the Threshold Crossing approach, described in Section 4.3.

The downside of this approach is that when the ellipses, corresponding to the positions of the persons, are too close each other, this approach will not be able detect the second person. On the other hand, this method gives a way to automate extracting the information related to the second person (e.g., the presence and bistatic range estimation) from the correlation matrix.

5.5.3 Detection and Ranging Results

The detection and ranging results are provided for the measurement scenarios given in Table 5.1 (visualized in Fig. 5.4). The detection performance results for the second person for different threshold values are tabulated in Table 5.4. The detection rate shows the number of cases where the presence of the second person is detected divided by the number of all cases (i.e., in all these cases the first person is detected.). It is started with the threshold value of 0.12, as it is just higher than most correlation values measured when there is no person in the environment (see Fig. 5.13 red line). The results show that the detection rate initially increases for increasing threshold, up to a certain level, which is 0.22 for our measurements. This is resulted from the reason that the normalized correlation values between the delay samples affected by different persons can be higher than the threshold determined from the maximum correlation values and obtained in the absence of the person. For instance, the second person is detected in eight cases, when the threshold is 0.12. However, when the threshold is set to 0.22, in sixteen cases the second person is detected. For the threshold values above 0.22, the detection rate starts to decrease as the

algorithm is unable to detect the second person, because the correlation values between the delay samples corresponding to the second person are below the threshold. The results also show that a third person might be falsely detected when the threshold is too high. This is because, as the threshold is increased, combinations of some of the delay samples, which are among the correlated bin group for the same person, stay below the correlation threshold. In some scenarios, these delay samples lie in the middle and an another island is formed. In order to explain it in more detail, a possible case is illustrated in an example map in Fig. 5.17. This figure is redrawn from the earlier example map, given in Fig. 5.16, considering a higher correlation threshold. As the threshold is increased, another island is formed between the delay samples 6 and 8. Even though the delay samples between 3 and 8 are affected by the same person, the delay samples between 6 and 8 are having normalized correlation values lower than the threshold with the delay samples 3 to 5. This can happen in practice because the correlation values within an island are not all the same and commonly they get lower around the edges of the island.

In Table 5.5, the true bistatic range and the estimated error are given for each person. The results are shown for a threshold value of 0.2. By single correlation matrices, it is not possible to determine which group of delay bins corresponds to each person. Therefore, using the knowledge of actual positions of the person, the group of delay bins and corresponding person are matched

Table 5.4: Threshold vs. the detection rate for the second person.

Threshold	**Detection rate**	**Observations**
0.12	8/18	For the remaining ten cases, the correlation values between the delay samples corresponding to different people are above the threshold.
0.14	8/18	
0.16	11/18	As the threshold increases the second person is detected in three additional cases.
0.18	13/18	
0.20	15/18	
0.22	16/18	While the second person can be detected in an additional case, the algorithm falsely detects a third person in an another case.
0.24	15/18	For this threshold, no more than one person is detectable for the case where a third person was detected by mistake. In an another case, a third person was detected again by mistake.
0.26	13/18	No third person is detected by mistake.
0.28	13/18	
0.30	11/18	In two cases, a third person is detected by mistake.

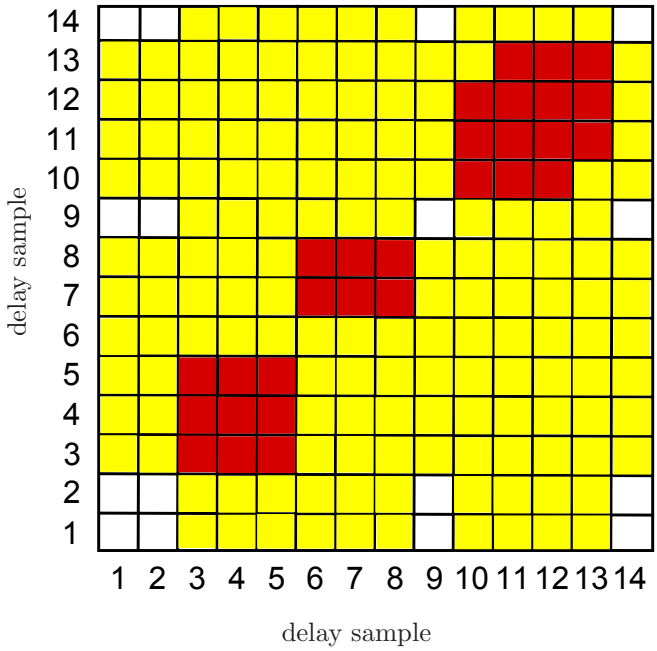

Figure 5.17: A visualization of the correlation matrix for a single link. The red color indicates that the correlation between these delay samples is above the threshold. The yellow color indicates the delay samples which are above the threshold for the person detection.

after the algorithm finds the relevant bins for each person. In this way, it is possible to provide the device-free ranging results from the knowledge of the true bistatic range of each person. Overall, absolute bistatic range errors lower than 0.25 are obtained. The rms error over 18 and 15 measurements for the first and second person are obtained as 0.09 m and 0.15 m, respectively. In most of these cases, the bistatic range has negative values. This is because of the reason that the body has certain width and the reflection point can be different than the center of the body which is considered as the position of the person.

5.6 Correlation Analysis for Multiple-Link Measurements

In this section, the experimental results for the correlation between multiple link measurements will be provided. The results will be discussed in two cases that can be applied to any pair of links:

Table 5.5: Experimental results for device-free ranging of each person.

Position	True range [m]		Error [m]	
	1st person	2nd person	1st person	2nd person
1	1.12	2.97	−0.16	−0.14
2	1.12	2.90	−0.04	no detection
3	1.12	2.85	−0.11	−0.07
4	1.12	2.83	−0.05	−0.14
5	1.12	2.82	−0.02	−0.13
6	1.12	2.83	−0.05	−0.14
7	1.12	2.85	−0.04	−0.11
8	1.12	2.90	−0.05	−0.14
9	1.12	2.97	0.00	−0.14
10	2.97	1.12	−0.11	−0.16
11	2.90	1.12	−0.07	−0.05
12	2.85	1.12	−0.09	no detection
13	2.83	1.12	−0.16	−0.25
14	2.82	1.12	−0.15	no detection
15	2.83	1.12	−0.13	−0.17
16	2.85	1.12	0.05	−0.18
17	2.90	1.12	0.09	−0.17
18	2.97	1.12	0.05	−0.14

1. One of the persons affects one of the links and the other person affects the other link.

2. At least one of the two links is influenced by both persons,

These two cases determined by the limited bistatic range of the links. For each case, example results supporting our method will be provided with other results which address the challenge of multiple person detection with this method. Example results are chosen from the localization measurements described in Section 5.3. The results will be shown in a similar way to Section 5.5.1, however the correlations between different links will be presented in this section.

5.6.1 Each link affected by different persons

When both links are affected by only one person and if those persons are different, then low correlations will occur, depending on the movement of the person. Two example results are plotted in Fig. 5.18 and Fig. 5.19. Both results show the same scenario such that same positions are chosen for two persons but the persons stood at each measurement was different (i.e., first person (P1) took the second person's (P2) position and vice versa.). In Fig. 5.18, all the correlation values lie between 0 and 0.07. On the other hand, Fig. 5.19 shows relatively high correlations around the samples 30 to 40 for both links. The correlation values among these delay samples get larger than 0.1. Here each person stands in between the link, blocking the LOS.

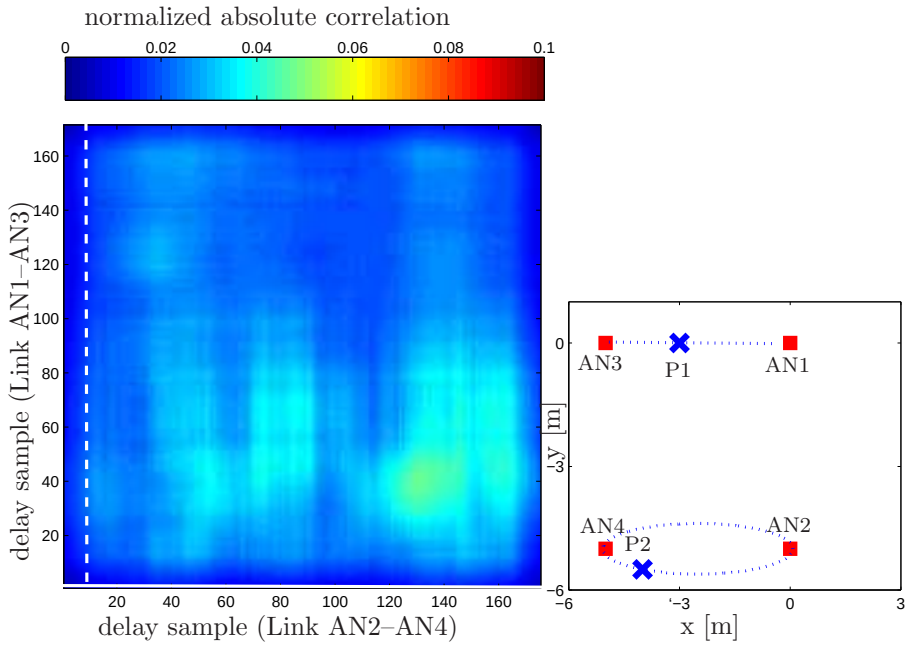

Figure 5.18: Example of a measured normalized absolute correlation between the delay samples of two different links. The solid (zero delay) and dashed white lines show the delay samples which correspond to the true position of the first and second persons, shown in the figure on the right as P1 and P2, respectively.

5.6.2 Both links affected by the same person

In this section, the cases when at least one of the two links is influenced by both persons are investigated. This section is further divided into two parts.

Case I: One Link Affected by One Person, While the Other Link is Affected by Both Persons

In this case, the correlation between multiple links is investigated when one of the links is affected by both persons and the other link is affected by only one of these two persons.

For the measurements presented in Fig. 5.20, Person 1 stands in between the antennas of AN1 and AN3, blocking the LOS between these two antennas. For this link, Person 2 stands outside the detectable region because of the delay window limitations of the radios. Person 1 also affects the link between AN2 and AN3 together with Person 2. According to this observation, high correlation values are obtained between the delay samples around the ones

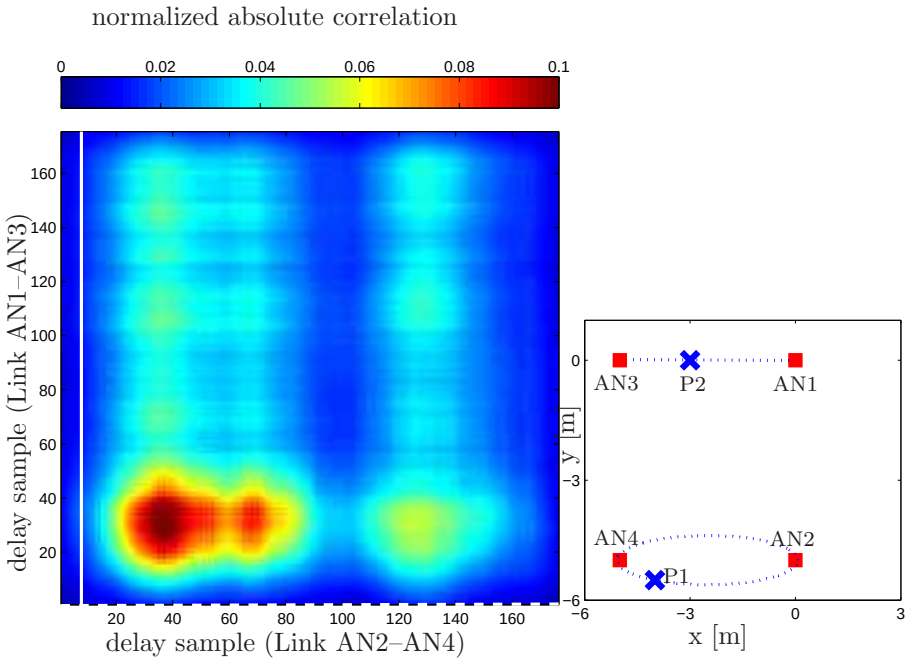

Figure 5.19: Example of a measured normalized absolute correlation between the delay samples of two different links. The solid and dashed (zero delay) white lines show the delay samples which correspond to the true position of the first and second persons, shown in the figure on the right as P1 and P2, respectively.

corresponding to the position of Person 1. On the other hand, the delay samples around ones corresponding to the position of Person 2 for the link between AN2 and AN3 show low correlations with the delay samples of the link between AN1 and AN3. This figure shows a clear result for high correlation between the delay samples of two different links affected by the same person, and low correlation when they are affected by two different persons.

On the other hand, the movement of two persons might occasionally show correlations as shown in Fig. 5.21 and Fig. 5.22. Fig. 5.21 shows that the delay samples corresponding to Person 1 for the link between AN1 and AN3 also shows correlations with the delay samples corresponding to Person 2 of the link between AN1 and AN4. Here, the maximum correlation value for the corresponding delay samples of Person 1 (between 20 to 80 for the link between AN1 and AN3, and 120 to 160 for the link between AN1 and AN4) is around 0.15 which is slightly higher than the correlation between the delay samples of Person 1 (for the link between AN1 and AN3) and Person 2 (for the link between AN1 and AN4). The latter correlation value is around 0.12. This

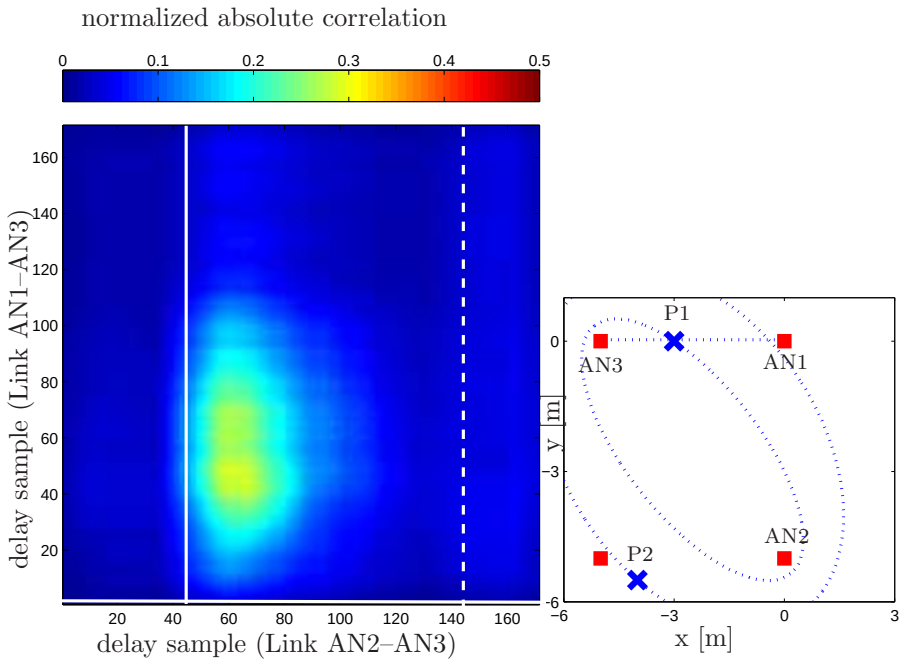

Figure 5.20: Example of a measured normalized absolute correlation between the delay samples of two different links. The solid and dashed white lines show the delay samples which correspond to the true position of the first and second persons, shown in the figure on the right as P1 and P2, respectively.

result shows that the correlation values between the delay samples for different people may occasionally be comparable to the cases when they are affected by the same person. In Fig. 5.22, the correlation values between the delay samples affected by the Person 2 (140 to 160 for the link between AN1 and AN4, and 15 to 80 for the link between AN1 and AN3) are around 0.23. This figure also shows three other regions where the correlations between the combinations of the delay samples are higher than 0.1. These are between the delay samples 25 to 40 (Link AN1–AN3) and 60 to 80 (Link AN1–AN4), 120 to 140 (Link AN1–AN3) and 60 to 80 (Link AN1–AN4), and 120 to 130 (Link AN1–AN3) and 150 to 160. This is because the delay samples corresponding to Person 1 in the link between AN1 and AN4 show correlations with the delay samples corresponding to Person 2 in the link between AN1 and AN3. Furthermore, different from the Fig. 5.21, Person 2 influences the link between AN1 and AN3 in such a way that indirect reflections occur. The delay samples which are affected by these indirect reflections also show correlations with the delay samples which are affected by Person 1 and Person 2 in the link between AN1

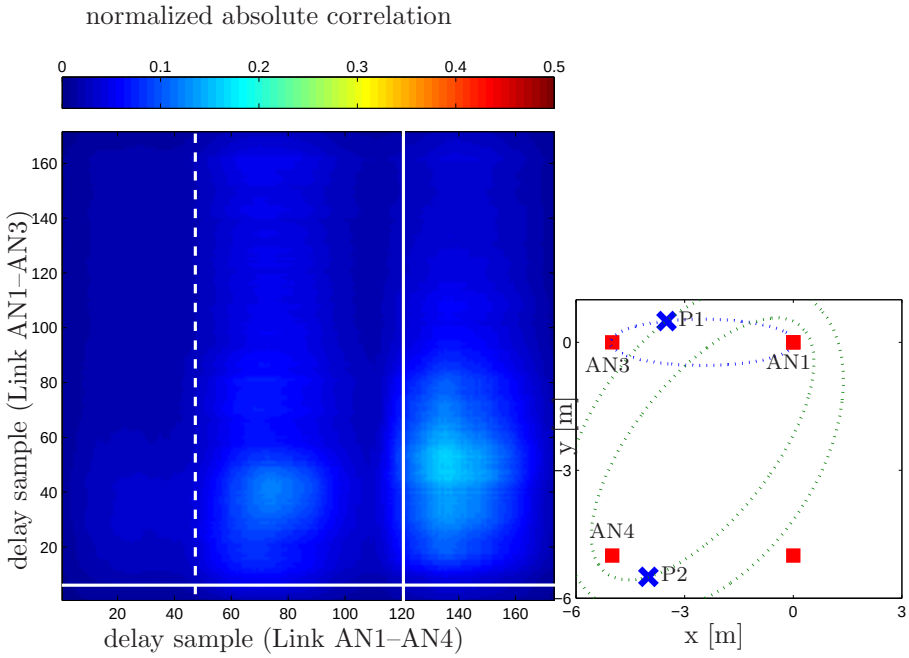

Figure 5.21: Example of a measured normalized absolute correlation between the delay samples of two different links. The solid and dashed white lines show the delay samples which correspond to the true position of the first and second persons, shown in the figure on the right as P1 and P2, respectively.

and AN4. Considering Fig. 5.21 and Fig. 5.22, the correlations between the delay samples corresponding to Person 1 and Person 2 can be avoided by increasing the threshold. However, by increasing the threshold too much, it may not be possible to detect the correlation between the delay samples which are affected by the same person. This can be especially seen in Fig. 5.21, where the correlation values between the delay samples affected by the same person and the correlation values between the delay samples affected by different persons are quite close (their maximum values are 0.12 and 0.15, respectively). Considering this trade-off and based on the experimental results we obtained, this threshold was chosen as 0.1 for the rest of this chapter. In general, according to the earlier analysis shown in Fig. 5.13, the maximum correlation values between the delay samples corresponding to different persons are less than 0.1 in 90% of the cases.

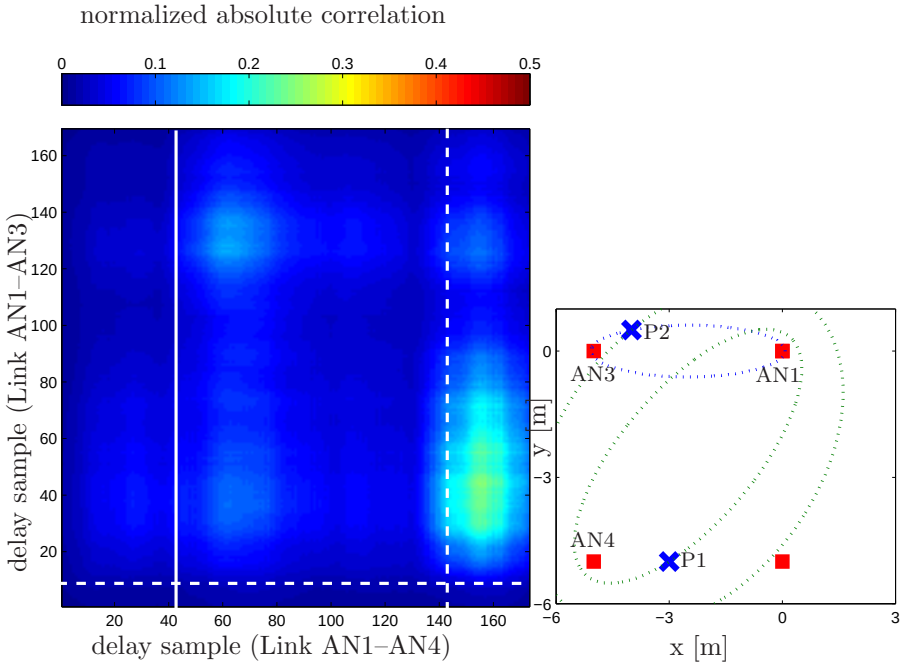

Figure 5.22: Example of a measured normalized absolute correlation between the delay samples of two different links. The solid and dashed white lines show the delay samples which correspond to the true position of the first and second persons, shown in the figure on the right as P1 and P2, respectively.

Case II: Both Links Affected by Both Persons

In this section, the correlation between multiple links is investigated for the case when both links are affected by both persons. Similar to the previous section, example results will be provided to explain our general observations based on the experiments. These results will be provided to demonstrate that the correlations that are generally obtained between the delay samples of two different links, which are affected by two persons. The results will be investigated for the cases when the difference between the actual bistatic ranges of each person is low for one link and high for the other link. When this difference is low, the delay samples that are affected by each person is very close to each other and it is even more likely that both persons affect the same delay samples. Furthermore, the results will be also investigated for the cases when this difference is low and high for both links.

Fig. 5.23 shows the result when the true bistatic ranges of the two persons are close for only one of the links. As seen in this figure, the corresponding

delay samples for the positions of Person 1 and Person 2 are 73 and 42 for the link between AN1 and AN4, respectively. This gives 31 delay samples of difference. For the link between AN2 and AN3, the difference between corresponding delay samples is 100. The same figure also shows that the delay samples corresponding to Person 2 of the link between AN1 and AN4 (delay sample 42 to 70), and to Person 1 of the link between AN2 and AN3 (delay sample 42 to 80) have low correlations. On the other hand, the delay samples corresponding to Person 1 of the link between AN1 and AN4 (delay sample 72 to 110) and to Person 2 of the link between AN2 and AN3 (delay sample 140 to 165) have relatively high correlations. This is because the two persons are close to each other (in bistatic ranges) so that Person 2 also affects some of the delay samples corresponding to the position of Person 1 for the link between AN1 and AN4. The same figure also shows that the later delay samples of the link between AN1 and AN4, which are influenced by Person 1 (delay sample 100 to 120), have low correlation values with the delay samples corresponding to Person 2 in the link between AN2 and AN3 (delay sample 140 to 165). This shows that the influence of Person 2 on the delay samples corresponding to Person 1 for the link between AN1 and AN4 is limited (i.e., some of these bins affected by Person 1 are not also influenced by the later-arriving reflections introduced by Person 2.).

Fig. 5.24 shows a similar case where the bistatic ranges of both persons are close to each other for both links. Similar to the previous results, the correlation between the delay samples corresponding to the same person is high. However, there is only one region in the figure with high correlations. This is because both persons are close to each other in bistatic range. Nevertheless, it could still be possible to detect the second person because the part of the delay samples corresponding to Person 1 in the link between AN1 and AN4 (delay sample 90 to 120), and to Person 2 in the link between AN3 and AN4 (delay sample 85 to 120) show low correlations. This is also the case for the other way around such that between the delay samples affected by Person 2 in the link between AN1 and AN4, and Person 1 in the link between AN3 and AN4.

In Fig. 5.25, the delay samples corresponding to the positions of Person 1 and Person 2 show relatively high correlations. This can be clearly observed for the samples affected by Person 1 for the link between AN2 and AN3 and by Person 2 for the link between AN1 and AN4. The correlation matrix shows four regions with higher correlations. In Fig. 5.26, all of the delay samples corresponding to Person 1 in the link between AN2 and AN3 (delay sample 40 to 80), and to Person 2 in the link between AN3 and AN4 (delay sample 80 to 120) have low correlations. This suggests that the correlation between the random movement of two persons are low in this case. On the other hand, the same figure also shows that there is relatively high correlation between the delay samples 140 to 165 and 120 to 165 in the links between AN2 and AN3, and AN3 and AN4, respectively. These delay samples are expected to be affected by different persons, considering the delay samples corresponding to the position of each person. The reason of this observation might be that the

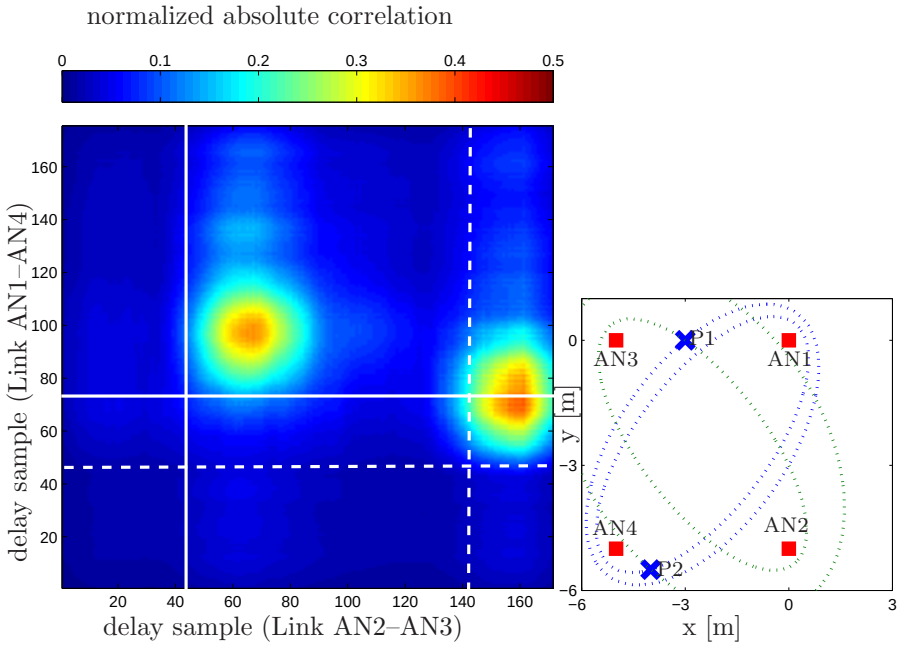

Figure 5.23: Example of a measured normalized absolute correlation between the delay samples of two different links. The solid and dashed white lines show the delay samples which correspond to the true position of the first and second persons, shown in the figure on the right as P1 and P2, respectively.

signals reflected off Person 1 may also interact with Person 2 before arriving to AN4. This interaction may introduce additional correlation between the delay samples corresponding to different persons.

5.7 Localization Algorithm

In this section, an algorithm for the localization of more than one person is developed. The main idea of this algorithm is to combine the correlations between the delay samples of single and multiple links to detect the people and find the bistatic range estimates for each person in each link. As results showed in Section 5.5.3, it is possible to detect the second person and estimate the bistatic range based on the single-link correlation analysis. However, it is not enough for localization as we also need to know which persons are affecting each link. Multiple-link correlation analysis is also employed to find the links and the delay samples in these links which are affected by the same person. This analysis is performed for many link combinations and the delay samples

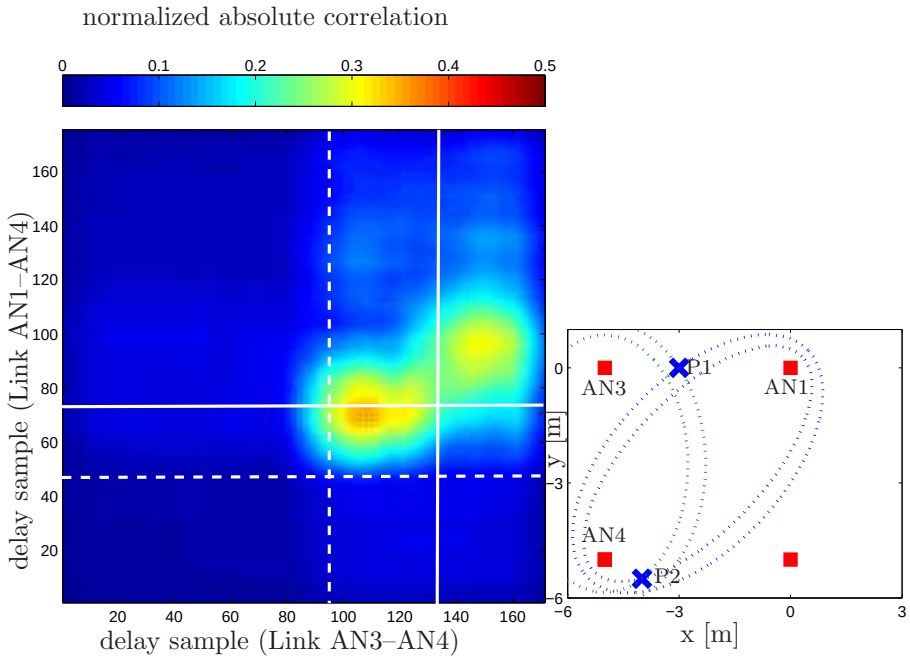

Figure 5.24: Example of a measured normalized absolute correlation between the delay samples of two different links. The solid and dashed white lines show the delay samples which correspond to the true position of the first and second persons, shown in the figure on the right as P1 and P2, respectively.

and the links for each person is determined. In general, five steps are followed as shown in Fig. 5.27. These five steps will be discussed in detail.

Step 1: Single person detection

This step is accomplished exactly in the same way as described in Chapter 3. With this step, it is decided whether the link is affected by any person. The following steps are performed for the links in which a person is detected.

Step 2: Single-link correlation analysis

This step is performed based on the algorithm that is developed for the detection of the second person using the single-link correlation matrix and described in Section 5.5.2. The threshold for the correlation is chosen as 0.2, as this value gives the highest detection rate without any false detection of the third person. The output of this step is the link index with the affected bin intervals for each person.

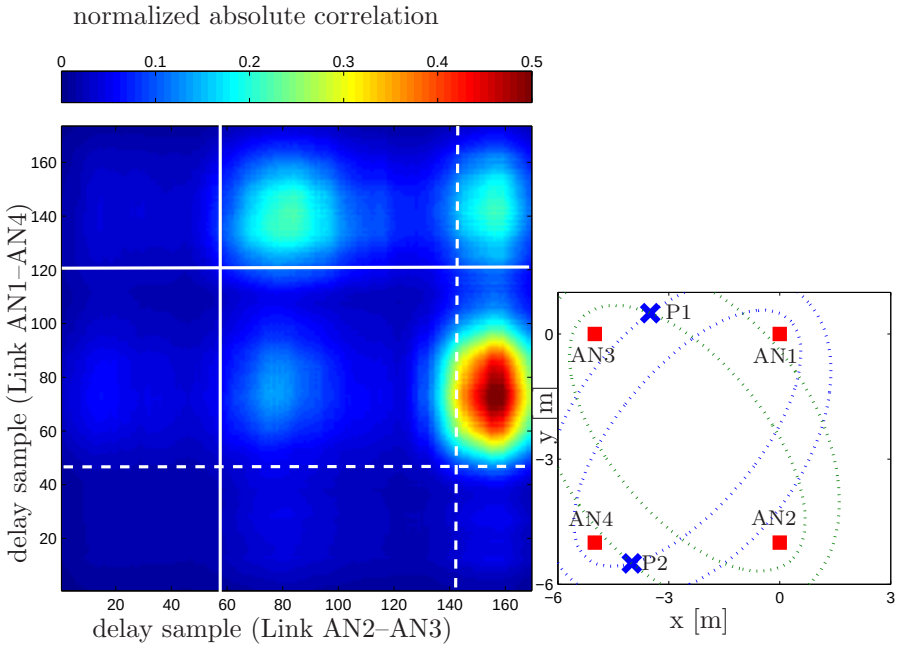

Figure 5.25: Example of a measured normalized absolute correlation for the delay samples between multiple links. The solid and dashed white lines show the delay samples which correspond to the true position of the first and second persons, shown in the figure on the right as P1 and P2, respectively.

Step 3: Multiple-link correlation analysis

In this step, the bins affected by the same person in both Link i and Link j are found (i.e., i, j is the all possible link combinations after Step 1 and Step 2 where $i \neq j$). The input to this step is the affected bin intervals of Link i and Link j, which are determined from the single-link correlation analysis.

First the correlations between the bins of Link i and Link j are computed, and they are compared with a threshold. Here, the goal is to find that whether the bin intervals of Link j are corresponding to the same person for each of the bin intervals of Link i. For instance, for a link there might be a single bin interval which is an isolated interval of bins having correlation with bins in the other link crossing the threshold. It is also possible that there are two isolated bin intervals which mean that there are two isolated interval of bins having correlation with bins in the other link crossing the threshold. The threshold is set to 0.1, considering the trade-off mentioned in Section 5.6.1. At the end of this operation, the following cases are possible.

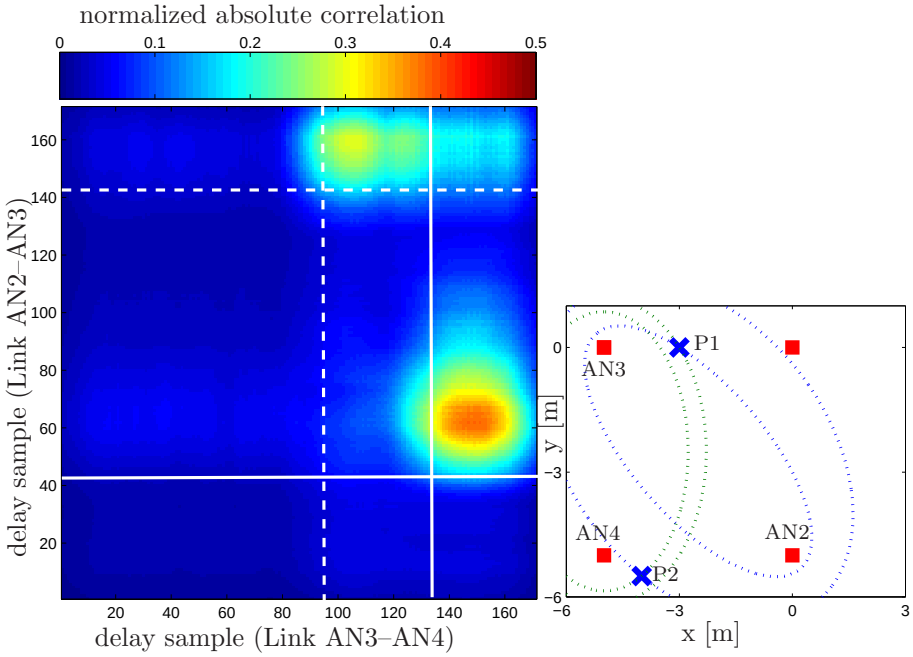

Figure 5.26: Example of a measured normalized absolute correlation between the delay samples of two different links. The solid and dashed white lines show the delay samples which correspond to the true position of the first and second persons, shown in the figure on the right as P1 and P2, respectively.

1. The correlations between all bins of Link i and Link j are below the threshold. In this case, both links are affected by a different person.

2. Both Link i and Link j have single bin intervals, corresponding to the same person.

3. Link i has two bin intervals while Link j has a single bin interval. In this case, it is considered that Link j has two persons who are affecting the same bin interval of Link i. This also means that the bi-static ranges of these people are the same for Link i. The same case also holds when Link j has two bin intervals and Link i has a single bin interval.

4. Both Link i and Link j are affected by two different bin intervals. This means that both links are affected by two different persons with found bin intervals.

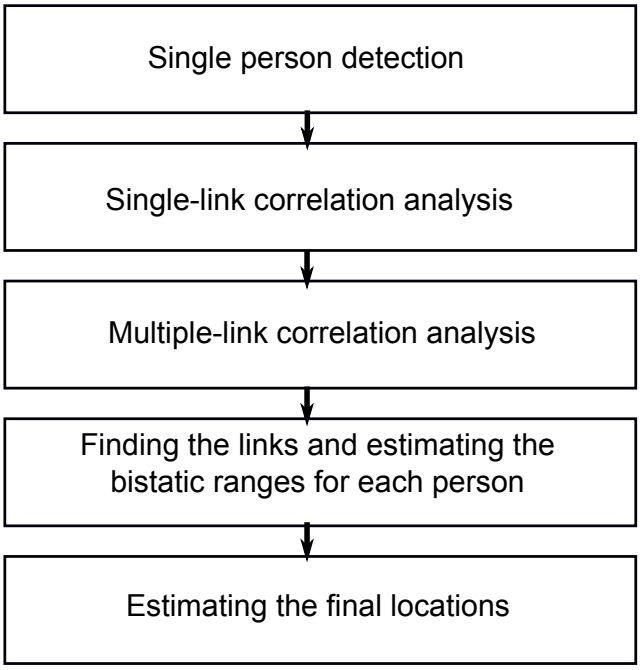

Figure 5.27: Block diagram of the localization algorithm steps.

Step 4: Finding the links and estimating the bistatic ranges for each person

Multiple-link correlation analysis only shows the delay samples affected by the same person for two links. However, it is needed to determine all the links and the delay samples for each person. In this step, a search method is developed to find the corresponding links and bin intervals for each person. In order to explain this step, an example case is drawn in Fig. 5.28. In this drawing, the circles denote the links (L1 to L4), while the lines denote the effect of a person on two connecting links with the symbols (i.e., a, b, c, d, e, f) to indicate the affected bin intervals. For instance, both L1 and L2 are affected in two different bin intervals. For the bin interval d in L1, the corresponding bin interval is e in L2, while for the bin interval a in L1, the corresponding bin interval is b in L2.

The algorithm starts from d of L1 and finds the corresponding bin interval in L2. Then, it continues with e of L2 and finds the corresponding bin interval in L3. As there is no other link corresponding to f of L3, the algorithm finishes the search for the first person. After that, it continues with a of L1 to find the other person and repeat the same procedure until there are no links and bin intervals left. The algorithm always starts from the earliest bin interval of the first link and continues with the neighboring links.

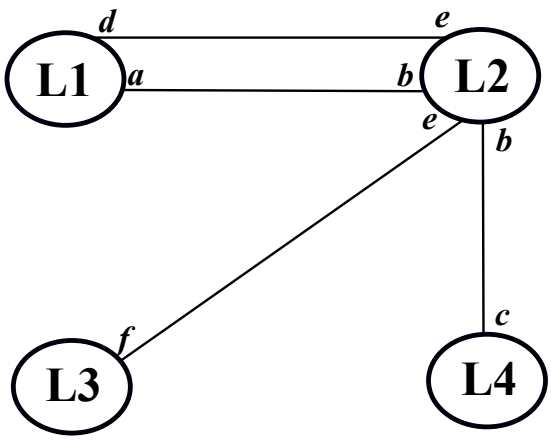

Figure 5.28: A drawing to illustrate an example case to find the links for each person.

The bistatic ranges of each person are estimated as the first sample in the bin interval that yields a correlation value which crosses the threshold. This is similar to the Threshold Crossing method that was proposed in Chapter 4, as it involves the earliest delay sample among all the delay samples affected by the person.

Step 5: Estimating the final locations

Given the bistatic ranges and the known positions of the anchor nodes, the location of each person is estimated according to (4.3).

5.8 Localization Results

In Fig. 5.29 and Fig. 5.30, the localization results are shown for the measurement positions tabulated in Table 5.3. The anchor positions are shown as red squares, the positions of the first and second person are shown as blue and purple crosses and the location estimates are shown as black circles. A dashed line between the true positions and the estimates is drawn by finding the nearest estimate for each person's position. The dashed line is not drawn for the measurements with a single location estimate (i.e., measurement scenarios 1, 4, 15, 16, 17.), and when there is an ambiguity to find the corresponding person for an estimate (e.g., measurement scenario 5, where one of the estimates has a smaller distances than the other estimate has towards each person.). For the rest of the measurements, the localization error for each person is tabulated in Table 5.6.

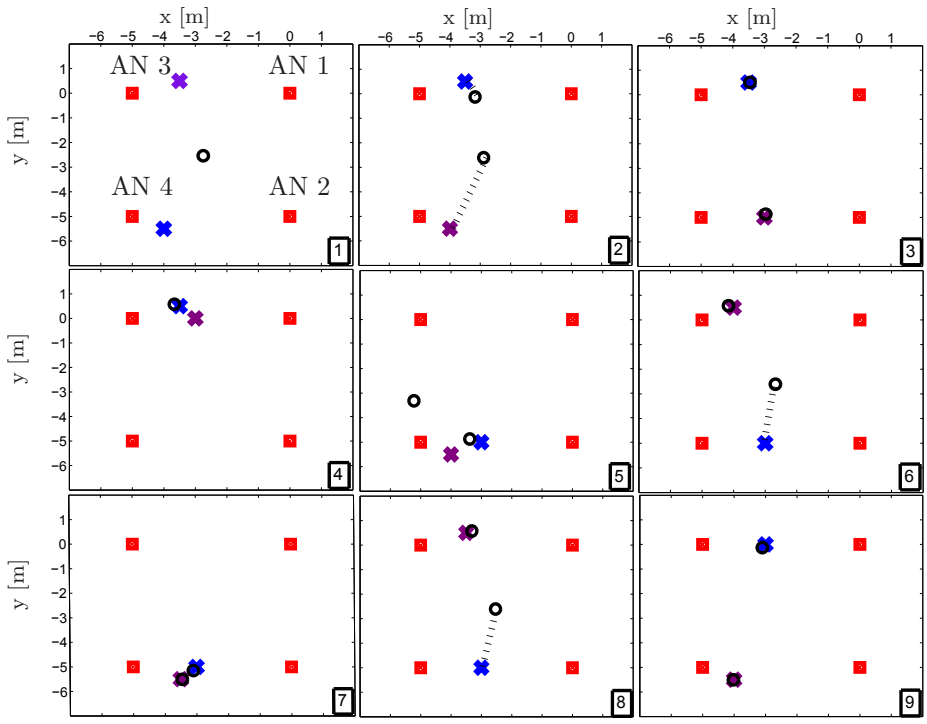

Figure 5.29: Two-person localization results for measurements 1 to 9. The positions of the first and second person are shown as blue and purple crosses, respectively. The location estimates are shown as black circles and the position of the anchor nodes are shown as red squares.

Fig. 5.29, Fig. 5.30 and Table 5.3 show that the localization errors are below 40 cm for measurement locations of 3, 7, 9, 10 and 14. For measurements of 2, 6 and 8, the localization errors gets higher than 2.4 m for one of the persons. For all these three cases, a second person is detected by mistake for Link 2[4], where only a single person affects the link. For measurement 2, the second person is falsely detected for Link 2 because the correlations between Link 2 and Link 4 is higher than the threshold for two isolated bin intervals. A similar observation is also obtained for measurement 6 and 8 between Link 2 and Link 3. A similar case is plotted in Fig. 5.21 and Fig. 5.22. This suggests that Link 2 is influenced by two persons, standing with similar bistatic ranges. The false detection of the person in Link 2 causes a high location error as the final localization algorithm also considers the false location estimate. If the false estimate of Link 2 had not been considered, then location errors of 12 cm, 0.23 cm and 0.36 cm would

[4]The link indices between anchor pairs are given in Table 5.2.

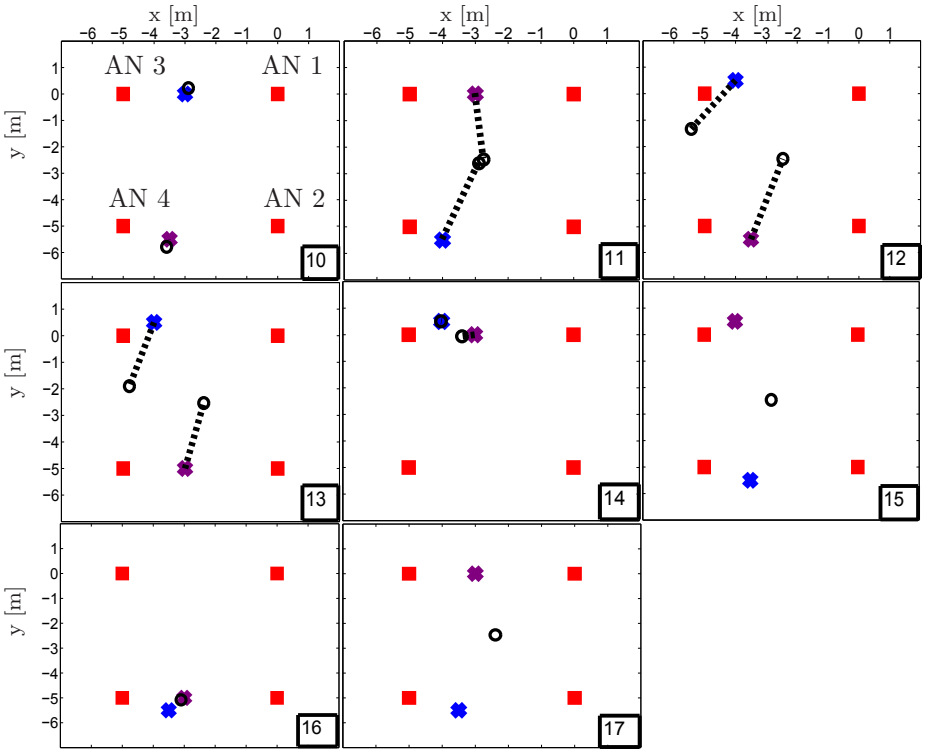

Figure 5.30: Two-person localization results for measurements 10 to 17. The positions of the first and second person are shown as blue and purple crosses, respectively. The location estimates are shown as black circles and the position of the anchor nodes are shown as red squares.

have been obtained for the second person in measurement 2, and first person in measurements 6 and 8, respectively.

For measurement positions 11, 12 and 13, very high location errors for both persons were obtained, even though it was possible to detect both of them. Similar to the previous case, two persons were falsely detected by Link 2 and Link 5, where only one person affects the link. For Link 2, the first person affects the link in measurements 12 and 13, while the second person affects in measurement 11. For Link 5, the first person affects the link in measurement 11, and the second person has an effect on the link in measurements 12 and 13.

For measurement positions 1, 4, 15, 16 and 17, it is not possible to detect the second person with correlation analysis of a single link or correlation analysis between different links. For these measurements, the location error for a single person can be quite high, as the bistatic range estimation errors are also high.

Table 5.6: Localization errors for unambiguous two person detection cases.

	Localization error [m]	
Measurement number	**Person 1**	**Person 2**
2	0.71	3.10
3	0.05	0.14
6	2.42	0.18
7	0.18	0.05
8	2.44	0.20
9	0.17	0.02
10	0.25	0.30
11	3.10	2.48
12	2.32	3.21
13	2.53	2.54
14	0.02	0.39

Besides that, the algorithm is not capable of finding the links which are affected by the same person (e.g., the algorithm falsely determines Link 2 among the links affected by first person, even though it is affected by the second person.).

Comparing this result to the previous studies, in [47] an rms error of 0.45 m is obtained for two targets in an open environment of 70 m^2 and with 30 Zigbee nodes. This is the best reported accuracy in the literature. Based on this result, the multiple people localization with UWB radios is still open for quite large performance improvements. One advantage with UWB could be achieving these accuracies with fewer nodes.

5.9 Conclusion

In this chapter, a novel multiple-person detection and localization method was developed. The method exploits the random movement of people and it is based upon the idea that high correlations occur between two delay samples if they correspond to the same person and low correlations occur if they correspond to different persons. Experiments were performed in an open indoor environment with two persons who are standing still in different positions. The analysis shows that hardware impairments also have an effect on the correlation between the delay samples of a single link. Therefore, a way to normalize the correlation between the delay samples was chosen. The analysis also shows that the delay samples, affected by each person do not show low correlations every time. In some cases, the correlations between the delay samples, which are affected by different people, can be close to correlations between the delay samples affected by the same person. The method presented in this chapter first detects the presence of a person and then finds out if there are more than one person in the environment by analyzing the correlations between the delay samples of

single and two different links. Then, it finds the delay samples, affected by the same person in different links, and estimates the bistatic ranges and the locations for each person.

The results show that it is not always possible to detect the second person, because of some degree of correlation between the delay samples that do not correspond to the same person. A simple cause of the problem could be that N_{rep} is simply too low, so that, even if the movements of the people are statistically completely uncorrelated, a finite correlation would be occasionally measured. However, in practical scenarios the system is always limited by N_{rep} as it determines how often the system gives the detection and localization results. Hence, it will not be possible to take very long measurements. Considering the finite measurement durations, the threshold selection for the correlation values to detect the second person is one of the issues in practical systems. In this work, the threshold selection was performed based on experimental analysis. Our localization results show that it is possible to detect the second person in 70% of our measurements. Furthermore, a median and an rms localization error of 0.4 m and 1.7 m was obtained for the cases when both persons were detected, respectively.

Chapter 6

Conclusions and Future Work

6.1 Conclusions

In this work, the impact of the presence of a person on UWB transmission is investigated, first to understand the effect on UWB time-based device-to-device ranging, and second to develop a novel signal processing method for device-free people detection and localization using UWB networks.

In this thesis, the effect of the human body on the energy of the direct-path signal component and on the TOA range estimates is shown for UWB propagation channels (Chapter 2). It is observed that the human body attenuates the direct-path signal component, when standing between the antennas, causing a shadowing effect. However, the person does not introduce any additional ranging error for a threshold-based TOA range estimation technique with an appropriate choice of the leading edge threshold. This is due to the fact that, even though the direct path is blocked, the signal diffracts around the body. In our setup, the ranging error is observed since the difference between the lengths of the diffracted paths and the direct path is smaller than the range resolution of our system.

By further analysis of the same measurement set and the ones taken with off-the-shelf UWB radios, it was also observed that the human body induces slow variations in the UWB signal, even when the person is standing still. From these observations, a signal model is adopted from the time-variant tapped delay line model for device-free ranging and localization purposes. Using this model, a novel signal processing method is developed for device-free detection and localization (Chapter 3). Our experimental activities pointed out a common practical problem in UWB transmission, which is known as timing jitter, and has an effect on the detection and localization performance. Timing jitter causes different background noise for each delay sample, proportional to the time-derivative of the signal around that sample. Experimental results also showed that there is not only a single MPC because of the reflection from the person, but there are also later-arriving MPCs having slow variations due to

the person. This is because the same signal, that is reflected off the body, also reflect off the environment before arriving at the receiver. Considering this effect and hardware problems such as timing jitter, three practical estimation criteria are proposed for the delay of the human-body reflection, and their performance is shown in experimental settings for both ranging and localization (Chapter 4). Among them, the Threshold Crossing criterion has lower bistatic range error, and its performance is strongly dependent on the threshold value that is chosen. If the threshold is determined by the analytical results an rms bistatic range and localization errors of 1 m and 0.9 m were obtained, respectively. There are outliers in bistatic range estimation due to the effect of the hardware impairments and/or later-arriving reflections, and these effects were not considered in the analytical results. If the optimal threshold value is chosen, based on the experimental results, an rms error of around 0.4 m was obtained. However, at the optimum threshold value, our results showed that there are 21 unavailable range estimates. Similarly, an rms localization error of 0.7 m was obtained for the optimum threshold. That is different than the optimum threshold for the bistatic range. For this threshold there were two unavailable location estimates. Comparing these results to the results in narrowband domain, in [43] the localization accuracy of around 0.2 m was obtained. Even though the results were better, this work includes training measurements in the environment when the person was not in the environment. [48] and [49], in which the methods were based on the variations in the RSS, obtained the accuracies around 0.5 m with 34 and fourteen nodes (comparing to four nodes in our work), respectively. In comparison to the results in UWB domain, in [72], HMM-based approach shows around 0.9 m for the bistatic range estimation and 0.75 m for one of the environments they performed these experiments. The approach is a bit different as the authors built an HMM-model based on the changes of the CIR (between the presence and the absence of the person). However, it gives a good aspect when detecting the person and perform the localization since it also involves the changes in the later delay samples which are due to the indirect reflections.

The detection technique is not enough for the cases with more than one person, because of the ambiguity resulted from the indirect reflections. Therefore, the detection technique was extended for multiple people detection by using the correlation information between the delay samples of a single link. The correlations between the delay samples of different links were also used to perform localization (Chapter 5). Hardware impairments introduce additional challenges for measuring the correlation between the delay samples of a single link. In addition, the random variations in the signal due to each person are not uncorrelated in all the cases. Therefore, in general, determining the threshold is another challenge. By the proper choice of the threshold, it was shown that it is possible to detect the second person in 83% of our measurements with a single link. These challenges also have an effect on the final localization algorithm. In 70% of our measurements it was possible to detect the second person and a median localization error of 40 cm was obtained. Our results also showed

large outliers (up to a localization error of 3.2 m) and rms localization error of 1.74 m was obtained. Other multi-target tracking methods were implemented with the narrowband radios. In these methods, moving people are considered. As a best reported accuracy, in [47] an rms error of 0.45 m is obtained for two targets in an open environment of 70 m^2 and with 30 nodes. Comparing to this result, the multiple people localization with UWB radios is open for quite large performance improvements, and one advantage with UWB could be achieving these accuracies with fewer nodes.

6.2 Future Work

During this work, the main focus was on understanding the human-body effect on UWB transmission in indoor environments, formulating a model for the UWB received signal in the presence of the person, developing a signal processing technique for detection and localization of one and more than one person, understanding how the Time Domain modules work, and identifying issues in these modules which have a direct effect on our system. While doing the research work, a number of other challenging research directions were also identified. These research directions can be pursued in the future. In the following subsections, some of these directions will be mentioned.

6.2.1 Improving the Device-free Ranging Accuracy

The results show that the best localization accuracy can be achieved by the Threshold Crossing method. However, in some scenarios the threshold is falsely crossed by the earlier samples because of the hardware effects. Especially the timing jitter is one common problem in the UWB literature. By incorporating a suitable timing jitter model into the received UWB signal model, a more reliable threshold can be developed for the decision statistic (and even a more reliable decision statistic can be developed.). Choosing the threshold is even more challenging in the multiple-person case because of, in addition to the timing jitter effect in the single link case, the possible correlation between the random variations in the signal (i.e., limited by the number of repetitions N_{rep}) due to two persons. Therefore, another way is to determine the threshold in a dynamic manner relative to the strength of the person's movement in each case (i.e., from the energy of the delay samples varying slowly over time). In this case, there would be more energy in the low-frequency part of the signals for those people whose movements cause higher fluctuations in the amplitude of the low-frequency part of the signal. Even though the correlation is already normalized, because of the normalization to the total signal energy, still high normalized correlation values might be obtained between the delay samples affected by this person, and an another person whose movements cause relatively lower amplitude fluctuations considering the finite duration of the signals. Determining the possible correlation values, which are obtained between delay

samples corresponds to different persons can be done with a further experimental analysis. Moreover, experimental results also showed that when the person block the LOS the signal variations are much less in the earlier delay samples corresponding to the position of the person. As a result, the threshold is usually crossed in the later samples. Therefore, the method presented in this thesis can also be combined with techniques based on RSS levels to be more robust against these cases.

6.2.2 Extension of the Measurement Setup

One of the main limitations of our experimental activities is that it was not possible to get more than 10 ns of delay window with the Time Domain modules. This is because these modules were not really designed for passive localization purposes. Therefore, the maximum bistatic range that could be measured was around 3 m. This limitation was considered while designing our experimental activities. These experiments can be extended to larger coverage areas with receivers which can provide a larger delay window. In this way, it is possible to see the maximum detection range for a standing person with a single link. Besides that, the measurements can be extended to scenarios with people behind different obstructions (such as walls), and the signal processing challenges related to the detection and localization can be addressed [60].

6.2.3 Investigating the Presence of Other Moving Objects

The capability of a UWB system to detect even respiratory movements of a person make it also vulnerable to the movement of, for example, fans, objects moving due to the wind, and machinery [105]. Throughout this research, the effect of other moving objects on the detection performance was not particularly investigated. The environment was kept completely stationary, except for the presence of the person. The detection method might give false alarms because of the changes in signal due to other autonomous systems, hence reducing the applicability of the system in some environments. Such changes in signal might depend on, for instance, the main material of the object (as it influences the reflection properties), its shape (which affects how many delay samples will be directly affected) and the periodicity of the movement. These points can be considered in the detection method by inspecting the dynamic nature of the environment when it is not populated. For instance, an industrial environment can be highly dynamic due to the machinery, whereas office and home environments are rarely dynamic except from a person's presence. By measuring these effects, new detection methods can be developed to prevent false alarms due to these movements. This can be a very challenging task in the presence of hardware-related issues such as presented in this thesis. The detection and localization technique of this thesis can also be combined with those in [30, 39, 45, 48], such that the received signal amplitude can also be employed. This might be a way to improve the detection performance, when

the person stands exactly in between the antennas.

6.2.4 Breathing and Heart Rate Estimation

Our analysis showed that it is possible to detect a person even through its respiratory movements. In this thesis, only the detection and localization problems were considered, but there is also a growing interest in respiration rate and heart rate estimation in a noninvasive manner, using the capability of the wireless signals. This has a lot of application areas, especially in the medical domain. For instance, these applications could be to monitor the vital signs of patients in hospitals or of elderly people at their houses, or the stress level of people through for instance measuring the heart rate variability [106, 107]. For UWB signals, experimental results were already given in [56, 60, 108, 109] which demonstrate the possibility of these systems. Specifically, in [60, 108], UWB systems which are compatible with the FCC mask are used. These works only consider a single link, where the person is usually 1 m away from the transmitter and/or receiver. This area has not been investigated for UWB networks. Possibly, the estimation performance can be improved by investigating and combining the effect of a person on more than a single UWB link. Besides, it may also extend the coverage area for such systems. In addition, this research can be extended to the case when the person is moving. Such research could be especially important for applications such as elderly monitoring. There are also development efforts for large-scale applications. Recently, Novelda [110] claimed that they developed a complete CMOS radar transceiver on a single chip based on impulse radio, and among the application areas they mentioned breathing and heart rate estimation for elderly monitoring.

6.2.5 Indoor Mapping

In this research, it was also pointed out that the signals are directly reflected off the person, but in some cases they are also reflected off the environment before arriving at the receiver. These are called the indirect reflections in this thesis. The indirect reflections may also give information about the obstacles around the person and can be utilized to map the environment. This can be obtained by processing the indirect reflections for different positions of the person and finding the distances to the walls in a room. If the arrival delay of an indirect reflection is known, then the position of the obstacle can be on an ellipse drawn around the person and the transmitter or receiver. In this case, the focal points will be the positions of the person and the transmitter or receiver, and the major axis length will be determined by the arrival time difference between the direct reflection and the indirect reflection. It can be possible to determine whether the obstacle is positioned on an ellipse around the transmitter or receiver in the following way: if the signal first reflects off the person and then the obstacle, then the position of this obstacle will be on an ellipse around the person and the receiver. On the other hand, if the

signal first reflects off the obstacle and then the person, then this obstacle will be on an ellipse around the person and the transmitter. One challenge is to determine whether the object is in between the transmitter and the person or the receiver and the person. One way to deal with this challenge can be to also utilize the information regarding to the locations of the multipath sources that can directly be obtained from the received signal [3], as the wall reflections will also arrive as MPCs. Application scenarios can be the cases where the UWB infrastructure is available in an environment for which the map is not known in advance. This method can be investigated for such scenarios by combining with other available technologies in simultaneous localization and mapping.

6.2.6 Effect of the Geometry

Another open research question is the effect of the geometry on the performance of the device-free localization. This includes the optimal arrangement of the anchors, and the position of the person and its effect on the final positioning accuracy. For instance, depending on the position of the person, different position errors are obtained for the same error in the bistatic range estimation. The reason is that the distance between the ellipses depends on where the person is located. This can be seen from Fig. 2.3, which shows that the difference gets smaller when the person is closer to the transmitter or receiver. Through this knowledge, different techniques can also be considered for combining the bistatic range estimates, such as weighted least squares estimation.

References

[1] G. Sun, J. Chen, W. Guo, and K. J. R. Liu, "Signal processing techniques in network-aided positioning: a survey of state-of-the-art positioning designs," *IEEE Signal Process. Mag.*, vol. 22, no. 4, pp. 12–23, Jul. 2005.

[2] K. Pahlavan, X. Li, and J. P. Makela, "Indoor geolocation science and technology," *IEEE Comm. Mag.*, vol. 40, no. 2, pp. 112–118, Feb. 2002.

[3] Z Sahinoglu, S. Gezici, and I. Guvenc, *Ultra-wideband positioning systems theoretical limits, ranging algorithms, and protocols*, Cambridge, U.K: Cambridge University Press, 2008, Ch. 5, Sec. 3, pp. 108–109.

[4] J. J. Caffery and G. L. Stuber, "Overview of radiolocation in CDMA cellular systems," *IEEE Communications Magazine*, vol. 36, no. 4, pp. 38–45, April 1998.

[5] G. M. Djuknic and R. E. Richton, "Geo-location and assisted GPS," *IEEE Computer*, vol. 34, no. 2, pp. 123–125, Feb. 2001.

[6] V. Otsason, A. Varshavsky, A. Lamarca, and E. de Lara, "Accurate indoor GSM localization," in *Proc. UbiComp 2005*, Lecture Notes Computer Science, Springer Verlag, vol. 3660, pp. 141–158, 2005.

[7] Y. Chen and H. Kobayashi, "Signal strength based indoor geolocation," in *Proc. 2002 Int. Conf. on Comm. (ICC)*, New York, May 2002, pp. 436–439.

[8] A. S. Krishnakumar and P. Krishnan, "On the accuracy of signal strength-based estimation techniques," in *Proc. INFOCOM 2005*, Miami, Mar. 2005, pp. 642–650.

[9] H. Liu, H. Darabi, P. Banerjee, and J. Liu, "Survey of wireless indoor positioning techniques and systems," *IEEE Trans. Syst. Man. Cybern. C, Appl. Rev.*, vol. 37, no. 6, pp. 1067–1080, Nov. 2007.

[10] P. Bahl and V. N. Padmanabhan, "RADAR: An in-building RF-based user location and tracking system," in *Proc. INFOCOM 2000*, Tel Aviv, Israel, Mar. 2000, pp. 775–784.

[11] M. A. Youssef, A. Agrawala, and A. Udaya Shankar, "WLAN location determination via clustering and probability distributions," in *Proc. Pervasive Comp. and Comm. (PerCom)*, Fort Worth, TX, Mar. 2003, pp. 143–150.

[12] T. Roos, P. Myllymaki, H. Tirri, P. Misikangas, and J. Sievanen, "A probabilistic approach to WLAN user location estimation," *Int. J. Wireless Inf. Networks*, vol. 9, no. 3, pp. 155–164, July 2002.

[13] P. Castro, P. Chiu, T. Kremenek, and R. Muntz, "A probabilistic room location service for wireless networked environments," in *Proc. UbiComp 2001*, Lecture Notes Computer Science, Springer Verlag, pp. 18–34, 2001.

[14] T. P. Deasy and W. G. Scanlon, "Stepwise algorithms for improving the accuracy of both deterministic and probabilistic methods in WLAN-based indoor user localisation," in *Int. J. of Wireless Inf. Netw.*, vol. 11, no. 4, pp. 18–34, Oct. 2004.

[15] Y. Gu, A. Lo, and I. Niemeegers, "A survey of indoor positioning systems for wireless personal networks," *IEEE Commun. Surveys & Tutorials*, vol. 11, no. 1, pp. 13–32, First Quarter 2009.

[16] J. Hightower, R. Want, and G. Borriello, "SpotON: An indoor 3D location sensing technology based on RF signal strength," Univ. Washington, Seattle, Tech. Rep. UW CSE 2000-02-02, Feb. 2000.

[17] L. M. Ni, Y. Liu, Y. C. Lau, and A. P. Patil, "LANDMARC: Indoor location sensing using active RFID," *Wireless Netw.*, vol. 10, no. 6, pp. 701–710, Nov. 2004.

[18] E. Martin, O. Vinyals, G. Friedland, and R. Bajcsy, "Precise indoor localization using smart phones," in *Proc. of Int. Conf. on Multimedia (MM'10)*, Firenze, Italy, Oct. 2010, pp. 787–790.

[19] J. Lee and R. A. Scholtz, "Ranging in a dense multipath environment using an UWB radio link," *IEEE J. Sel. Areas Commun.*, vol. 20, no. 9, pp. 1677–1683, Dec. 2002.

[20] C. Falsi, D. Dardari, L. Mucchi, and M. Z. Win, "Time of arrival estimation for UWB localizers in realistic environments," *EURASIP J. on Applied Signal Processing* (special issue on *Wireless Location Technologies and Applications*), vol. 2006, pp. 1–13, 2006.

[21] D. B. Jourdan, D. Dardari, and M. Z. Win, "Position error bound for UWB localization in dense cluttered environments," *IEEE Trans. Aerosp. Electron. Syst.*, vol. 44, no. 2, pp. 613–628, Apr. 2008.

[22] D. Dardari, A. Conti, U. J. Ferner, A. Giorgetti, and M. Z. Win, "Ranging with ultra-widebandwidth signals in multipath environments," *Proc.*

of IEEE (special issue on *Ultra-Wide Bandwidth (UWB) Technology & Emerging Applications.*), vol. 97, no. 2, pp. 404–426, Feb. 2009.

[23] S. Gezici, Z. Tian, G. B. Giannakis, Z. Sahinoglu, H. Kobayashi, A. F. Molisch, and H. V. Poor, "Localization via ultra-wideband radios," *IEEE Signal Process. Mag.*, vol. 22, no. 4, pp. 70–84, July 2005.

[24] Federal Communications Commission, ""Revision of Part 15 of the Commission's rules regarding ultra-wideband transmission systems," *First Report and Order 02-48*, ET-Docket 98-153, FCC 02-48, Feb. 2002.

[25] W. Hirt, "The European UWB radio regulatory and standards framework: Overview and implications," in *Proc. IEEE Int. Conf. on Ultra-Wideband (ICUWB)*, 2007, Singapore, Sept. 2007, pp. 135–144.

[26] ETSI EN 302 065-1, "Electromagnetic compatibility and Radio spectrum Matters (ERM); Short Range Devices (SRD) using Ultra Wide Band technology (UWB); Harmonized EN covering the essential requirements of article 3.2 of the R&TTE Directive; Part 1: Requirements for Generic UWB applications," *Harmonized European Standard*, V1.3.1 (2014-04).

[27] A. F. Molisch, *Wireless Communications*, John Wiley & Sons Ltd, 2009.

[28] R. Zhang, L. Cai, S. He, X. Dong, and J. Pan, "Modeling, validation and performance evaluation of body shadowing effect in ultra-wideband networks," *Phys. Commun.*, vol. 2, no. 4, pp. 237–247, 2009.

[29] K. I. Ziri-Castro, N. E. Evans, and W. G. Scanlon, "Propagation modelling and measurements in a populated indoor environment at 5.2 GHz," in *Proc. Auswireless Conf.*, Sydney, Australia, March 2006, pp. 1–8.

[30] N. Patwari and J. Wilson, "Spatial models for human motion-induced signal strength variance on static links," *IEEE Trans. Inf. Forens. Security*, vol. 6, no. 3, pp. 791–802, Sept. 2011.

[31] K. Yu, I. Sharp and Y. J. Guo, *Ground-based Wireless Positioning*, John Wiley & Sons Ltd, 2009.

[32] T. Teixeira, G. Dublon, and A. Savvides, "A survey of human-sensing: Methods for detecting presence, count, location, track, and identity," *ACM Comput. Surveys*, vol. 5, issue 1, pp. 59–69, 2010.

[33] M. A. Turk and A. P. Pentland, "Face recognition using eigenface," in *Proc. IEEE Conf. on Computer Vision and Pattern Recognition*, Lahaina, HI, June 1991, pp. 586–591.

[34] J. Krumm, S. Harris, B. Meyers, B. Brumitt, M. Hale, and S. Shafer, "Multi-camera multi-person tracking for EasyLiving," in *Proc. 3rd IEEE Int. Workshop on Visual Surveillance*, Dublin, 2000, pp. 3–10.

[35] X. Luo, B. Shen, X. Guo, G. Luo, and G. Wang, "Human tracking using ceiling pyroelectric infrared sensors," in *Proc. IEEE Int. Conf. on Control and Automation*, Christchurch, Dec. 2009, pp. 1716–1721.

[36] G. Deak, K. Curran, and J. Condell, "A survey of active and passive indoor localization systems," *Computer Communications*, vol. 35, no. 16, pp. 1939–1954, Sept. 2012.

[37] J. Paradiso, C. Abler, K. Hsiao, and M. Reynolds, "The Magic Carpet: Physical sensing for immersive environments," in *Extended Abstracts on Human Factors in Computing Systems CHI'97*, Mar. 1997, pp. 277–278.

[38] M. Valtonen, J. Maentausta, and J. Vanhala, "TileTrack: Capacitive human tracking using floor tiles," in *Proc. IEEE Int. Conf. on Pervasive Computing and Communications (PerComm 2009)*, Galveston, TX, Mar. 2009, pp. 1–10.

[39] N. Patwari and J. Wilson, "RF sensor networks for device-free localization: Measurements, models, and algorithms," *Proc. IEEE*, vol. 98, no. 11, pp. 1961–1973, Nov. 2010.

[40] K. Woyach, D. Puccinelli, and M. Haenggi, "Sensorless Sensing in Wireless Networks: Implementation and Measurements," in *Proc. 2nd Intl Workshop Wireless Network Measurement (WinMee 06)*, Boston, MA, April 2006.

[41] J. Wilson and N. Patwari, "Radio tomographic imaging with wireless networks," *IEEE Trans. Mobile Comput.*, vol. 9, no. 5, pp. 621–632, May 2010.

[42] J. Wilson and N. Patwari, "A fade level skew-Laplace signal strength model for device-free localization with wireless networks, *IEEE Trans. Mobile Computing*, vol. 11, no. 6, pp. 947–958, June 2012.

[43] M. Youssef, M. Mah, and A. Agrawala, "Challenges: Device-Free Passive Localization for Wireless Environments," in *Proc. ACM MobiCom*, pp. 222–229, Sept. 2007.

[44] C. Xu, B. Firner, Y. Zhang, R. Howard, J. Li, and X. Lin, "Improving RF-based device-free passive localization in cluttered indoor environments through probabilistic classification methods," in *Proc. Information Processing in Sensor Networks (IPSN-2012)*, April 2012, pp. 209–220.

[45] A. E. Kosba, A. Saeed, and M. Youssef, " Robust WLAN device-free passive motion detection," in *Proc Wireless Comm. and Networking Conf. (WCNC)*, April 2012, pp. 3284–3289.

[46] S. Nannuru, Y. Li, Y. Zeng, M. Coates, and B. Yang, "Radio frequency tomography for passive indoor multi-target tracking," *IEEE Trans. Mobile Computing*, vol. 12, no. 12, pp. 2322–2333, Dec. 2013.

[47] M. Bocca, O. Kaltiokallio, N. Patwari, and S. Venkatasubramanian, "Multiple target tracking with RF sensor networks," *IEEE Trans. Mobile Computing.*, vol. 13, no. 8, pp. 1787–1800, Aug. 2014.

[48] J. Wilson and N. Patwari, "See through walls: Motion tracking using variance-based radio tomography networks," *IEEE Trans. Mobile Comput.*, vol. 10, no. 5, pp. 612–621, May 2011.

[49] S. Savazzi, M. Nicoli, and M. Riva, "Radio imaging by cooperative wireless network: Localization algorithms and experiments," in *Proc Wireless Comm. and Networking Conf. (WCNC)*, April 2012, pp. 2357–2361.

[50] T. Pratt, S. Nguyen, and B. T. Walkenhorst, "Dual-polarized architectures for sensing with wireless communications signals," in *Proc. 2008 Military Comm. Conf. (MILCOM)*, San Diego, CA, Nov. 2008, pp. 1–6.

[51] A. G. Yarovoy, L. P. Ligthart, J. Matuzas, and B. Levitas, "UWB radar for human being detection," *IEEE Aerosp. Electron. Syst. Mag.*, vol. 21, no. 3, pp. 10–14, March 2006.

[52] G. Ossberger, T. Buchegger, E. Schimback, A. Stelzer, and R. Weigel, "Non-invasive respiratory movement detection and monitoring of hidden humans using ultra wideband pulse radar," in *Proc. 2004 Int. Workshop on Ultra Wideband Systems, Joint with Conf. on Ultrawideband Systems and Technologies (Joint UWBST & IWUWBS)*, 18–21 May 2004, pp. 395–399.

[53] A. Nezirovic, S. Tesfay, A. S. E. Valavan, and A. Yarovoy, "Experimental study on human breathing cross section using UWB impulse radar ," in *Proc. 2008 European Radar Conf. (EuRAD)*, 30–31 Oct. 2008, pp. 1–4.

[54] J. Sachs, M. Helbig, R. Herrmann, M. Kmec, K. Schilling, and E. Zaikov, "Remote vital sign detection for rescue, security, and medical care by ultra-wideband pseudo noise radar," *Ad Hoc Netw.*, vol. 13, pp. 42–53, Feb. 2014.

[55] J. Li, Z. Zeng, J. Sun, and F. Liu, "Through-wall detection of human beings movement by UWB radar," *IEEE Geosci. Remote Sens. Lett.*, vol. 9, no. 6, pp. 1079–1083, Nov. 2012.

[56] S. Venkatesh, C. R. Anderson, N. V. Rivera, and R. M. Buehrer, "Implementation and analysis of respiration-rate estimation using impulse-based UWB," in *Proc. 2005 IEEE Military Comm. Conf. (MILCOM)*, 17–20 Oct. 2005, pp. 3314–3320.

[57] S. Gezici, "Theoretical limits for estimation of periodic movements in pulse-based UWB systems," *IEEE J. Sel. Topics Signal Process.*, vol. 1, no. 3, pp. 405–417, Oct. 2007.

[58] N. Rivera, S. Venkatesh, C. Anderson, and R. Buehrer, "Multi-target estimation of heart and respiration rates using ultra wide-band sensors," in *14th European Signal Processing Conference (EUSIPCO)*, 2006.

[59] V. Casadei, N. Nanna, and D. Dardari, "Experimental study in breath detection and human target ranging in the presence of obstacles using ultra-wideband signals," *Int. J. Ultra Wideband Communications and Systems*, vol. 2, no. 2, pp. 116–123, 2011.

[60] A. Lazaro, D. Girbau, and R. Villarino, "Performance analysis of UWB systems in the presence of timing jitter," *Progress in Electromagnetics Research (PIER)*, vol. 100, pp. 265–284, 2010.

[61] S. Chang, N. Mitsumoto, and J. W. Burdick, "An algorithm for UWB radar-based human detection," in *Proc. 2009 IEEE Radar Conf. (RadarCon)*, Pasadena, CA, May 2009, pp. 1–6.

[62] S. Chang, R. Sharan, M. Wolf, N. Mitsumoto, and J. W. Burdick, "UWB radar-based human target tracking," in *Proc. 2009 IEEE Radar Conf. (RadarCon)*, Pasadena, CA, May 2009, pp. 1–6.

[63] Y. He, F. Le Chevalier, and A. G. Yarovoy, "Association of range-doppler video sequences in multistatic UWB radar for human tracking," in *Proc. 2012 European Radar Conf.*, Amsterdam, Nov. 2012, pp. 281–221.

[64] C. Chang and A. Sahai, "Object tracking in a 2D UWB sensor network," in *Proc. 38th Asimolar Conf. Signals Syst. Comput.*, Nov 2004, pp. 1252–1256.

[65] R. Thomä, O. Hirsch, J. Sachs, and R. Zetik, "UWB sensor networks for position location and imaging of objects and environments," in *Proc. 2nd Eur. Conf. Antennas Propag.*, Edinburgh, U.K, Nov. 2007, pp. 1–9.

[66] W. Guo, N. P. Filer, and R. Zetik, "Indoor mapping and positioning using impulse radios," in *Proc. IEEE/ION Position Location Navigat. Symp.*, April 2006, San Diego, CA, pp. 153–163.

[67] E. Paolini, A. Giorgetti, M. Chiani, R. Minutolo, and M. Montanari, "Localization capability of cooperative anti-intruder radar systems," *EURASIP J. on Advances in Signal Processing*, vol. 2008, pp. 1–14.

[68] M. Arik and O. B. Akan, "Collaborative mobile target imaging in UWB wireless radar sensor networks," *IEEE J. Sel. Areas Commun.*, vol. 28, no. 6, pp. 950–961, Aug. 2010.

[69] M. Chiani, A. Giorgetti, M. Mazzotti, R. Minutolo, and E. Paolini, "Target detection metrics and tracking for UWB radar sensor networks," in *Proc. IEEE Int. Conf. on Ultra-Wideband (ICUWB)*, Vancouver, BC, Sept. 2009, pp. 1–6.

[70] J. Shen and A. F. Molisch, "Discerning direct and indirect paths: Principle and application in passive target positioning systems," in *Proc. Global Commun. Conf. (Globecom 2011)*, Houston, TX, Dec. 2011, pp. 1–6.

[71] O. Hirsch, M. Janson, W. Wiesbeck, and R. S. Thoma, "Indirect localization and imaging of objects in an UWB sensor network," *IEEE Trans. Instrum. Meas.*, vol. 59, no. 11, pp. 2949–2957, Nov. 2010.

[72] M. McCracken and Neal Patwari, "Hidden Markov estimation of bistatic range from cluttered ultra-wideband impulse responses," *IEEE Trans. Mobile Computing.*, vol. 13, no. 7, pp. 1509–1521, July 2014.

[73] Y. Kilic, A. J. Ali, A. Meijerink, M. J. Bentum, and W. G. Scanlon, "The effect of human-body shadowing on indoor UWB TOA-based ranging systems," in *Proc. IEEE Workshop on Positioning, Navigation and Commun. (WPNC)*, Dresden, Germany, March 2012, pp. 126–130.

[74] A. F. Molisch, "UWB propagation channels-Theory, measurement and modeling," *IEEE Trans. Veh. Technol.*, vol. 54, no. 5, pp. 1528–1545, Sept. 2005.

[75] A. F. Molisch, "Ultra-wide band propagation channels," *Proc. of IEEE* (special issue on *Ultra-Wide Bandwidth (UWB) Technology & Emerging Applications.*), vol. 97, no. 2, pp. 353–371, Feb. 2009.

[76] A. Meijerink and A. F. Molisch, "On the physical interpretation of the Saleh-Valenzuela model and the definition of its power delay profiles," *IEEE Trans. Antennas. Prop.*, vol. 62, no. 9, pp. 4780–4793, Sept. 2014.

[77] D. Dardari, A. Conti, J. Lien, and M. Z. Win, "The effect of cooperation on localization systems using UWB experimental data," *EURASIP Journal on Applied Signal Processing* (special issue on *wireless cooperative networks*), vol. 2008, pp. 1–11, 2008.

[78] A. Conti, M. Guerra, D. Dardari, N. Decarli, and M. Z. Win, "Network experimentation for cooperative localization," *IEEE J. Sel. Areas Commun.*, vol. 30, no. 2, pp. 467–475, Feb. 2012.

[79] D. Dardari, C. C. Chong, and M. Z. Win, "Threshold-based time-of-arrival estimators in UWB dense multipath channels," *IEEE Trans. on Commun.*, vol. 56, no. 8, pp. 1366–1378, Aug. 2008.

[80] I. Guvenc and Z. Sahinoglu, "Threshold-based TOA estimation for impulse radio UWB systems," in *Proc. Int. Conf. on UWB (ICUWB)*, Zurich, Switzerland, Sept. 2005, pp. 420–425.

[81] N. A. Alsindi, B. Alavi, and K. Pahlavan, "Measurement and modeling of ultrawideband TOA-based ranging in indoor multipath environments," *IEEE Trans. on Veh. Technol.*, vol. 58, no. 3, pp. 1046–1058, March 2009.

[82] I. Guvenc, C. Chong, and F. Watanabe, "NLOS identification and mitigation for UWB localization systems," in *Proc. IEEE Wireless Communication and Networking Conf. (WCNC)*, pp. 1571–1576, Mar. 2007.

[83] F. Benedetto, G. Giunta, A. Toscano, and L. Vegni, "Dynamic LOS/NLOS statistical discrimination of wireless mobile channels," in *Proc. IEEE Semiannual Vehicular Technology Conf.*, Los Angeles, CA, April 2007, pp. 3071–3075.

[84] L. Mucchi and P. Marcocci, "A new parameter for UWB indoor channel profile identification," *IEEE Trans. Wireless Commun.*, vol. 8, no. 4, pp. 1597–1602, Apr. 2009.

[85] S. Marano, W. M. Gifford, H. Wymeersch, and M. Z. Win, "NLOS identification and mitigation for localization based on UWB experimental data," *IEEE J. Sel. Areas Commun.*, vol. 28, no. 7, pp. 1026–1035, Sept. 2010.

[86] M. Heidari and K. Pahlavan, "Identification of the absence of direct path in TOA-based indoor localization systems," *Int. J. Wireless Information Networks*, vol. 15, no. 3–4, pp. 117–127, 2008.

[87] P. C. Chen, "A non-line-of-sight error mitigation algorithm in location estimation," in *Proc. IEEE Wireless Communication and Networking Conf.*, Los Angeles, CA, Sept. 1999, pp. 316–320.

[88] Z. Irahhauten, J. Dacuna, G. J. M. Janssen, and H. Nikookar, "UWB channel measurements and results for wireless personal area networks application," in *Proc. European Conf. Wireless Technology*, Paris, France, Oct. 2005, pp. 189–192.

[89] T. Zasowski, G. Meyer, F. Althaus, and A. Wittneben, "Propagation effects in UWB body area networks," in *Proc. Int. Conf. on UWB (ICUWB)*, Zurich, Switzerland, Sept. 2005, pp. 16–21.

[90] M. Ghaddar, L. Talbi, T. A. Denidni, and A. Sebak, "A conducting cylinder for modeling human body presence in indoor propagation channel," *IEEE Trans. Antennas. Propag.*, vol. 55, no. 11, pp. 3099–3103, 2007.

[91] BroadSpec UWB antenna, TimeDomain PulsOn 400 Data Sheet. Available online at `http://www.timedomain.com/datasheets/TD_Broadspec_Antenna.pdf`.

[92] T. Dammes, W. Endemann, and R. Kays, "Frequency domain channel measurements for wireless localization - practical considerations and effects of the measurement," in *Proc. of European Wireless 2012*, Poznan, Poland, April 2012, pp. 1–8.

[93] Rohde & Schwarz ZVB Vector Network Analyzer Specifications, version 08.02, June 2011. Available online at `http://www.google.nl/url?sa=t&rct=j&q=&esrc=s&source=web&cd=1&ved=0CDMQFjAA&url=http%3A%2F%2Fwww.rohde-schwarz.de%2Ffile%2FZVB_dat_sw_en.pdf&ei=Qqj-VP-PJoOL7AbMqIHAAw&usg=AFQjCNH28OKLcHFMwPNtVsPzSYry31WowA&sig2=fa2AfCZOV4ydUQRs-9oO5A&bvm=bv.87611401,d.ZGU&cad=rja`.

[94] Y. Kilic, H. Wymeersch, A. Meijerink, M. J. Bentum, and W. G. Scanlon, "Device-free person detection and ranging in UWB networks," *IEEE J. Sel. Topics Signal Process.* (special issue on *non-cooperative localization networks.*), vol. 8, no. 1, pp. 43–54, Feb. 2014.

[95] Y. Kilic, H. Wymeersch, A. Meijerink, M. J. Bentum, and W. G. Scanlon, "An experimental study of UWB device-free person detection and ranging," in *Proc. IEEE Int. Conf. on Ultra-Wideband (ICUWB)*, Sydney, Australia, Sept. 2009, pp. 43–48.

[96] S. M. Kay, *Fundamentals of Statistical Signal Processing: Estimation Theory*, Prentice-Hall, 1993.

[97] S. M. Kay, *Fundamentals of Statistical Signal Processing: Detection Theory*, Prentice-Hall, 1998.

[98] M. G. Di Benedetto, and G. Giancola, *Understanding Ultra Wide Band Radio Fundamentals*, Pearson Eduacation Inc., 2004.

[99] Time Domain Corp., *Ranging and Communications Application Programming Interface (API) Specification*, Technical document, version 2.4, March 2014. Available online at `http://www.timedomain.com/datasheets/320-0282F%20RCM%20API%20Specification.pdf`.

[100] M. Z. Win, "A unified spectral analysis of generalized time-hopping spread-spectrum signal in the presence of the timing jitter," *IEEE J. Sel. Areas Commun.*, vol. 20, no. 9, pp. 1664–1676, Dec. 2002.

[101] M. Z. Win, "Spectral density of random UWB signals," *IEEE Commun. Lett.*, vol. 6, no. 12, pp. 526–528, Dec. 2002.

[102] M. Z. Win, "On the power spectral density of digital pulse streams generated by M-ary cyclostationary sequences in the presence of stationary timing jitter," *IEEE Trans. Commun.*, vol. 46, no. 9, pp. 1135–1145, Sept. 1998.

[103] I. Guvenc and H. Arslan, "Performance analysis of UWB systems in the presence of timing jitter," *J. of Commun. and Networks*, vol. 6, no. 2, pp. 1–10, June 2004.

[104] J. A. Snyman, *Practical Mathematical Optimization*, Springer, 2005.

[105] Y. Zhao and N. Patwari, "Noise reduction for variance-based device-free localization and tracking," in *Proc. 8th annual IEEE Commun. Society Conf. on Sensor, Mesh and Ad Hoc Commun. and Netw. (SECON 2011)*, Salt Lake City, Utah, U.S., June 2011, pp. 179–187.

[106] E. M. Staderini, "UWB radars in medicine," *IEEE Trans. Aerosp. Electron. Syst. Mag.*, vol. 17, no. 1, pp. 13–18, Jan. 2002.

[107] C. G. Bilich, "Bio-medical sensing using Ultra Wideband communications and radar technology: A feasibility study," in *Proc. Pervasive Health Conf. and Workshops*, Innsbruck, Austria, Nov. 2006, pp. 1–9.

[108] E. Sharifahmadian and A. Ahmadian, "Adaptive signal processing algorithm for remote detection of heart rate using ultra-wideband waveforms based on principal component analysis," in *Proc. 31st annual Int. Conf. of the IEEE EMBS*, Minneapolis, Minnesota, U.S., Sept. 2009, pp. 5717–5720.

[109] S. N. Pavlov and S. V. Samkov, "Algorithm of signal processing in ultra-wideband radar designed for remote measuring parameters of patient's cardiac activity," in *Proc. Int. Conf. on Ultrawideband and ultrashort impulse signals*, Sevastopol, Ukraine, Sept. 2004, pp. 205–207.

[110] D. T. Wisland, "Nanoscale CMOS impulse radar–from research to product," in *NORCHIP 2012*, Copenhagen, Denmark, Nov. 2012.

[111] W. C. van Etten, *Introduction to Random Signals and Noise*, John Wiley & Sons, 2005.

[112] Time Domain Corp., *Using Channel Analysis Tool to Implement Multistatic Radar, Technical document*, June 2013. Available online at `http://www.timedomain.com/datasheets/320-0311A%20Using%20CAT%20to%20Implement%20Multistatic%20Radar.pdf`

Appendix A

Conditional Statistics of the Decision Variable

In this part, we derive the conditional statistics, in particular the conditional variance, and conditional mean and variance of the decision variable for the cases in which the person is absent and present, respectively.

A.1 Conditional Statistics in the Absence of a Person

We recall that in the absence of a person

$$D(\tau^*) = \frac{1}{T_\mathrm{p} N_0 \beta W^2 N_\mathrm{rep}} \sum_{m=(\tau^*-T_\mathrm{p}/2)W}^{(\tau^*+T_\mathrm{p}/2)W} \|\mathbf{n}_{m,\mathrm{L}}\|^2, \tag{A.1}$$

where $\{n_{m,\mathrm{L}}(k)\}$ are Gaussian noise samples obtained after low-pass filtering of $n_m(k)$ with a discrete low-pass filter with unity gain in the normalized frequency band $[-\beta,\beta]$. The variance of $n_{m,\mathrm{L}}(k)$ follows from calculating the output power after low-pass filtering [111] and is obtained as $N_0 W\beta$.

Since the mean of $n_{m,\mathrm{L}}(k)$ is zero, the variance equals $N_0 W\beta$. For determination of σ_f^2, we first calculate

$$\begin{aligned}\mathbb{E}\left\{D^2(\tau^*)|\text{no person}\right\} &= \frac{1}{\left(T_\mathrm{p} N_0 \beta W^2 N_\mathrm{rep}\right)^2} \sum_m \sum_{m'} \mathbb{E}\left\{\|\mathbf{n}_{m,\mathrm{L}}\|^2 \|\mathbf{n}_{m',\mathrm{L}}\|^2\right\}, \\ &= \frac{1}{T_\mathrm{p}^2 W^2} \sum_{m,m'} \psi(m,m'), \end{aligned} \tag{A.2}$$

where the summation goes over an interval of length $T_\mathrm{p}W$ (in two dimensions),

and we have introduced

$$\psi(m,m') = \frac{1}{N_0^2\beta^2W^2N_{\text{rep}}^2}\sum_{k=0}^{N_{\text{rep}}-1}\sum_{k'=0}^{N_{\text{rep}}-1}\mathbb{E}\left\{n_{m,\text{L}}^2(k)n_{m',\text{L}}^2(k')\right\}. \tag{A.3}$$

When $m \neq m'$, we find that

$$\begin{aligned}\psi(m,m') &= \frac{1}{N_0^2\beta^2W^2N_{\text{rep}}^2}\sum_{k=0}^{N_{\text{rep}}-1}\sum_{k'=0}^{N_{\text{rep}}-1}\mathbb{E}\left\{n_{m,\text{L}}^2(k)\right\}\mathbb{E}\left\{n_{m',\text{L}}^2(k')\right\},\\ &= 1,\end{aligned} \tag{A.4}$$

while for $m = m'$ since $n_{m,\text{L}}(k)$ and $n_{m,\text{L}}(k')$ are jointly Gaussian, we can make use of the relationship that

$$\begin{aligned}\mathbb{E}\left\{n_{m,\text{L}}^2(k)n_{m,\text{L}}^2(k')\right\} &= \mathbb{E}\left\{n_{m,\text{L}}^2(k)\right\}\mathbb{E}\left\{n_{m,\text{L}}^2(k')\right\}\\ &\quad + 2\mathbb{E}^2\left\{n_{m,\text{L}}(k)n_{m,\text{L}}(k')\right\},\end{aligned} \tag{A.5}$$

where

$$\begin{aligned}\mathbb{E}\left\{n_{m,\text{L}}(k)n_{m,\text{L}}(k')\right\} &= \mathbb{E}\left\{\sum_l\sum_{l'}h(l)h(l')n_m(k-l)n_m(k'-l')\right\}\\ &= \sum_l\sum_{l'}h(l)h(l')\mathbb{E}\left\{n_m(k-l)n_m(k'-l')\right\}\\ &= \sum_l h(l)h(l-k+k')\frac{N_0W}{2}\\ &= \frac{N_0W}{2}g(k-k'),\end{aligned} \tag{A.6}$$

where $g(k)$ is defined as

$$g(k) = \sum_l h(l)h(l-k) \tag{A.7}$$

in which $h(k)$ is the discrete-time impulse response of the filter. Hence, (A.5) can be rewritten as

$$\mathbb{E}\left\{n_{m,\text{L}}^2(k)n_{m,\text{L}}^2(k')\right\} = \left(N_0W\beta\right)^2 + \frac{1}{2}N_0^2W^2g^2(k-k'). \tag{A.8}$$

We further obtain

$$\begin{aligned}\psi(m,m) =& \frac{1}{N_0^2\beta^2W^2N_{\text{rep}}^2}\Big[\left(N_0W\beta N_{\text{rep}}\right)^2\\ &+ \frac{N_0^2W^2}{2}\sum_{k=0}^{N_{\text{rep}}-1}\sum_{k'=0}^{N_{\text{rep}}-1}g^2(k-k')\Big].\end{aligned} \tag{A.9}$$

If $\beta N_{\text{rep}} \gg 1$, the width of $g(k)$ becomes much smaller than N_{rep} and thus the second part of (A.9) can be approximated. Because of this, for the second part of (A.9), the main contributions comes from the cases when $k \approx k'$. Hence, we can further write

$$\begin{aligned}\psi(m,m) &\approx \frac{1}{N_0^2\beta^2W^2N_{\text{rep}}^2}\Big[(N_0W\beta N_{\text{rep}})^2 + \frac{N_0^2W^2N_{\text{rep}}}{2}\sum_{k=-\infty}^{\infty} g^2(k)\Big] \\ &= \frac{1}{N_0^2\beta^2W^2N_{\text{rep}}^2}\Big[(N_0W\beta N_{\text{rep}})^2 + N_0^2W^2\beta N_{\text{rep}}\Big] \\ &= 1 + 1/(\beta N_{\text{rep}}). \end{aligned} \tag{A.10}$$

Substitution of (A.4) and (A.10) into (A.2) leads to

$$\begin{aligned}\mathbb{E}\left\{D^2(\tau^*)|\text{no person}\right\} &= \frac{1}{T_{\text{p}}^2W^2}\left(\sum_m \psi(m,m) + \sum_{m\neq m'}\psi(m,m')\right) \\ &= \frac{1}{T_{\text{p}}^2W^2}\Big(T_{\text{p}}W\left(1+1/(\beta N_{\text{rep}})\right) + \left(T_{\text{p}}^2W^2 - T_{\text{p}}W\right)\cdot 1\Big) \\ &= 1 + \frac{1}{T_{\text{p}}\beta W N_{\text{rep}}}, \end{aligned} \tag{A.11}$$

so that we obtain

$$\begin{aligned}\sigma_{\text{f}}^2 &= \mathbb{E}\left\{D^2(\tau^*)\right\} - \mu_{\text{f}}^2 \\ &= \frac{1}{T_{\text{p}}\beta W N_{\text{rep}}}. \end{aligned} \tag{A.12}$$

A.2 Conditional Statistics in the Presence of a Person

We recall that in the presence of a person,

$$\begin{aligned}D(\tau^*) = &\frac{1}{T_{\text{p}}N_0\beta W^2N_{\text{rep}}}\sum_{m=(\tau^*-T_{\text{p}}/2)W}^{(\tau^*+T_{\text{p}}/2)W}\Big(G(\tau_{\text{p}})E_{\text{s}}p^2(m/W-\tau_{\text{p}})\left\|\mathbf{w}\right\|^2 \\ &+ \left\|\mathbf{n}_{m,\text{L}}\right\|^2 + 2\mathbf{x}_m^T\mathbf{n}_{m,\text{L}}\Big). \end{aligned} \tag{A.13}$$

μ_{d} can be easily obtained, using $\mathbb{E}[\left\|\mathbf{w}\right\|^2] = N_{\text{rep}}$ and $\sum_m p^2(m/W-\tau_p) = W$ (i.e., a unit-energy pulse is considered), as

$$\mathbb{E}\left\{D(\tau^*)|\text{person present}\right\} = \frac{G(\tau_{\text{p}})E_s}{T_{\text{p}}N_0\beta W} + 1. \tag{A.14}$$

To find σ_{d}^2, we first recall that odd-order moments of zero-mean Gaussian random variables are zero. Then, we determine $\mathbb{E}\left\{D^2(\tau^*)\right\}$ explicitly as

$$\begin{aligned}\mathbb{E}\left\{D^2(\tau^*)|\text{person present}\right\} = &\left(\frac{G(\tau_{\mathrm{p}})E_s}{T_{\mathrm{p}}N_0\beta W N_{\mathrm{rep}}}\right)^2 \cdot \mathbb{E}\left[\|\mathbf{w}\|^4\right] \\ &+ \mathbb{E}\left\{\left(\frac{1}{T_{\mathrm{p}}N_0\beta W^2 N_{\mathrm{rep}}}\sum_m\sum_k n_{m,\mathrm{L}}^2(k)\right)^2\right\} \\ &+ \mathbb{E}\left\{\left(\frac{2}{T_{\mathrm{p}}N_0\beta W^2 N_{\mathrm{rep}}}\sum_m\sum_k n_{m,\mathrm{L}}(k)x_m(k)\right)^2\right\} \\ &+ \frac{2G(\tau_{\mathrm{p}})E_s}{T_{\mathrm{p}}^2N_0^2\beta^2 W^3 N_{\mathrm{rep}}}\sum_m\sum_k \mathbb{E}\left\{n_{m,\mathrm{L}}^2(k)\right\}.\end{aligned} \tag{A.15}$$

Note that $\|\mathbf{w}\|^2 = E_w = \sum_{k=0}^{N_{\mathrm{rep}}-1} w^2(k)$ is the total energy in normalized variations $w(k)$ over N_{rep} snapshots. We can write

$$\mathbb{E}\left[\|\mathbf{w}\|^4\right] = \mathbb{E}\left[E_{\mathrm{w}}^2\right] = \mathbb{E}^2\left[E_{\mathrm{w}}\right] + \sigma_{E_w}^2, \tag{A.16}$$

so that, considering the variance of E_w is small compared to $\mathbb{E}^2\left[E_w\right]$, we have

$$\mathbb{E}\left[\|\mathbf{w}\|^4\right] \approx \mathbb{E}^2\left[E_w\right] = \mathbb{E}^2\left[\|\mathbf{w}\|^2\right] = N_{\mathrm{rep}}^2. \tag{A.17}$$

This is the case when the variation in the variation energy is relatively low. In other words, when the number of samples over which $x_m(k)$ can be assumed constant (i.e., the correlation time of $x_m(k)$ expressed in number of samples) is much smaller than N_{rep}. Considering this approximation, the first term simplifies to

$$\mathrm{Term}_1 = \left(\frac{G(\tau_{\mathrm{p}})E_s}{T_{\mathrm{p}}N_0\beta W}\right)^2. \tag{A.18}$$

The second term simplifies to $1 + 1/(T_{\mathrm{p}}\beta W N_{\mathrm{rep}})$, which is obtained following the same way as in (A.2). The fourth term is obtained as $2G(\tau_{\mathrm{p}})E_s/(T_{\mathrm{p}}N_0\beta W)$. The third term is equal to

$$\begin{aligned}\mathrm{Term}_3 = &\left(\frac{2}{T_{\mathrm{p}}N_0\beta W^2 N_{\mathrm{rep}}}\right)^2 \sum_{m,m'}\sum_{k,k'} \mathbb{E}\left\{n_{m,\mathrm{L}}(k)n_{m',\mathrm{L}}(k')\right\} \\ &\cdot \mathbb{E}\left\{x_m(k)x_{m'}(k')\right\},\end{aligned} \tag{A.19}$$

in which all terms with $m' \neq m$ cancel. Therefore,

$$\begin{aligned}\text{Term}_3 &= \left(\frac{2}{T_\text{p} N_0 \beta W^2 N_\text{rep}}\right)^2 \sum_m \sum_k \sum_{k'} \mathbb{E}\left\{n_{m,\text{L}}(k) n_{m,\text{L}}(k')\right\} \mathbb{E}\left\{x_m(k) x_{m'}(k')\right\} \\ &= \left(\frac{2}{T_\text{p} N_0 \beta W^2 N_\text{rep}}\right)^2 \sum_m \frac{N_0 W}{2} \sum_k \sum_{k'} g(k-k') \mathbb{E}\left\{x_m(k) x_{m'}(k')\right\},\end{aligned} \tag{A.20}$$

in which (A.6) was used. For the assumption that $x_\text{m}(.)$ is wide-sense stationary, we can write $\mathbb{E}\left\{x_m(k) x_{m'}(k')\right\} = R_{x_m}(k-k')$. Furthermore, the bandwidth of the filter is assumed to be larger than the bandwidth of $x_m(k)$ and we can further approximate $g(k-k') R_{x_m}(k-k') \approx g(k-k') R_{x_m}(0)$. Moreover, the width of $g(k)$ is considered to be small compared to N_rep and hence we can further write

$$\sum_{k=0}^{N_\text{rep}-1} g(k-k') \approx \sum_{k=-\infty}^{\infty} g(k) = G(0) = |H(0)|^2 = 1. \tag{A.21}$$

Therefore, the third term can be written as

$$\begin{aligned}\text{Term}_3 &\approx \left(\frac{2}{T_\text{p} N_0 \beta W^2 N_\text{rep}}\right)^2 \sum_m \frac{N_0 W}{2} \sum_k \mathbb{E}\left\{x_m^2(k)\right\} \\ &= \frac{2 G(\tau_\text{p}) E_s}{T_\text{p}^2 N_0 \beta^2 W^3 N_\text{rep}^2} \sum_m \sum_k p^2(m/W - \tau_\text{p}) \mathbb{E}\left\{w^2(k)\right\} \\ &= \frac{2 G(\tau_\text{p}) E_s}{T_\text{p}^2 N_0 \beta^2 W^2 N_\text{rep}}.\end{aligned} \tag{A.22}$$

Putting everything together, we find

$$\begin{aligned}\mathbb{E}\left\{D^2(\tau^*) | \text{person present}\right\} \approx \left(\frac{G(\tau_\text{p}) E_s}{T_\text{p} N_0 \beta W}\right)^2 + 1 + \frac{1}{T_\text{p} \beta W N_\text{rep}} \\ + \frac{2 G(\tau_\text{p}) E_s}{N_0 T_\text{p} \beta W} \left(1 + \frac{1}{T_\text{p} \beta W N_\text{rep}}\right).\end{aligned} \tag{A.23}$$

Subtracting

$$\mathbb{E}^2\left\{D(\tau^*) | \text{person present}\right\} = 1 + \frac{2 G(\tau_\text{p}) E_s}{T_\text{p} N_0 \beta W} + \left(\frac{G(\tau_\text{p}) E_s}{T_\text{p} N_0 \beta W}\right)^2, \tag{A.24}$$

gives us

$$\sigma_\text{d}^2 \approx \frac{1}{T_\text{p} \beta W N_\text{rep}} \left(1 + \frac{2 G(\tau_\text{p}) E_s}{T_\text{p} N_0 \beta W}\right). \tag{A.25}$$

Appendix B

Parameter Extraction for Modeling the Time-Varying Signal

In this section, we discuss the extraction of the parameter values $G(\tau_{\text{ref}})$, τ_{ref} and η, that are defined in Section 3.3. In order to find these values we used the experimental setup, *Measurement Set 1*, described in Section 3.7.1. We only considered the cases when the person is not blocking the LOS. Hence we excluded the shadowing effect induced by the person while extracting the above parameter values. When the person is in the LOS, the signals are diffracted around the body (unlike the other positions in which the signals are reflected off the body) and the variations of the signal due to the human body are very weak. Therefore, it results in very low values of $G(\tau_{\text{p}})$ for the same instant as the arrival time of the signal, leading to a sudden jump in the values of $G(\tau_{\text{p}})$ after the early delay instants between 0 ns to 1.4 ns (the duration of the pulse). This makes it hard to fit to any model. Moreover, this is not the range of τ_{p} values which are interesting for the method considered here (i.e., people entering the LOS are easy to detect using more straightforward methods).

For the rest of the measurement points, the following procedure is pursued to find above-mentioned parameters. We first define a reference received signal as the first $T_{\text{p}}W$ samples of the received waveform after the leading edge at a given transmitter and the receiver distance. For the same distance, we calculated the total energy of the human-body-induced delay samples again over the length of $T_{\text{p}}W$, after removing the mean from the signal. These human-body-induced paths were easily found as we know the real position of the person. Finally, we divided the total energy of the human-body-induced variations by the energy of the reference signal. The value of η was obtained by linear fitting in the logarithmic domain and $G(\tau_{\text{ref}})$ and τ_{ref} were chosen as close to the lower boundary of the range in which the fitting was performed. Since our

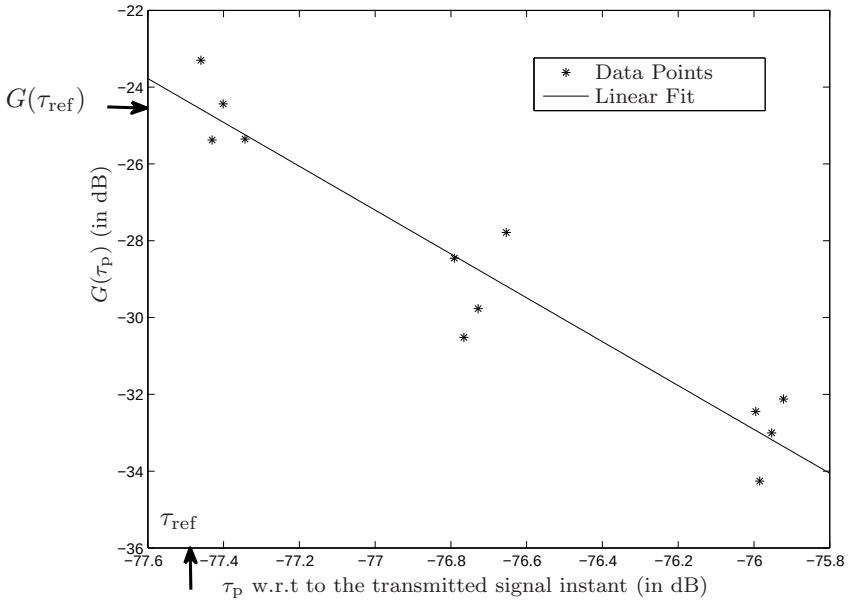

Figure B.1: The relation between the human-body induced delay values $\tau_{\rm p}$ and $G(\tau_{\rm p})$.

measurement units are able to provide waveforms with durations up to 10 ns, we could only obtain the relation between $G(\tau)$ versus τ for excess delay values up to 10 ns. The data points and the least squares fit are shown in Fig. B.1. In this figure, $\tau_{\rm p}$ values are shown with respect to transmitted signal instant such that it shows the total delay of the signal, that is reflected off the person, from transmitter to the receiver. This is obtained by adding the delay corresponding to the transmitter and receiver distance to the excess delay of the signal, which is reflected from the person. Moreover, both $G(\tau_{\rm p})$ and $\tau_{\rm p}$ are shown in logarithmic scale, i.e., $10\log_{10}(.)$. Here, the data points are assumed to be diverging from the trend function in a roughly additive manner in the logarithmic domain. From the fitting parameters, we found $G(\tau_{\rm ref}) = 3.6 \times 10^{-3}$, $\tau_{\rm ref} = 17.8$ ns and $\eta = 5.5$ (the slope of the linear fit gives $-\eta$).

Appendix C

Note on the Gaussian Approximation of the Decision Statistic

To show how the Gaussian approximation is affected by the number of samples we do the following exercise. The Gaussian approximation does not completely describe the distribution of the decision statistic given in (3.13) for lower values of N_{rep}. Empirical distributions for the decision statistic are given for $SNR = 15$ dB, and $N_{\text{rep}} = 100$ and $N_{\text{rep}} = 1,000$ in Fig. C.1(a) and Fig. C.1(b), respectively. As shown in Fig. C.1(a), there is a very slight mismatch in the tail (on the left side) of the distributions. In this case, the distribution of the statistic has asymmetric properties which are not well-captured by the Gaussian distribution. In contrast, for higher values of N_{rep}, the Gaussian approximation is more appropriate (due to the Central Limit Theorem), as shown in Fig. C.1(b).

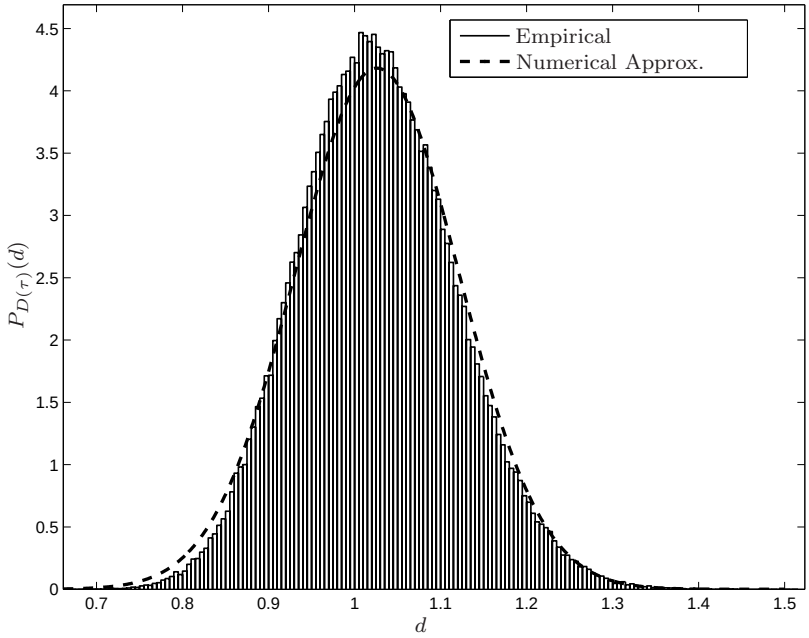

(a) $N_{\text{rep}} = 100$ and SNR $= 15$ dB.

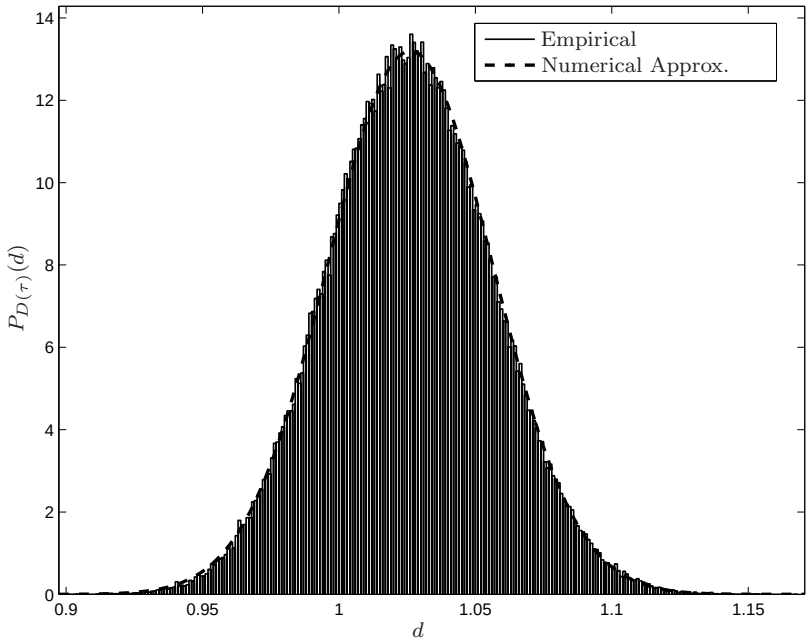

(b) $N_{\text{rep}} = 1,000$ and SNR $= 15$ dB.

Figure C.1: Probability density function of $D(\tau)$ given in (3.13), obtained through empirical (blue bars) and analytical results (red line).

Appendix D

The Effect of Lock Spot Choice on Background Variations

The experimental equipment has an implementation issue which also causes bin-dependent variations in addition to the timing jitter. This is related to the choice of the lock spots, which is described in [112]. Each captured waveform is measured relative to the lockspot (i.e., the delay samples of each waveform are taken relative to the lockspot). The system is implemented in such a way that the lock spot is chosen based on a zero crossing that is close to the delay samples with the largest amplitudes. This is depicted in Fig. D.1, which shows an example of a measured waveform with 8 ps of sampling instants[1]. In the figure, the potential lock spots are shown as red dots. Because of the choice of the lock spots, at each reception the received waveform is shifted by an integer multiple of the number of samples between two successive zero crossings. In Fig. D.2, for a total of 140 consecutive measurements, we show the required shifts to perfectly align all these 140 received waveforms. The shift values are determined relative to a reference waveform, chosen among these measurements. The number of samples between zero crossings is either 17 or 16.

If we align all the waveforms based on these shift values, we obtain the received waveforms in two dimensions as shown in Fig. D.3. The variations starting after the 800^{th} sample are due to the presence of the people in the environment. In the figure, these variations are shown in a dashed box. In order to show the effect of choosing different lock spots on the variation of the delay samples, we calculate the standard deviations of the delay samples for all the waveforms, and for the waveforms with the same lock spot, respectively.

[1]These measurements were taken from Time Domain Corp. to describe the issue with the lock spot choice in this Appendix. Our own equipment has the capability to sample the received waveform every 61 ps with a fixed sampling rate.

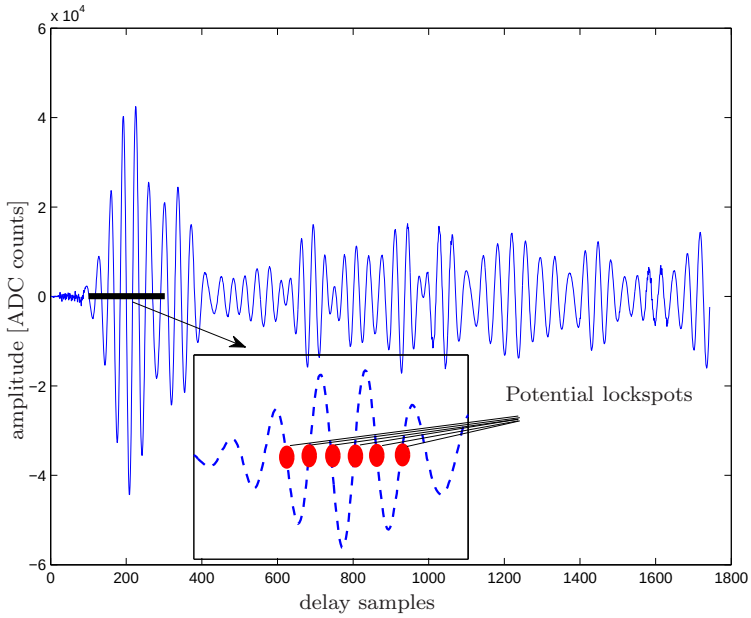

Figure D.1: An example of a measured received waveform.

The results are plotted in Fig. D.4. As for the waveforms with the same lock spot, we only show the results for the waveforms which do not require a shift. The results show that the standard deviation of the variations is reduced when we only consider the waveforms with the same lock spot. We can derive this conclusion from the early samples (i.e., before the 800^{th} sample), where there is no influence of the people. We also note that after the 800^{th} sample, the standard deviations do not show any considerable difference, since for these samples, the main variations are caused by the movement of the people.

This exercise explains that the experimental equipment has an implementation issue with the lock spot choice which also contributes to strong background variations. This issue, together with the timing jitter, causes signal samples to change over time much more than the receiver noise, even when the person is not affecting the signal.

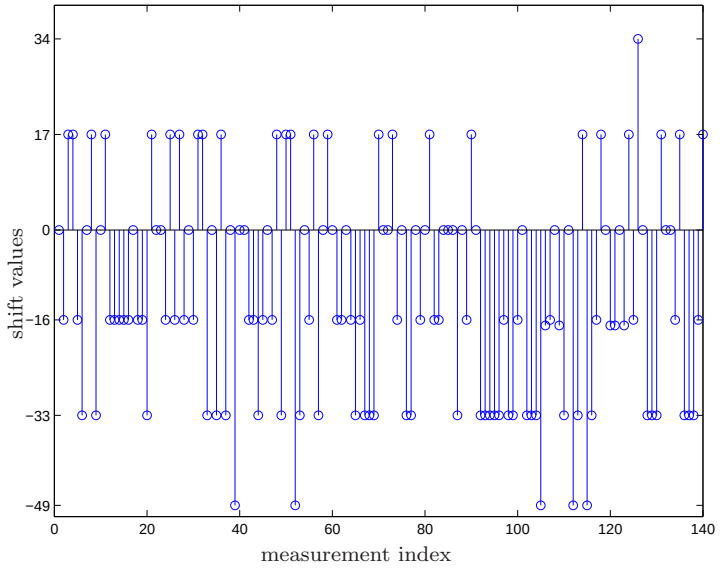

Figure D.2: The required shift values (for each measurement) to perfectly align 140 received waveforms, relative to a reference waveform.

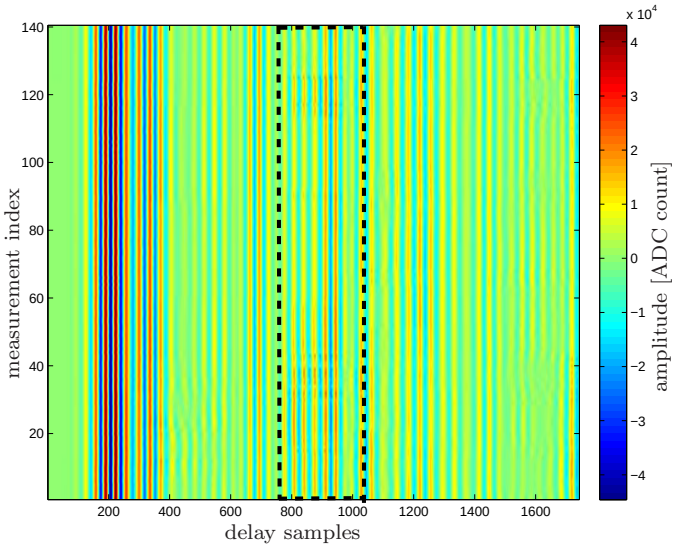

Figure D.3: 140 received waveforms, after aligning them according to the shift values shown in Fig. D.2.

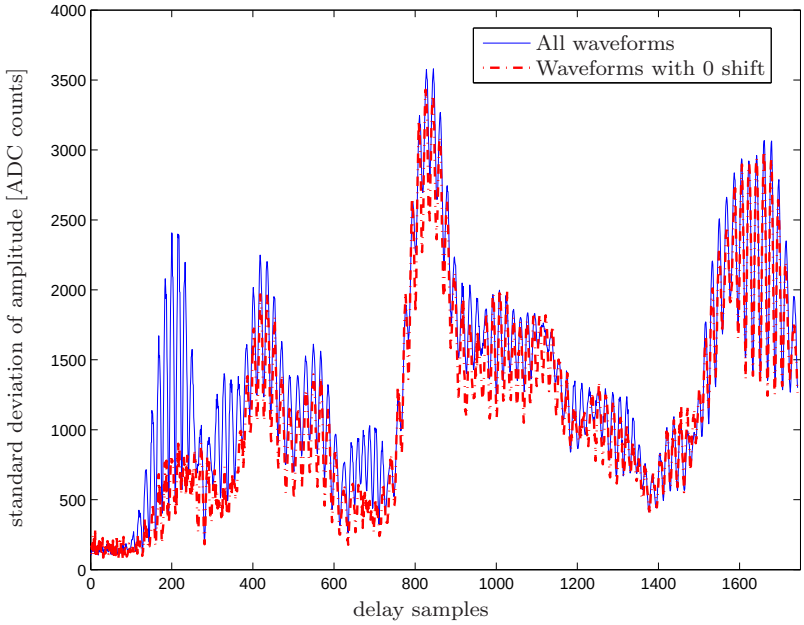

Figure D.4: The standard deviation of the delay samples for all waveforms after the alignment (shown as a blue solid line) and the waveforms which require zero shift (shown as a dashed red line). The standard deviation is calculated over 34 measurements for the case in which only the waveforms with zero shift value are considered, and 140 measurements for the case which includes all waveforms.

List of Abbreviations

ADC	Analog-to-digital Converter
A-GPS	Assisted-GPS
AN	Anchor Node
AOA	Angle of Arrival
CDF	Cumulative Distribution Function
CEPT	European Conference of Postal and Telecommunications Administrations
CIR	Channel Impulse Response
CLT	Central Limit Theorem
EC	European Commission
ECC	Electronic Communications Committee
EIRP	Equivalent Isotropically Radiated Power
FCC	Federal Communications Commission
GPS	Global Positioning System
GSM	Global System for Mobile Communications
HMM	Hidden Markov Model
IEEE	Institute of Electrical and Electronics Engineers
IFFT	Inverse Fast Fourier Transform
IFI	Inter-frame Interference
IR	Impulse Radio
LOS	Line-of-sight
LS	Least Squares
MIMO	Multiple Input Multiple Output
MPC	Multipath Component
NLOS	Non-line-of-sight

RF	Radio-frequency
RFID	Radio-frequency Identification
rms	Root Mean-square
RSC	Radio Spectrum Committee
RSS	Received Signal Strength
RSSI	Received Signal Strength Indicators
Rx	Receiver
SMA	Subminiature Version A
SNR	Signal-to-noise Ratio
SVD	Singular Value Decomposition
TDOA	Time Difference of Arrival
TOA	Time of Arrival
Tx	Transmitter
UWB	Ultra-wideband
VNA	Vector Network Analyzer
WLAN	Wireless Local Area Network

Acknowledgments

In his precious talk "You and Your Research", Richard W. Hamming cites Pasteur for his quote: "Luck favors the prepared mind". It was undoubtedly the hopeless moment in my research when I came across to these five words. Around two and half years in my research, I was very happy because I got my "lucky" observation which gave me enough passion to continue and come this far. Still, the passion was not always enough to climb up to the hill, I needed the knowledge to get there and belief that the view is amazing. I lacked the knowledge obviously and somehow lost the belief on the way. However, I met great people to compensate. Hereby, I would like to thank everyone involved in this process.

First of all, I would like to thank Arjan Meijerink, Mark Bentum and William Scanlon for giving me the opportunity and freedom to do this research. My understanding on the random signals and noise has obviously expanded after knowing Arjan. I truly enjoyed being the teaching assistant of that course for three years. Thank you for conveying your enthusiasm in this field and also very detailed reading of this thesis. Mark, I am very thankful to you for your understanding and supportive attitude. Your conflict management skills definitely helped during many of our research meetings. William, I am simply grateful to work with you. Your expertise, enthusiasm and also inspiration kept me on the track. I really would like to love electromagnetic signal propagation as much as you do.

I spent an unforgettable eight and a half months at the Chalmers University of Technology in Henk Wymeersch's research team. Henk, I definitely learned a lot from you, not only on the technical aspects of my research but also about how to do a good research and publish it. I was very "lucky" to know and work with you. Hartelijk dank!

I also would like to thank Frank Leferink, Raymond Veldhuis, Andrë Kokkeler, Peter Baltus and Gerard Janssen for being part of my committee and their valuable feedbacks on this thesis.

All the not research-related issues were very easily solved with Lilian. Thank you also being a good listener of my problems. Thank you Eduard for your help with some of my indoor UWB measurements at UT. Moreover, other TE members: Alex, Stefan, Ibrahim Bilal, Olga, Ben, Robert, Pieter, Bart and the members of Microwave Photonics Mafia: Mauri, Reza, David, Leimeng,

Caterina. Thank you all for your friendship. During this process, I also had the opportunity to be a daily supervisor of two master students. Sjoerd, it was amazing what you did in such a short time and Merhawi I admire your efforts as the measurement facilities were rather limited in your case.

The winter of 2012 in Gothenburg was particularly cold, but I really felt warm when I was at the Chalmers University of Technology with the friendship of Gabo, Rocco, Christopher, Christian, Katharina, Mica, Lotfollah, Kasra and Philipp. Thank you for fruitful research discussions and easily accepting me to your friendly research environment.

Writing this thesis would be very hard without the PhD coach, Arjenne Louter. Arjenne, thank you for all your methods which really helped me to keep up.

Overall, it was hard to get used to the life in Enschede in the first few months. Turkish Student Association at Twente (TUSAT) kept me busy for my initial two years as a board member. With others, we achieved a fairly good reputation at the university - still proud with the Henk Zijm International Award. I would like thank other board members: Muharrem (also for being a very good housemate), Can Altunlu, Aykan, Haktan, Ugur, Can Arslan, Cagri. I also would like to thank my other friends Oğuzcan, Kardelen, Hayrettin, Alim, Recep, Hasan, Burcu, Mustafa Akın, Sertan, Özlem, Didem, Semih, Engin, Berk, Pınar, Sinem. Finally, Ansfrida, thank you very much for all the beautiful memories and listening my endless complaints for four years.

Finally, I would like to thank my family for giving me the freedom to take my own decisions and always being supportive even though the things are not going well. Sevgili ailem, hayatımın her aşamasında bana verdiğiniz destekten ötürü size ne kadar teşekkür etsem azdır. Her ne kadar son altı senedir sizlerden ayrı olsam da sizin varlığınız bana her zaman güç verdi.

Yakup Kılıç
Istanbul, Turkey
December 22, 2015

Biography

Yakup Kılıç was born in Istanbul, Turkey, in 1985. In June 2007, he received his B.Sc. degree in Electronics and Communication Engineering from Yildiz Technical University, Istanbul, Turkey. Later, he continued his study in the Electrical and Electronics Engineering Department of Bogazici University, Istanbul, and obtained his M.Sc. degree in September 2009 for his thesis on multiple input multiple output transmission techniques and link adaptation in wireless systems with dual-polarized antennas. Between August 2008 and September 2009, he also worked for Airties Inc. for some of his time and was involved in a project which aimed to improve the robustness of IEEE 802.11n links to channel failures and co-channel interference. Right after the M.Sc., he started to work in the Telecommunication Engineering Group at the University of Twente, the Netherlands for his Ph.D. thesis. He was a visiting researcher in the Signal and Systems Department in Chalmers University of Technology, Sweden, between August 2012 and April 2013. His research interests include statistical signal processing and channel modeling for wireless localization and communication.

List of publications

Journal publications

1. Y. Kılıç, H. Wymeersch, A. Meijerink, M. J. Bentum, and W. G. Scanlon, "Device-free person detection and ranging in UWB networks", *IEEE Journal of Selected Topics in Signal Processing*, vol. 8, no. 1, pp. 43–54, Feb. 2014.

Conference publications (peer-reviewed)

1. Y. Kılıç, H. Wymeersch, A. Meijerink, M. J. Bentum, and W. G. Scanlon, "An experimental study of UWB device-free person detection and ranging," in *Proc. IEEE Int. Conf. on Ultra-Wideband (ICUWB)*, Sydney, Australia, Sept. 2013, pp. 43–48.

2. Y. Kılıç, A. J. Ali, A. Meijerink, M. J. Bentum, and W. G. Scanlon, "The effect of human-body shadowing on indoor UWB TOA-based ranging systems," in *Proc. IEEE Workshop on Positioning, Navigation and Commun. (WPNC)*, Dresden, Germany, March 2012, pp. 126–130.

Other publications (not peer-reviewed)

1. Y. Kılıç, A. Meijerink, and M. J. Bentum, "Environment classification and range error mitigation in UWB time-based ranging systems," *Sense of Contact*, Soesterberg, The Netherlands, April 2012. (Poster presentation)

2. Y. Kılıç, A. Meijerink, and M. J. Bentum, "Locating the information: applications, technologies and future aspects", *De Vonk*, pp. 25. (Scintilla Student Magazine)

3. Y. Kılıç, A. Meijerink, and M. J. Bentum, "Localization in smart dust sensor networks", *URSI Benelux Forum*, Brussels, May 2010. (Poster presentation)

Invited talk

1. Y. Kılıç, "UWB device-free person detection and localization," *Workshop on Localization Research in Sweden*, Swedish Defence Research Agency (FOI), Stockholm, Sweden, March 2013.

Publications not related to this thesis

1. Y. Kılıç, M. Koca, and E. Anarım, "Space-Time-Polarization diversity in multiple input multiple output communication systems", in *Proc. of IEEE African Commun. Conf. (AFRICON)*, Nairobi, Kenya, Sept. 2009, pp. 1–6.

2. Y. Kılıç, M. Koca, and E. Anarım, "Cok girdili cok ciktili iletisim sistemlerinde uzay zaman kutuplama cesitlemesi" (in Turkish), in *Proc. of IEEE Signal Process. and Applications Conf. (SIU)*, Antalya, Turkey, April 2009, pp. 1–4.